MEASUREMENTS OF THE EFFECTS OF TUNNEL WALL PROXIMITY ON THE VELOCITY FIELD UPSTREAM OF A ROD WITH VORTEX SHEDDING IN LOW-SPEED FLOW

THESIS
David R. Hopper
Captain, USAF

AFIT/GAE/ENY/00M-07

DEPARTMENT OF THE AIR FORCE
AIR UNIVERSITY
AIR FORCE INSTITUTE OF TECHNOLOGY
Wright-Patterson Air Force Base, Ohio

The views expressed in this thesis are those of the author and do not reflect the official policy or position of the United States Air Force, Department of Defense, or the U.S. Government.

AFIT/GAE/ENY/00M-07

MEASUREMENTS OF THE EFFECTS OF TUNNEL WALL PROXIMITY ON THE VELOCITY FIELD UPSTREAM OF A ROD WITH VORTEX SHEDDING IN LOW-SPEED FLOW

THESIS

Presented to the faculty of the Graduate School of Engineering and Management

of the Air Force Institute of Technology

Air University

In Partial Fulfillment of the

Requirements for the Degree of

Master of Science in Aeronautical Engineering

David R. Hopper, B.S.

Captain, USAF

June, 2000

AFIT/GAE/ENY/00M-07

MEASUREMENTS OF THE EFFECTS OF TUNNEL WALL PROXIMITY ON THE VELOCITY FIELD UPSTREAM OF A ROD WITH VORTEX SHEDDING IN LOW-SPEED FLOW

David R. Hopper, B.S.
Captain, USAF

Approved:

Paul I. King
Thesis Advisor

14 Apr 2000
Date

Milton E. Franke
Committee Member

14 Apr 2000
Date

William Elrod
Committee Member

14 Apr 2000
Date

Acknowledgements

I could not have made it to this point on my own. I owe a debt of gratitude to many, that I can only hope to repay.

First, thanks to my thesis advisor, Dr. Paul King. His advice and leadership guided me through the painful process of discovery. Along the way, I also made liberal use of the assistance of Captain Patrick Wade. His work will follow mine, and I hope I made the path a little easier to pursue. Thanks to James Hall, who was right alongside for most of my AFIT education and way out front in my physical education. Thanks also to Ryan Pendleton and Dave Pritchard, to Greg Gilbreath, who has a lien on my diploma, and to many other friends who helped me through. Thanks to Andy Pitts and Jay Anderson, and the staff of the ENY laboratories.

For her patience, understanding, caring, and love, I thank my lovely wife, Jennifer. She always had the right words to say when the work became overwhelming. Finally, I thank the Lord for giving me all that I have—my family, my home, my country, and the opportunity to serve my country in such a unique and enriching way.

David R. Hopper

Table of Contents

List of Figures

Page

Page

Page

Page

List of Tables

List of Symbols

a	speed of sound (m/s)
A	amplitude
A_c	amplitude of combined wave
A_f	amplitude of fundamental frequency
A_h	amplitude of harmonic frequency
B	amplitude of sine portion of combined waves
c	acoustic speed (m/s)
C	amplitude of cosine portion of combined waves
CTA	constant temperature anemometer
D	diameter (m)
f	frequency
f_f	fundamental frequency (Hz)
k	hotwire directional calibration constant
k	constant used in amplitude model
k'	constant used in multi-cylinder amplitude model
M	Mach number
n	power term of amplitude model
R	radius (m)
r	distance from cylinder (incompressible) or apparent distance from cylinder (compressible) (m)
r_g	geometric distance from cylinder (compressible) (m)
S	Strouhal number
t	time (s)
U	velocity in laboratory x direction (m/s)
U_∞	freestream velocity (m/s)
$U_{1,2}$	velocity in wire 1 or wire 2 coordinate direction (m/s)

$U_{1,2cal}$	calibration velocity on wire 1 or wire 2 (m/s)
U_N	velocity normal to wire (m/s)
U_T	velocity tangential to wire (m/s)
$U_{x,yeff}$	effective velocity in the probe x or y direction (m/s)
V	velocity in laboratory y direction (m/s)
x_L	laboratory x direction
x_P	probe x direction
y_L	laboratory y direction
y_P	probe y direction

Greek Letters

$\alpha_{1,2}$	angles between wires 1 and 2 and the laboratory x-axis
δ	phase of combined waves (rad)
Γ	circulation (m^2/s)
ϕ	phase (rad)
ϕ_f	phase of the fundamental frequency (rad)
ϕ_h	phase of the harmonic frequency (rad)
ϕ_{lhs}	phase shift of left side of x perturbation model (rad)
ϕ_{shift}	phase shift of model (rad)
θ	angle of measurement position (rad)
ω_f	fundamental frequency (rad/s)
ω_h	harmonic frequency = $2\omega_f$ (rad/s)

Subscripts and Superscripts

1, 2	wire 1, wire 2
1, 2, 3	cylinder 1, cylinder 2, cylinder 3
c	combined
cal	calibration

eff	effective
f	fundamental (frequency)
g	geometric
h	harmonic (frequency)
L	laboratory
lhs	left hand side
N	normal
p	probe
shift	denotes arbitrary phase shift
T	tangential
x	x-direction
y	y-direction
∞	freestream
^	denotes coordinate axis direction

Abstract

High cycle fatigue is an important consideration in blade design for turbomachinery. Blades in an engine undergo countless loading cycles in a lifetime, the result of pressure waves that propagate upstream and downstream from disturbances in the flow. Better understanding of these effects would allow blade designers to reduce the effects of high cycle fatigue, such as costly recurring maintenance or catastrophic engine failure. An experimental study was undertaken to determine the unsteady flowfield upstream of a single cylinder in a subsonic flow. Von Karman vortex shedding from the cylinder produced a forcing function much like periodic blade passage in a turbine engine. A hot wire in constant temperature mode was used to measure the velocities upstream of the cylinder. Data were ensemble averaged and phase locked with the shedding from the cylinder to allow quasi-simultaneous comparison. The phase and amplitude of unsteady velocity data taken at a series of upstream locations were compared to a model developed from potential theory. The potential flow model for a single cylinder did not accurately predict the phase and amplitude change upstream the cylinder except when the cylinder was near the center of the tunnel. When virtual cylinders were added to account for endwall reflection, the prediction more closely approximated the behavior of the data. While much is yet to be understood, the results of this study indicate that the flowfield upstream of a disturbance may be reasonably predicted using elements of potential flow theory.

MEASUREMENTS OF THE EFFECTS OF TUNNEL WALL PROXIMITY ON THE VELOCITY FIELD UPSTREAM OF A ROD WITH VORTEX SHEDDING IN LOW-SPEED FLOW

1. Introduction

1.1 Background

High cycle fatigue is a leading cause of required maintenance and failures in turbine engine rotating components. Blades in an engine are subjected to large stresses due to high pressures and temperatures. Additionally, blades experience countless loading cycles in the form of pressure disturbances propagated from upstream and downstream components. Blade design has traditionally been based primarily on the steady forces on a blade. However, even small aerodynamic force fluctuations can have a large impact on the structural life of a blade if they coincide with the critical vibration frequencies of the blade [1]. When accounting for unknown unsteady forces on a blade, the engineer is required to overdesign the blade in order to prevent failure. Accurate prediction and modeling of the unsteady forces on a blade would allow the blade to be strengthened and stiffened as necessary to prevent oscillations at critical frequencies, while decreasing the need for blade overdesign and hence, the overall weight of the blade.

As rotor blades move past stator blades in an engine, each experiences fluctuating pressures. The frequency of this fluctuation is dependent on the ratio of stator blades to

rotor blades, or pitch ratio. A set of blades in an axial flow produces two forms of disturbances. The first is a convected disturbance generated by the boundary layer of a blade, seen in the form of a velocity deficit in the wake of each passing blade [2]. Because convected disturbances move with the flow, they affect only downstream components. The second is a potential disturbance, an inviscid effect that propagates radially outward from the blade at acoustic speed (c), or the vector sum of the local flow velocity and the speed of sound (a). Additional sources of unsteadiness, such as flutter of the blade rows and flow changes due to cooling in turbine blade rows, are present in the flow in an engine [3-4]. The flow model presented herein is limited in scope, and does not consider these additional disturbance sources.

To date, much work has focused on disturbances emanating from upstream wakes and potential disturbances. Fabian and Jumper showed that the disturbance field can be modeled through the superposition of convected wake vorticity and propagated potential disturbances moving into the flow with sonic velocity [5-9]. Korakianitis discussed the potential and convected wakes of a blade row and discussed methods for minimization of the excitation of the two effects through destructive interference by varying the stator/rotor gap and the pitch ratio [2-4].

Less work has been reported on the effect of potential disturbances propagated upstream into a flow. Wilson and Korakianitis indicate that the potential disturbance propagates both upstream and downstream into the flow, but consider only the downstream effects [10]. Fabian showed, however, that the upstream-propagated potential disturbance was on the same order of amplitude as the convected wake

downstream [5]. Fabian and Jumper [6-9] showed that unsteady pressures of high amplitude are seen near the trailing edges of a vane in cascade when components downstream excite the velocity field. The implication of the high amplitude near the trailing edge of blades in a cascade is a possible trailing edge singularity. Some theoreticians have rejected the possibility of a trailing edge singularity in unsteady flow, in harmony with the Kutta condition, which forbids a trailing edge singularity in steady flow. Others have suggested that such a condition may exist in a flow with unsteady component normal to the blade surface at the trailing edge [8]. If a trailing edge singularity did exist, it could be quite damaging to engine components. Determining whether or not a singularity might exist is an important part of characterizing blade row interactions in an engine. An accurate knowledge of the manner of upstream disturbance propagation was necessary to the investigation of a possible trailing edge singularity.

1.2 Periodic Fluctuations

A laboratory method of determining upstream effects of potential disturbances was sought. Commerford and Carta demonstrated a technique that employed the periodic Von Karman vortex shedding from a circular cylinder to provide a fluctuating velocity field that suits itself well to this type of investigation [15]. Fabian, Jumper and Falk used this technique in their experimentation [6-9, 11-14]. The periodic vortex shedding from a cylinder is comparable to the effects of blade passage in an engine, where rotor blades pass stator blades in a periodic fashion. The wakes of upstream blades in a flow cause changes in the incidence angles of the downstream blades. As a result, the circulation around the downstream blade, as well as the lift force, are altered. This creates a

disturbance which propagates both upstream and downstream into the flow. A cylinder shedding vortices also experiences a fluctuating lift force, indicating that the circulation around the cylinder alternates in much the same way as engine blades passing through upstream blade wakes.

A cylinder, then, is a reasonable model for a disturbance that would propagate upstream from a blade row in an engine. Changing the cylinder diameter and the flow velocity over the cylinder would control the frequency of shedding over a large range of Reynolds numbers. This allows the designer to select the frequency appropriate to the given model.

Each vortex shed from the cylinder produces a bound vortex of equal strength and opposite sign on the cylinder. At a point 90 degrees from the steady-state stagnation point on the surface of cylinder, the pressure varies sinusoidally as the separation point changes. Each pair of alternating-sense vortices creates one period of pressure variation, which propagates into the flow as a potential disturbance.

1.3 Strouhal Number and Predicted Shedding Frequency

The dimensionless frequency, or Strouhal number (S), is important in predicting the frequency at which vortices will shed from a cylinder. It is defined as

$$S = \frac{fD}{V} \tag{1}$$

where f is the frequency of shedding in Hz, D is the cylinder diameter, and V is the velocity of the flow. Roshko [16] shows a correlation of experimental data

demonstrating that for a large range of Reynolds numbers (from 10,000 to 200,000), S is nearly constant at approximately 0.2. The implication of this is that, in this range of Reynolds numbers, there exists an almost linear correlation between shedding frequency and flow velocity for a given cylinder diameter.

1.4 Purpose of Thesis

The main purpose of this experiment was to determine the magnitude and the character of the velocity fluctuations upstream of a periodic flow disturbance caused by the alternate shedding of Von Karman vortices from a single circular cylinder. The vortex shedding caused upstream disturbances similar to those from the fluctuating bound vorticity around a blade experiencing changes in incidence caused by the upstream wakes of passing blades. This experiment was designed so the cylinder would shed vortices at a frequency of approximately 2.6 kHz. The cylinder was placed perpendicular to the flow in a rectangular test section and the velocity field upstream of the cylinder was measured using a cross-wire hotwire in constant temperature mode.

The equipment used in this experimental study is described in Chapter 2. Chapter 3 outlines the procedures used in the experiment and Chapter 4 contains the results. Chapter 5 presents a model for the data using equations based on the theory of potential flows. Chapters 6 and 7 contain conclusions drawn from the experiment and recommendations for further work.

2. Equipment and Calibration

2.1 Tunnel

This testing was conducted in the compressor cascade test facility located at the Air Force Institute of Technology (Figure 1). A 40-hp (30 kW) centrifugal blower rated at 3000 ft^3/min (85.0 m^3/min) at 1.6 psig (11.0 kPa) total head provides airflow for the cascade. The blower pulls outside or room air through an electrostatic filter. Both filter and blower are in separate chambers inside a large wooden box insulated with foam rubber. Outside air is supplied to the blower through a 12 in (30-cm) duct. Laboratory air may be mixed with outside air by opening the door on the filter side of the box. The air is pulled through the filter by the pressure differential created by the blower, and into the chamber containing the blower. From there it passes through the blower into a diffuser nine feet (2.7 m) in length. Additional airflow is also available from a 100-psig permanent centralized ejector supply system directly to the diffuser section. The flow slows to about 20 ft/sec (6.1 m/s) at the stilling chamber entrance. A center body plug in the stilling chamber continues diffusing the flow down to about 10 ft/sec (3.0 m/s) and obstructs the acoustic path between the blower and the test section. The flow is filtered and straightened by a series of meshes and a 4 in (10.2-cm) thick aluminum honeycomb. A 2-D long radius ASME bell mouth nozzle accelerates the flow for entrance into the test section. Additional information about the design and performance of the cascade test facility is found in Allison [17].

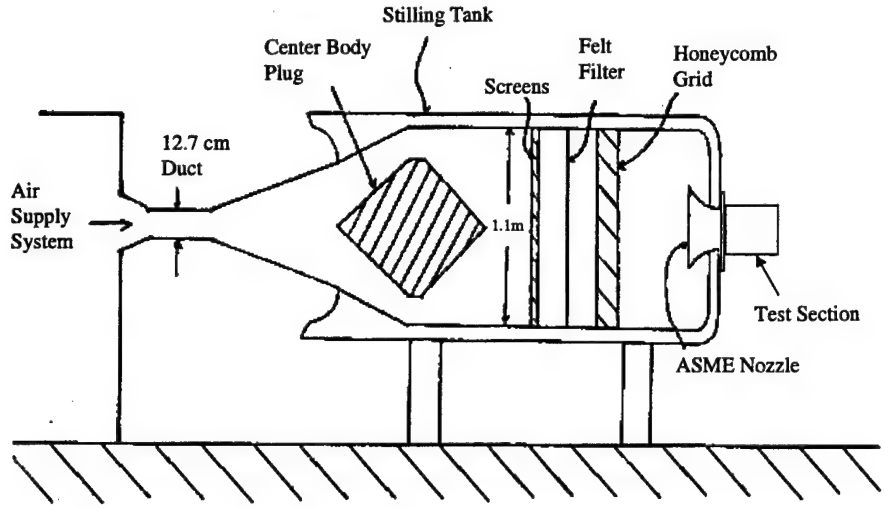

Figure 1. AFIT cascade test facility (adapted from Costello [18])

2.2 Test Section

The test section contains the cylindrical rod and is a rectangular box constructed of 2024 aluminum. The box has inner dimensions 2 in (5.1 cm) wide by 8 in (20.3 cm) high (Figure 2). The dimensions of the box were chosen to match the dimensions of the existing mating collar on the tunnel throat which had a throat area of 16 in^2 (103 cm^2) as recommended by Allison [17]. The walls of the test section slide to vary its length in the streamwise (longitudinal) direction from 7.5 in (19 cm) to 9.75 in (24.8 cm). The purpose of the sliding walls is to move the cylinder in the x direction with respect to the hotwire measurement point. When the walls are extended the gap between the sliding

portion of the wall and the stationary portion is covered with tape or filled with an aluminum spacer of the appropriate dimension.

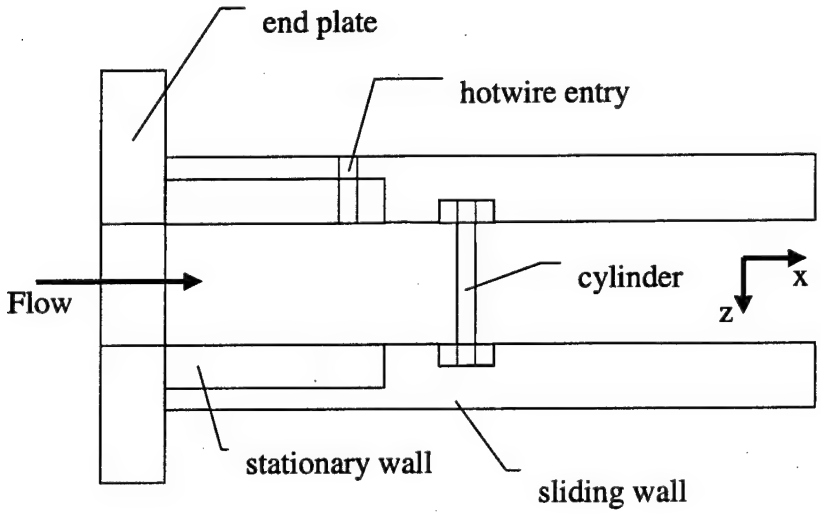

Figure 2. Top view of test section

A hotwire insertion point is located on one wall of the test section. The cylinder was placed on a slider recessed into the walls of the test section. Lateral movement of the hotwire was combined with transverse rod movement and longitudinal test box movement to provide complete 3-dimensional flowfield measurement capability upstream of the cylinder.

2.2.1 Cylindrical Rod

The cylindrical rod was machined to 3/16 in (0.48-cm) diameter from round aluminum stock. A hole was also bored from one end of the cylinder halfway down its length to accept a pressure transducer. As discussed in section 1.3, the choice of cylinder diameter in part determines the shedding frequency. Fabian [5] used a factor called reduced frequency to determine the proper cylinder size. Reduced frequency is a parameter used in cascade design, which normalizes frequency by the chord length of the blades in the cascade. Fabian designed his cascade to mimic the operation of the F109 engine compressor. To this end, he selected the cylinder diameter and tunnel speed so that the reduced frequency of the tunnel was the same as the reduced frequency due to blade passage in the F109 compressor. Since no cascade was used in this experiment to provide a chord length reference, reduced frequency had no meaning. It was decided to use the same cylinder diameter as Fabian. This had the advantage of direct comparison between the results of this experiment and Fabian's results.

2.2.2 Two-Dimensional Flow Assumption

Early in this experimentation, a short study was undertaken to determine whether the flow in the tunnel could be assumed two-dimensional. A series of nine data sets was taken across the center of the tunnel, the z location of the probe varying from –0.5 in to +0.5 in (+/- 1.27 cm) where z = 0 was the center of the tunnel. This was done with the cylinder resting against the bottom surface of the test section. While not completely eliminating its effect in the flow, there would be no vortices shedding from the cylinder and the steady flow velocities of the tunnel could be estimated. The velocities across

these nine points agreed with each other within 1 percent. No boundary layer or other abnormal effects were observed in the measured region. As a result, the flow was assumed to be two-dimensional across the center portion of the tunnel. A single z location was used for the remainder of the data collection. The point z = -0.25 in (0.64 cm) was selected to keep as much of the hotwire probe out of the flow as possible to minimize probe interference, but would still be well inside the region of known two-dimensional flow.

2.2.3 Flow Speeds

When the 30 kW blower was operated at full speed, and without using supplemental house air, the flow velocity was found to be approximately 130 m/s, corresponding to a Mach number of approximately 0.37. This was near enough the flow speeds used by Fabian [5] to allow direct comparison with his results. At this flow velocity the fundamental or shedding frequency of the cylinder was found to be approximately 5.1 kHz, corresponding to a Strouhal number of 0.187. In addition to the fundamental frequency, a significant quantity of noise was also present in the signal at about 8 kHz. In fact, this noise remained in an ensemble of 250 runs, indicating that it was either phase locked with the cylinder shedding or that it was extremely large in amplitude so that ensembling failed to eliminate it. This 8 kHz noise, including attempts to identify and isolate it, is discussed in more detail in section 3.3.1. Because this noise was between the fundamental frequency of 5.1 kHz and a possible first harmonic at 10.2 kHz, it was not desirable to eliminate it using a low pass filter. Notch filtering of the data at this frequency was attempted, but introduced unacceptable levels of bias into the data.

A new flow speed at half the first was selected. The blower was operated at half speed, again without the use of supplemental house air, and the flow velocity was found to be approximately 65 m/s or Mach 0.18. The shedding frequency at this speed was approximately 2600 Hz, corresponding to a Strouhal number of 0.183. The 8 kHz noise was still present at this tunnel speed. Because the new fundamental frequency and its first harmonic were both well below the noise frequency, the data were low-pass filtered with a 3dB cutoff frequency of 6.0 kHz to eliminate it.

2.3 Data Acquisition System

2.3.1 Hotwire Velocity Measurement

The velocity data were taken using a cross-wire hotwire in constant temperature mode. The hotwires used were TSI model 1240-20 hot film transducers, designed to have an upper frequency resolution of approximately 250 kHz. Excitation, amplification, low-pass filtering (30 kHz), and voltage offset were provided to the hotwire by two Dantec model 90C10 CTA Modules mounted in a model 90N10 frame. The 90N10 frame also provided for temperature measurement. A temperature probe was positioned just outside the flow downstream from the test section to provide an ambient temperature reference for thermal correction of hotwire velocity. The hotwire signal conditioner was controlled by a software package called Streamware, which was provided by Dantec with the 90C10 CTA system.

2.3.2 Kulite Pressure Transducers

Unsteady pressures at the surface of the cylinder were used to trigger the data acquisition. An ultraminiature Kulite XCS-062 differential pressure transducer was used for this purpose. The Kulite was inserted into a hole drilled axially from one end of the cylinder. Another smaller hole drilled perpendicular to the first from the surface of the cylinder allowed the Kulite to measure the surface pressure. The cylinder was mounted in the test section so that the surface pressure measurement point was at the top of the cylinder. Excitation (5V), amplification, low-pass filtering (10 kHz), and voltage offset for the pressure signal were provided by a Vishay Measurements Group Incorporated model 2310 signal conditioner. Figure 3 shows the pressure signal over a typical data sample.

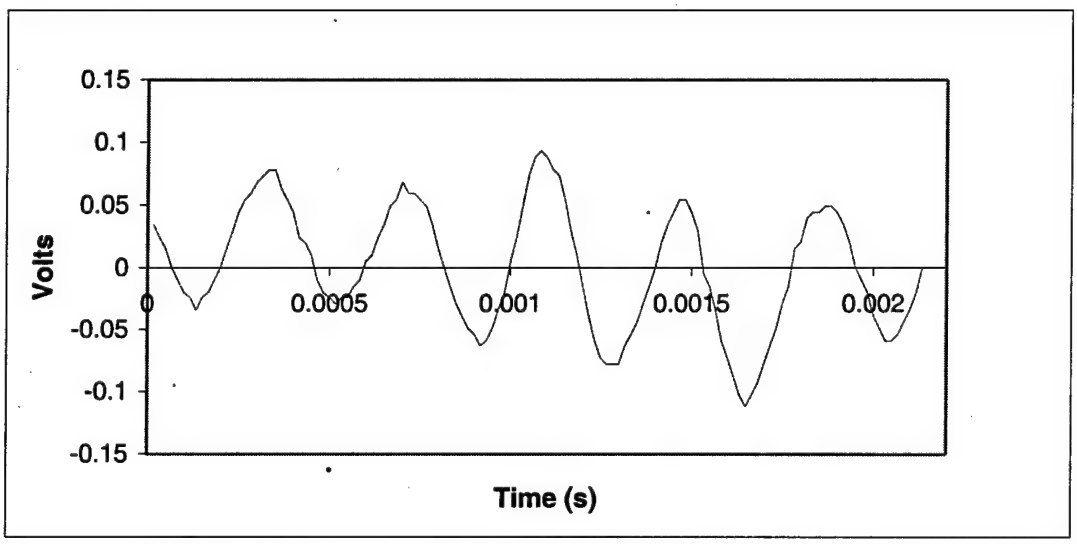

Figure 3. Single run trace of pressure signal voltage

The pressure signal proved to be quite consistent in frequency, but the amplitude was rather irregular. The mean value of the pressure signal also tended to wander. To

make the signal somewhat more consistent for triggering purposes, the signal conditioner was set to accept only the alternating current or unsteady portion of the signal. This had the effect of making the pressure alternate about a more constant mean of zero. Because the mean pressure level was lost, the pressure voltage was not converted to units of pressure.

2.3.3 Triggering

The data collection was triggered when the pressure signal voltage reached a selected level on a positive slope. The trigger point in Figure 3 is the peak in the center of the figure. The trigger level was selected to be near the absolute maximum reached by the pressure signal. This forced the trigger point to be at or near a peak in the pressure wave. It was necessary to trigger exactly at a peak in order to phase lock the data. A more complete discussion of phase locking of the data is in section 3.1. To ensure the trigger was at a pressure peak, the voltage at the trigger point was compared to the voltage at two points immediately before and after the trigger. If the comparison showed the trigger point to be a maximum then the data were kept and written to a file. Otherwise the run was discarded. Each run consisted of 128 data points with half before and half after the trigger point. At each measurement location, 250 runs were collected into a single data file.

2.3.4 Recording

Analog data were brought from the temperature probe, the hotwire (2 channels, one for each wire) and the pressure transducer through a National Instruments SCB-68 shielded connector box. Data were then recorded on the hard drive of a Dell computer

with an Intel Pentium 400 MHz processor. Analog-to-digital conversion was carried out by a National Instruments AT-MIO-16E-1 board, a sequential sampling board capable of sampling 8 differential inputs at a total rate of 1.25×10^6 samples each second. The AT-MIO-16E-1 board had a minimum resolution of 4.88 mV and was controlled by National Instruments Labview version 5.0.

2.4 Hotwire Calibration

2.4.1 Hotwire Calibration System

The hotwire anemometers were calibrated using a TSI model 1125 calibrator that provided the capability for both velocity and directional calibration. Airflow to the calibrator was from the 100-psig permanent centralized air supply system. A pressure gage displayed the differential pressure of the airflow into the calibrator, which correlated directly with the velocity of the air through the calibrator orifice. This correlation was taken from a table provided by the calibrator manufacturer that was valid for calibrator speeds from 2.5 to 300 m/s [19]. A 220V heater with a feedback-controlled thermostat was installed upstream of the calibrator to allow control of the air temperature into the calibrator.

The hotwire probe and probe holder were first mounted in the TSI 1125 calibrator and the airflow was turned on. The angles of the wires on the TSI 1240-20 hotwire probes could not be measured using the overhead projector technique described by St. Germain [20] because of the crossflow configuration of the probes. Instead, the wires were assumed to be perpendicular to each other, verified by an inspection of the wires

under a microscope, but without a strict measurement of the angle. The hotwire was oriented in the calibrator so that the flow bisected the angle between the wires by visually aligning the prongs of the hotwire vertically over the calibrator air orifice.

2.4.2 Velocity Calibration

Velocity calibration of the hotwires consisted of a series of 21 points of known velocities between 60 and 85 m/s or between 100 and 150 m/s depending on the tunnel speed for which the calibration was being performed. These velocity ranges were much smaller than the tabulated range provided by TSI, so a cubic spline was fit to the tabular data. Points were then taken from the curve fit as required to space evenly about the planned tunnel speed. Velocity calibration produced a curve fit to a velocity versus voltage curve, in the form of either of the following two equations.

$$E^2 = A + BU_{cal}^n \tag{2}$$

$$U_{cal} = C_0 + C_1 E + C_2 E^2 + C_3 E^3 \tag{3}$$

Equation 2 is called the power law or King's Law and equation 3 is the polynomial law. In either case, the coefficients (A, B, and n for equation 2 or C_0, C_1, C_2, and C_3 for equation 3) provide the necessary information to convert between hotwire bridge voltage (E) and calibrated velocity (U_{cal}). The Streamware software automatically produced both sets of coefficients and the calibration error for each. For this reason, the equation with the best curve fit to the calibration data was used to decompose the data. More information about the calibration of hotwires, including the development of the

above equations from heat transfer principles can be found in Bruun [21] and DeCook [22].

2.4.3 Directional Calibration

A hotwire in constant temperature mode varies the current in the wire to maintain constant temperature through electrical power dissipation. As flow velocity changes, the voltage across the wire changes as well. Predictably, the heat transfer from a wire perpendicular to a flow is substantially higher than from a wire parallel to a flow. A flow crossing a single wire at an arbitrary angle will have components normal to the wire and tangential to the wire. The velocity measured by the wire is dependent on the angle between the wire and the flow and is given as

$$U_{cal}^{\ 2} = U_N^{\ 2} + k^2 U_T^{\ 2} \tag{4}$$

where U_N and U_T are the normal and tangential components of velocity (also called effective velocities) across the wire and k^2 is a small positive constant. When the velocity is normal to the wire, U_{cal} will be equal to U_N. When parallel to the wire, U_{cal} is equal to kU_T. In order to calculate the value of k, the wire voltage at a series of points at a known flow velocity and different angles with the flow are recorded. In this case, 9 points were used with different flow angles. The calculation of k was performed automatically by Streamware.

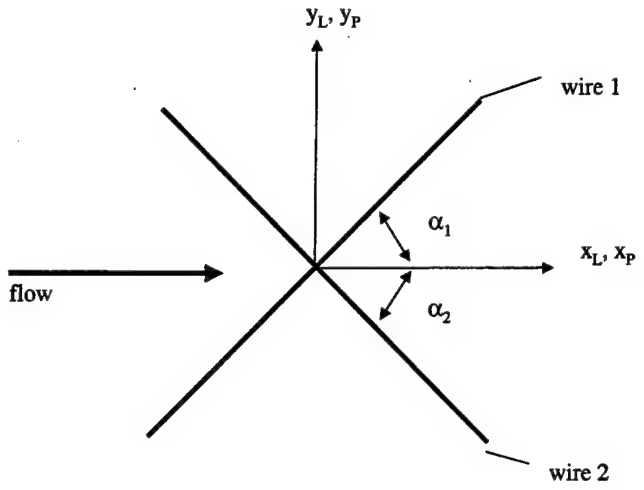

Figure 4. Hotwire orientation with probe and laboratory axes.

The hotwire probe shown in Figure 4 is aligned with the tunnel or laboratory axis. The positive x direction for the laboratory (x_L) is in the flow direction, as is the positive x of the probe. The angles between the wires and the laboratory x direction, α_1 and α_2, are both 45 degrees. When the probe is rotated about the z-axis, the probe axes no longer align with the laboratory axes and the two angles α_1 and α_2 are no longer equal. When the hotwire was placed in the tunnel, it was oriented so that the probe x-axis coincided with the laboratory x-axis as shown in Figure 4. The procedure for this alignment is in section 2.4.5.

2.4.4 Verification of Calibration

The velocity and directional calibrations were verified by setting an arbitrary velocity and probe angle in the calibrator and recording the wire voltages. The voltages were converted to velocities in the laboratory x and y directions, as detailed in sections 2.4.2, 2.4.3 and 2.4.6. The steady state indicated velocities on the probe were in all cases within 2 percent of the known velocity from the calibrator.

2.4.5 Aligning the Hotwires in the Test Section

Following calibration, the hotwire was placed in the test section and aligned so the steady state flow bisected the angle between the wires. Because of the difficulty of removing the forcing cylinder from the test section, the cylinder was lowered until it rested on the lower endwall of the test section. To compensate for the asymmetric effects this would produce, another cylinder of the same diameter was temporarily affixed with an adhesive to the upper endwall of the test section, directly opposite the lower cylinder. Using the velocity calibration coefficients and the directional calibration obtained earlier, the hotwire was turned in the flow until both wires registered the same steady-state velocity. The wire velocities were either viewed through the directional calibration function of Streamware, or by recording data and processing it through the velocity decomposition algorithm described in section 2.4.6.

2.4.6 Velocity Conversion of Hotwire Data

The voltages from the hotwires were modified by the Dantec signal conditioner to have an offset and a gain. This was done to have the largest signal amplitude possible

that would still fall in the +/-10V range of the A/D board. To convert these voltages to the hotwire bridge voltages, the following relation was applied.

$$E = \frac{E_{out}}{Gain} + E_{off} \tag{5}$$

In this expression, E is the bridge voltage, E_{out} is the output voltage, and E_{off} is the offset voltage.

Bridge voltages were converted to velocities by either the power law or the polynomial law (equations 2 and 3), whichever showed the least error in the calibration data curve fit. The velocities obtained by equations 2 and 3 are referred to as calibration velocity, U_{cal}. Calibration velocities were converted to effective wire cooling velocities in the probe x and y direction by [23]

$$U_{xeff}^2 = U_{1cal}^2 (1 + k_1^2) \cos^2(\pi - \pi/2) \tag{6}$$

and

$$U_{yeff}^2 = U_{2cal}^2 (1 + k_2^2) \cos^2(\pi + \pi/2) \tag{7}$$

Effective velocities were then converted to velocities in the wire 1 and wire 2 directions by rewriting equation (4) as

$$U_{xeff}^2 = k_1^2 U_1^2 + U_2^2 \tag{8}$$

and

$$U_{yeff}^2 = U_1^2 + k_2^2 U_2^2 \tag{9}$$

and solving for U_1 and U_2.

Finally, velocities in the wire 1 and wire 2 directions were converted to velocities in the laboratory x and y directions by

$$U = U_1 \cos\alpha_1 + U_2 \cos\alpha_2 \tag{10}$$

and

$$V = U_1 \sin\alpha_1 - U_2 \sin\alpha_2 \tag{11}$$

where U is the velocity in the laboratory x direction, V is the velocity in the laboratory y direction, and α_1 and α_2 are the angles between the wires and the laboratory x direction as defined in section 2.4.3. Intermediate conversion to probe x and y coordinates was avoided by aligning the probe axes with the laboratory axes by the procedure of section 2.4.5. Thus both α_1 and α_2 were taken to be equal to 45 degrees.

2.4.7 Uncertainties

Several points of uncertainty exist in the hotwire calibration and its placement in the tunnel. First, the known velocity of the calibrator was accepted because there was no method to verify it. The calibrated probe, however, showed velocities in the tunnel that were within 2 m/s of values measured using a pitot-static probe. This indicated that the calibrator velocities were fairly accurate, but the accuracy of the pitot-static system was not known. The steady state velocity was not important to the outcome of this experiment, however. The relative amplitudes of the unsteady velocities at different locations were important, and in theory, would be largely unaffected by uncertainty in the steady state velocity.

The wires of the hotwire probe were visually examined to verify orthogonality, but no method was available to measure the exact angle between the two. A related concern was the accuracy in orienting the hotwire probe in the calibrator. The best method found for aligning the probe so the flow bisected the angle between the wires was visually aligning the parallel prongs vertically by viewing from above and rotating the probe until the upper pair of prongs completely obscured the lower pair. When the calibration was performed, the potential errors of wire angle and probe orientation should not have much effect as long as they are not gross. The calibration will find the proper correlation between velocity and voltage. The calibration for the wire used in this experiment made use of a second order polynomial curve that fit the calibration data with an error of less than 1 percent.

The hotwire was oriented in the tunnel by rotating it until the wire velocities were the same. If the wire velocities are exactly the same, the orientation relative to the flow will be exactly the same as in the calibrator. In all cases, the velocities in the wire 1 and wire 2 directions were matched to within 1 m/s in the tunnel.

The effects of temperature on the hotwire output voltage were addressed by performing calibrations at different air temperatures. After a short period of data acquisition, however, it was seen that the tunnel temperature could be easily controlled within 1 degree Celsius of the calibration temperature by mixing warm laboratory air with cold outside air in the tunnel intake. For this reason, temperature compensation of the hotwire output was considered unnecessary and was not pursued.

2.5 Kulite Calibration

The Kulite XCS-062 ultraminiature pressure transducer used to measure surface pressure of the cylinder was calibrated using a handheld vacuum pump with digital display, the Measurements Group 2310 signal conditioner and a voltmeter. A series of pressures were input to the transducer using the handheld vacuum pump through a length of flexible tubing. The corresponding voltages were then read from the voltmeter, which was connected to the output of the signal conditioner. The same excitation voltage (5V) used in calibration was used during data collection.

3. Experimental Procedures

3.1 Phase-Locking the Data

Velocity data were taken at a large number of discrete points, and it was desired to compare these data in a quasi-simultaneous fashion in terms of phase and amplitude. Additionally, a single velocity measurement sample in the test section showed a large amount of high frequency noise. One source of this noise is discussed in section 3.3.1. In order to create a usable signal, a large group of runs was ensemble averaged. The number of runs required in an ensemble to suppress the noise was determined experimentally to be approximately 250. To preserve the information from the rod-based disturbance over a large ensemble set, and to be able to compare data taken at one discrete location to data taken at the next, it was necessary to trigger each data set at exactly the same relative point in the pressure wave.

This was accomplished by sending the voltage signal from the pressure transducer into a trigger channel in the data acquisition card (see section 2.3 for a complete description of the data acquisition system). A Labview program was designed to trigger the data acquisition at a specific voltage and write to a file. The trigger voltage was set to be near the highest maximum voltage observed from the pressure transducer for the given tunnel speed. This would force the trigger to be at or near a peak of the pressure signal. The trigger point was further screened by comparing it to its nearest four neighbors, two on either side. If the trigger point was not greater than or equal to its nearest neighbors, and those two points not greater than or equal to their neighbors, the sample was rejected.

In this manner, only samples that triggered at exactly a peak in the pressure wave were accepted. This forced the relative phase of successive samples to be the same. This process is termed phase-locking the data, and allows multiple data sets to be analyzed as though they were taken at the same time.

3.2 Tunnel Conditions

For the results reported herein, the tunnel flow velocity was held constant at approximately 65 m/s, corresponding to a Mach number of 0.18. Temperature in the test section was controlled at 24 degrees C (the same temperature at which the hotwire probe was calibrated) by mixing laboratory air with outside air. Fairly close temperature control was possible, so the temperature never varied more than 1 degree C in either direction.

3.2.1 Measurement Locations

Velocity measurements were taken in the locations shown in Figure 5. Locations of the cylinder are shown as small circles on the chart, with the flow moving left to right. The hotwire was fixed in the center of the tunnel and the cylinder moved on a slider in the y direction and with the tunnel sidewalls in the x direction. Since it was desired to know the flowfield upstream the cylinder, the cylinder was used as the origin of the axis system. In Figure 5 the negative x axis is in the direction of flow, meaning that, as the cylinder was displaced further from the hotwire measurement location, the x distance from the cylinder to the hotwire became more negative. A positive y displacement indicates that the cylinder was moved below the hotwire.

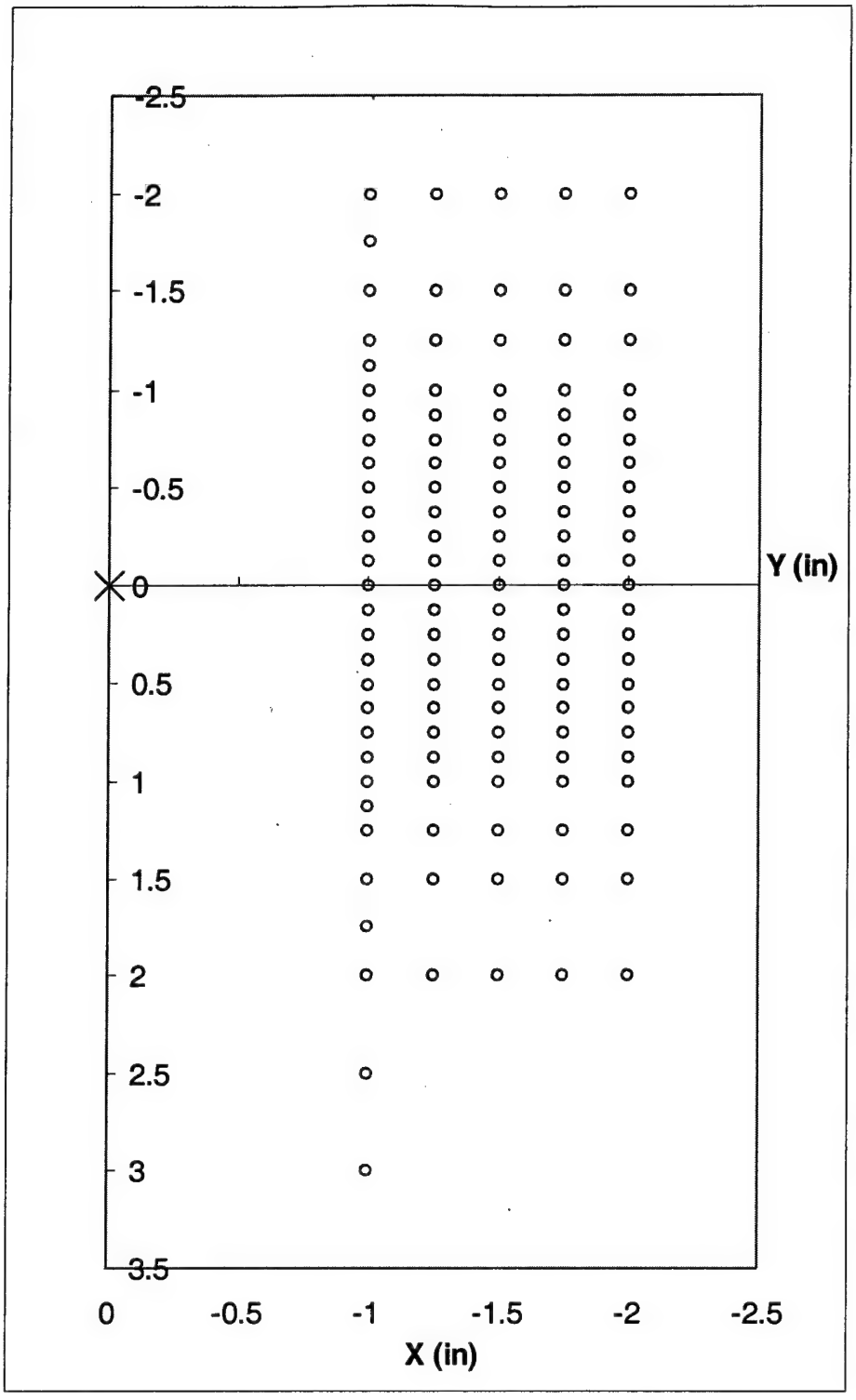

Figure 5. Cylinder locations with hotwire fixed at tunnel center

3.2.2 Off-Centerline Location

Additional data were taken with the hotwire positioned 1.625 in (4.13 cm) above the centerline of the tunnel. Again, the cylinder was used as the origin of the axis system, with y values ranging from 4.625 in to -1.625 in (11.75 cm to -4.13 cm). Only one x location was examined with the hotwire off the tunnel center, x = -1 in (-2.54 cm).

3.3 Data Acquisition

A clean Karman vortex street was not expected at the Reynolds numbers of this experiment. Schlicting [24] says that regular shedding of this type occurs only for Reynolds numbers between 60 and 5000. Instead the data were quite irregular in amplitude, as seen in Figure 3 of section 2.3.2. The method Fabian used to overcome the irregularity in the signal was to ensemble average numerous runs [5]. The shedding from the cylinder proved to be quite consistent in frequency and was used to trigger the data collection. In order to preserve the time behavior of the data when averaged over a large number of runs, the runs were phase locked. The trigger was taken to be in the center of the data file, with half of the data collected before the trigger and half afterward.

The data collection was supervised by a routine written in National Instruments Labview version 5.0 graphical programming language. The bulk of the routine came from a sample program included with the Labview software. This program was modified so it would automatically trigger the data collection, compare the value of the pressure signal at the trigger point to its four nearest neighbors to determine if the trigger occurred at a true maximum, and if so, write the data to a file. Because the process was automated,

files of 250 runs could be collected in just a few minutes. Data at a single location were always taken during a single tunnel run with no interruptions. In most cases, entire sets of data at a single x location were taken during the same tunnel run, as the tunnel did not need to be shut down to move the cylinder in the y direction.

3.3.1 Tunnel Vibration

Early in the data collection process, an anomaly was observed in the data. For a tunnel speed of approximately 133 m/s, a shedding frequency (fundamental) of 5.1 kHz was expected, with a possible harmonic at 10.2 kHz. The fundamental frequency was observed, however, a second frequency at approximately 8 kHz was also present in the reduced data. Since the theory made no account for this frequency, an investigation was undertaken to find its source.

Using an accelerometer and a frequency spectrum analyzer, vibration readings were taken from various locations on the exterior of the test section, stilling chamber, and associated air supply system. Readings were also taken on the end of the hotwire probe holder. With the cylinder in the flow, vibrations at the fundamental frequency were observed at most locations on or near the test section, including the probe holder. Also present, though, and typically larger in amplitude, were vibrations in the 8 kHz region. These vibrations were present at all locations along the stilling chamber and air supply system and regardless of whether the cylinder was in or out of the flow. When the flow velocity was changed, the shedding frequency of the cylinder changed according to theory, but the 8 kHz vibration did not noticeably change in frequency. The 8 kHz vibration was also present when the permanent centralized air supply system was used to

provide flow instead of the 30 kW blower. With the accelerometer mounted on the test section and no airflow, the tunnel was struck at various locations using a rubber mallet, and a ringing at 8 kHz was observed. This combination of observations led to the conclusion that the 8 kHz vibration was an inherent structural mode of the tunnel and not a flow effect.

An attempt was made to isolate the stand used to support the hotwire probe and probe holder from this vibration using various forms of rubber gasket and other insulating material. Additionally, the cables from the hotwire probe to the signal conditioner were insulated with soft foam rubber at each point they contacted a surface. With the probe out of the flow, overall vibrations were reduced on the probe holder, but as soon as the probe was reintroduced to the flow, the vibrations returned at their previously observed amplitudes. At this point it became apparent that isolation against the vibration was not possible because, while not inherently a flow phenomenon, the vibration was being transferred to the flow and would be present in any velocity measurements in the flow.

3.3.2 Solution to Tunnel Vibration

Determination of the source of the vibration would likely have required complete disassembly of the diffuser and stilling chamber without a guaranteed result. Because of time constraints on the research, this approach was not considered practical. Instead, it was decided to reduce the flow velocity in the test section to approximately half its previous value. Assuming Strouhal number (S) to remain constant, this would result in halving the fundamental frequency. The data could then be filtered at a frequency that would allow both the fundamental and the harmonic frequencies to pass while excluding

the 8 kHz vibration. When the tunnel was run at half the speed, the shedding from the cylinder was observed to be approximately 2600 Hz, roughly half of the frequency at the higher tunnel speed. This result supports the assumption of constant S in this region.

3.4 Data Reduction

The data were processed using programs written for Matlab software. First, a routine called ensfilt would read a file containing any given number of runs (typically 250), ensemble average them, filter out signal content above a predetermined frequency level, convert the hotwire voltages to velocities, and output a data file of averaged temperature, velocity and pressure. This routine also provided the capability to view the frequency content of the data by use of a digital fast-Fourier transform and to view the data in terms of wire voltages, effective velocities, x and y velocities or cylindrical coordinate velocities. Each file contained data taken at a separate tunnel location.

A second routine called minim was used to fit the data to a two-frequency sinusoidal curve through minimization of the error between the two. This program used the Matlab function fminsearch to minimize the error between the data and sinusoidal approximations to the pressure and velocity data. The Matlab code for all routines used in the processing of the data can be found in Appendix A.

3.4.1 Average and Filter the Data

Ensemble averaging consisted of taking the data file of four columns (temperature, 2 hotwire, and pressure), each 128 times the number of runs in length, adding each of the 128 data points to all the corresponding points in successive runs, then

dividing by the number of runs. Phase locking the data at the time of its collection caused the files to be aligned so this simple averaging process would not cause relevant information to be lost.

Filtering of the velocity data was accomplished using a fourth order low pass Butterworth filter with a cutoff frequency of 6 kHz. The filter was applied with the Matlab filtfilt command that uses a forward and reverse digital filtering process that minimizes phase distortion of the filtered data. The effect of filtering on the phase of the data was examined by reducing two data files with and without the filter. The phase of filtered and unfiltered waves at the fundamental frequency agreed within 0.01 rad.

Some startup and ending transients were observed in the filtered data, so an attempt was made to emphasize the center portion of the data file using a Hanning window [25]. This windowing multiplies the data by half a cosine wave, aligned so the center portion of the data is multiplied by one and the endpoints of the data are multiplied by zero. For the nth element of an N element data set, the function looks like:

$$data(n) = \left[\left(data(n) - mean \right) * \frac{1}{2} \left(1 - \cos \frac{2\pi n}{N} \right) \right] + mean \tag{12}$$

Notice that the mean of the data set is first subtracted from the nth point and then added back again after the cosine window is applied so that the signal mean is unaffected by the windowing process. After filtering the data the windowing was reversed to return the natural character of the data.

In some cases, the Hanning window was not sufficient to remove startup and ending transients from the data. To prevent these transients from interfering with the interpretation of the data, the first and last 10 points were removed from the filtered data sets. Filtering of the pressure data was not necessary, but the pressure files were truncated in the same manner as the velocity data in order to make an easier comparison of the resulting wave shapes. An example of pressure and hotwire voltages after completing this process is shown in Figure 6.

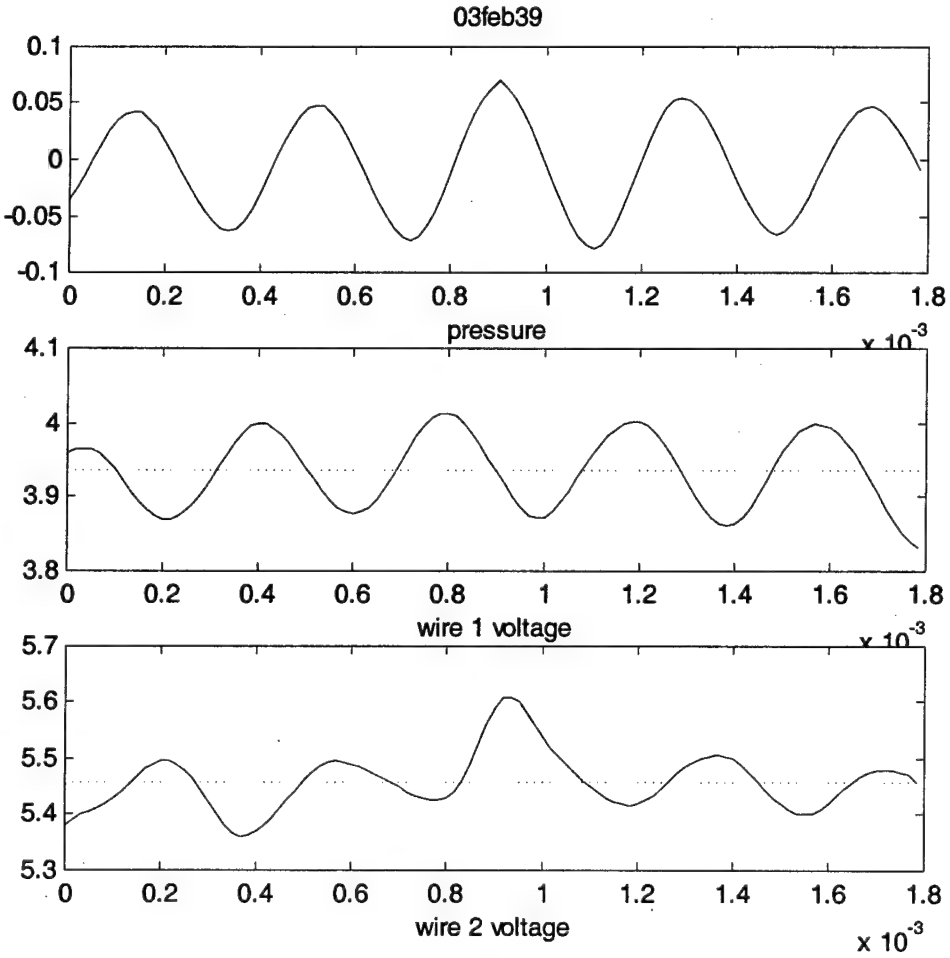

Figure 6. Pressure and hotwire voltages at x = -1.25 in, y = 0.5 in

3.4.2 Velocity Decomposition

Following the averaging and filtering of the data, the hotwire voltages were first converted to velocity in the wire 1 and wire 2 directions using the algorithm outlined in section 2.4.6. An example of the resulting velocities is shown in Figure 7.

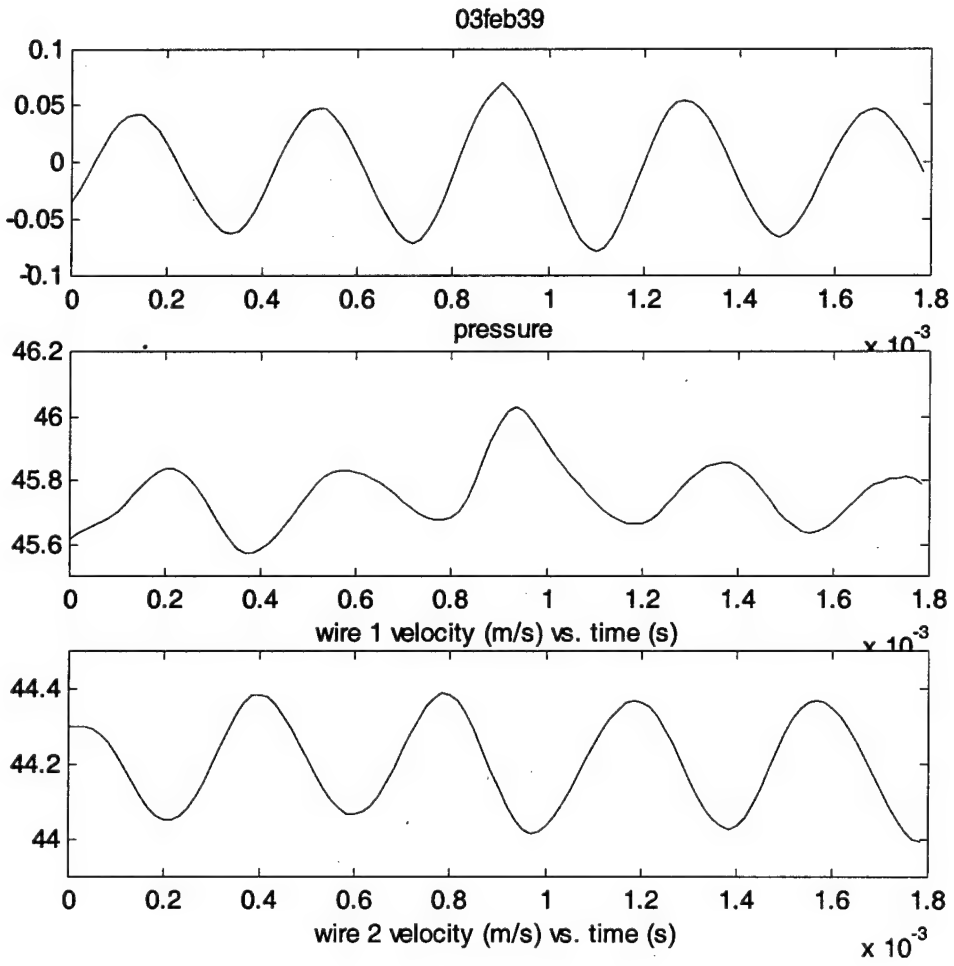

Figure 7. Pressure and velocities in the wire directions at x = -1.25 in, y = 0.5 in

The y-axis of the pressure plot is the voltage from the pressure transducer. The direct current portion of the pressure signal was subtracted in signal conditioning to make more consistent triggering possible. Because the actual voltage level from the transducer was discarded in this manner, conversion of the transducer voltage to pressure was not considered to add any significant information in terms of discovering the flowfield upstream of the cylinder. For order of magnitude purposes, however, 1 V measured on the differential pressure transducer was approximately equal to 1 psi.

The wire direction velocities were converted to velocity in the x and y directions, again using the algorithm of section 2.4.6, and are displayed in Figure 8.

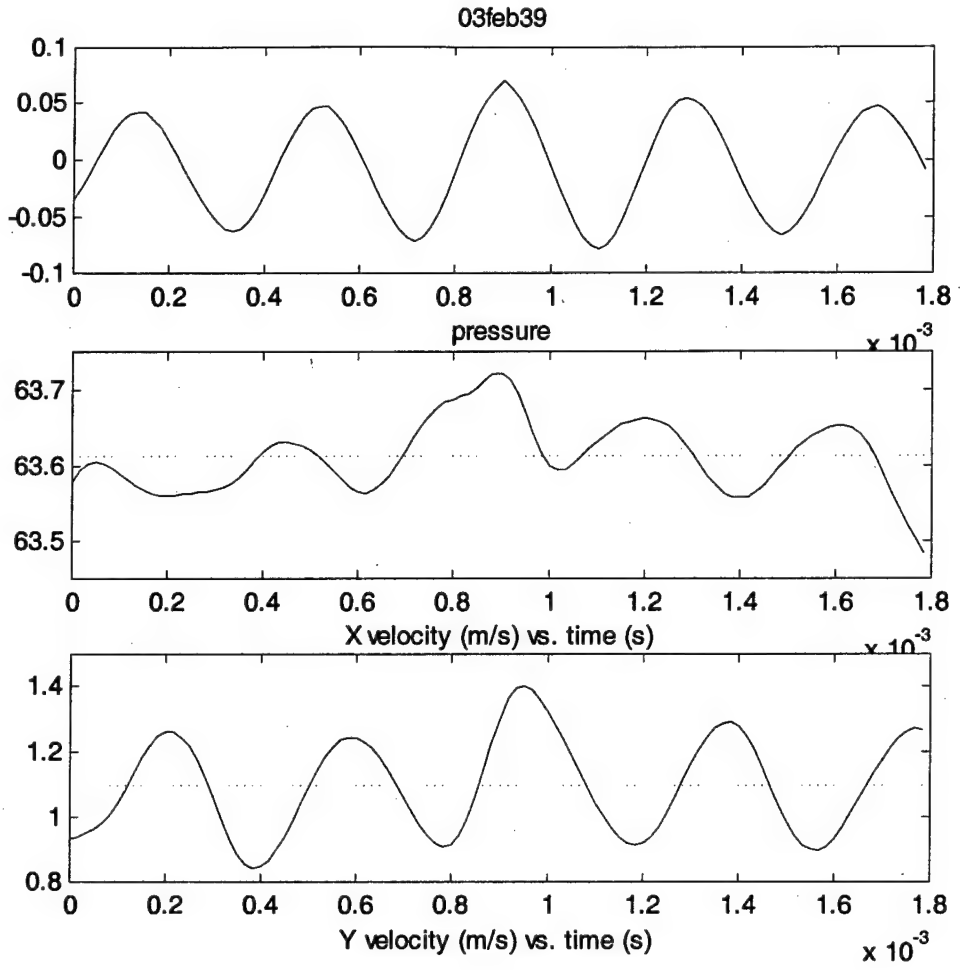

Figure 8. Pressure voltage and x, y velocities at x = -1.25 in, y = 0.5 in

It should be noted that the above procedure of ensemble averaging then converting to velocity deviates from the accepted procedure, which dictates the reverse order. This was done because comparison of the two methods showed almost no difference in the resulting wave shapes. A comparison of order of operations is shown in Figure 9. By ensemble averaging first, the number of required operations was reduced by

a factor of the number of runs, typically 250. This meant a processing time of seconds instead of more than 14 minutes for each file.

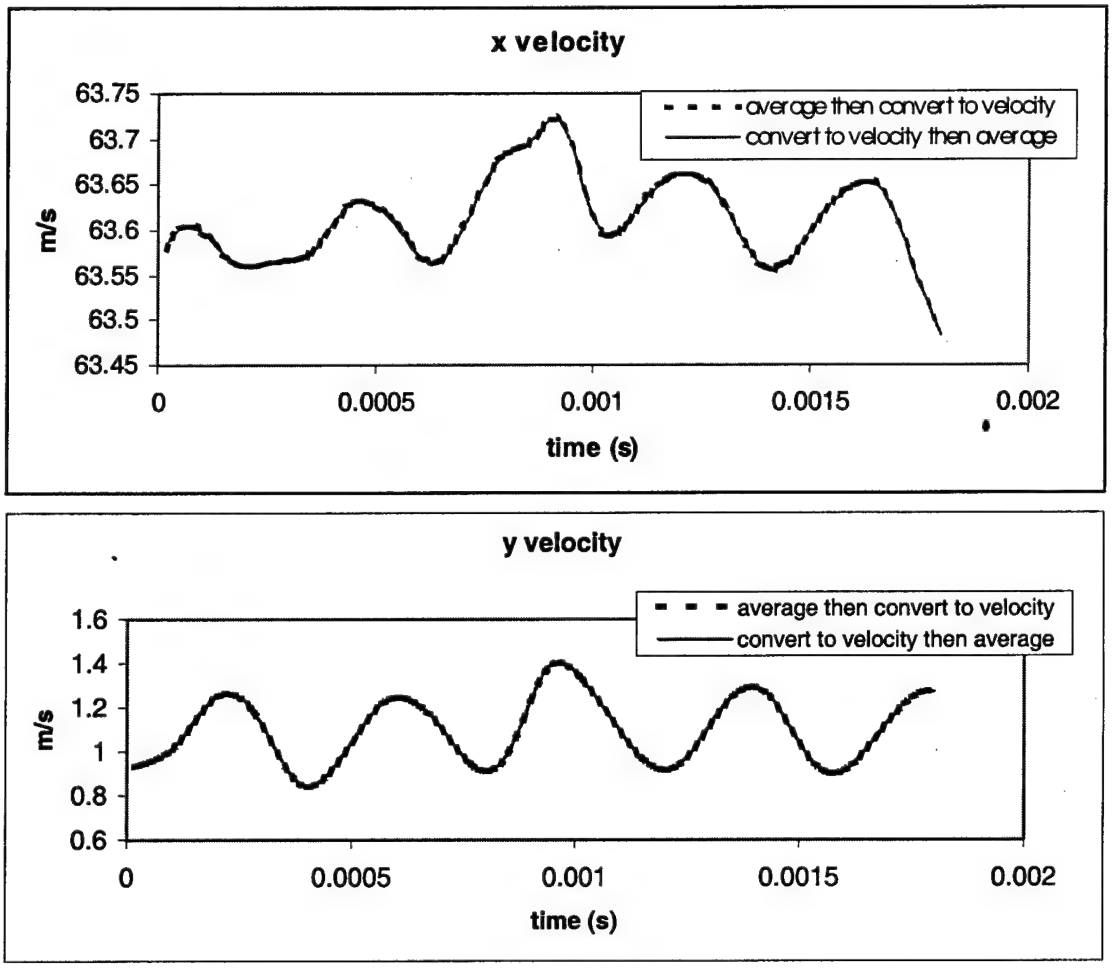

Figure 9. Comparison of order of operations, x = -1.25 in, y = 0.5 in

3.4.3 Least Squares Minimization

To determine the frequency, phase and amplitude of the unsteady velocity data, an approach similar to the simulated annealing used by Fabian, Jumper, and Falk was employed [5]-[9], [11]-[14]. First, a two-frequency sinusoid of the form

$$W(t) = A_f \sin(\omega_f t + \phi_f) + A_h \sin(\omega_h t + \phi_h) \tag{13}$$

was created. Initial guesses of the fundamental and harmonic amplitudes and phases were created arbitrarily through random number generation. The fundamental frequency was guessed to be near the theoretical shedding frequency of the cylinder, and the harmonic frequency was initially assumed to be twice that value. A Matlab function called jfunc (Appendix A) was written to compare the averaged pressure or velocity data point by point to this arbitrary wave and calculate the least squared error between the two. The sum of the least squared errors was used as a cost function for minimization. Using the Matlab function fminsearch, the cost function was minimized using the amplitude, frequency and phase of equation 13 as input parameters. The function fminsearch uses the Nelder-Mead simplex direct search method, finding the local minimum of a cost function by allowing input values to vary and iterating until a certain minimum change in the cost function is reached. First the pressure signal was evaluated by allowing both amplitudes, both phases, and the fundamental frequency to vary. The harmonic frequency was set to be twice the fundamental frequency as determined by the minimization. Once the value of the fundamental frequency was found for the pressure signal, it was held constant while evaluating the velocity data. Only the amplitudes and

phases were allowed to vary while minimizing the error between the velocity data and the two-frequency approximation. To ensure that a global minimum was reached, each wave was evaluated multiple times with different random initial guesses, and the resulting cost functions compared. Because the cost functions for each wave were almost always the same regardless of the initial values, it was determined that evaluating each wave twice was sufficient to locate the global minimum.

An example of the output of the least squares minimization is shown in Figure 10. The two-frequency approximation is given in the form of equation 13. The frequencies are rounded off to the nearest 50 Hz, the amplitudes are rounded to the nearest 0.001 m/s, and the phases are rounded to the nearest 0.001 rad.

The approximations of Figure 10 can clearly be seen to follow the data in terms of frequency. There is some variation in the amplitudes of the several peaks in each run. The minimization program, which is restricted to a single amplitude at each of its frequencies, selects an intermediate level. Because of this restriction on the approximated wave, inconsistent features in the data are largely ignored. For example, the largest peak in the center of each of the velocity traces stands well above the surrounding peaks, but the approximate wave is at a level more appropriate to the other waves in the run.

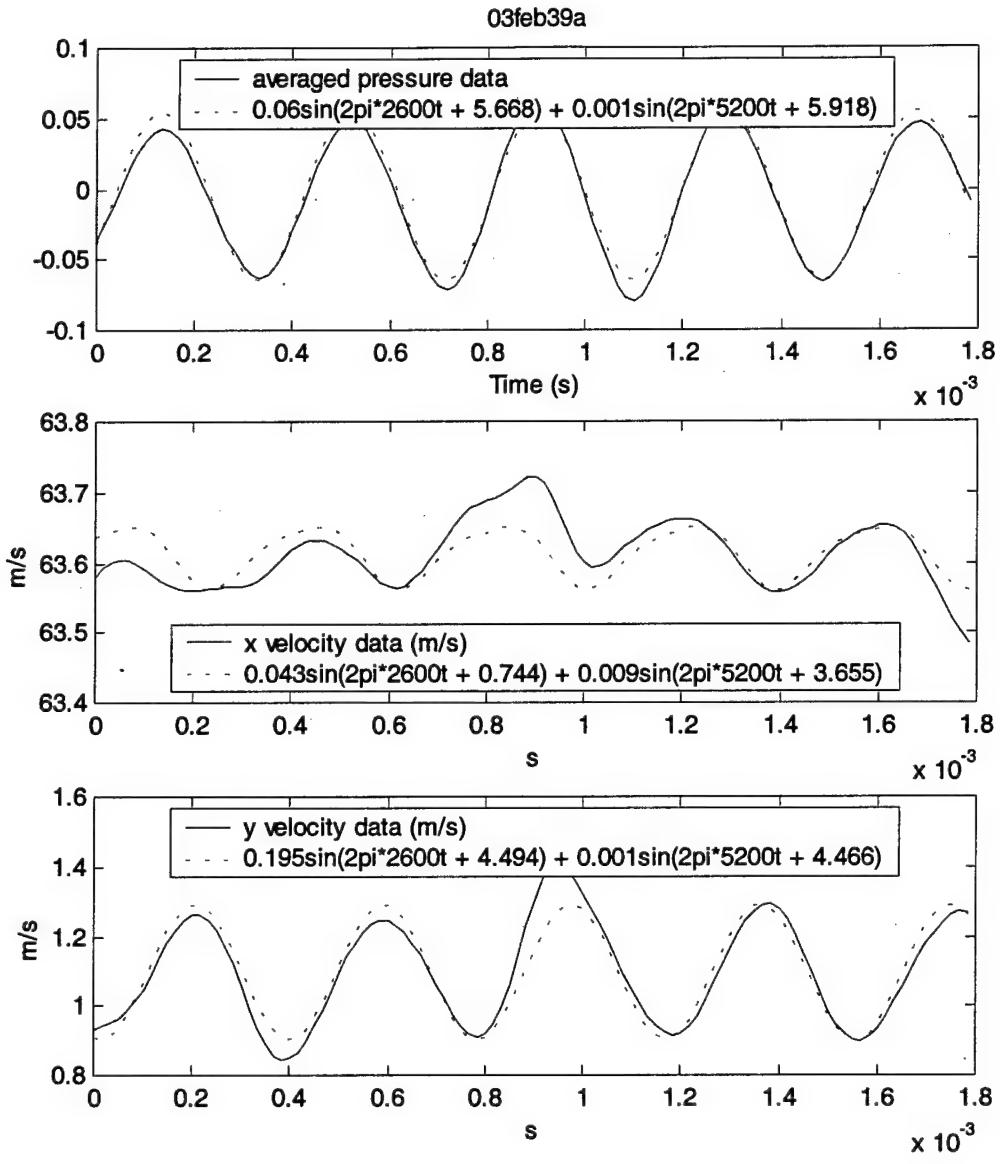

Figure 10. Data and two frequency approximation at x = -1.25 in, y = 0.5 in

3.4.4 Uncertainties

The two-frequency approximations provided a method for assigning meaningful numbers to the data. Through the approximation, the amplitude and phase of the unsteady portion of the signal at each tunnel location were estimated. It was these estimates that were later used to correlate the results of one location with another and a model was fit to them. In some cases the two-frequency curve did not appear to fit the data very well, so the uncertainty of the phases and amplitudes derived therefrom was large. In most cases, the fundamental amplitude was much larger than the harmonic, but the influence of the presence of the harmonic on the amplitude and phase of the fundamental was not known.

With this question in mind, the least squares minimization program was revised to search for only a single frequency with accompanying amplitude and phase. The resulting phases and amplitudes were in all cases virtually identical to the fundamental frequency portion of the two-frequency approximations. The differences between the two were minimal, so the phase and amplitude of the fundamental frequency from the two-frequency approximation were used in analysis of the data.

In some cases the data did not fit the two-frequency approximation very well. This was not necessarily the fault of the minimization program, but rather on the constraints applied to the problem. In most cases where a poor fit was obtained, the minimization program would have provided a better fit if it was allowed to search for two independent frequencies for each velocity wave along with their accompanying amplitudes and phases. Since we were concerned with how the disturbance from the

cylinder propagated into the flow, however, we looked for the portion of the signal with the same frequency content as the disturbance and its first harmonic. Where this frequency pair did not match the frequencies measured by the hotwire the fit was poor.

3.5 Flow Characteristics

In the sections that follow, considerable discussion will be made about how the flow unsteadiness from the cylinder propagates upstream to where it is measured by the hotwire. This is all based on acceptance that the flow disturbance measured by the hotwire is the same disturbance created at the cylinder and that the disturbance measured at the cylinder is due to vortex shedding.

To show that this is the case, consider the 250-ensemble data set of Figure 10. The solid lines are the pressure, x-direction velocity and y-direction velocity measured with the cylinder 1.25 in (3.2 cm) downstream and 0.5 in (1.3 cm) below the hotwire. All three signals show a cyclic character at approximately the same frequency and a different phase. This is consistent with the idea that the disturbance at a particular frequency is created at the cylinder and propagates upstream. The pressure transducer measures a disturbance, and during the same time interval, the hotwire measures a signal of the same frequency, but at a different phase. Two simultaneous measurements of a disturbance, one at the disturbance source and the other at another location in the flow, will be out of phase by the amount of time it takes for the wave to travel from the disturbance source to the second location.

Now consider a run taken with the cylinder removed from the flow. Figure 11 is a 10-ensemble set taken as part of a hotwire alignment. The cylinder for this series rested on the bottom wall of the tunnel. Another cylinder was affixed to the top wall of the tunnel to provide symmetry for the hotwire alignment.

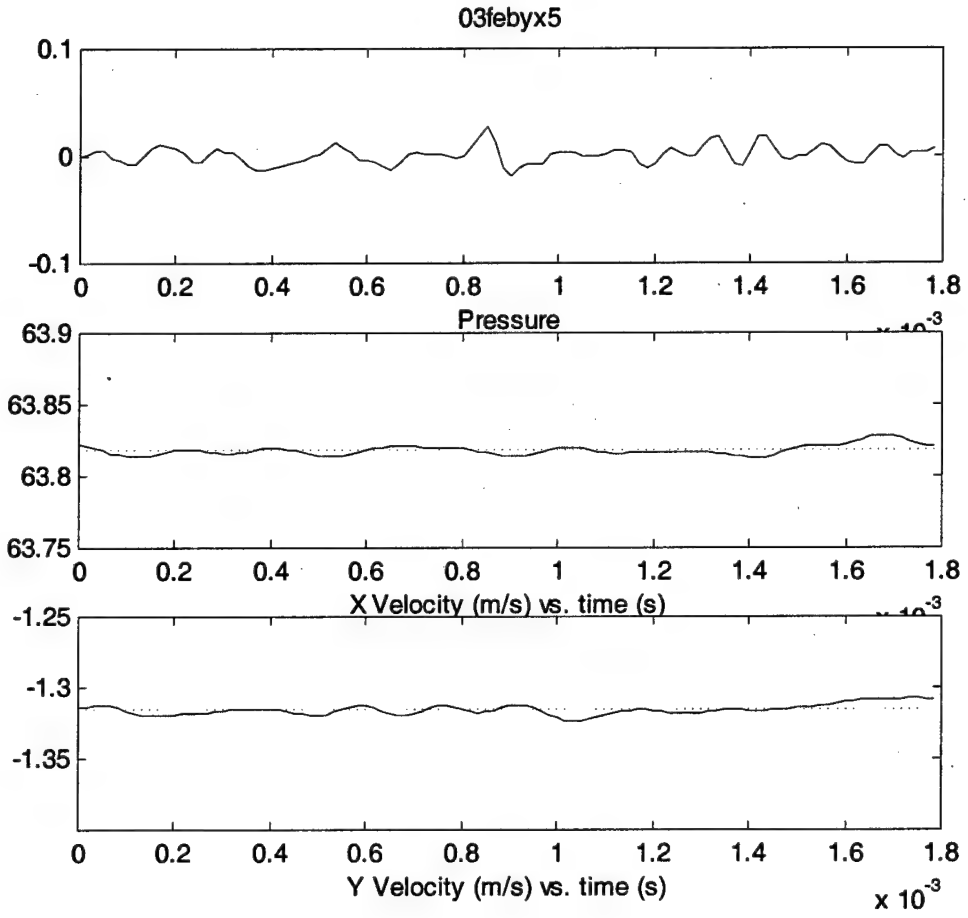

Figure 11. Sample run with cylinder removed from freestream

Probably the most significant feature of Figure 11 is that the cylinder is not shedding. In fact, there were no voltage peaks from the pressure signal to trigger from, so the triggering was manually initiated by momentarily depressing the auto balance

switch on the signal conditioner, creating a voltage spike of sufficient magnitude to trigger data acquisition. The velocity signals have no meaningful periodic information. Again, this is consistent with the idea that the flow disturbance measured by the hotwire is created by vortex shedding from the cylinder. When the cylinder shedding is stopped, the velocities lose their regular, unsteady content.

Finally, consider the pressure signal at two different tunnel speeds.

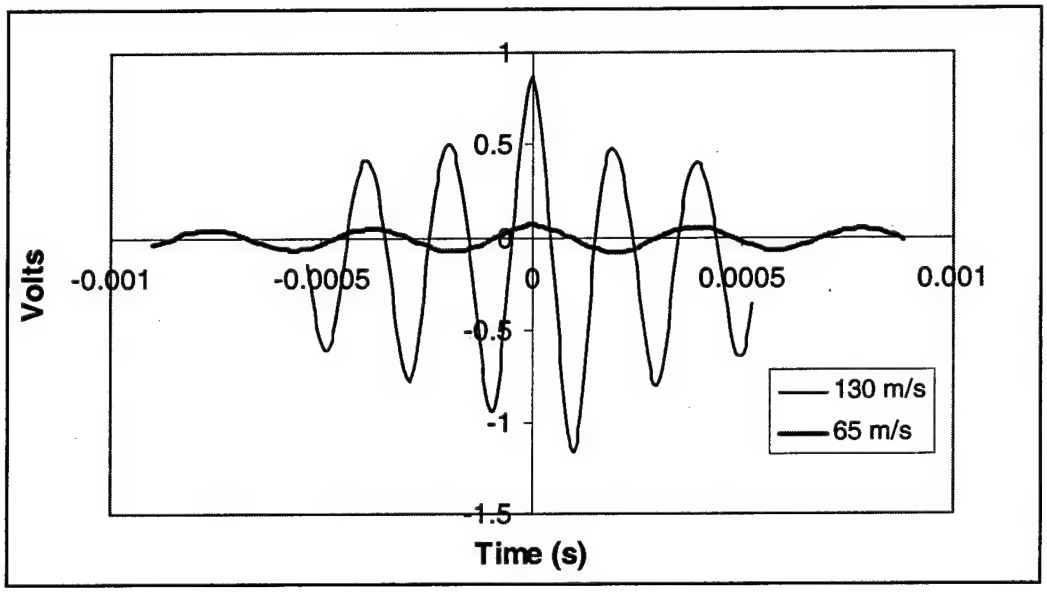

Figure 12. Comparison of pressure signal at two tunnel speeds

Figure 12 shows the shedding of the cylinder at 130 m/s and at 65 m/s. A slower sample rate was used at the lower tunnel speed, so the window of data capture was longer. The trigger point is shown as time zero in this figure so that the two runs align at the trigger point. It can be seen from the figure that the frequency of shedding at the slower tunnel speed is approximately half the frequency at the higher speed. Additionally, the amplitude of the pressure change is much higher at the higher tunnel

speed than at the lower tunnel speed. Both of these indicators are consistent with vortex shedding from a cylinder.

An additional evidence of vortex shedding was observed when the hotwire was directly upstream the cylinder in the flow. At these locations, a slight drop in the frequency of shedding was observed, both in the least squares minimization and the audible tone of the cylinder in the flow. It makes sense that when the freestream flow is disturbed, as in the wake of the hotwire probe, the frequency of shedding will be affected.

4. Results of Experiment

Raw data where the hotwire was 1.25 in upstream the cylinder are presented in this section. Correlations of phase and amplitude data at all locations are also presented. Additional raw data may be found in Appendix B.

4.1 Single Run Characteristics

The data are shown with the two frequency approximation for a series of y locations at x = -1.25 in, beginning with Figure 13 and continuing through Figure 35. The solid lines represent the pressure and velocity data that have been ensemble averaged, filtered, and processed as described in section 3.4. The dashed lines are the best-fit two-frequency approximation to the data.

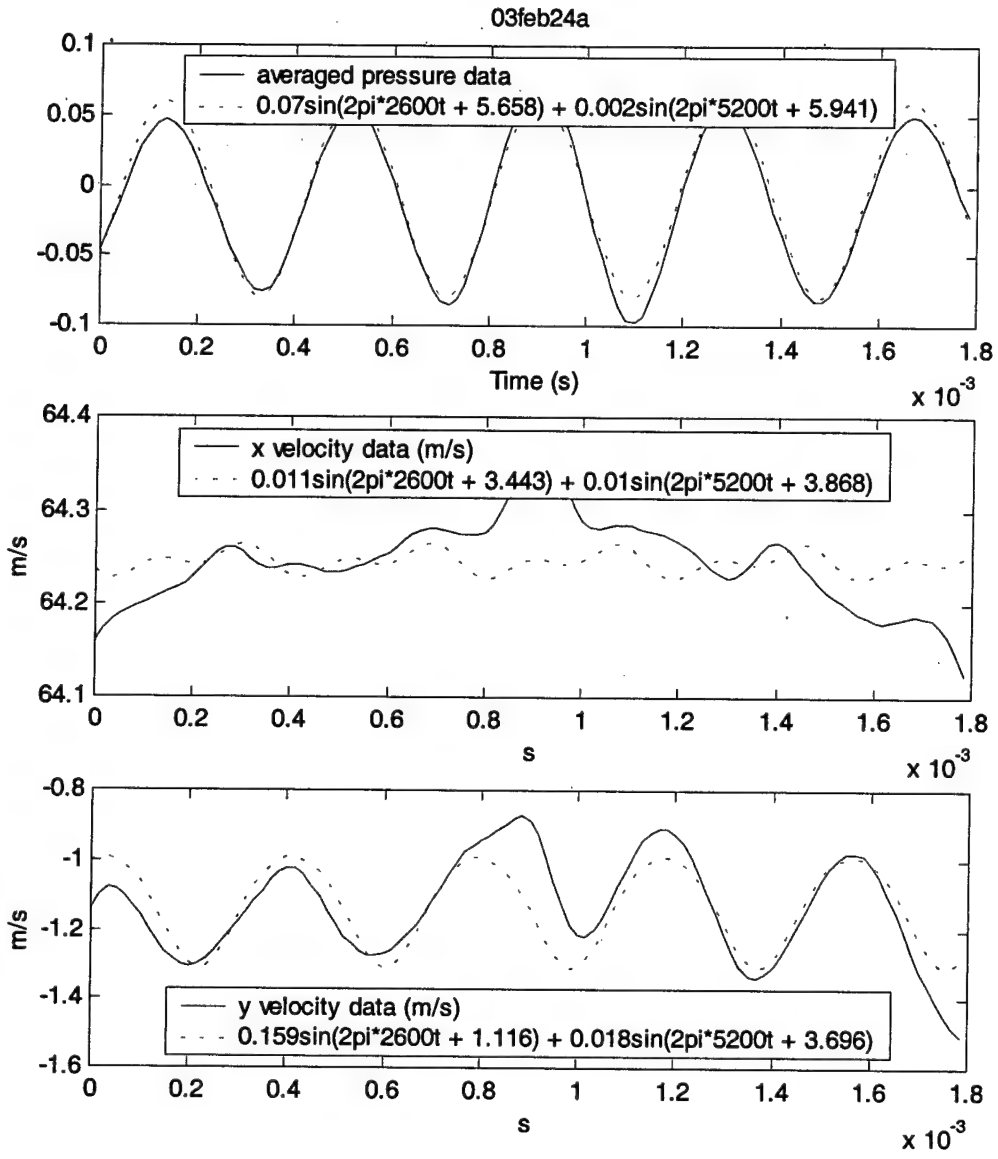

Figure 13. Data and two frequency approximation at x = -1.25 in, y = -2 in

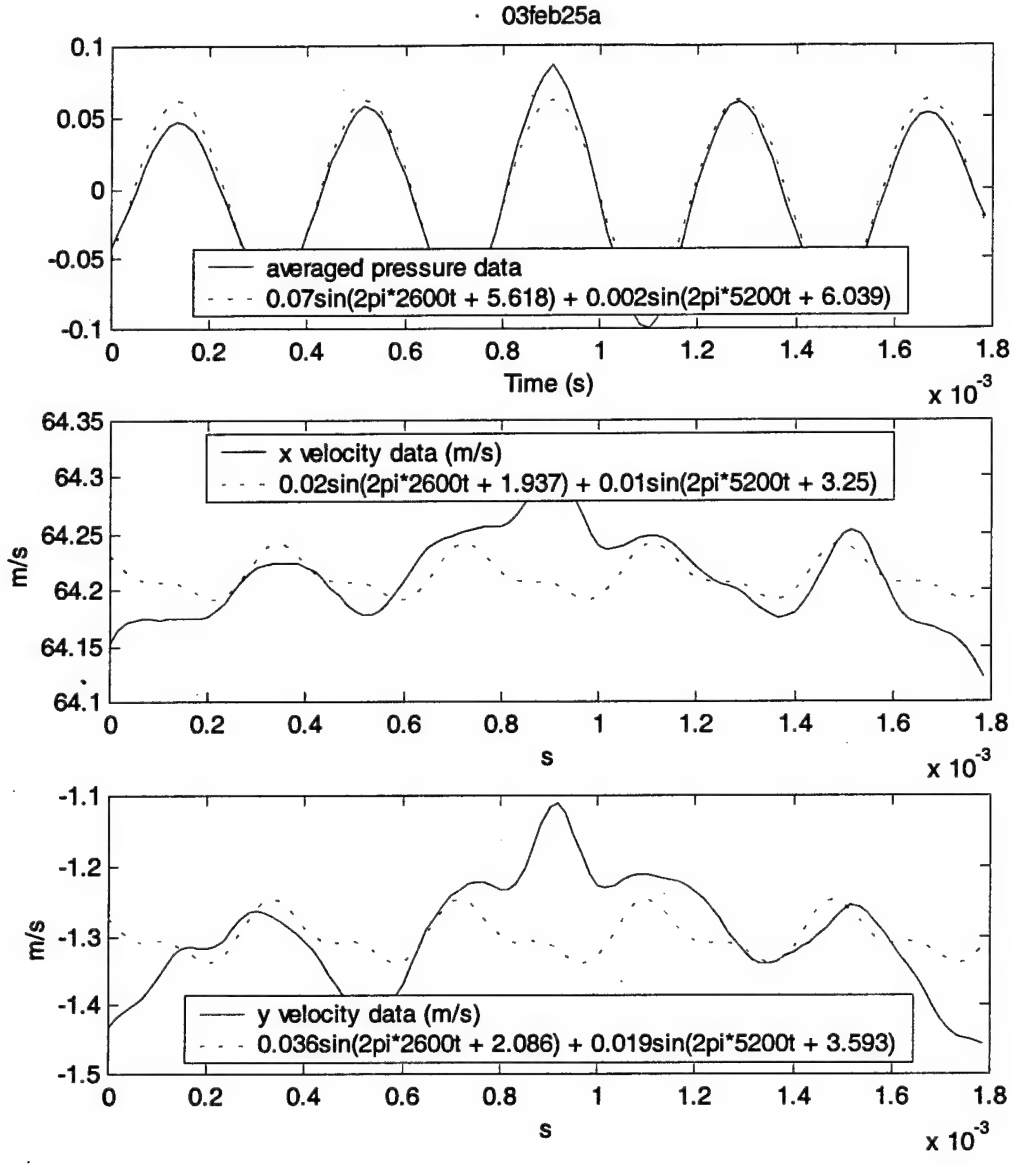

Figure 14. Data and two frequency approximation at x = -1.25 in, y = -1.5 in

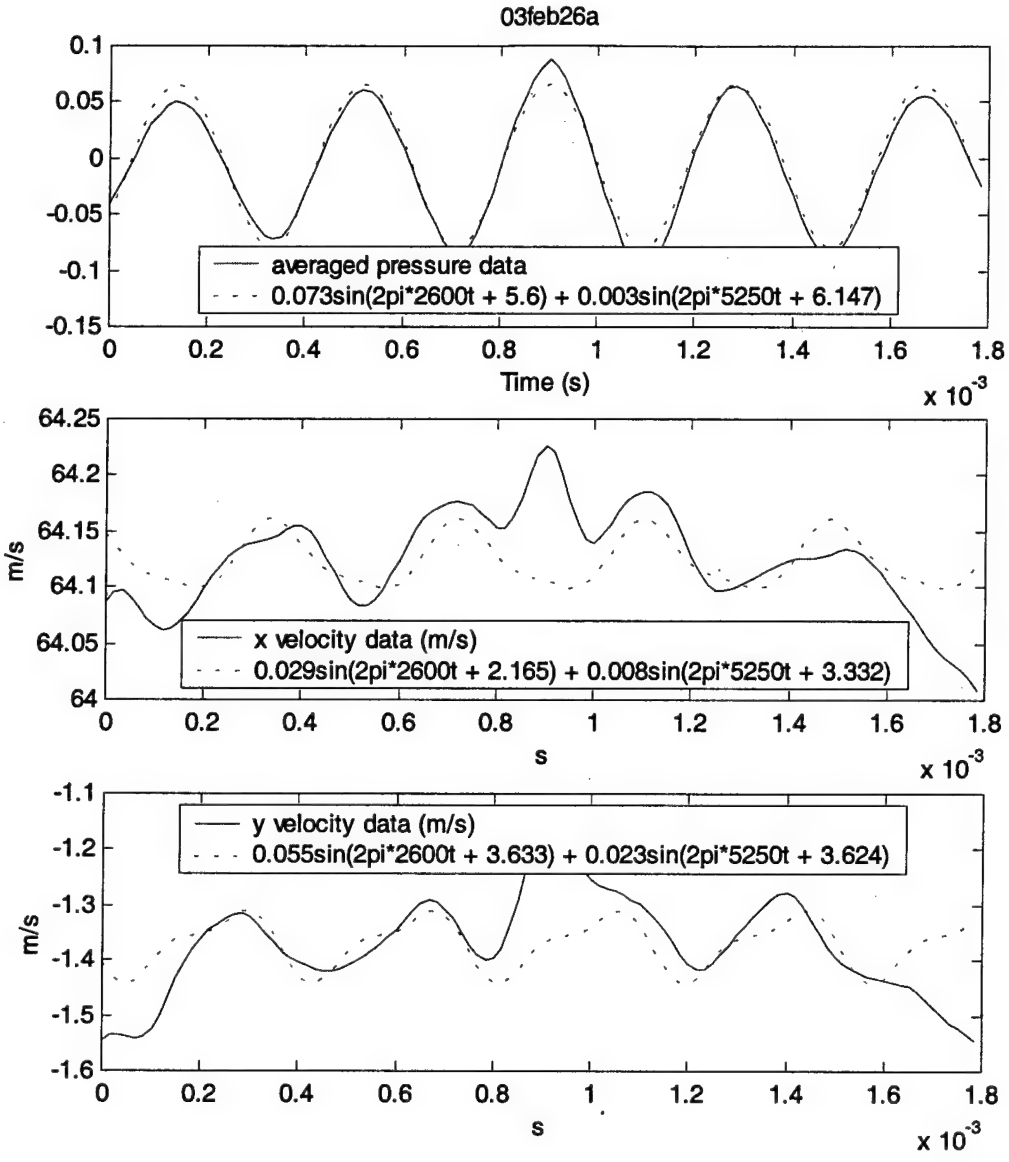

Figure 15. Data and two frequency approximation at x = -1.25 in, y = -1.25 in

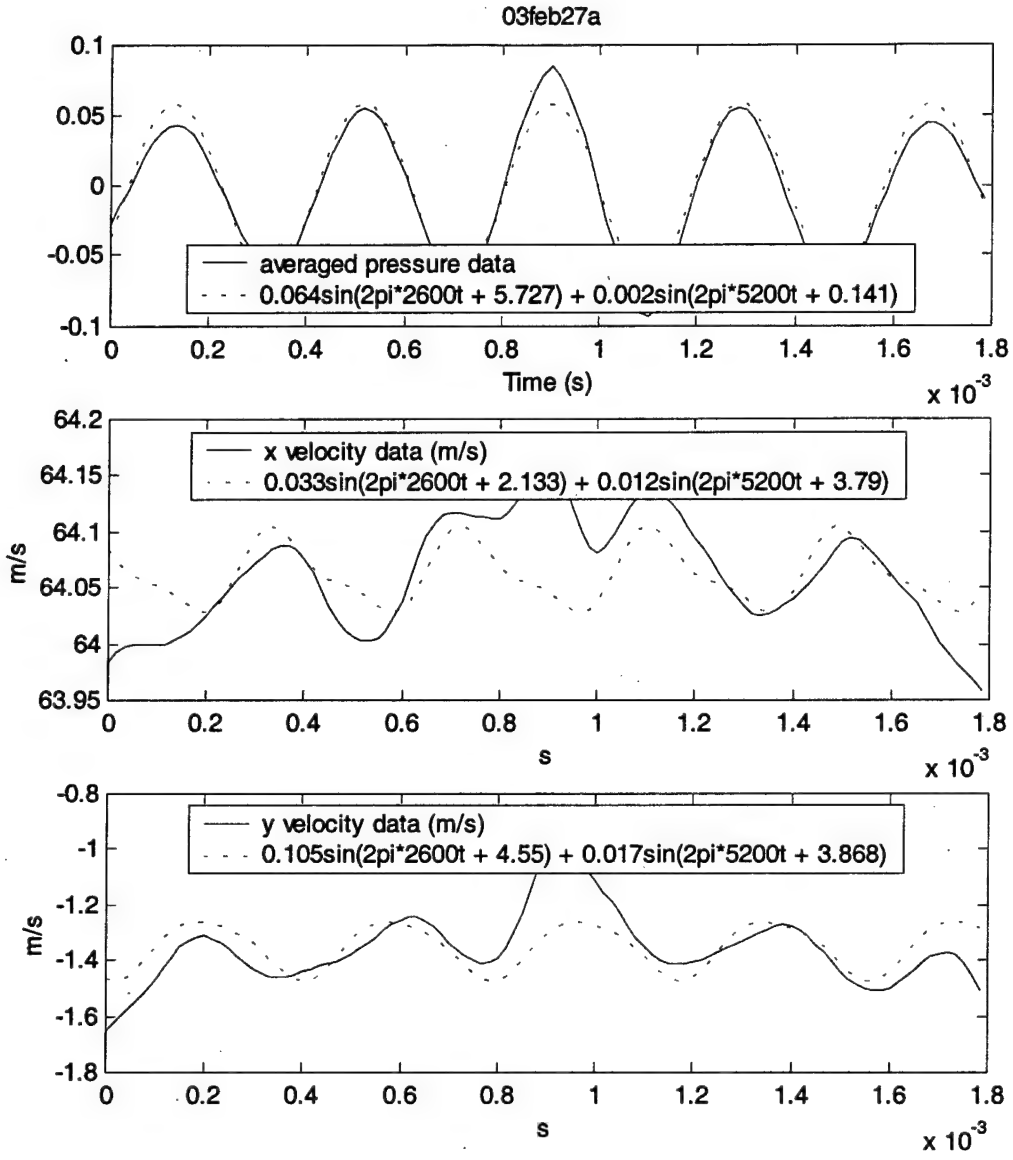

Figure 16. Data and two frequency approximation at x = -1.25 in, y = -1 in

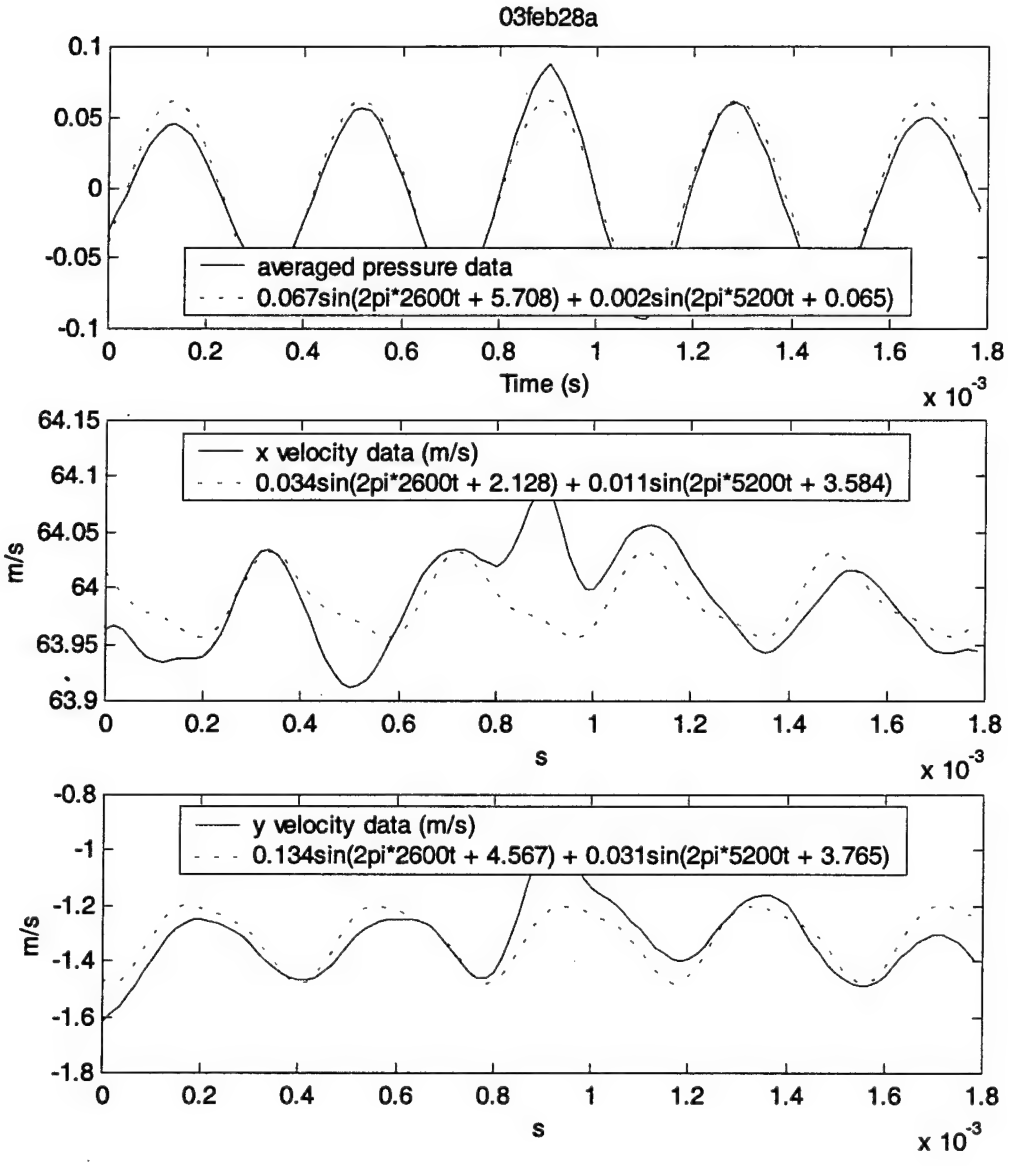

Figure 17. Data and two frequency approximation at x = -1.25 in, y = -0.875 in

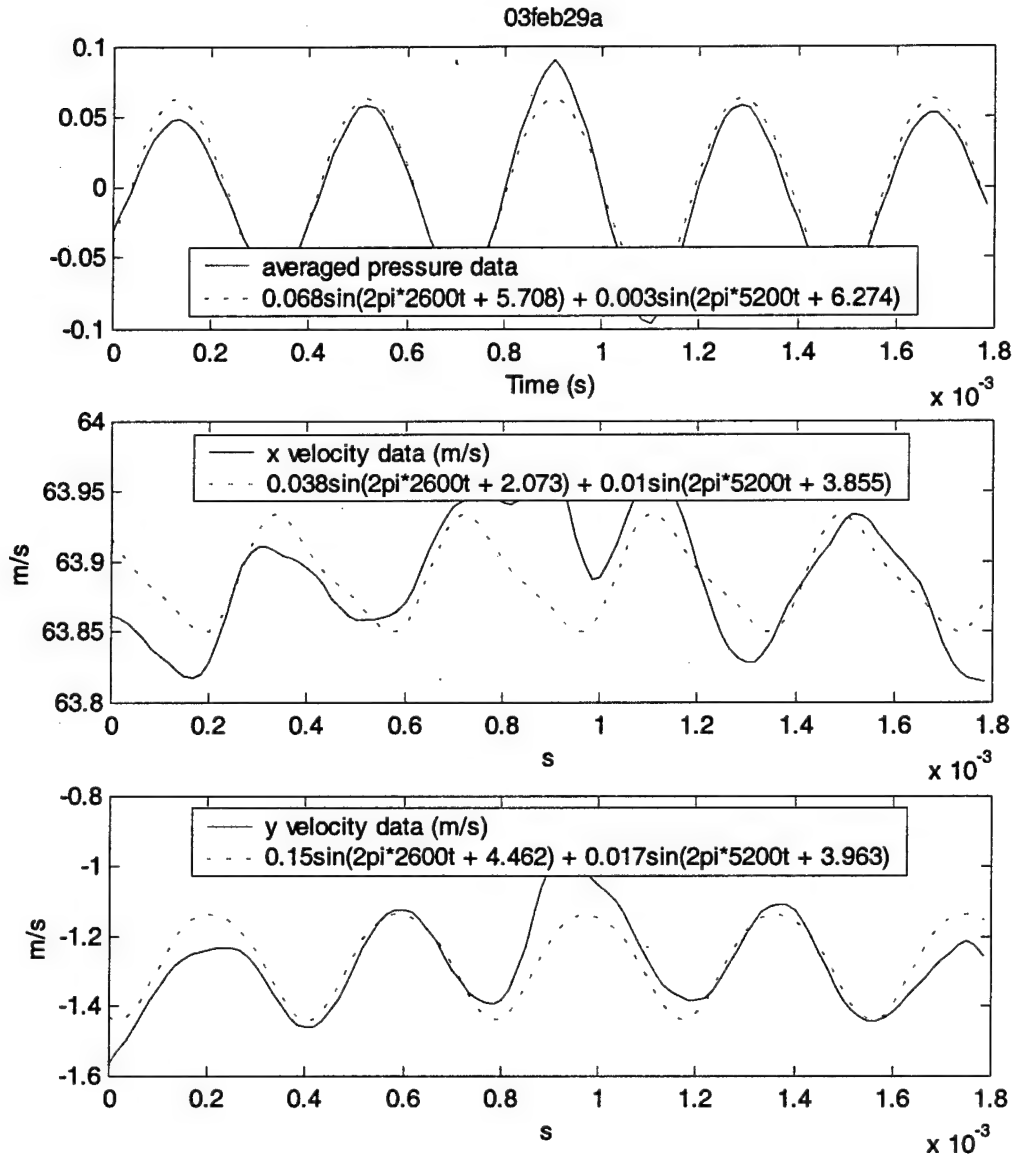

Figure 18. Data and two frequency approximation at x = -1.25 in, y = -0.75 in

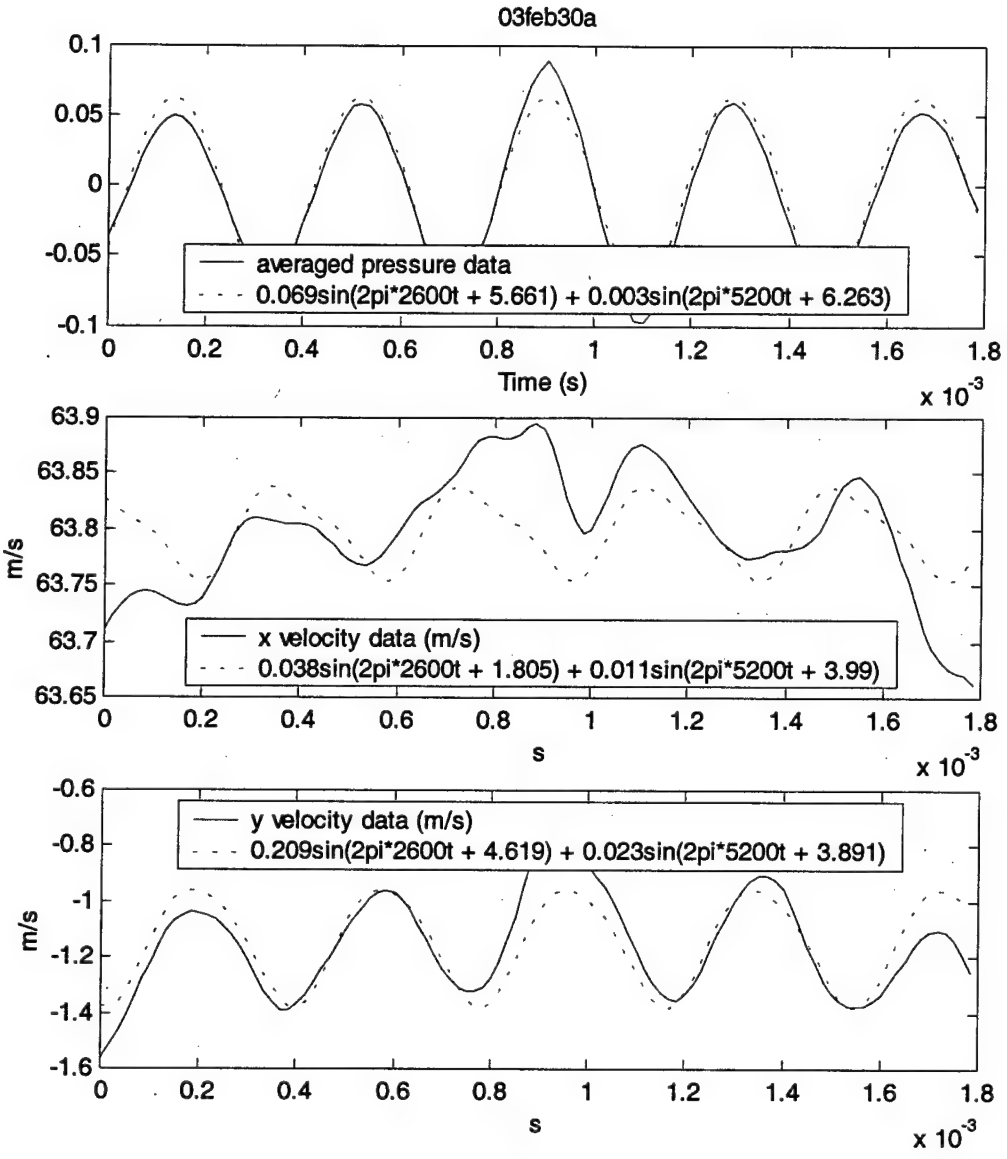

Figure 19. Data and two frequency approximation at x = -1.25 in, y = -0.625 in

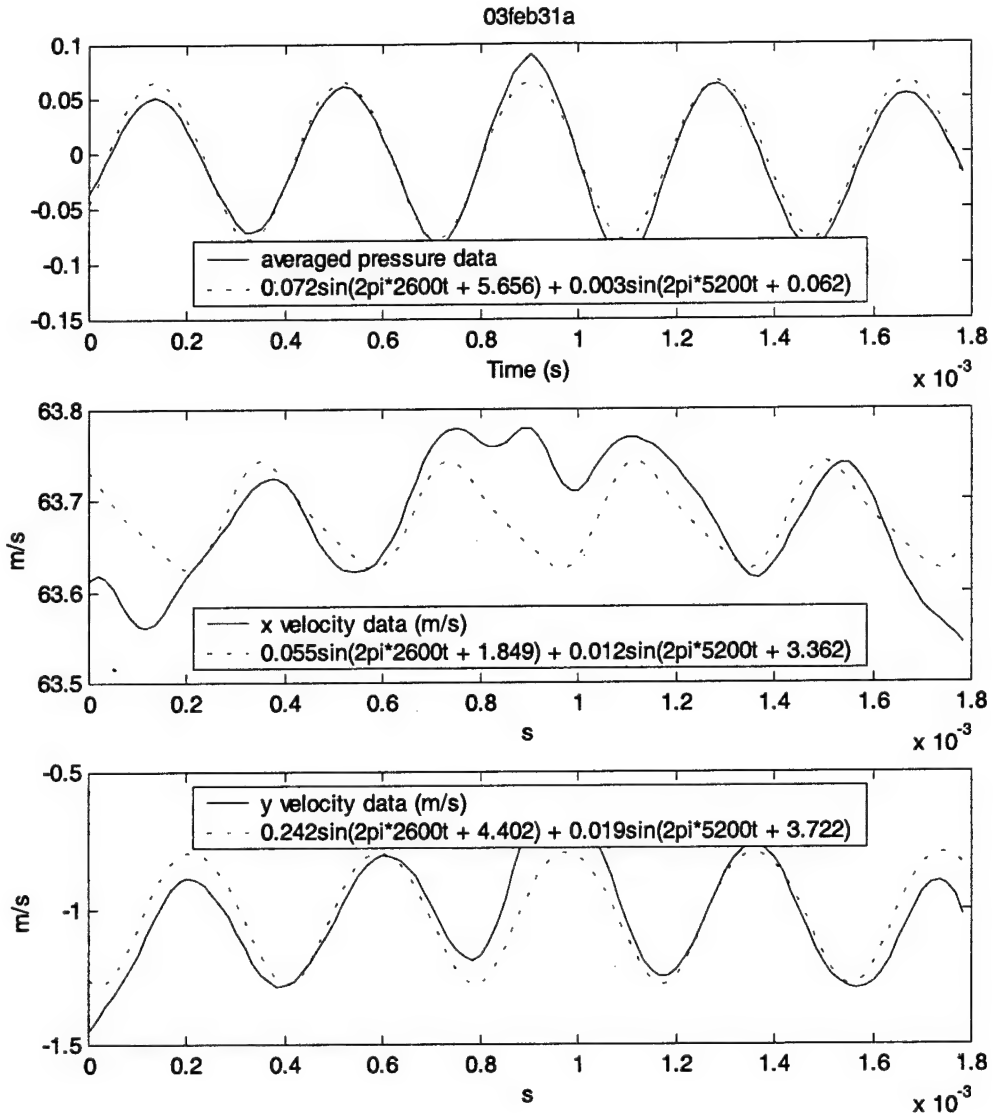

Figure 20. Data and two frequency approximation at x = -1.25 in, y = -0.5 in

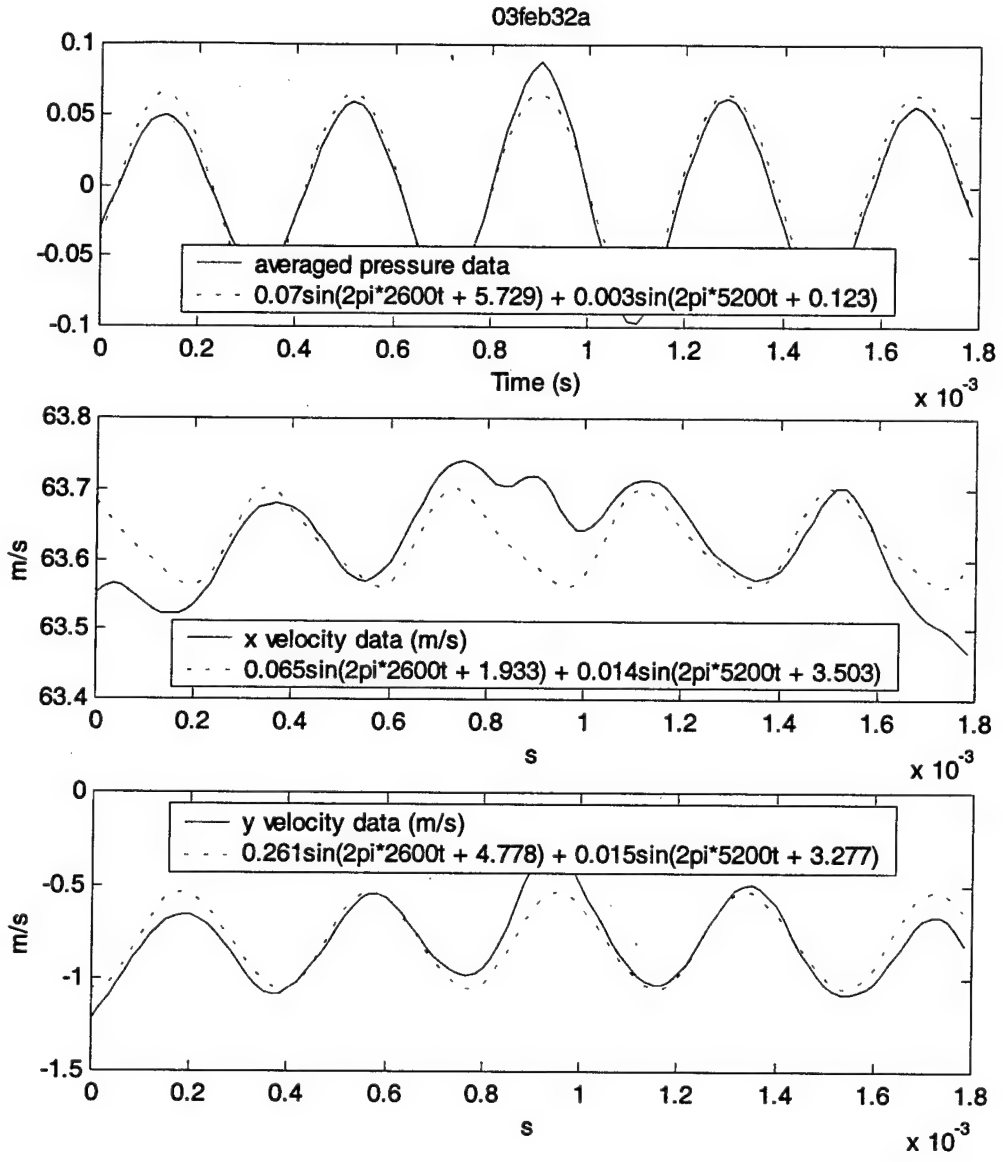

Figure 21. Data and two frequency approximation at x = -1.25 in, y = -0.375 in

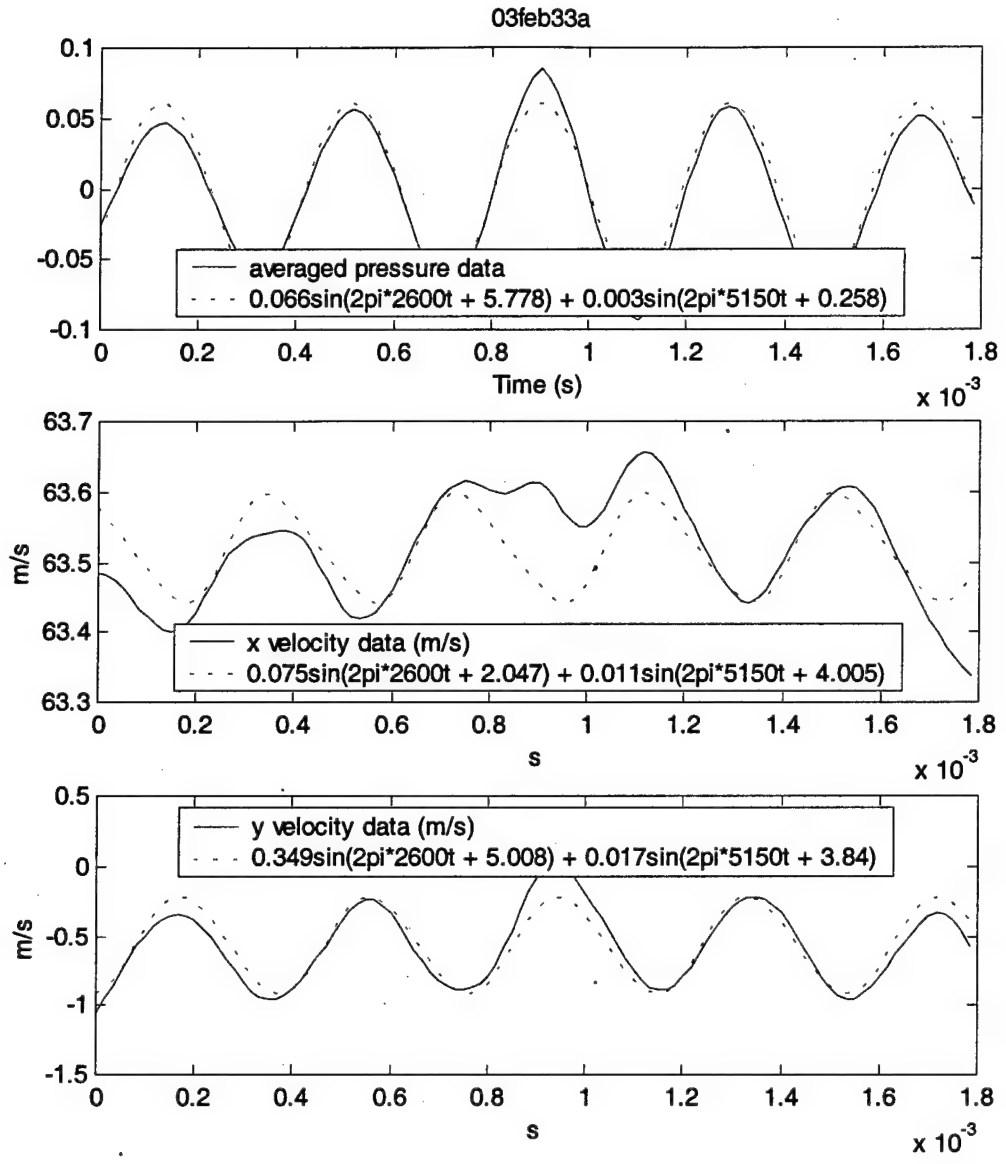

Figure 22. Data and two frequency approximation at x = -1.25 in, y = -0.25 in

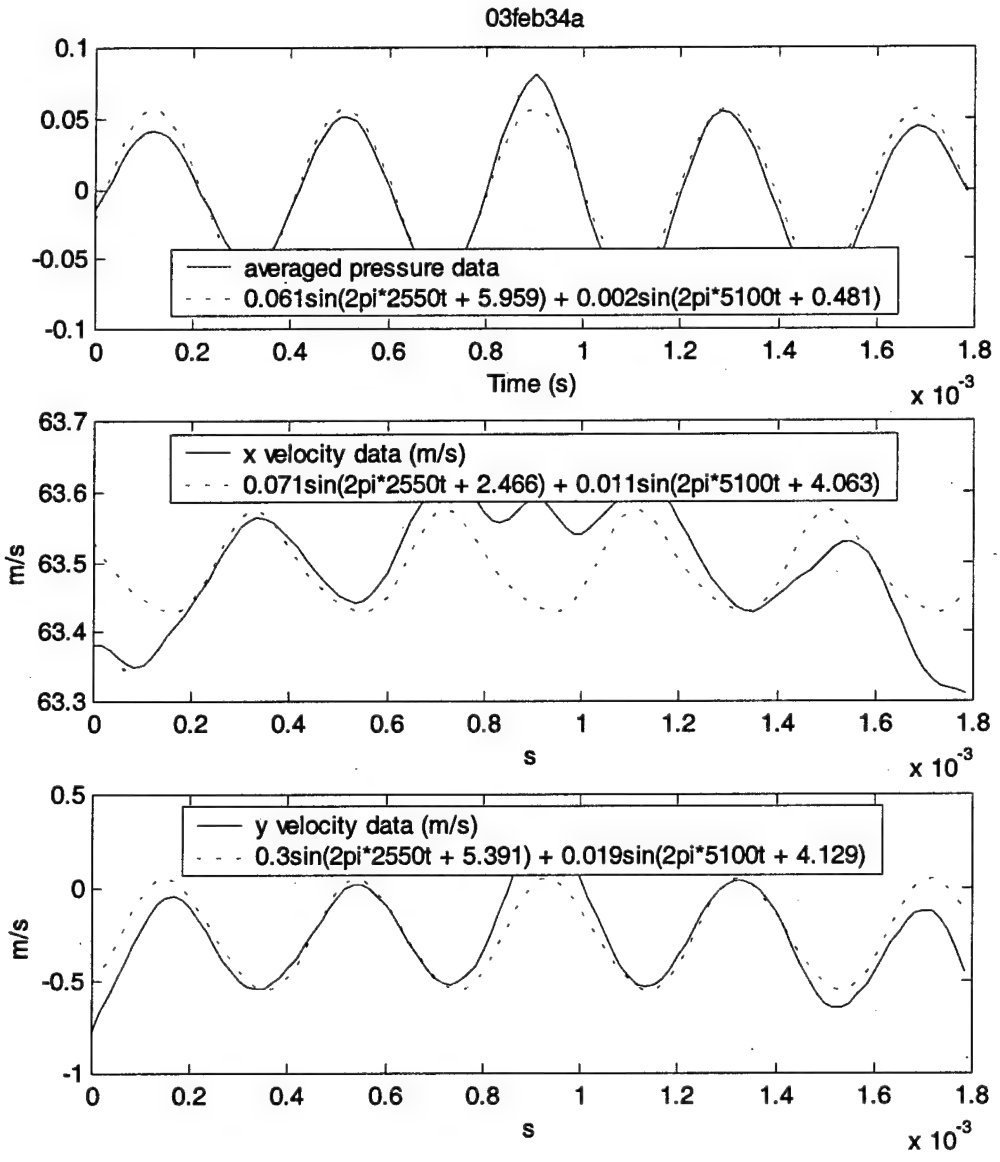

Figure 23. Data and two frequency approximation at x = -1.25 in, y = -0.125 in

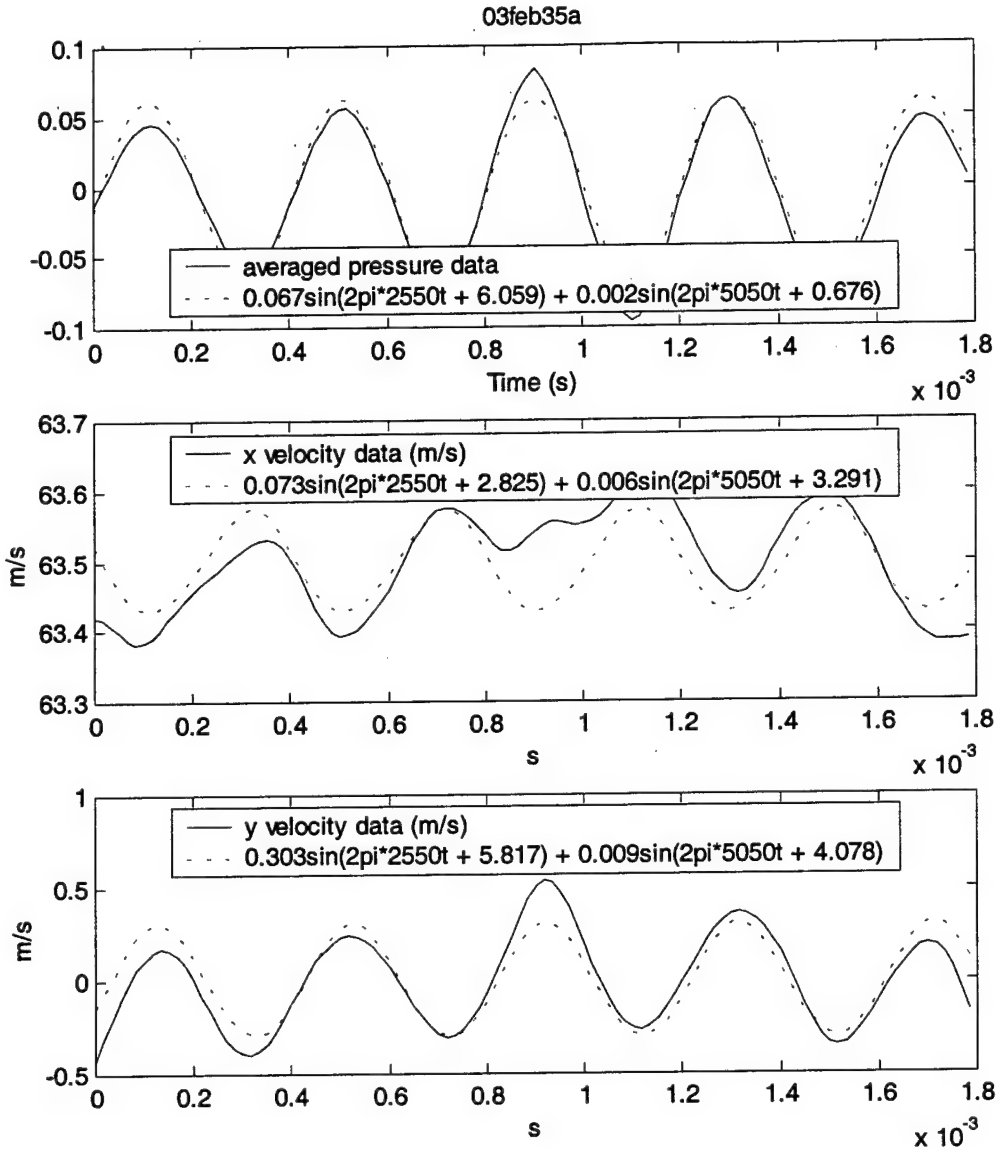

Figure 24. Data and two frequency approximation at x = -1.25 in, y = 0 in

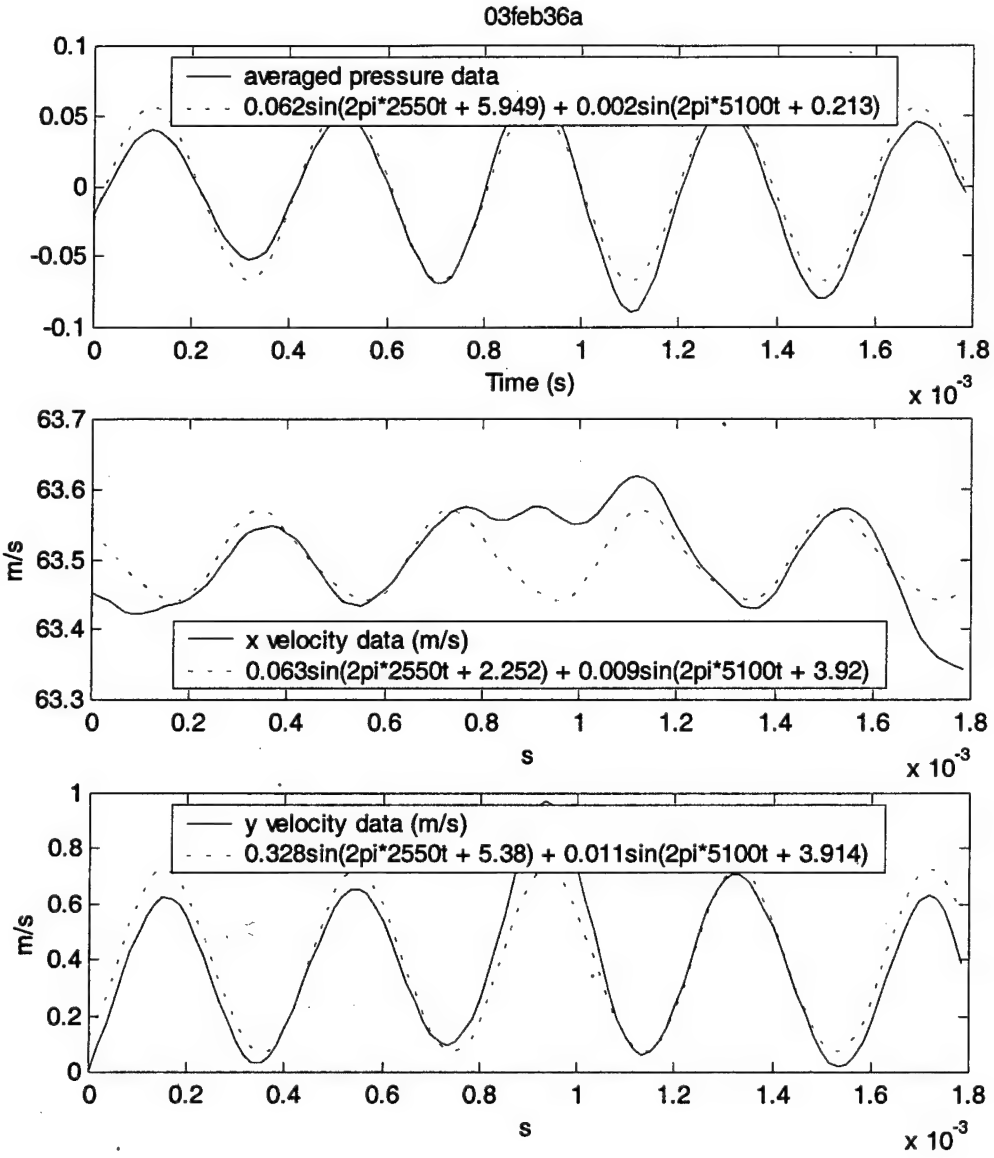

Figure 25. Data and two frequency approximation at x = -1.25 in, y = 0.125 in

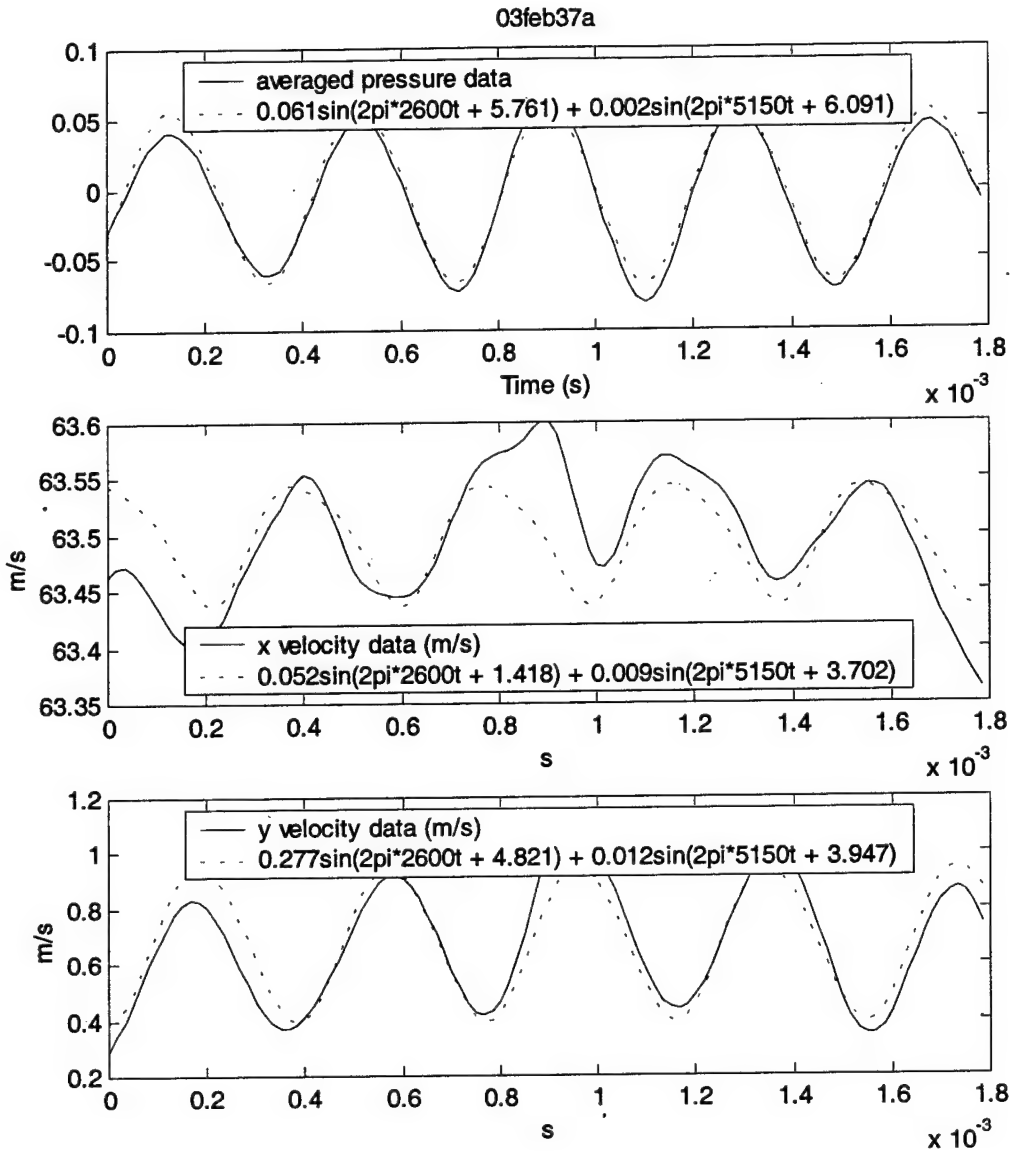

Figure 26. Data and two frequency approximation at x = -1.25 in, y = 0.25 in

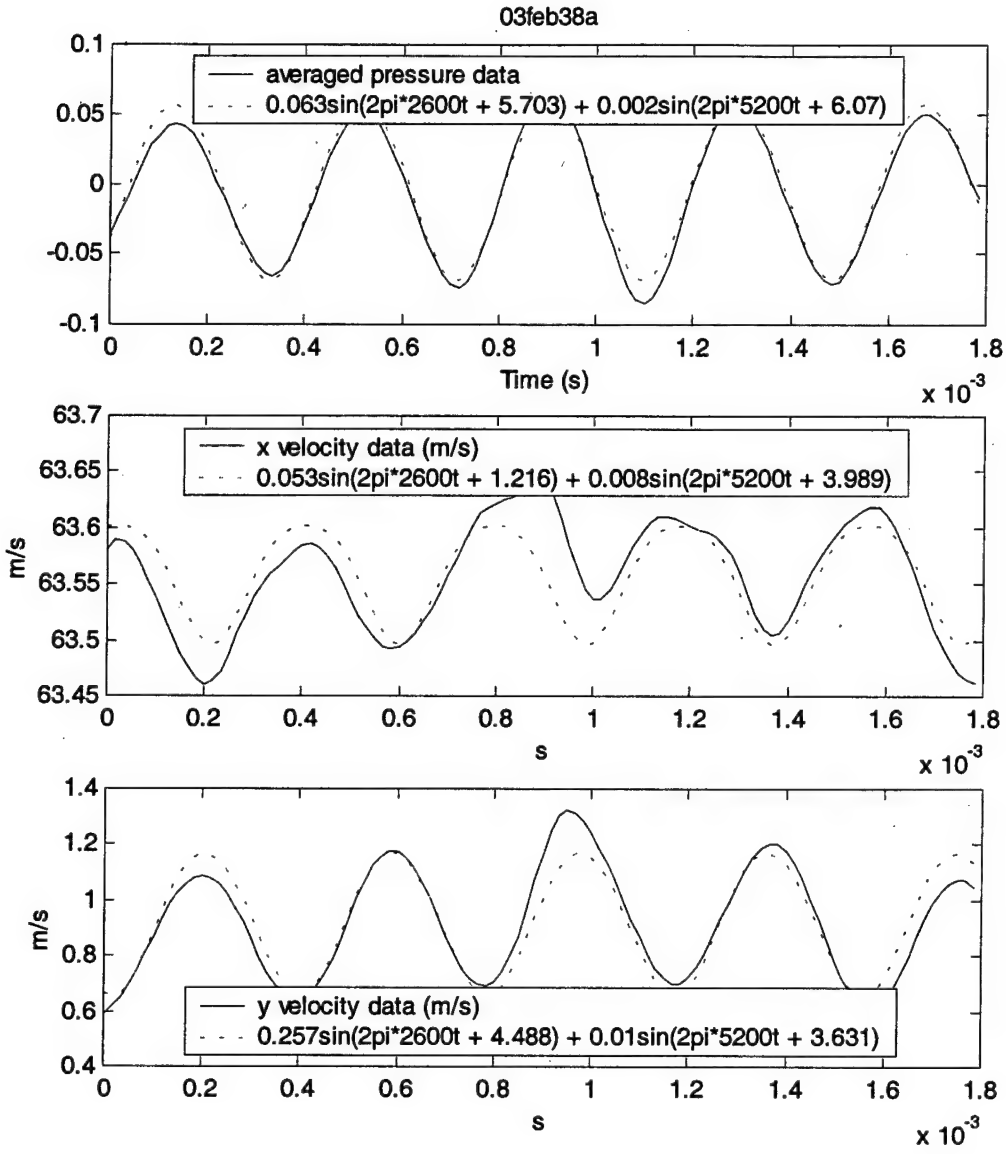

Figure 27. Data and two frequency approximation at x = -1.25 in, y = 0.375 in

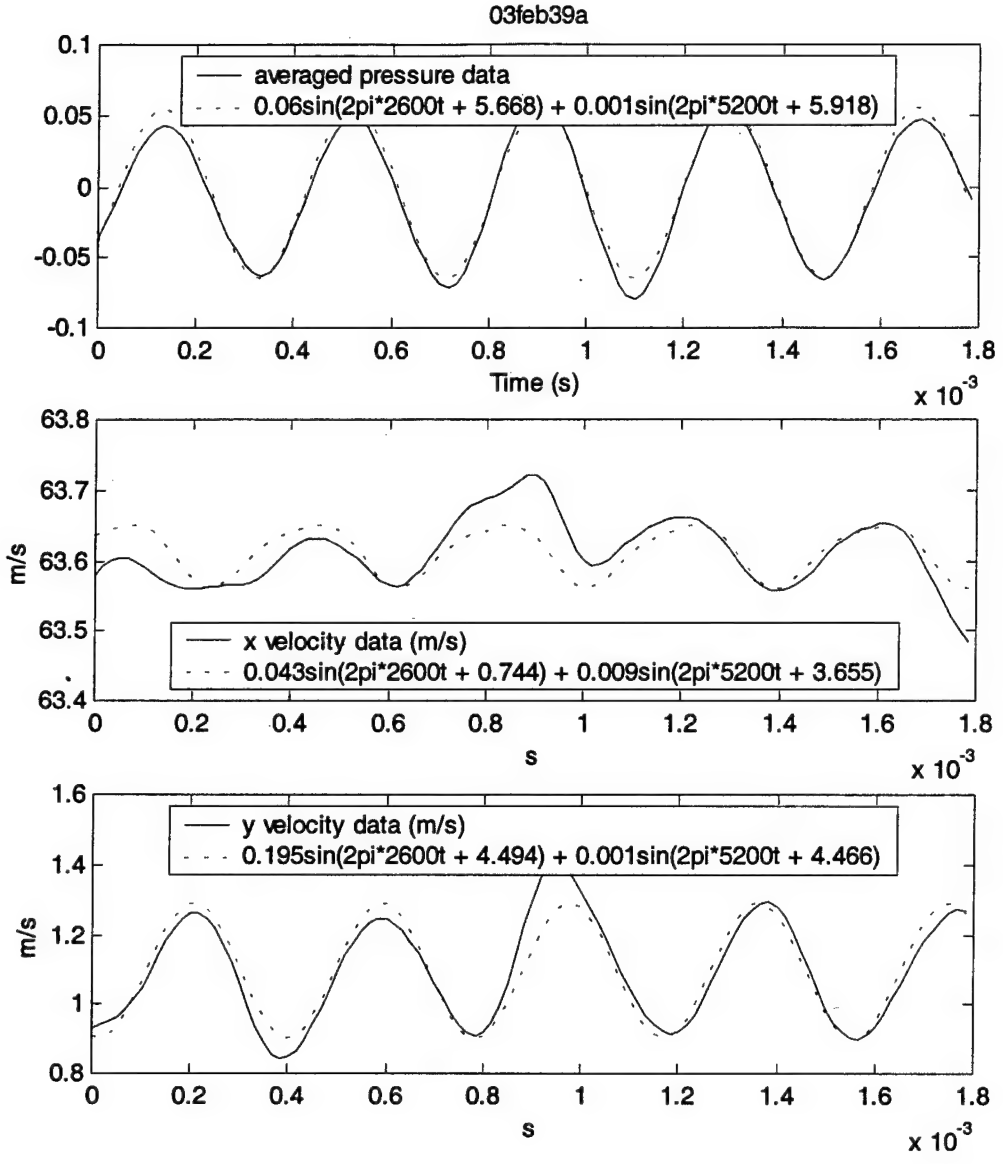

Figure 28. Data and two frequency approximation at x = -1.25 in, y = 0.5 in

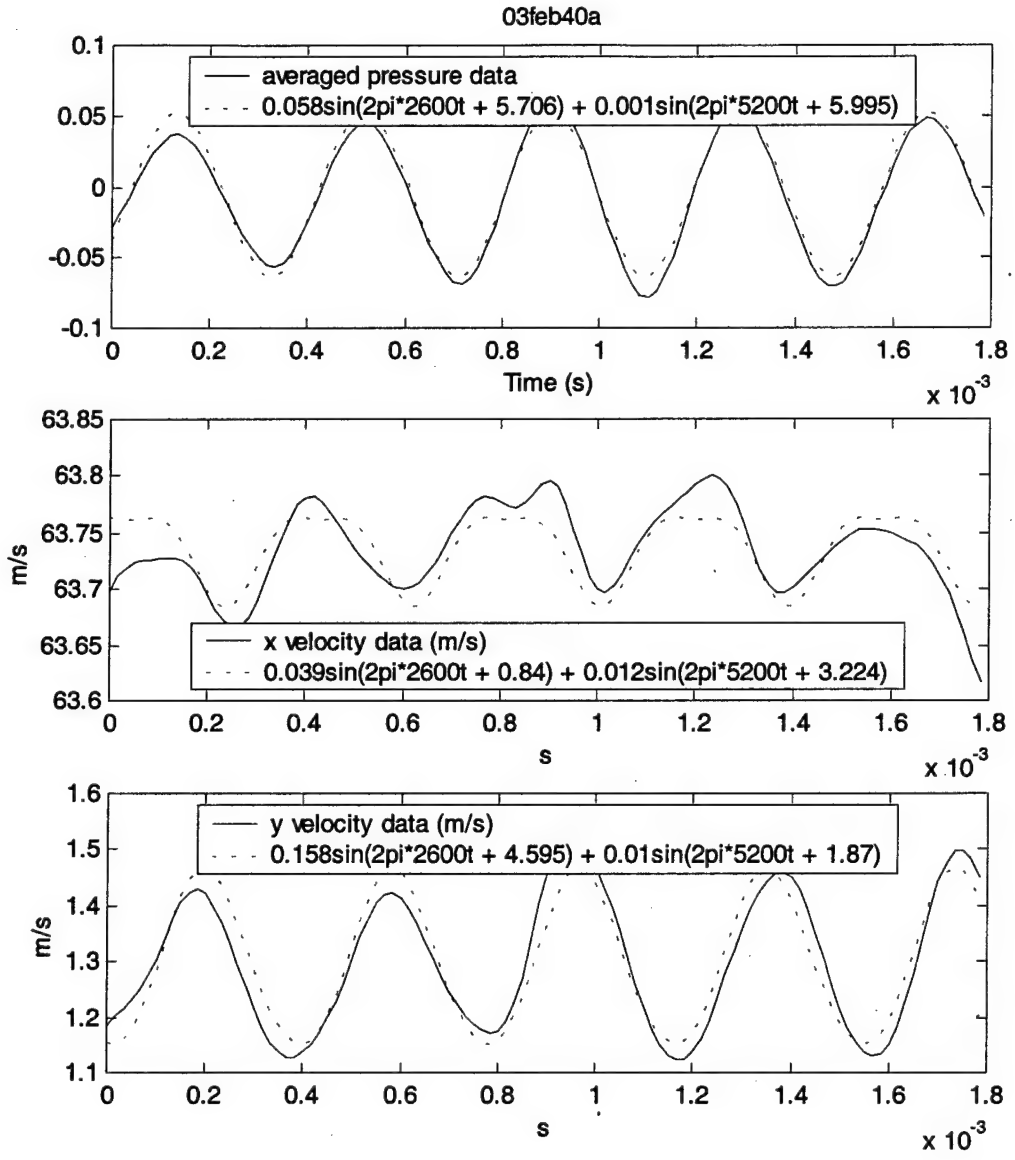

Figure 29. Data and two frequency approximation at x = -1.25 in, y = 0.625 in

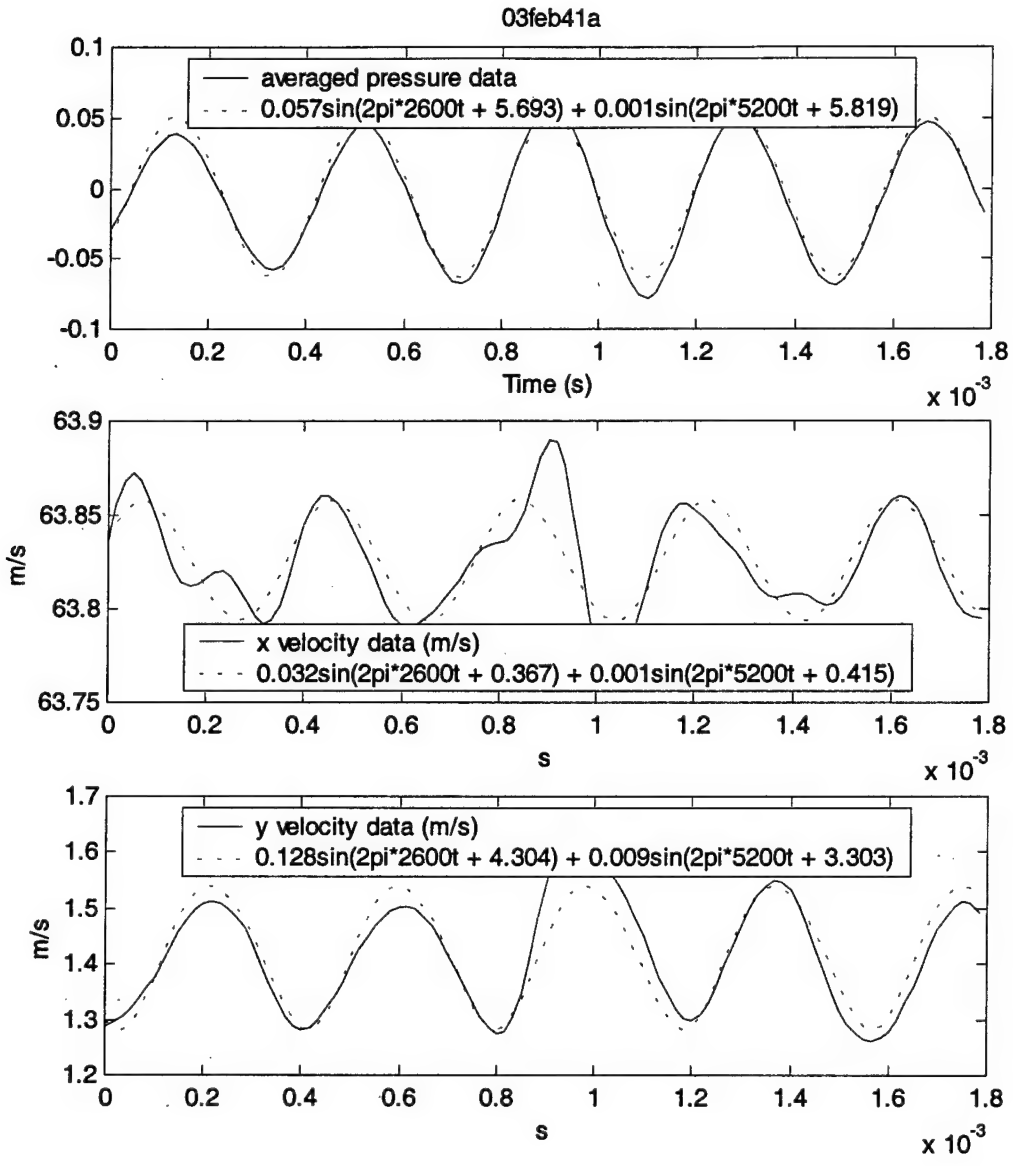

Figure 30. Data and two frequency approximation at x = -1.25 in, y = 0.75 in

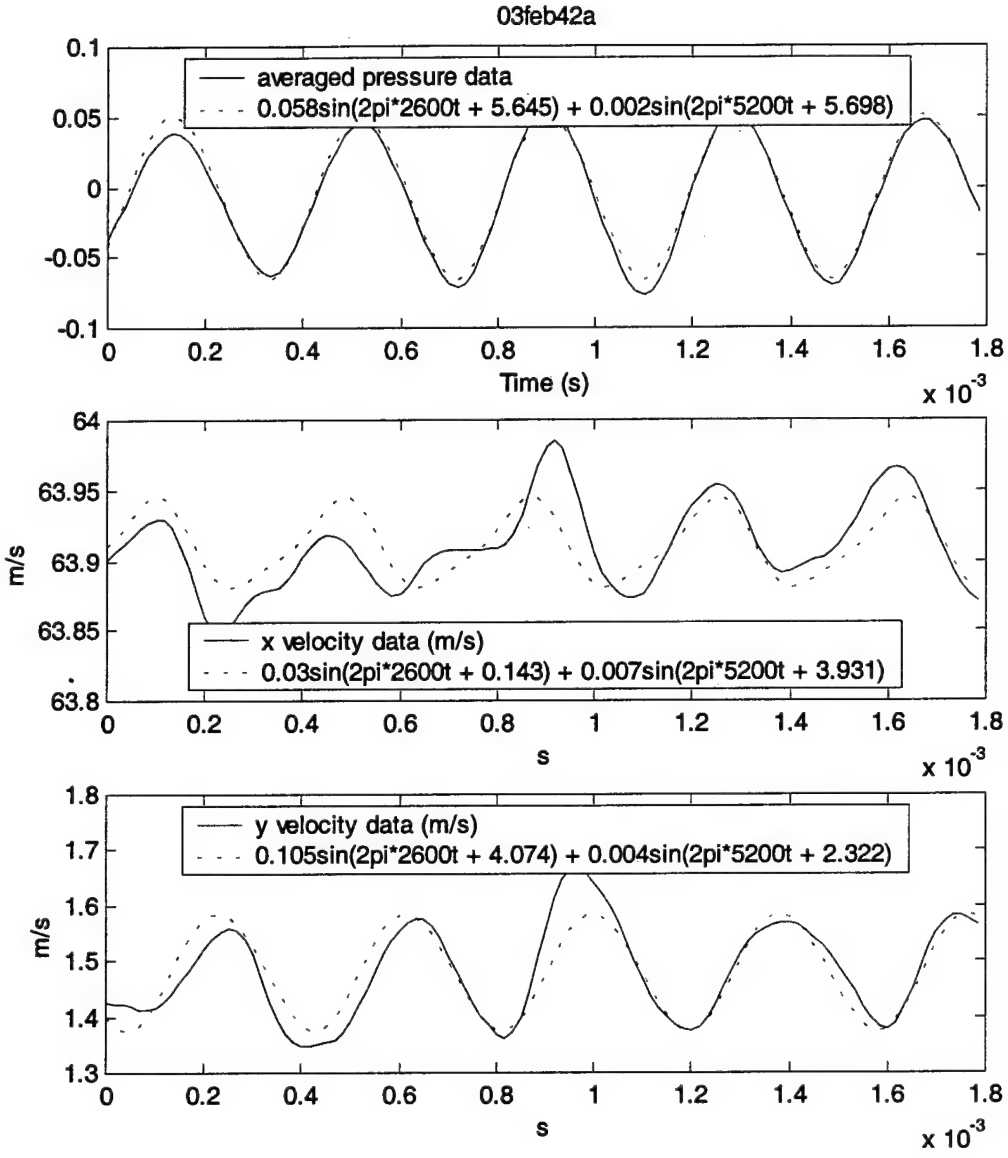

Figure 31. Data and two frequency approximation at x = -1.25 in, y = 0.875 in

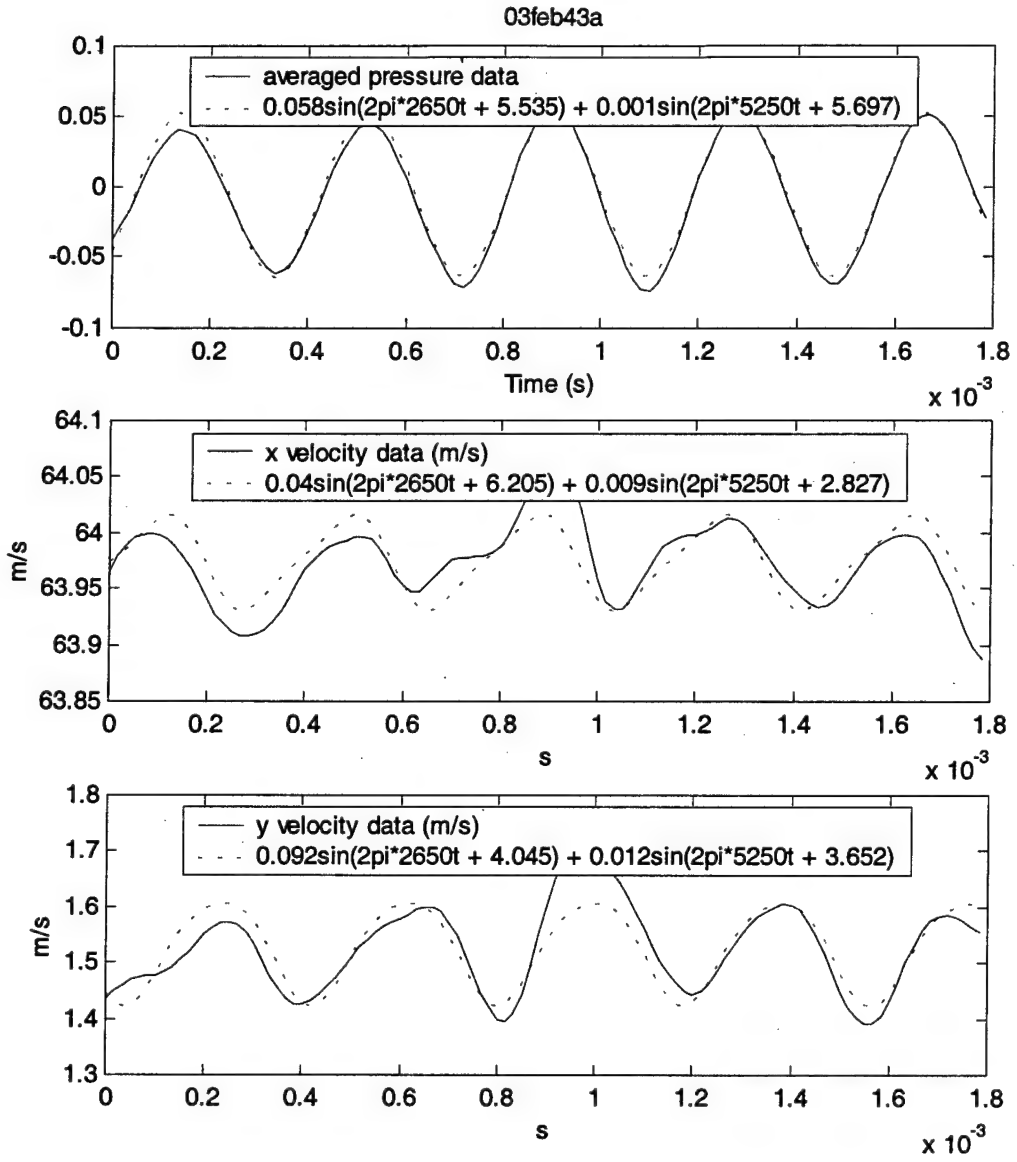

Figure 32. Data and two frequency approximation at x = -1.25 in, y = 1 in

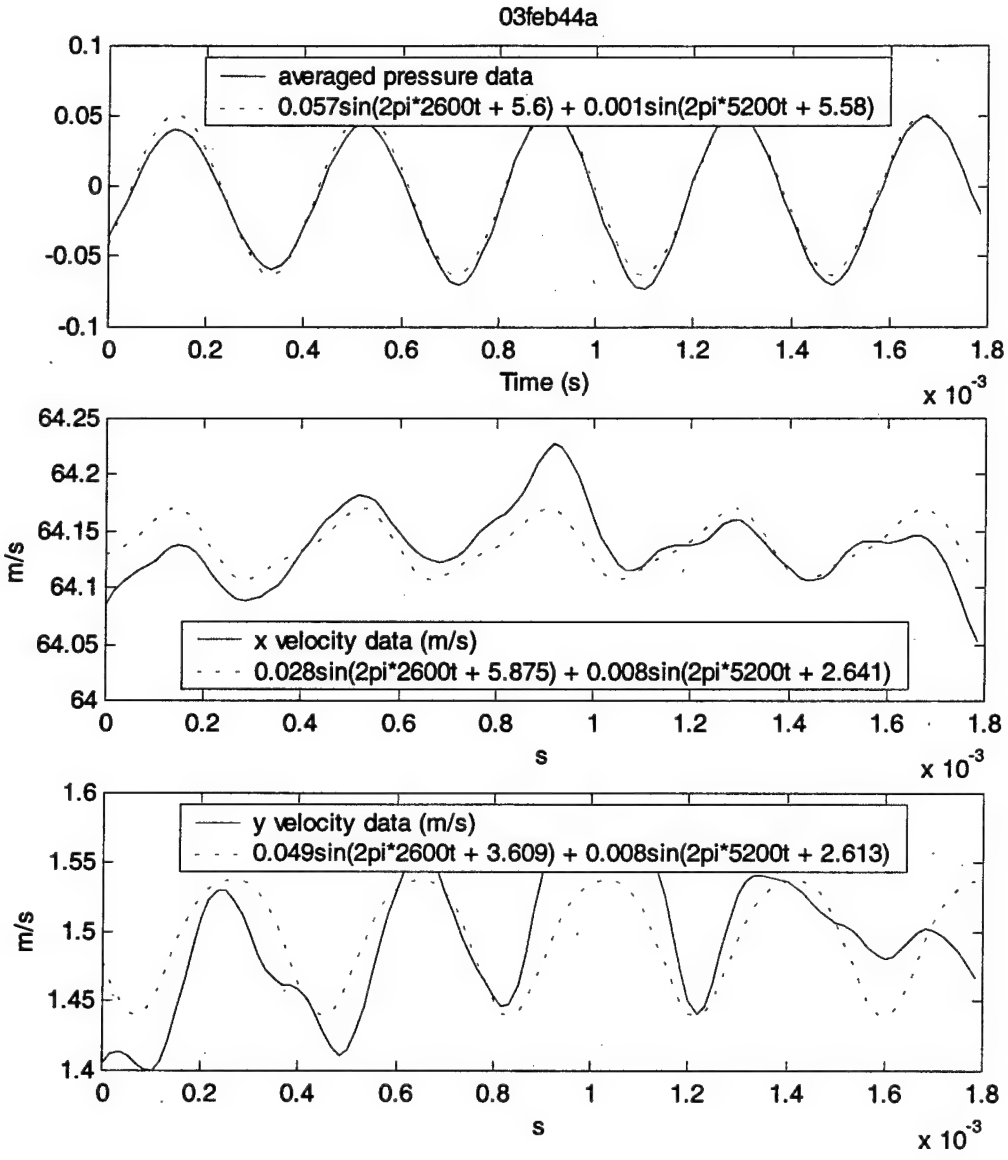

Figure 33. Data and two frequency approximation at x = -1.25 in, y = 1.25 in

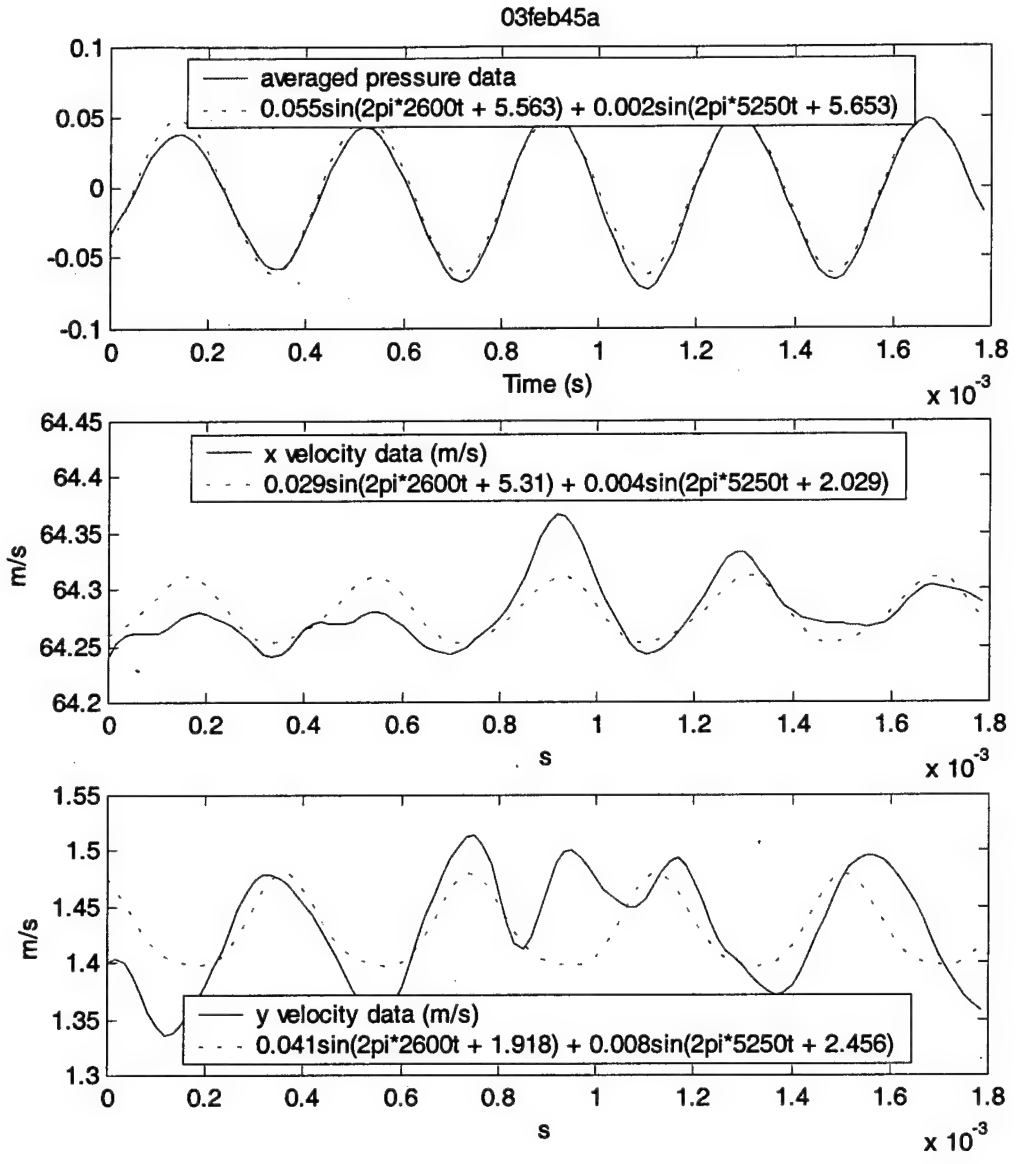

Figure 34. Data and two frequency approximation at x = -1.25 in, y = 1.5 in

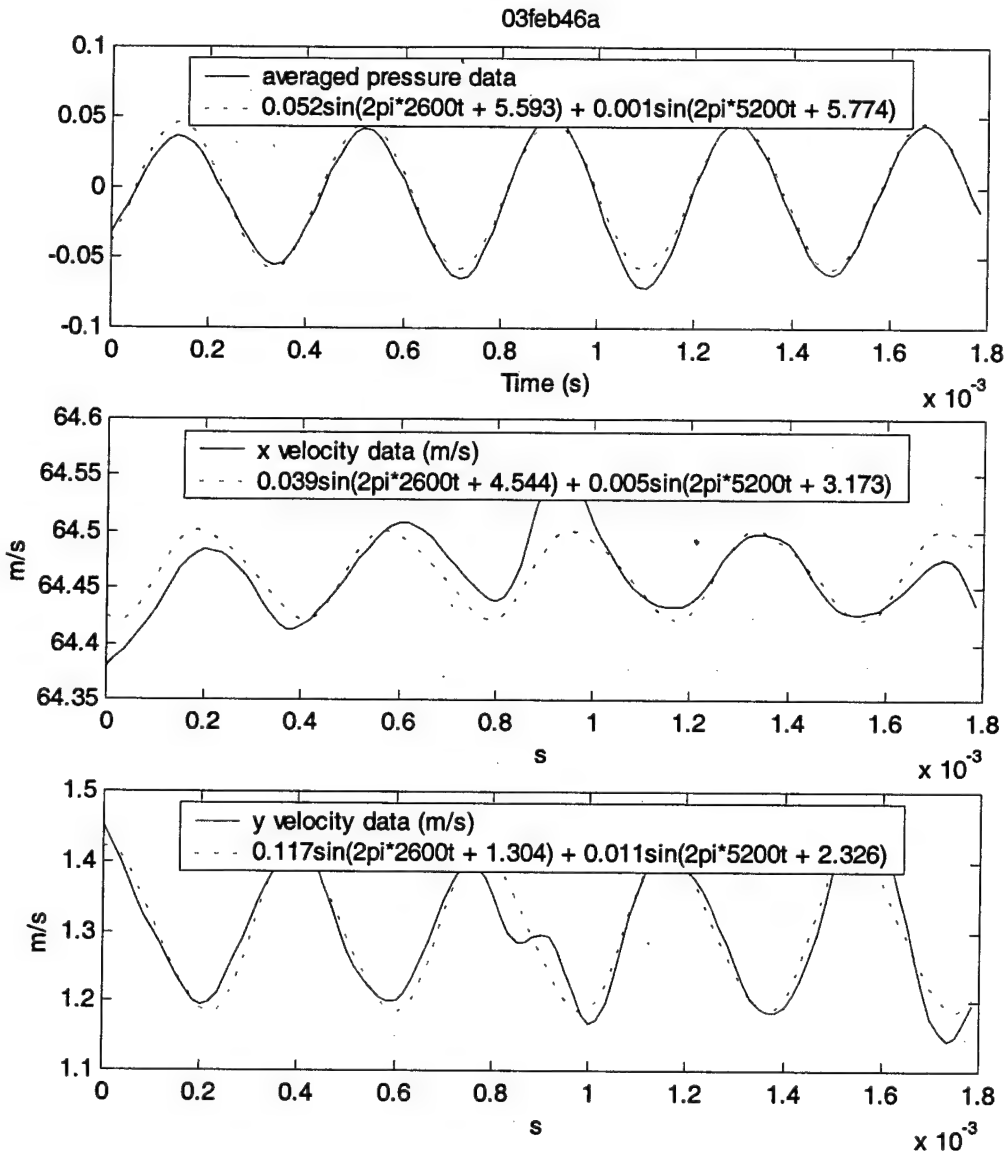

Figure 35. Data and two frequency approximation at x = -1.25 in, y = 2 in

Sections 4.1.1 through 4.1.3 discuss the data presented in Figure 13 through Figure 35 above.

4.1.1 Pressure Signal

The pressure signal was very nearly a single frequency sine wave for all data sets. The harmonic frequency does appear in the two-frequency approximation, but the amplitude is small enough compared to the amplitude of the fundamental frequency that it can probably be neglected.

A slight tapering of the pressure signal is also present, which can also be interpreted as low frequency modulation. Fabian and Jumper [6] saw this same modulation effect in their data. They hypothesized that it was a pump vibration or a tunnel mode. The fact that it was present in their work and in this research, however, indicates it is not a tunnel-specific effect.

There is another possible explanation for this tapering of the pressure signal. The trigger voltage is required to be near the maximum voltage attained by the pressure transducer. The voltage level from peak to peak has a large variation and only a few peaks actually reach the trigger level. As a result, the average voltage at the trigger point is higher than the surrounding peaks. It was necessary to trigger near the maximum voltage in order to consistently find peaks in the pressure wave. If a lower voltage was used, the trigger tended to occur at points other than the peak of the wave, and the ensemble averaged data lost their time-resolved character. The fact that the trigger point was consistently higher than surrounding points could cause this modulation effect.

4.1.2 Velocity Signal

Both x and y velocities show a fairly prominent oscillation at or very near the shedding frequency of the cylinder at most cylinder locations. The y velocity wave is larger in amplitude and generally more well-behaved than the x velocity wave. The relationship between amplitude and character of the wave is probably not a coincidence. The x velocity wave has a much larger mean (equal to the freestream velocity) and smaller amplitude. Unfiltered single runs contain a large amount of high frequency noise, among which is the 8 kHz vibration described in section 3.3.1. When the magnitude of the oscillation at the fundamental frequency is small, the noise will have more of a tendency to mask the presence of the fundamental frequency. As a result, the average of 250 data runs shows less clear information in the x velocity wave than in the larger amplitude y velocity wave.

The y velocity wave shows a nonzero mean. While this is somewhat surprising, the effect is at least symmetrical. The data taken with the hotwire above the cylinder show a small positive y velocity. Data taken below the cylinder show a small negative y velocity. This indicates that the cylinder presents a small but finite obstruction to the flow, resulting in a small amount of flow perpendicular to the freestream as the flow moves around the cylinder. Both x and y velocity waves show a significantly larger amplitude in the fundamental frequency than in the harmonic.

4.1.3 Uncertainties

Throughout the runs at x = -1.25 (3.18 cm) in and at the other x locations, there is a spike at the trigger time in both the x and y velocities. This is perhaps more noticeable

in the x velocity because the phase is more nearly opposite the pressure signal, so the spike shows as an extra peak midway between two regular peaks. In the y direction velocity where the phase is closer to that of the pressure signal, the spike often appears as an enlarged peak in the center of the data file. This spike at the trigger location is probably a result of crosstalk between channels during data acquisition.

Early in data collection, a floating ground was discovered on the trigger channel in the SCB-68 shielded connector box. Although this line was grounded, the trigger continued to be somewhat problematic throughout data collection. For instance, it was observed that the actual voltage level at the trigger point was typically one third to one half the level set as the trigger voltage in Labview.

It was decided that as long as the trigger occurred at a true peak in the data, the actual voltage level was probably not important. The appearance of crosstalk in the resulting data gives additional reason for concern, however. Although the crosstalk feature in the data is undesirable, the two frequency approximations do not appear to be much affected by it. Where the spike is between two peaks, the likely effect on the approximation would be additional content at the harmonic frequency. Where it coincides with a peak in the data, the approximation would overestimate the amplitude of the waveform. Neither of these appears to be the case, indicating that there were sufficient regular waveforms to outweigh a single voltage spike.

4.2 Phase Data

The phase of the unsteady velocities in the x and y directions was taken from the output of the least squares minimization as discussed in section 3.4.3 for each location where data were taken. The phase difference in the x and y directions was calculated as the phase of the pressure signal minus the phase of the unsteady velocity signal. The phase differences at 5 different x locations with the hotwire probe at the tunnel center are shown in Figure 36 through Figure 40. Phase data in these figures is plotted as a function of the y location of the hotwire probe relative to the cylinder. According to potential theory, the phase should change as a function of the distance r between the hotwire and the cylinder, which increases with both x and y distance, but it is instructive to examine the symmetry characteristics of the data when plotted as a function of y distance.

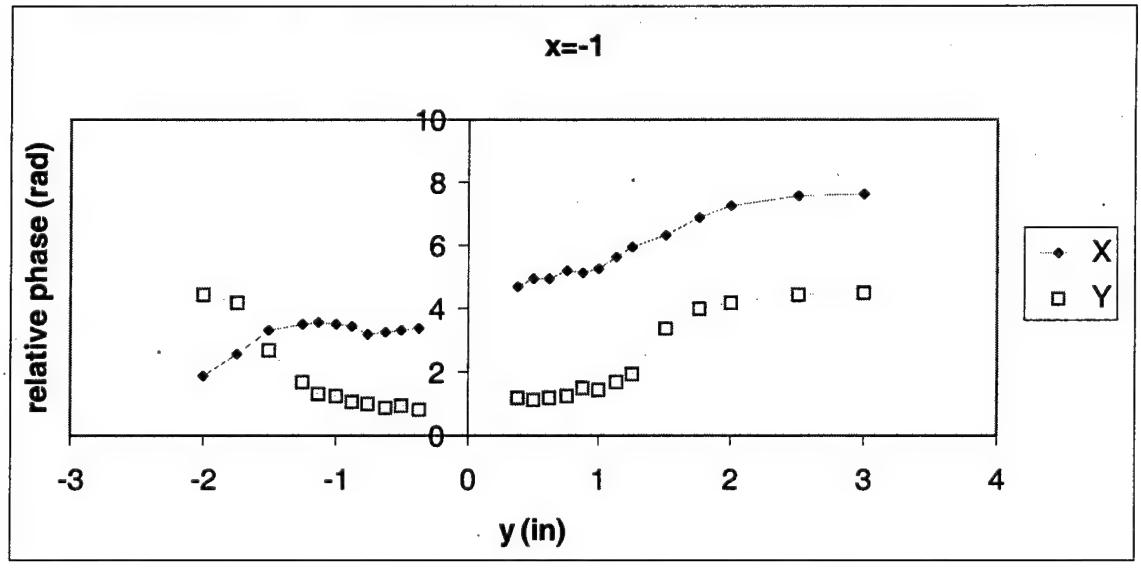

Figure 36. Phase data, x = -1 inches

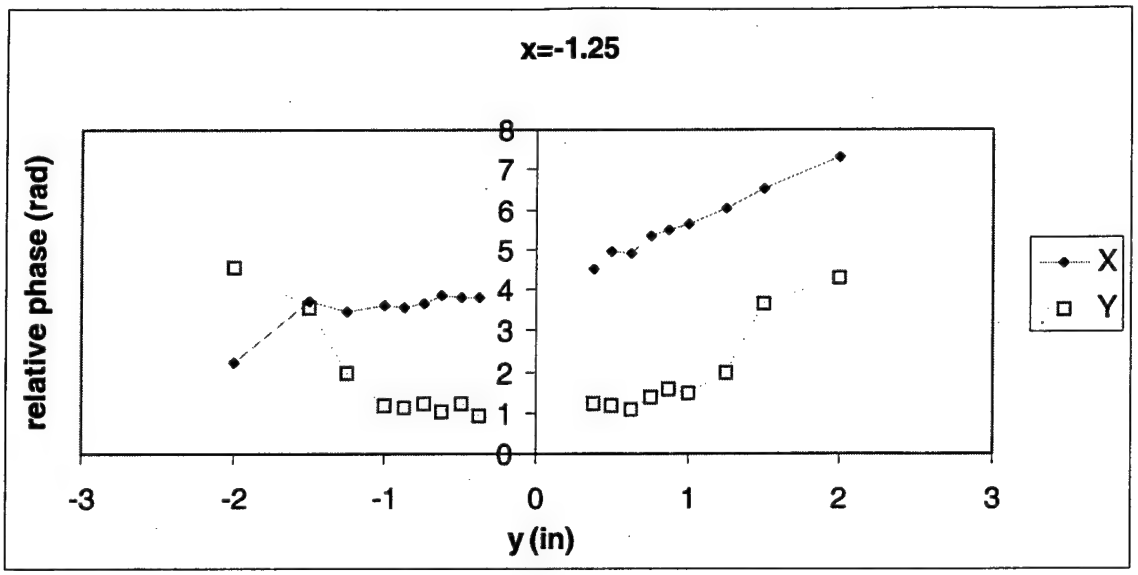

Figure 37. Phase data, x = -1.25 inches

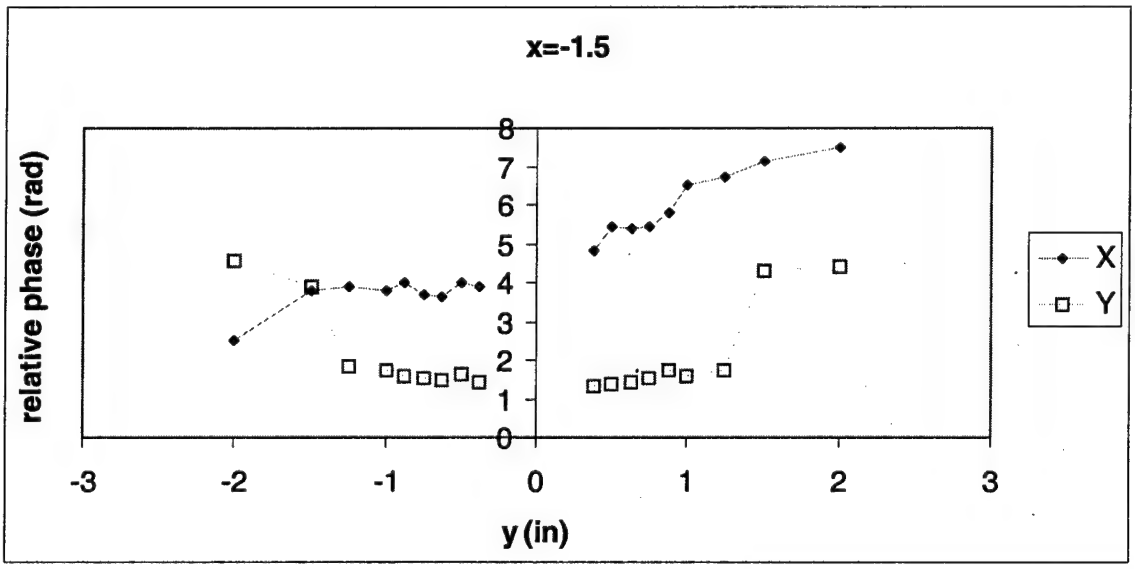

Figure 38. Phase data, x = -1.5 inches

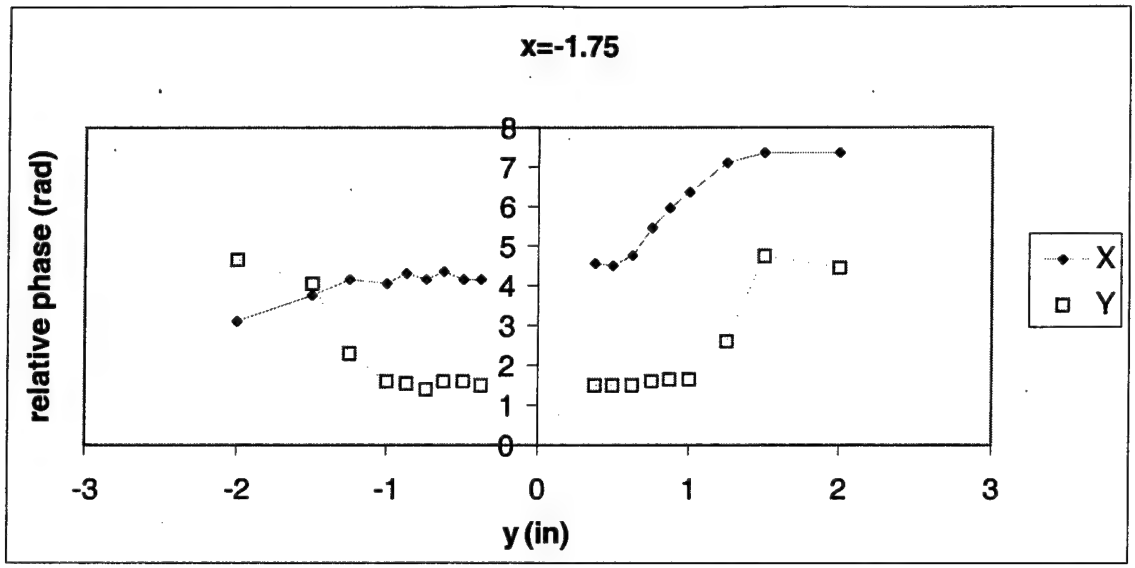

Figure 39. Phase data, x = -1.75 inches

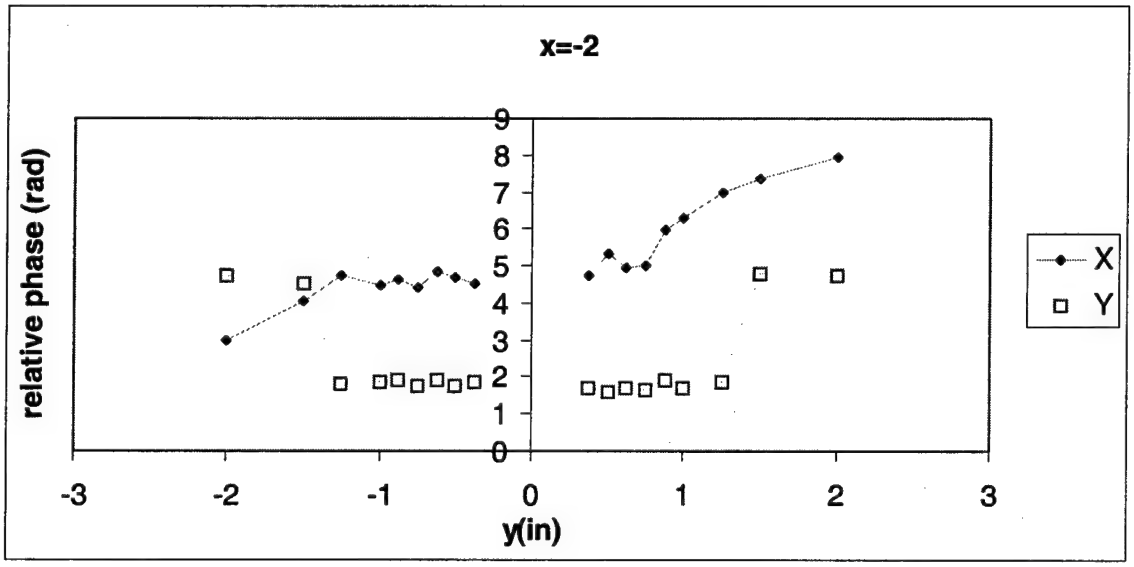

Figure 40. Phase data, x = -2 inches

The least squares minimization was designed to return phase between 0 and 2π. As a result, the phase, which would normally have a small change from one cylinder location to the next, occasionally had sudden jumps of approximately 2π when crossing either limit. In these cases, a full period of phase was added to or subtracted from the phase in order to retain a smooth curve in the data. The y-phase data show a sharp upward trend between y = +/- 1.5 and y = +/- 2.0 in (+/- 3.8 and +/- 5.1 cm). This trend was noted, and so the data of Figure 36, which were taken after the others, intentionally included data at closer intervals in this range, as well as additional locations outside the range of the other data sets. These additional data points show that there is a fairly smooth if rapid increase in y-phase between y = +/- 1.5 and y = +/- 2.0 in (+/- 3.8 and +/- 5.1 cm) and also that the data continue in a smooth curve beyond x = 2.0 in (5.1 cm).

One observed phenomenon in both x and the y was a drop in the relative phase when the hotwire was directly upstream the cylinder. The relative phase drop was the same in the x velocity phase as in the y velocity phase. The frequency of shedding also changed by approximately 50 Hz at these locations. It was suspected that the hotwire probe was interfering with the shedding of the cylinder when directly upstream. During subsequent data collection, the aural tone of the shedding frequency was observed to change when the hotwire was within 0.125 in (0.32 cm) of the cylinder. This confirmed the suspicion that the hotwire was interfering with the shedding when any portion of the hotwire probe was directly upstream the cylinder. The intent of this investigation was to find the upstream velocity field of a cylinder absent the presence of the hotwire probe.

Once it was discovered that probe interference existed, all phase and amplitude data within 0.25 in (0.64 cm) of the y location of the cylinder were discarded.

The phase data all appear to have a common character. The x phase steadily increases as y distance increases. The y phase, however, is nearly symmetrical about y = 0. A possible explanation for this is shown in Figure 41.

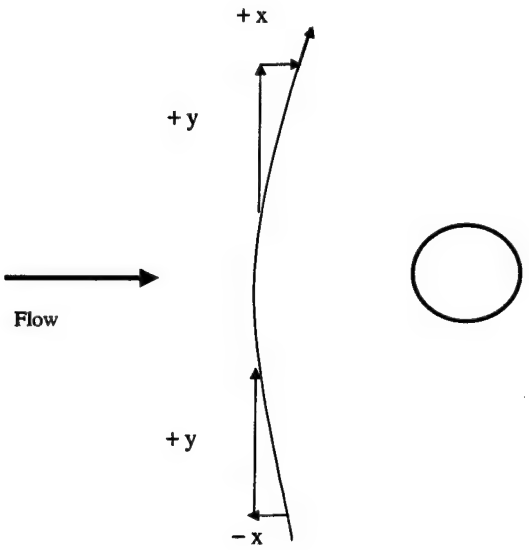

Figure 41. Circulatory model for flow disturbance

Figure 41 is a representation of a snapshot view at a given instant of time in the flowfield upstream the cylinder. The y = 0 plane includes all points directly upstream the cylinder. The curved arrow upstream the cylinder represents the flow perturbation at a single radial location about the cylinder at the given instant of time. For a point selected above the plane y = 0, there is an associated amplitude in the x direction and y direction.

For the mirror image point below the plane y = 0, the y amplitude is in the same direction (symmetric) and the x amplitude is in the opposite direction (asymmetric).

4.3 Amplitude Data

The amplitude of the unsteady velocity signal in the x and y directions (Figure 42 through Figure 46) was also determined using the least squares minimization of section 3.4.3. It is important to realize that these amplitudes are the result of an average of 250 runs that are approximated by a two-frequency sinusoid. In some cases the two-frequency sinusoidal approximation was quite consistent with the averaged data. In other cases, because the averaged data were somewhat irregular, the sinusoidal approximation was somewhat smaller in amplitude than the tallest peaks in the data. The amplitude data shown here show general trends of average amplitudes from one position to the next, but the actual magnitude of the unsteady velocity is quite irregular.

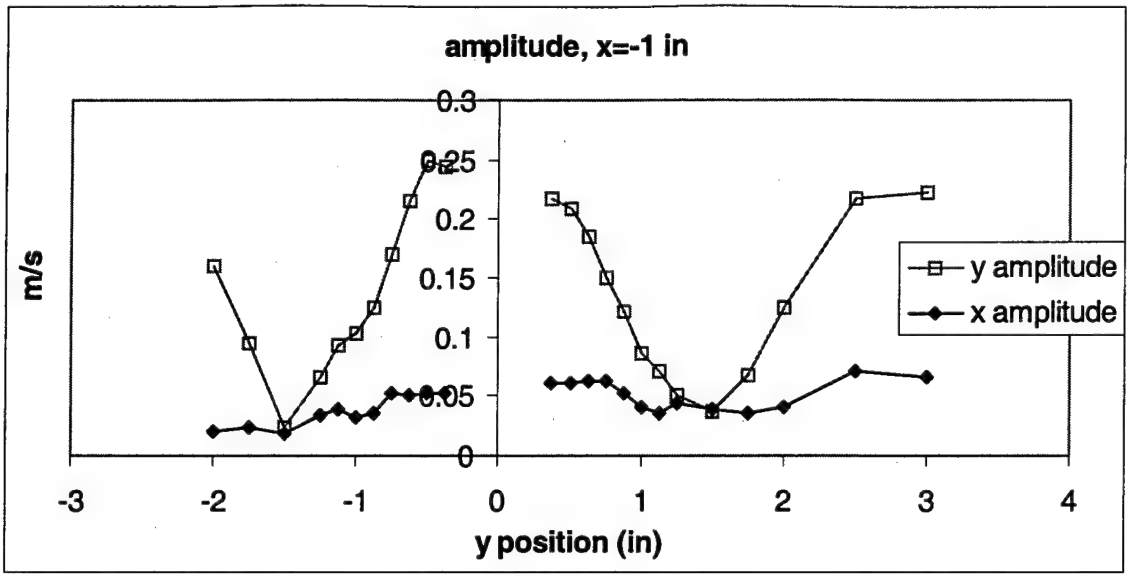

Figure 42. Amplitude data, x = -1 inches

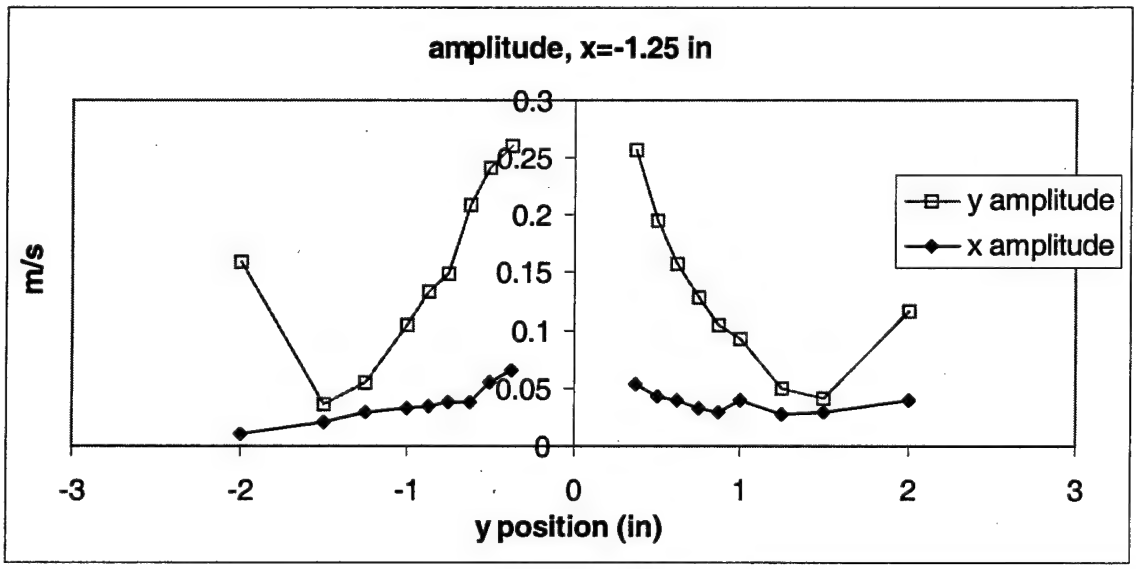

Figure 43. Amplitude data, x = -1.25 inches

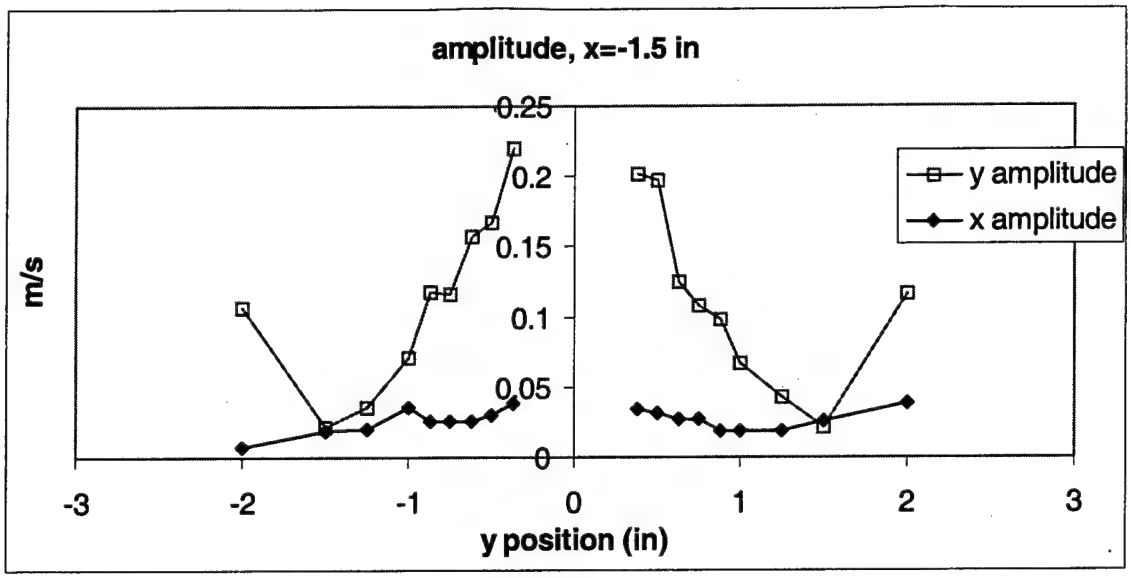

Figure 44. Amplitude data, x = -1.5 inches

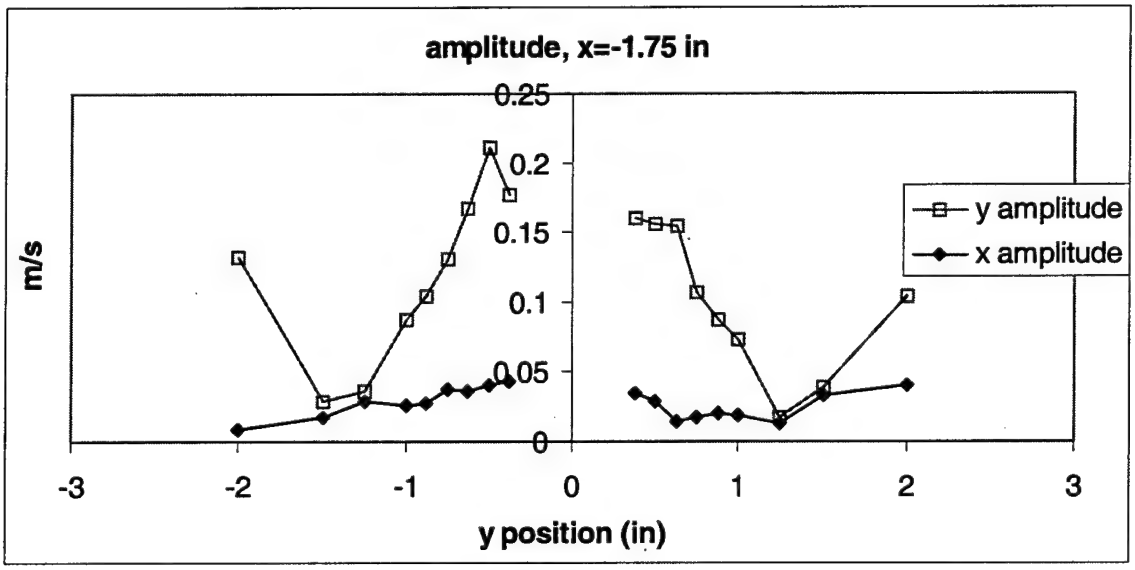

Figure 45. Amplitude data, x = -1.75 inches

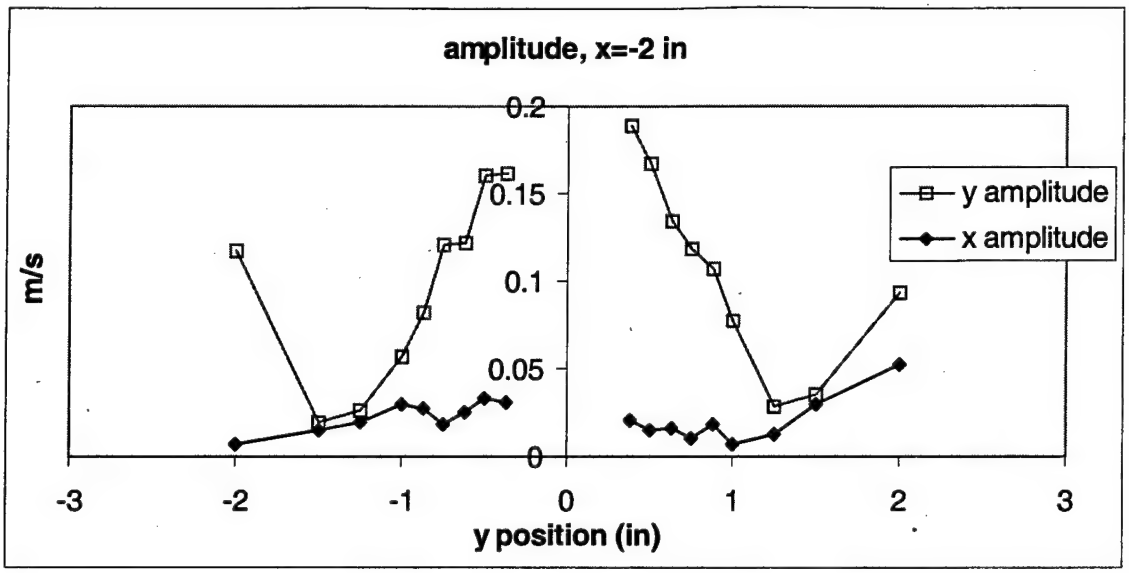

Figure 46. Amplitude data, x = -2 inches

The amplitude of the x-direction perturbation was much smaller than the y-direction perturbation in almost all locations. The shape of the x amplitude curve is similar to the y amplitude curve, just at a lower level. One difference between the two is seen in that the y amplitude curve is almost perfectly symmetrical about y = 0, while the x amplitude curve has an upturn on the positive y side and no such feature on the negative y side.

4.4 Off-Centerline Data

A new hotwire insertion point was drilled into the side of the test section 1.625 in (4.1 cm) above the tunnel centerline to determine whether the sudden jump in y phase and corresponding minimum amplitude were effects fixed in tunnel location or whether they were associated with the position of the cylinder relative to the hotwire. The phase

and amplitude data from this hotwire measurement location are shown in Figure 47 and Figure 48. The raw data for this hotwire location are contained in Appendix B.

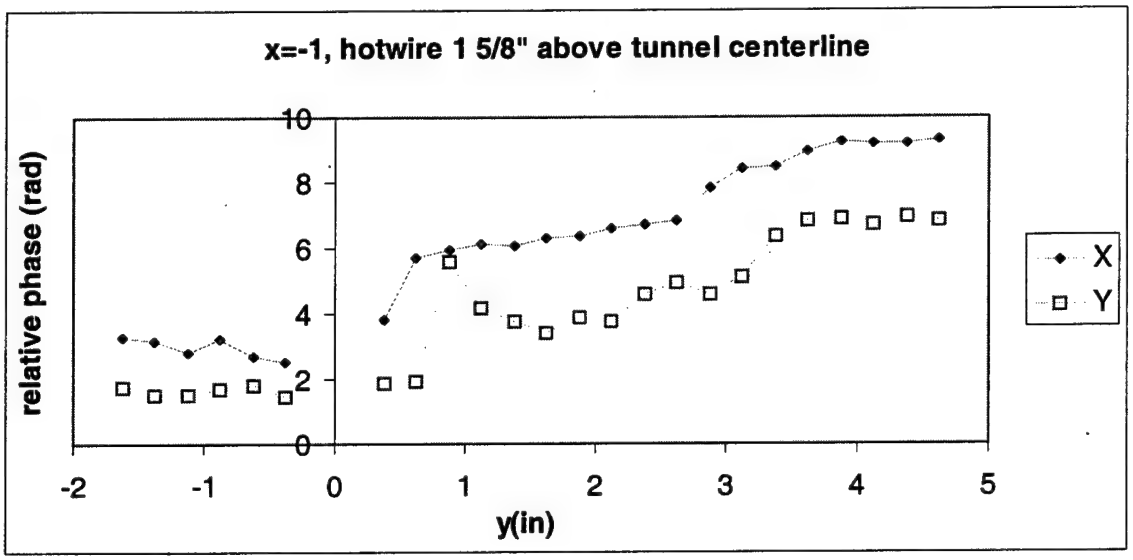

Figure 47. Phase data, hotwire 1 5/8 in above tunnel center

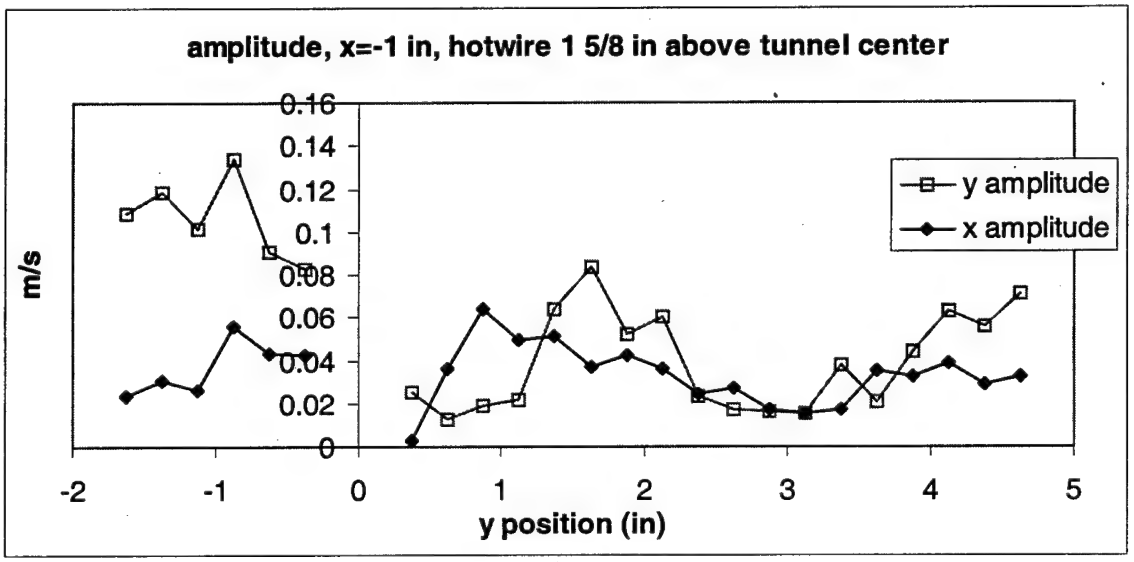

Figure 48. Amplitude data, hotwire 1 5/8 in above tunnel center

In general, all of the data at the new location were less regular, or more erratic, than the data taken at the tunnel centerline. The y phase data that were symmetrical about $y = 0$ with the hotwire at the tunnel center did not exhibit the same symmetry when the hotwire was moved. It became evident at this point that the tunnel endwalls were in some way affecting the velocity measurement at the hotwire. The nature of this endwall effect will be discussed later in more detail.

5. Discussion of Results

A model of the velocity field upstream of a cylinder was developed by Fabian and Jumper [8]. That model is here compared to the experimental data presented in section 4.

5.1 Model

The model originates from superposition of the potential solution for a uniform flow over a doublet, which simulates a cylinder in the flow. Then, to model the alternating bound circulation due to shedding from the cylinder, a vortex is added whose strength varies in sinusoidal fashion over time. The resulting expression for velocity as a function of time at any position in the flow in cylindrical coordinates is [26]

$$\vec{V}(r,\theta,t) = \left\{U_\infty \cos\theta\left(1-\frac{R^2}{r^2}\right)\right\}\hat{r} \quad - \quad \left\{U_\infty \sin\theta\left(1+\frac{R^2}{r^2}\right)+\frac{\Gamma\sin(\omega_f t)}{2\pi r}\right\}\hat{\theta} \qquad (14)$$

where U_∞ is the freestream velocity, θ is the angle measured counterclockwise from the downstream side of the cylinder, r is the distance from the center of the cylinder and R is the cylinder diameter. The last term accounts for the time variation of the velocity, showing that the circulation (Γ) changes sinusoidally at what is herein called the fundamental frequency, ω_f. Note that $\omega=2\pi f$ where ω is in radians/s and f is in Hz. One period of the circulation shift includes two opposing vortices, one shed from each side of the cylinder. The strength of the velocity disturbance is inversely proportional to the distance r from the cylinder.

On a ray directly upstream the steady state stagnation point of the cylinder (θ = 180 degrees) and far upstream (r >> R) equation 14 simplifies considerably.

$$\vec{V}_{lift}(t) \equiv -U_{\infty}\hat{r} \quad - \quad \frac{\Gamma \sin(\omega_f t)}{2\pi r}\hat{\theta} \tag{15}$$

The velocity in equation 15 is termed V_{lift} because the sinusoidally varying circulation on the cylinder produces an alternating lift force on the cylinder. On a ray directly upstream the cylinder, velocity variations in the θ direction are perpendicular to the freestream, and are in the lift force direction.

In equations 14 and 15 the distance r is the distance from the center of the cylinder in incompressible flow. If compressibility effects are considered, r becomes the apparent distance from the center of the cylinder and a new term, r_g, or geometric distance from the center of the cylinder, is introduced. Using the Prandtl-Glauert compressibility correction, the apparent distance directly into the flow is as shown in equation 16.

$$r = \frac{r_g}{\sqrt{1-M^2}} \tag{16}$$

At any point in a uniform flow in the x direction equation 16 becomes

$$r = \sqrt{\frac{x^2}{1-M^2} + y^2} \quad = r_g \sqrt{\frac{\cos^2\theta}{1-M^2} + \sin^2\theta} \tag{17}$$

The variable θ is measured counterclockwise from the positive x-axis. Additionally, the time for a wave to reach an upstream location is delayed. This has the effect of a phase lag (ϕ) in the sine term of equation 15, again taken at a point directly upstream the cylinder.

$$\phi = \frac{r_g \omega_f}{a(1-M)} \tag{18}$$

Equation 18 is simply distance divided by acoustic speed (c) and multiplied by the radian frequency of the wave. When taken at any point in the flow, the acoustic speed is rewritten as the magnitude of the vector sum of the velocity of the pressure wave and the freestream velocity, or

$$c = a\sqrt{1+2M\cos\theta + M^2} \tag{19}$$

Substituting equations 16-18 into equations 14 and 15 yields the following generalized expressions for velocity.

$$\vec{V}(t) = \left\{U_\infty \cos\theta\left(1-\frac{R^2}{r^2}\right)\right\}\hat{r} \quad - \quad \left\{U_\infty \sin\theta\left(1+\frac{R^2}{r^2}\right) \quad + \quad \frac{\Gamma}{2\pi r}\sin\left(\omega_f t - \frac{r\omega_f}{a\sqrt{1+2M\cos\theta+M^2)}}\right)\right\}\hat{\theta} \tag{20}$$

$$\vec{V}_{lift}(t) \cong -U_\infty \hat{r} \quad - \quad \frac{\Gamma}{2\pi r}\sin\left(\omega_f t - \frac{r\omega_f}{a(1-M)}\right)\hat{\theta} \tag{21}$$

In addition to the fluctuating lift, the Fabian and Jumper model showed a sinusoidally varying aerodynamic drag on the cylinder [8]. Each vortex, as it is released into the flow, creates an increase in drag on the cylinder, perturbing the velocity in the streamwise direction. On a ray directly upstream of the cylinder at a distance much larger than the cylinder radius, the velocity would fluctuate around the freestream value, as shown in equation 22.

$$\vec{V}_{drag}(t) \cong \left\{ U_{\infty} + V'_{drag} \sin\left(\omega_h t - \frac{r_g \omega_h}{a(1-M)} \right) \right\} \hat{r} \tag{22}$$

Since a drag perturbation occurs for each shed vortex, the drag fluctuates at twice the fundamental, or harmonic frequency (ω_h). The amplitude of the drag fluctuation (V'_{drag}) is not derived from potential theory but was shown by Fabian and Jumper to be of roughly the same order as the lift velocity fluctuation in a compressible cascade with rods downstream the cascade blade row [6].

5.2 General Observations

The shedding from the cylinder is very nearly a single frequency sinusoid. This is in accordance with the model. The model predicts a velocity fluctuation in the x direction at twice the fundamental, or harmonic, frequency as a result of vortices shedding off both sides of the cylinder. At a single point on the surface of the cylinder, however, the harmonic frequency is not expected to be present.

Both x and y velocity waves show a significantly larger amplitude in the fundamental frequency than in the harmonic. This is expected in y (lift) direction, but

according to the model there should be a strong harmonic in the x (drag) direction. The model does not predict any fundamental frequency content in the x-direction directly upstream the cylinder. This deviation from the model is believed to be a result of measurement around a single cylinder, not a row of cylinders. The flow disturbance around a single cylinder is more radial in nature than the flow disturbance of a row of cylinders. In a row of cylinders, the flow fluctuations in the freestream direction are a result of a vortex on either side of the cylinder partially blocking the passage between two cylinders. With a single cylinder in a flow, the flow passage is much larger, and the blockage effects of a vortex shedding off the cylinder are slight. The model was designed for the case of multiple cylinders in a flow, and in this respect, does not extend to the single cylinder case.

5.3 Phase and Amplitude Correlation

5.3.1 Single Cylinder Model

A model for the y-perturbation phase change as a function of distance r was created using the phase term of equation 20. The result was the prediction curve in Figure 49, showing the relationship between phases at different locations in the flow. The model did not specify that a particular point in the changing circulation around the cylinder corresponded to a particular flow reaction, so the prediction curve was shifted by a constant phase to produce the best fit to the data. The resulting phase equation is:

$$\phi = \phi_{shift} + \frac{r\omega_f}{a\sqrt{1+2M\cos\theta+M^2}} \tag{23}$$

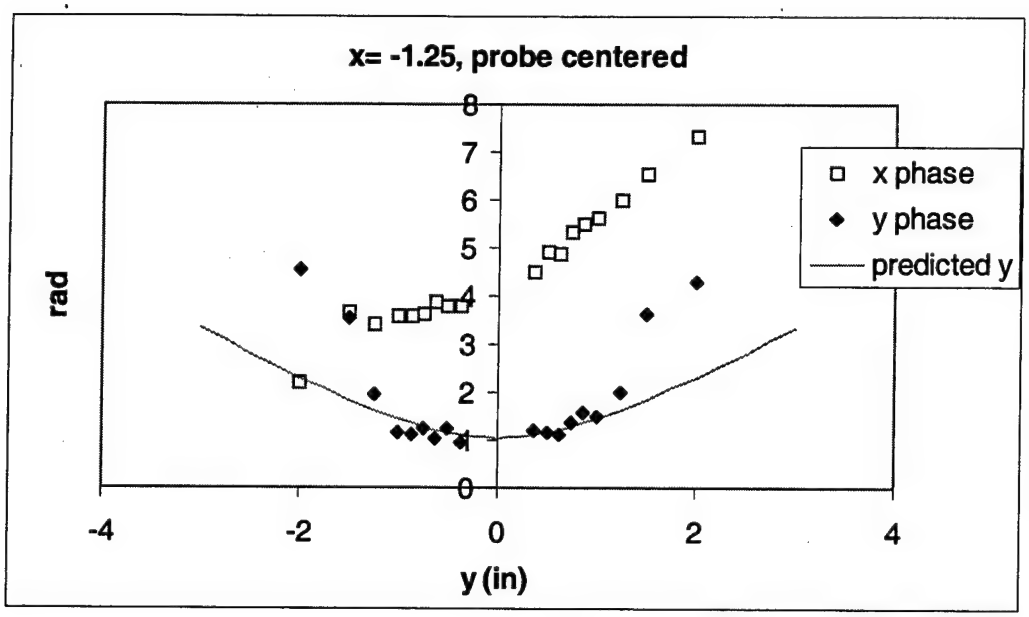

Figure 49. Single cylinder model fit to y phase data

For the points nearest the cylinder, the single cylinder prediction provides a fairly good description of the changing phase in y with $\phi_{shift} = -0.8$. Beyond approximately 1 in (2.54 cm) in either direction, however, the prediction does not follow the data. Additionally, at different x locations, different phase shifts were required to make the prediction fit the data. This seemed to indicate that the waves were propagating in a manner not fully described by a single cylinder model.

The phase of the x perturbation is also shown in Figure 49. Although the single cylinder model for x phase is the same as that for the y phase, the shape of the x data is clearly not predicted by a similar curve.

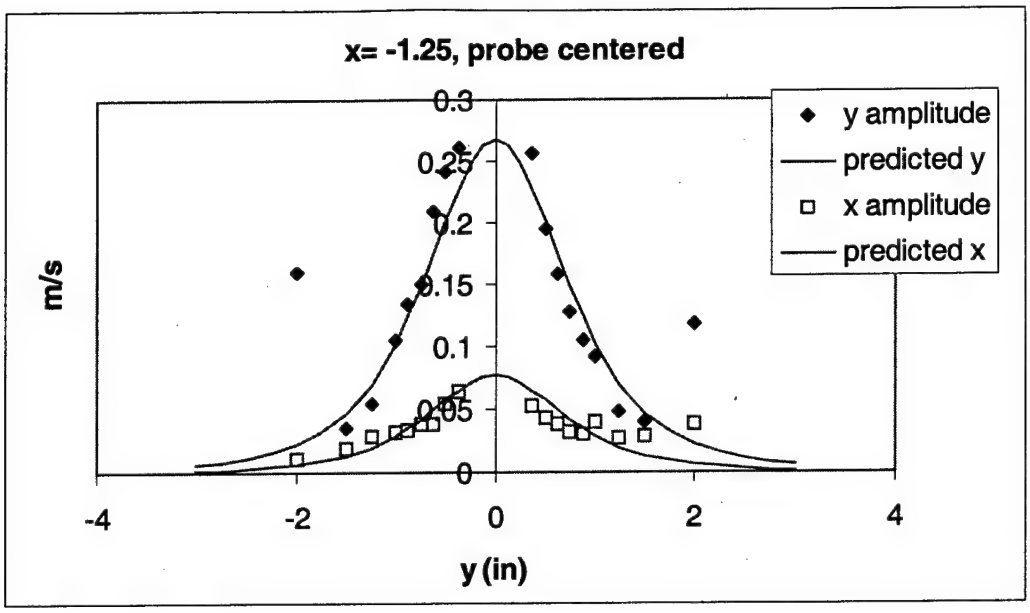

Figure 50. Single cylinder model fit to x and y amplitude data

The amplitude was also modeled using a form similar to the amplitude term of equation 20, k/r^n , where k was an arbitrary constant and n was an arbitrary power (Figure 50). According to the model, we would expect the power to be 1. The predictions of Figure 50 use a power of 4. At this x location, the x amplitude was matched fairly well with k = 0.2. Using a different constant, k = 0.7, the y amplitude was also matched, although there was a trend in the data away from the center of the tunnel that was not predicted. Beyond 1 in (2.54 cm) in either direction, the model broke down. Also, the constant and power used to fit the amplitude data at this x location did not produce a satisfactory fit at any other x location. In general, a higher power n and a larger constant k were needed as x distance from the cylinder increased.

5.3.2 *Reflected Cylinder Model*

The single cylinder model fit the data close to the cylinder in the y direction, but not the data further away. Because of the moving cylinder arrangement of this experiment, data taken further from the cylinder meant that the cylinder had moved closer to the top or bottom endwall of the tunnel. It was considered, then, that the endwalls were in some fashion affecting the upstream propagation of the disturbance.

Potential theory allows for wall reflection by considering a virtual cylinder equidistant and on the opposite side of the wall as the real cylinder. A new model was constructed with three disturbance sources: the real cylinder and two virtual cylinders, one on the opposite side of either endwall. At any point in the flow, the resultant effect of the three waves would be as follows.

$$A_c \sin(\omega t + \phi_c) = A_1 \sin(\omega t + \phi_1) + A_2 \sin(\omega t + \phi_2) + A_3 \sin(\omega t + \phi_3) \tag{24}$$

The subscript c in equation 24 indicates the phase and amplitude of the combined wave, and the subscripted numbers indicate the phase and amplitude of the component waves. The three amplitude terms ($A_{1,2,3}$) are of the same form (k/r^n) used in the single cylinder model, as are the three phase terms ($\phi_{1,2,3}$). All three component waves are expected to be at the same frequency, but since the second and third waves are reflections of the first, they were assumed to be 180 degrees out of phase with the first. Through some trigonometric manipulation, equation 24 becomes

$$A_c \sin(\omega t + \phi_c) = B \sin \omega t + C \cos \omega t \tag{25}$$

where

$$B = A_1 \cos\phi_1 + A_2 \cos\phi_2 + A_3 \cos\phi_3 \tag{26}$$

and

$$C = A_1 \sin\phi_1 + A_2 \sin\phi_2 + A_3 \sin\phi_3 \tag{27}$$

The right hand side terms of equation 25 can be rewritten as a single sine wave by

$$A_c \sin(\omega t + \phi_c) = \sqrt{B^2 + C^2} \sin(\omega t + \delta) \tag{28}$$

where the new phase term, δ, is given by

$$\tan\delta = \frac{C}{B} \tag{29}$$

The combined amplitude was modeled in the form

$$A_c = k' \sqrt{\left(\frac{\cos\phi_1}{r_1^n} + \frac{\cos\phi_2}{r_2^n} + \frac{\cos\phi_3}{r_3^n}\right)^2 + \left(\frac{\sin\phi_1}{r_1^n} + \frac{\sin\phi_2}{r_2^n} + \frac{\sin\phi_3}{r_3^n}\right)^2} \tag{30}$$

The amplitudes of all three cylinders were considered to be the same at their source locations, so the constant k was factored out of the expression and renamed k'. Similarly, the combined phase was modeled as

$$\phi_c = \phi_{shift} + \tan^{-1}\left(\frac{\sin\phi_1/r_1^n + \sin\phi_2/r_2^n + \sin\phi_3/r_3^n}{\cos\phi_1/r_1^n + \cos\phi_2/r_2^n + \cos\phi_3/r_3^n}\right) \tag{31}$$

In this case, the constant portion of the amplitude (k) was divided out of both numerator and denominator. The combined phase was allowed to shift by an arbitrary amount, as in the single cylinder model. Each phase term was calculated individually over a range of tunnel locations, then the combined phase and amplitude were created using equations 30 and 31. Because the inverse tangent calculation is not quadrant specific, sharp jumps in the combined phase model were common. Multiples of π were added to the combined phase as necessary to smooth the curve.

The combination of waves significantly increased the complexity of the model. Phase and amplitude of the combined model are function of the phase, amplitude and position of the individual cylinders. The phase and amplitude models can no longer be considered independently because each affects the other.

5.3.3 Constraints

This virtual cylinder model was fit to the phase and amplitude data through a lengthy search of power and amplitude terms as well as other features in an attempt to describe the data as accurately as possible. Along the way a number of parameters were constrained to produce a model that could be reasonably explained in physical terms. For example, the power n of the amplitude terms was required to be greater than zero. Negative powers of n produced some features in the model that fit the data quite well. However, a negative power would indicate that the amplitude does not fall off as the distance from the cylinder grows, but actually increases. One ramification of an amplitude that increases with distance from the measurement point is that, in a reflected cylinder model, the reflections, which are more distant from the measurement point, have

a greater effect than the real cylinder. This applies to not only the first reflection, but to the nth reflection from each wall. The result is a model that is extremely counterintuitive and would require an infinite number of virtual cylinders to make an accurate prediction.

Another feature that was varied in the search for a fit to the data was the phase of the cylinders, calculated as in equation 20 for the real and virtual cylinders, was multiplied by a constant. This resulted in effectively varying the speed of propagation of the disturbance. In this manner, the periodicity of the prediction could be controlled, shifting wave features and changing wave shapes. Some moderately appealing results were obtained in this manner, but ultimately were rejected because no explanation could be found for why the disturbance would propagate at other than acoustic speed.

Other factors were also varied in the search for the best fit to the data. The relative amplitudes of the real cylinder and two virtual cylinders were varied as though the shedding from the real cylinder was stronger than that of the virtual cylinders. It was decided, however, that equal strength for all three was more realistic. Potential interference of the boundary layer with the reflection of the disturbance wave was considered by varying the location of the reflected cylinders in the x, y and r directions. The phase of the reflected cylinders relative to the real cylinder was also varied by an arbitrary constant. In the final model, however, none of these parameters were varied.

The model suggested by equation 20 is in cylindrical coordinates. In this experiment, velocity perturbations in the x and y directions were measured. If the perturbation field propagated in a cylindrical manner, a simple coordinate transform would give the amplitude of the x perturbations as $A\sin\theta$ and the y perturbations as

$A\cos\theta$ where A is a general amplitude term as discussed in the single cylinder model of section 5.3.1. For the most part, however, a better fit to the phase and amplitude data was produced by considering x and y as separate perturbations and not as cosines and sines of a single circular perturbation. The only exception to this was in the points taken at a hotwire location off the centerline of the tunnel. The model for the data taken off the tunnel centerline will be discussed later in more detail.

5.3.4 X Phase and Amplitude Fits

The following figures show the fit of the three-cylinder model to the x phase and amplitude data. In all figures in this section and in the two sections that follow, the power n is 0.04, a very small positive power that was estimated from the minimal falloff in amplitude at the centerline of the tunnel from x= -1 to -2.

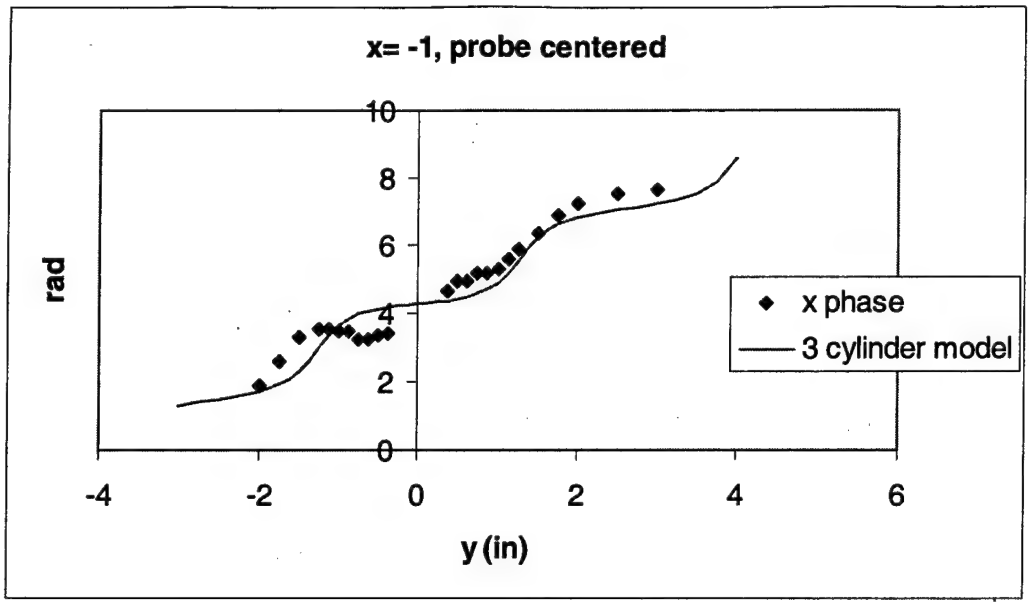

Figure 51. Three cylinder model for x phase, x=-1

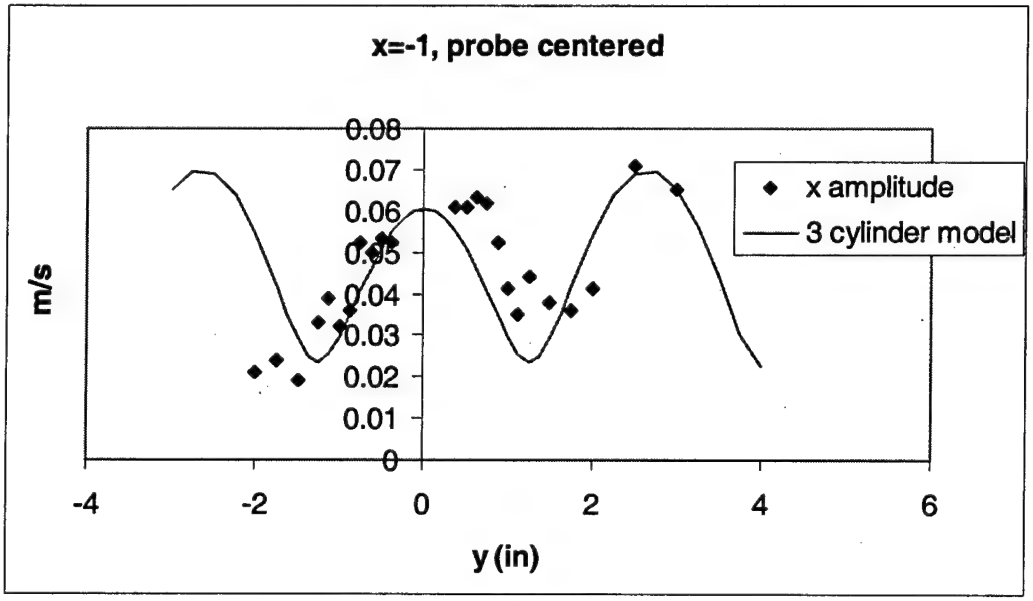

Figure 52. Three cylinder model for x amplitude, x=-1

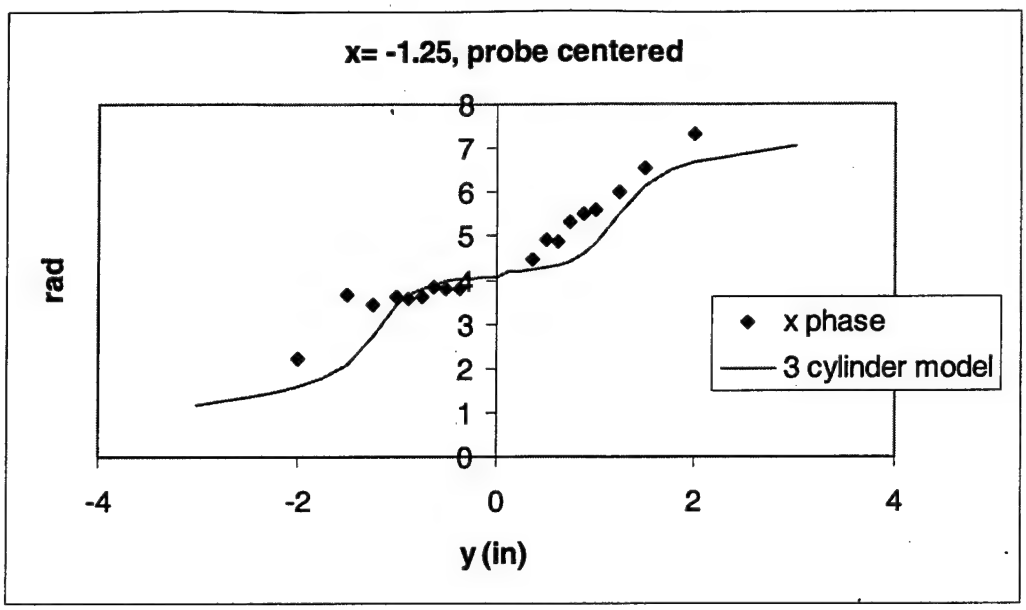

Figure 53. Three cylinder model for x phase, x=-1.25

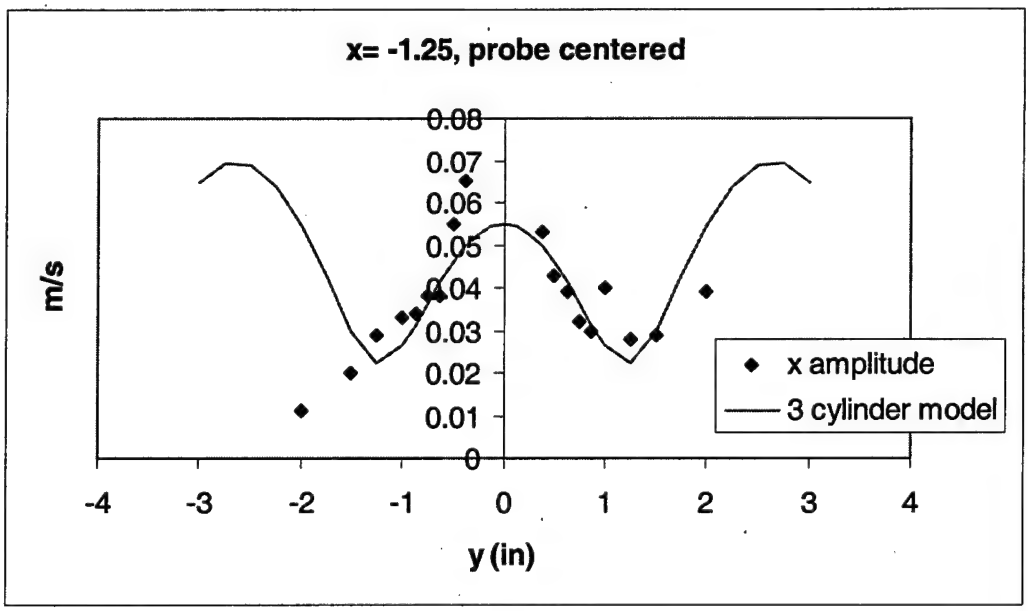

Figure 54. Three cylinder model for x amplitude, x=-1.25

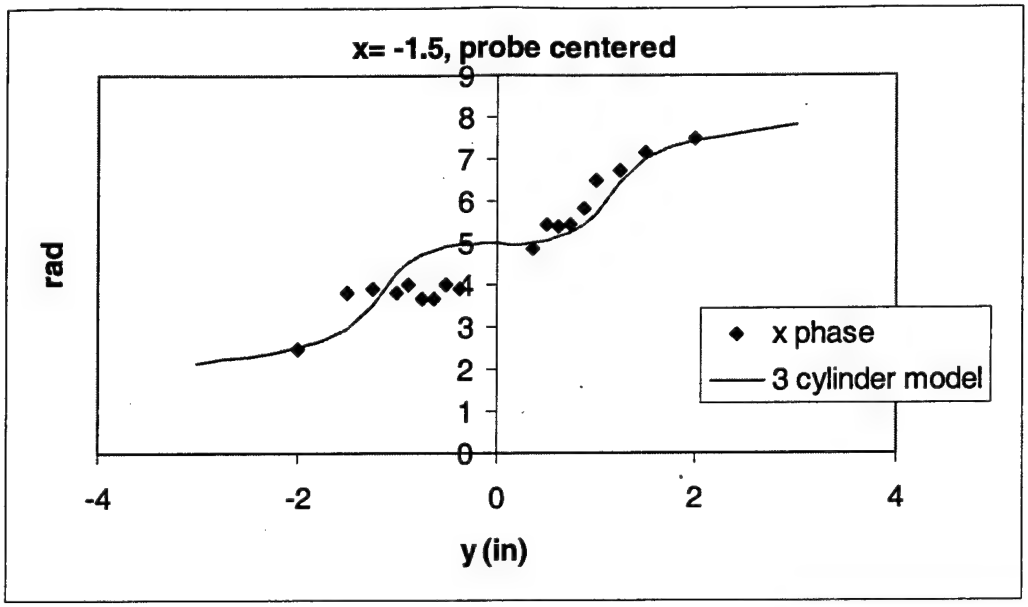

Figure 55. Three cylinder model for x phase, x=-1.5

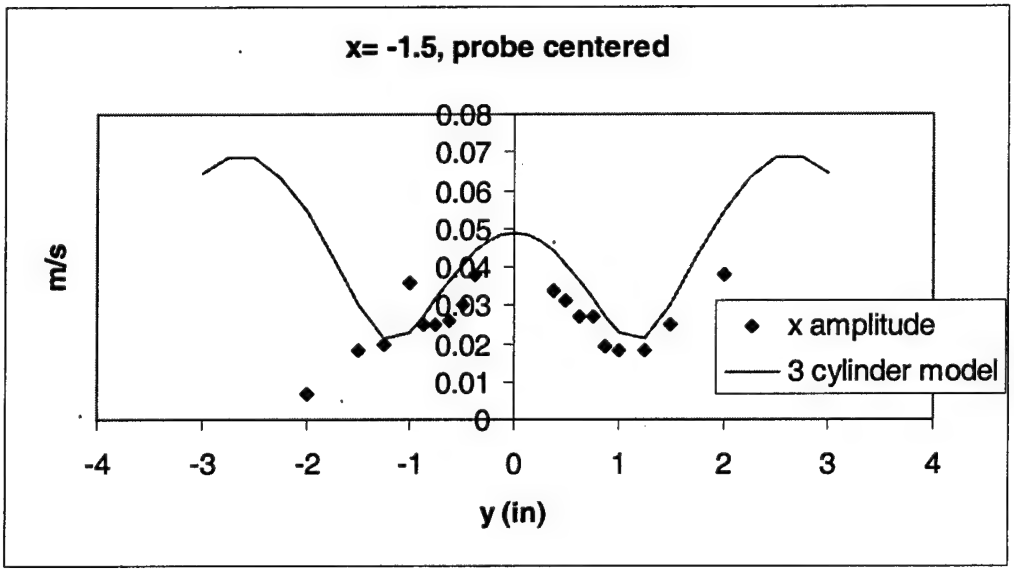

Figure 56. Three cylinder model for x amplitude, x=-1.5

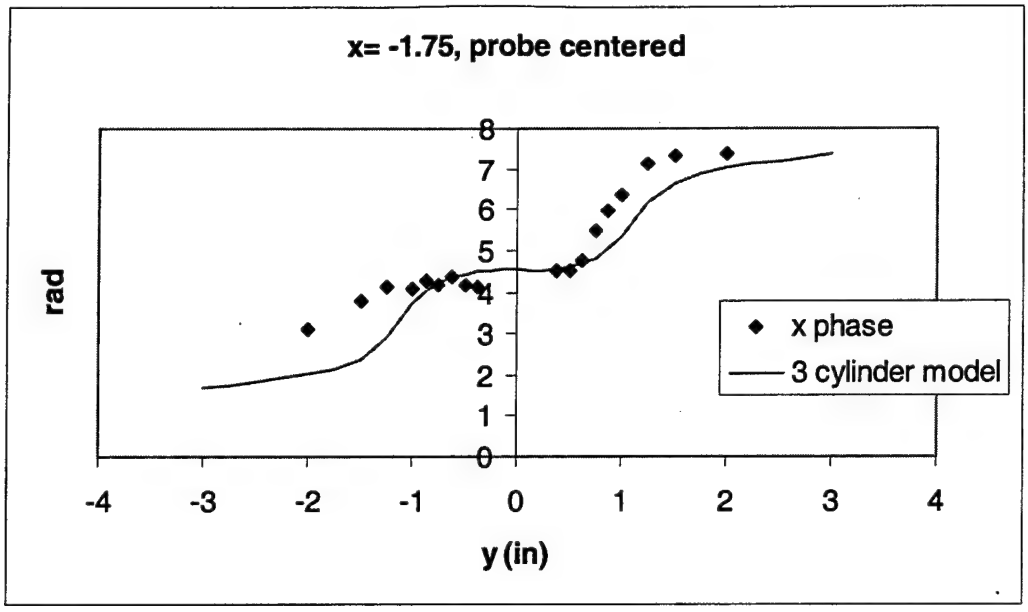

Figure 57. Three cylinder model for x phase, x=-1.75

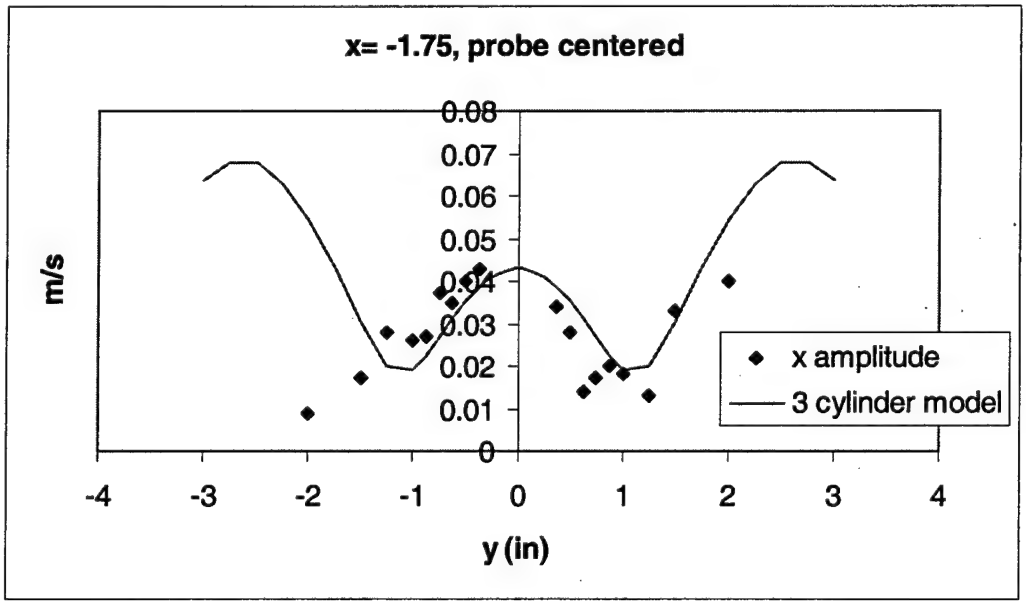

Figure 58. Three cylinder model for x amplitude, x=-1.75

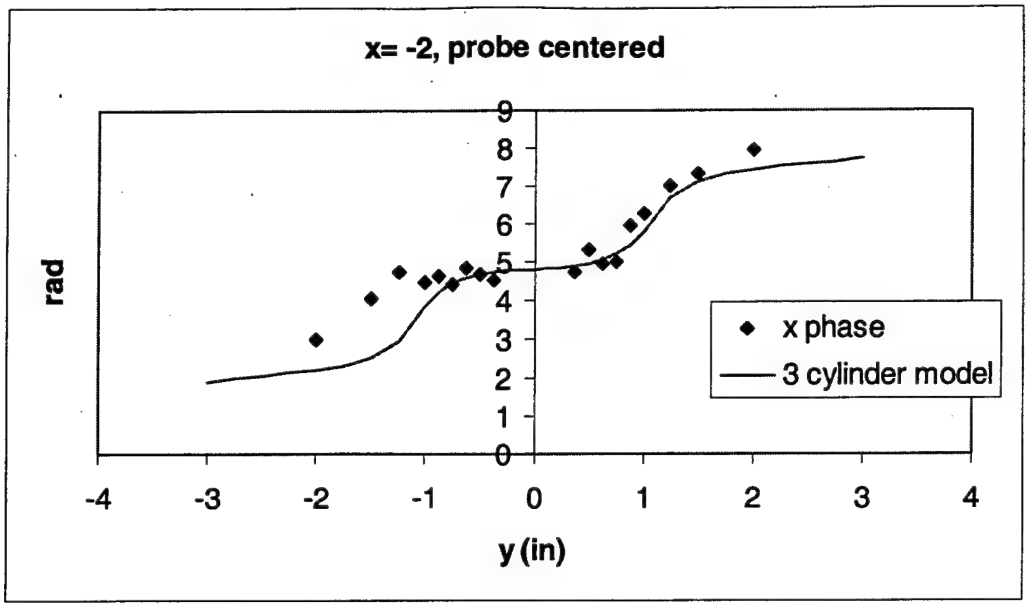

Figure 59. Three cylinder model for x phase, x=-2

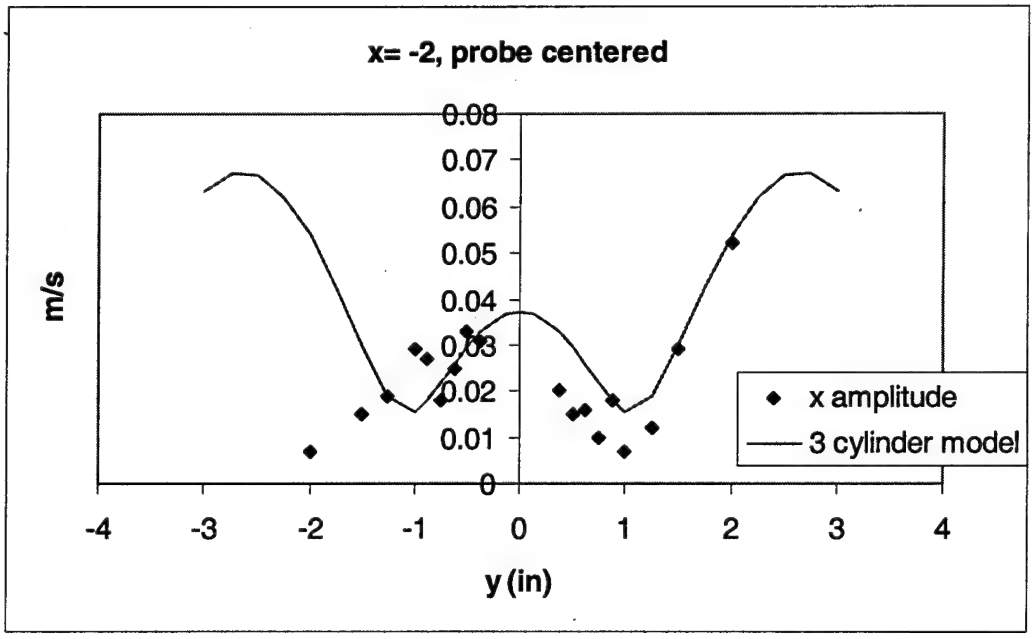

Figure 60. Three cylinder model for x amplitude, x=-2

For all phase and amplitude models shown in Figure 51 through Figure 60 above, the constant k' used in the amplitude estimation was the same, 0.025. The amplitude falloff with distance was only a very small fraction of the 1/r rate predicted by the potential flow solution (n = 0.04). For the most part, the essence of the amplitude data is captured using the model with constants as stated. One small deviation from the prediction is a slight asymmetry noted in all the x amplitude data. The data rise at the largest positive y locations, but there is no corresponding increase in the amplitude at the most negative y locations. The model does not predict this asymmetry.

A more pronounced asymmetry is exhibited in the x phase data above. Upon examination of the physical characteristics of the data the model was inverted on the left hand side to more closely approximate the behavior of the data. The x phase combined cylinder model is asymmetric about y = 0 and accurately predicts both the right hand side and left hand sides of the x phase data. The exact reason for the asymmetry in the data is not known, but a pure potential flow model assumes that the disturbance propagates from the same source for all upstream locations. In the case of the x perturbation, this is probably not a good assumption. A circular perturbation about the cylinder will have a different phase in the x direction above the cylinder than it will below the cylinder (see Figure 41).

The x-perturbation phase above the cylinder (δ_{up}) appeared to differ from the phase below the cylinder by $\delta_{low} = \pi - \delta_{up}$. In this expression, δ_{up} is the phase at an arbitrary point above the cylinder (y>0), whose source is assumed to be in phase with the pressure wave at the top of the cylinder. The quantity δ_{low} refers to the phase at an

arbitrary point below the cylinder (y<0) whose source is not in phase with the pressure at the top of the cylinder. An equivalent inversion was made to the left-hand side of the x phase model by taking the negative of the quantity inside the brackets of equation 31. In equation form this would be expressed $\tan(\pi-\delta) = \tan(-\delta)$. The inverted portion of the curve was then shifted by a phase constant (ϕ_{lhs}) to align it with the right hand portion of the curve. The resulting model for the left-hand side of the x perturbation phase was

$$\phi_c = \phi_{shift} + \phi_{lhs} + \tan^{-1}\left(\frac{-(\sin\phi_1/r_1^n + \sin\phi_2/r_2^n + \sin\phi_3/r_3^n)}{\cos\phi_1/r_1^n + \cos\phi_2/r_2^n + \cos\phi_3/r_3^n}\right) \tag{32}$$

and the model for the right-hand side of the x perturbation was equation 31. Table 1 shows the values of ϕ_{lhs} required to align the left-hand side with the right, and the required phase shifts for the entire x perturbation curve.

Table 1. Phase Shifts Used in x Perturbation Model

Position	Phase Shift (ϕ_{shift})	Left Hand Side Shift (ϕ_{lhs})
x = -1	3.6 rad	-1.8 rad
x = -1.25	3.3 rad	-1.5 rad
x = -1.5	3.9 rad	-1.0 rad
x = -1.75	3.3 rad	-0.7 rad
x = -2	3.5 rad	-0.5 rad

The required phase shifts for the x perturbation data varied somewhat, but showed no particular trend with x distance. The shift magnitude was selected by aesthetically matching the curve to the data at a particular x location without regard to other x locations. An average shift of 3.5 or 3.6 would probably yield acceptable results for all x locations. The left-hand side shifts, however, show a definite increasing trend with increased x distance.

5.3.5 Y Phase and Amplitude Fits

Figure 61 through Figure 70 below show the fit of the three-cylinder model to the phase and amplitude of the y perturbation data. As in the fit of the model to the x perturbation data, the power n is 0.04. Amplitudes and phases are derived from the two frequency approximations as described in section 3.4.3

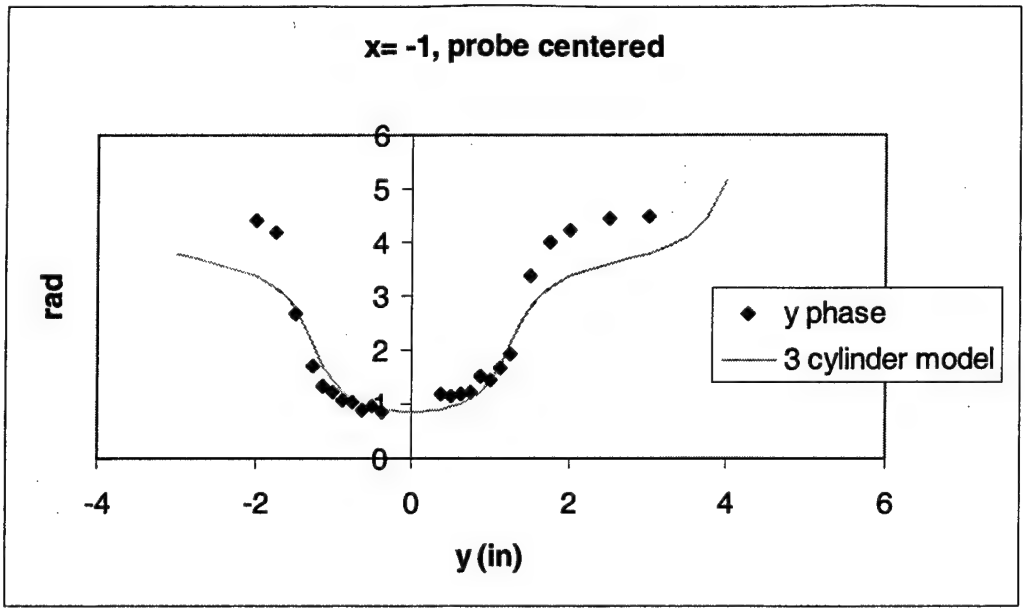

Figure 61. Three cylinder model for y phase, x=-1

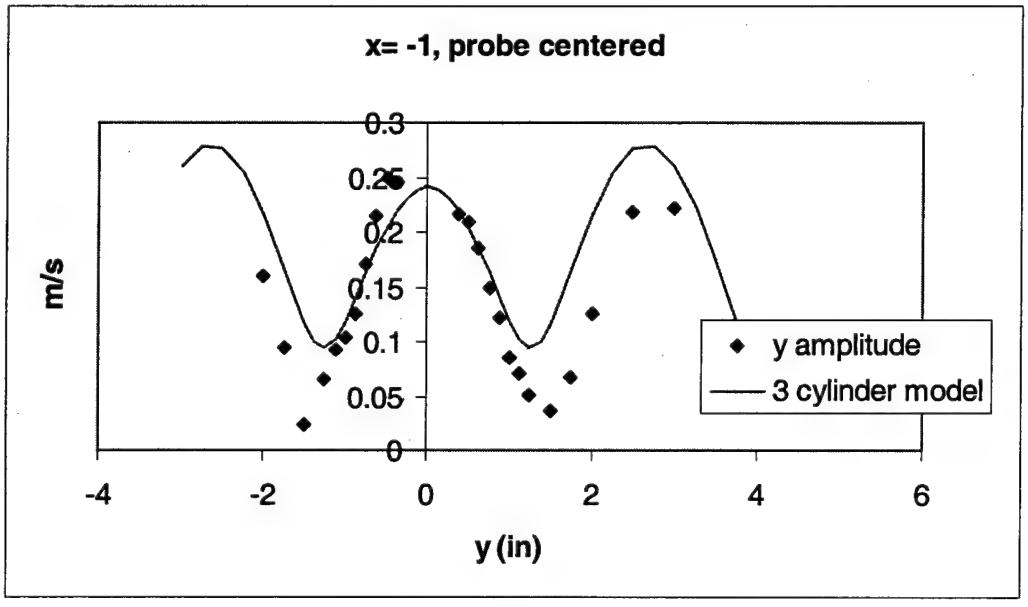

Figure 62. Three cylinder model for y amplitude, x=-1

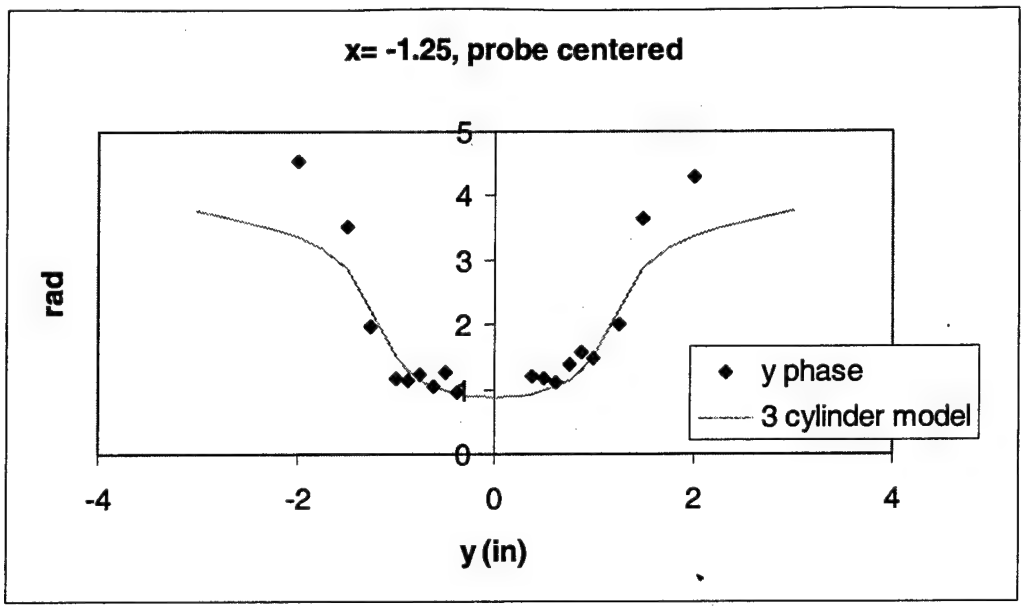

Figure 63. Three cylinder model for y phase, x=-1.25

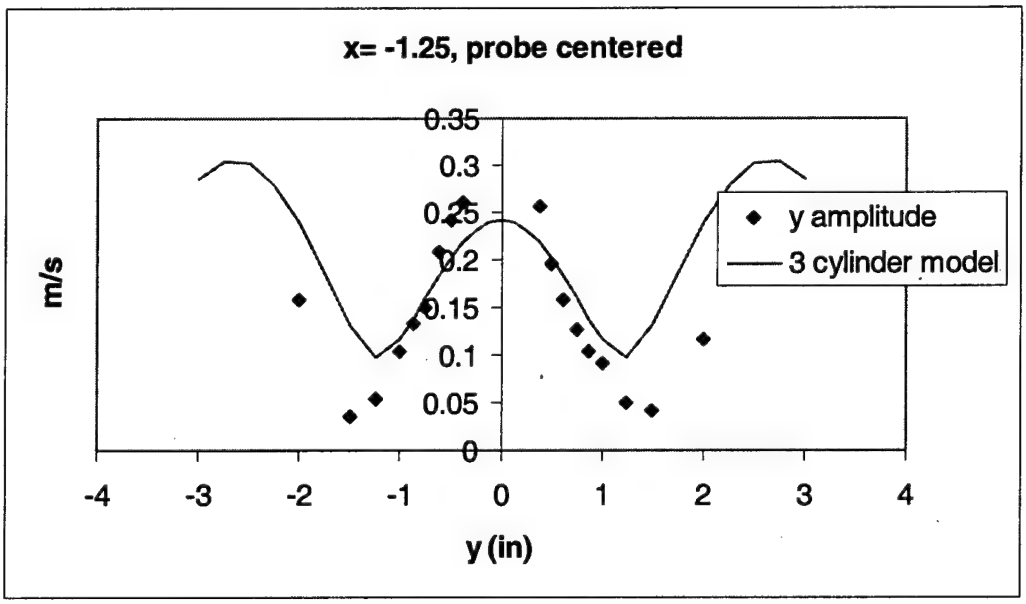

Figure 64. Three cylinder model for y amplitude, x=-1.25

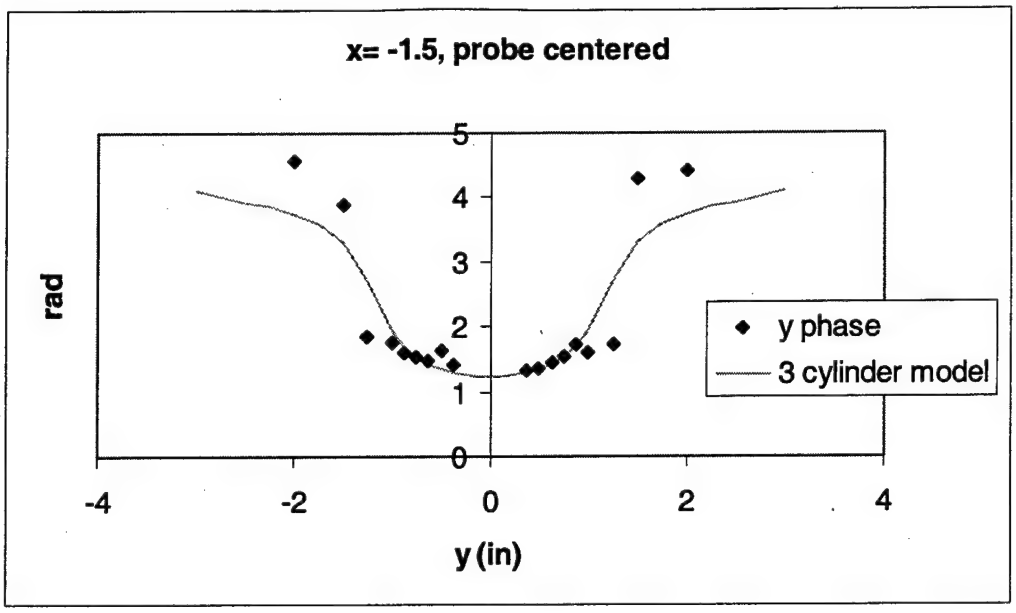

Figure 65. Three cylinder model for y phase, x=-1.5

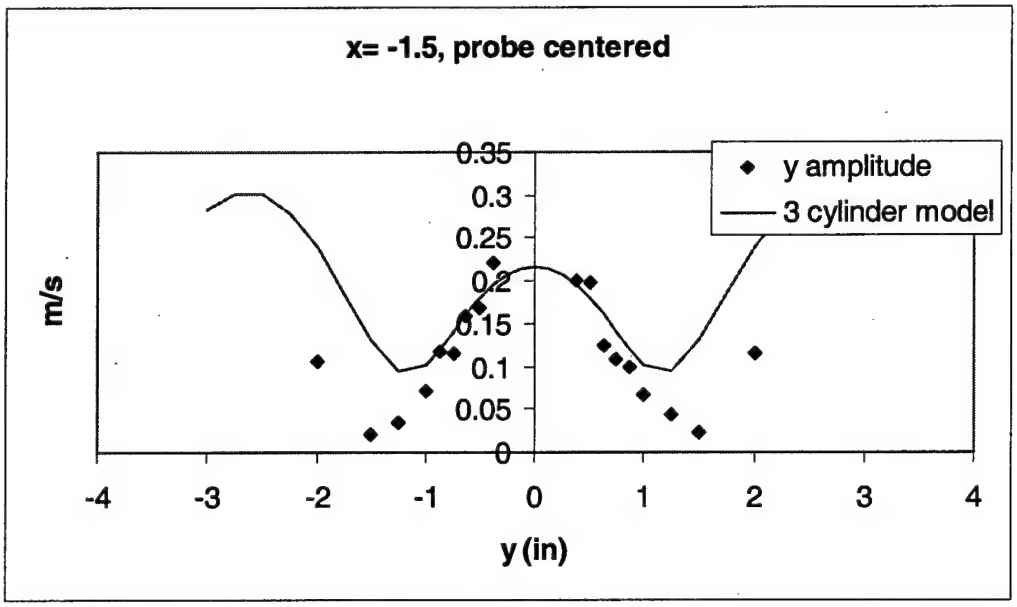

Figure 66. Three cylinder model for y amplitude, x=-1.5

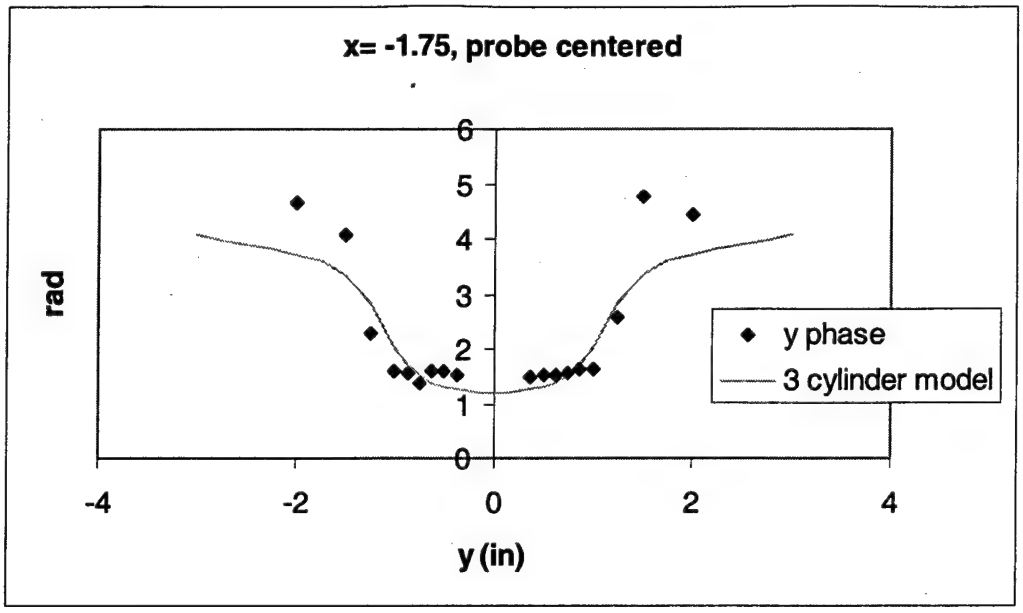

Figure 67. Three cylinder model for y phase, x=-1.75

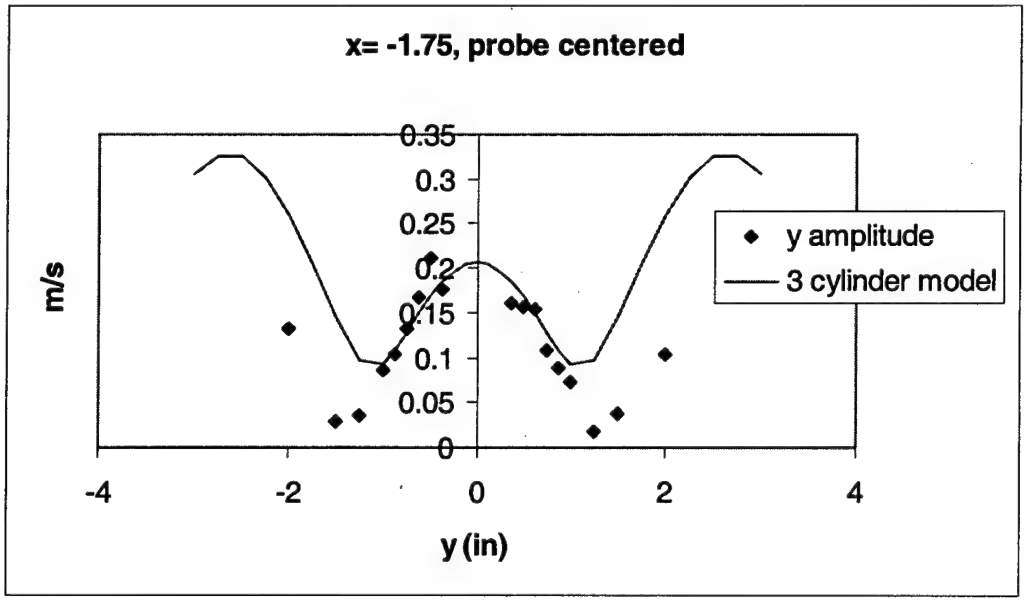

Figure 68. Three cylinder model for y amplitude, x=-1.75

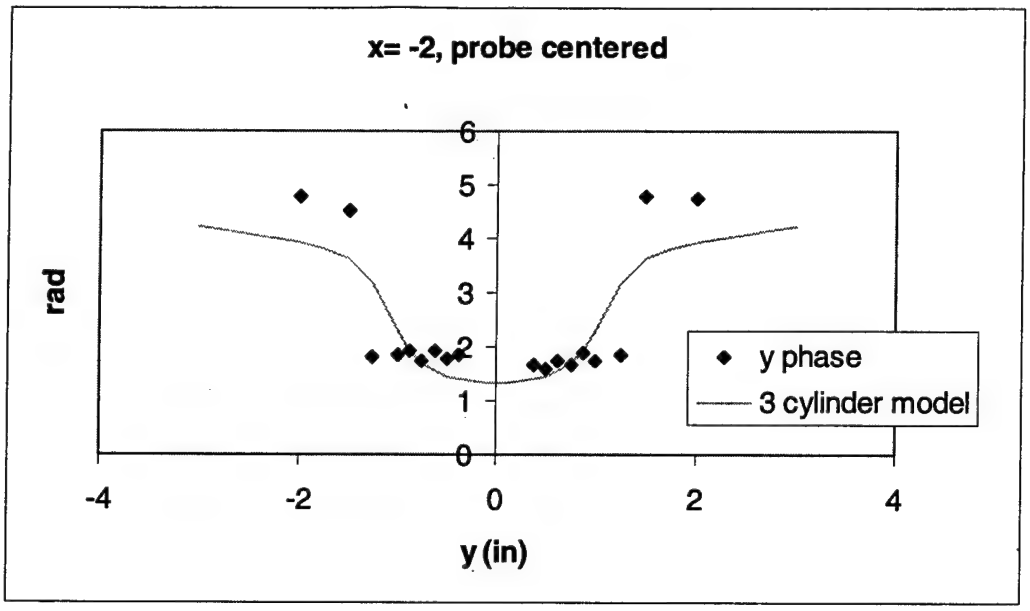

Figure 69. Three cylinder model for y phase, x=-2

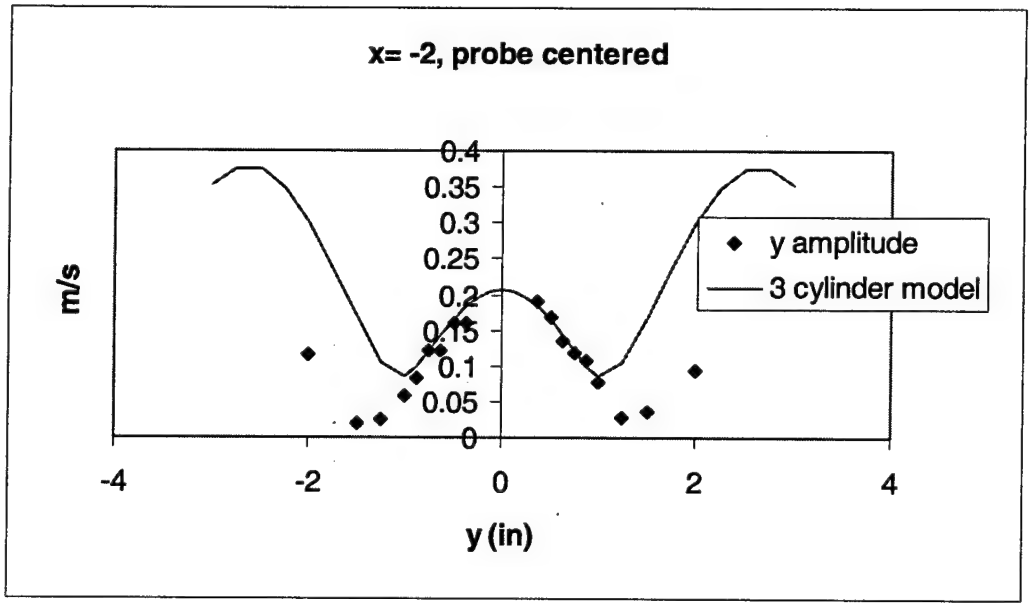

Figure 70. Three cylinder model for y amplitude, x=-2

The constant k' used for the y amplitude estimates showed more variation than that used for x. The value of k' varies from 0.1 to 0.14, as shown in Table 2. Despite the very low power of n used to describe the falloff of the amplitude, the y amplitude falloff was still less, requiring an increase in k'. There was almost no decay in y amplitude with x distance. Very little change was seen in the required phase shift.

Table 2. Phase Shifts and Constants Used in y Perturbation Model

Position	Phase Shift (ϕ_{shift})	Amplitude Constant (k')
x = -1	0.1 rad	0.1
x = -1.25	0 rad	0.11
x = -1.5	0.2 rad	0.11
x = -1.75	0 rad	0.12
x = -2	0 rad	0.14

The upper portion of the y amplitude prediction fits the data reasonably well. The location and the magnitude of the minimum amplitude are not well predicted, however. This fit can be improved somewhat by shifting the phase of the reflected cylinders relative to the real cylinder. The point of minimum amplitude on either side of the model is where the disturbances propagating from real and virtual cylinders add to produce the greatest wave cancellation. By shifting the phase of the reflections by a constant amount, the location of this point of maximum negative interference can be moved. It was decided not to shift the phase of the reflections in this manner, for the reasons stated in section 5.3.3.

The y phase predictions show all the basic characteristics of the data. In the center portion of the curve, the model accurately predicts the phase. Toward the more extreme y locations the prediction displays the proper trend, but does not completely follow the data. Again, this could be improved somewhat by arbitrarily shifting the phase of the reflected cylinders, but no justification to do so was found.

An additional inconsistency between the model and the y phase data is the point at which the phase begins to increase rapidly. Close to the cylinder, the model follows the data quite well, but further from the cylinder the model turns upward sooner than do the data. The difference between the model and the data increases with distance x. Negative powers n have a tendency to flatten the lower portion of the phase curve, but their use could not be justified, as discussed in section 5.3.3.

5.3.6 Phase and Amplitude Fits for Off-Centerline Data

The off-centerline data were modeled in a slightly different fashion than those with the hotwire at the tunnel center. The best fit for these data was obtained by using a model that was perhaps more consistent with potential flow theory than that used elsewhere. The velocity perturbation given in equation 20 is in the θ direction. To convert this to x and y perturbations the amplitude is multiplied by $\sin\theta$ for x and $\cos\theta$ for y. The result is an amplitude that changes not only as a function of distance from the cylinder, but with the direction as well. For a combined cylinder model, each term of equations 30 and 31 are multiplied by $\sin\theta$ for x and $\cos\theta$ for y. The resulting expressions are shown in equations 33 - 36.

$$\phi_{cx} = \phi_{xshift} + \tan^{-1}\left(\frac{\sin\theta_1 \sin\phi_1 / r_1^n + \sin\theta_2 \sin\phi_2 / r_2^n + \sin\theta_3 \sin\phi_3 / r_3^n}{\sin\theta_1 \cos\phi_1 / r_1^n + \sin\theta_2 \cos\phi_2 / r_2^n + \sin\theta_3 \cos\phi_3 / r_3^n} \right) \quad (33)$$

$$\phi_{cy} = \phi_{yshift} + \tan^{-1}\left(\frac{\cos\theta_1 \sin\phi_1 / r_1^n + \cos\theta_2 \sin\phi_2 / r_2^n + \cos\theta_3 \sin\phi_3 / r_3^n}{\cos\theta_1 \cos\phi_1 / r_1^n + \cos\theta_2 \cos\phi_2 / r_2^n + \cos\theta_3 \cos\phi_3 / r_3^n} \right) \quad (34)$$

$$A_{cx} = k' \sqrt{\left(\frac{s\theta_1 c\phi_1}{r_1^n} + \frac{s\theta_2 c\phi_2}{r_2^n} + \frac{s\theta_3 c\phi_3}{r_3^n} \right)^2 + \left(\frac{s\theta_1 s\phi_1}{r_1^n} + \frac{s\theta_2 s\phi_2}{r_2^n} + \frac{s\theta_3 s\phi_3}{r_3^n} \right)^2} \quad (35)$$

$$A_{cy} = k' \sqrt{\left(\frac{c\theta_1 c\phi_1}{r_1^n} + \frac{c\theta_2 c\phi_2}{r_2^n} + \frac{c\theta_3 c\phi_3}{r_3^n} \right)^2 + \left(\frac{c\theta_1 s\phi_1}{r_1^n} + \frac{c\theta_2 s\phi_2}{r_2^n} + \frac{c\theta_3 s\phi_3}{r_3^n} \right)^2} \quad (36)$$

In equations 35 and 36, sine and cosine are abbreviated as s and c, respectively. The amplitudes and phases calculated using equations 33 – 36 are shown in the four figures below.

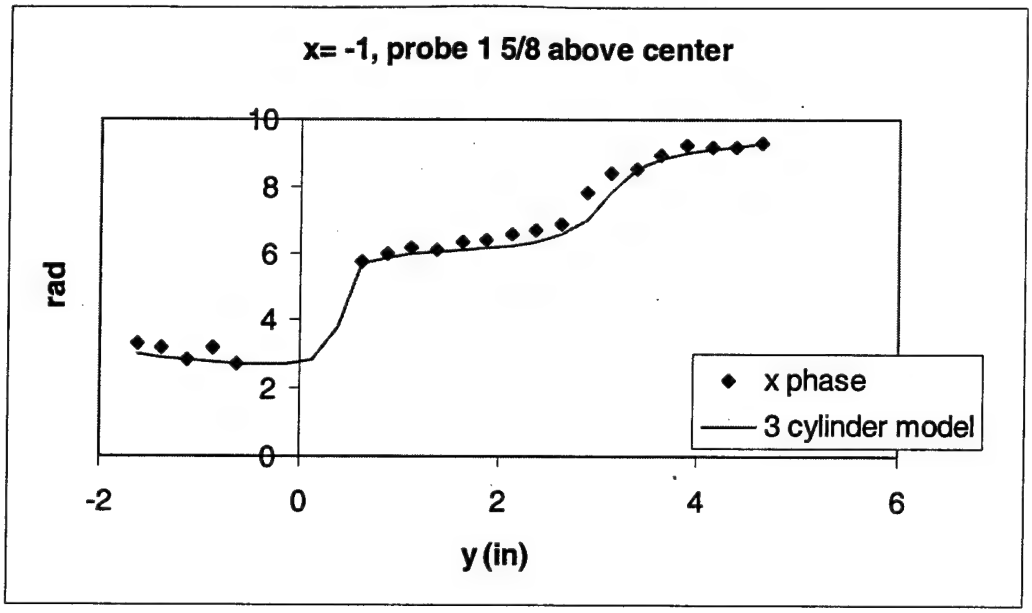

Figure 71. Three cylinder model for x phase with hotwire off center, x=-1

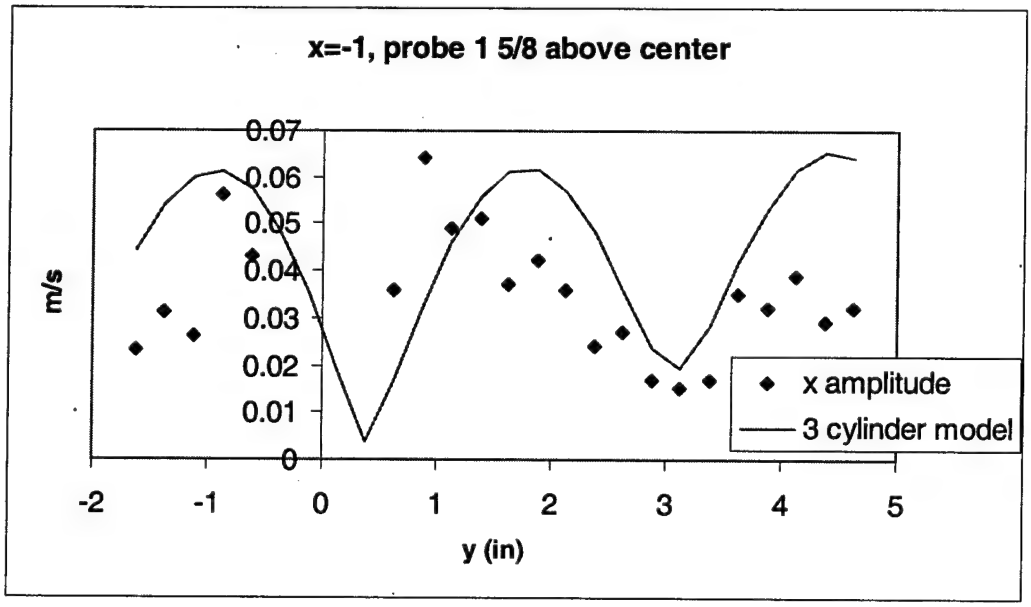

Figure 72. Three cylinder model for x amplitude with hotwire off center, x=-1

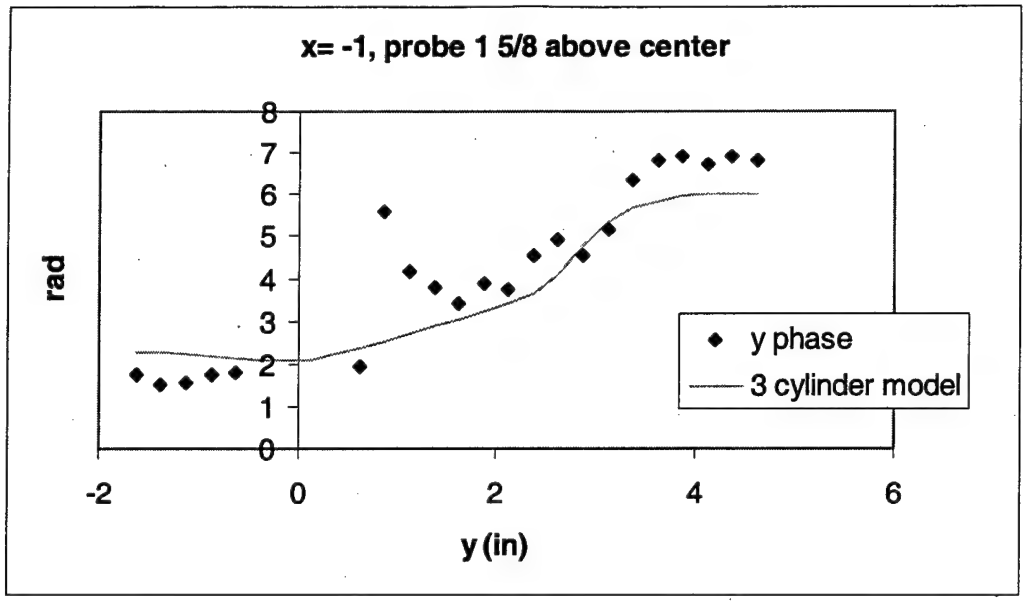

Figure 73. Three cylinder model for y phase with hotwire off center, x=-1

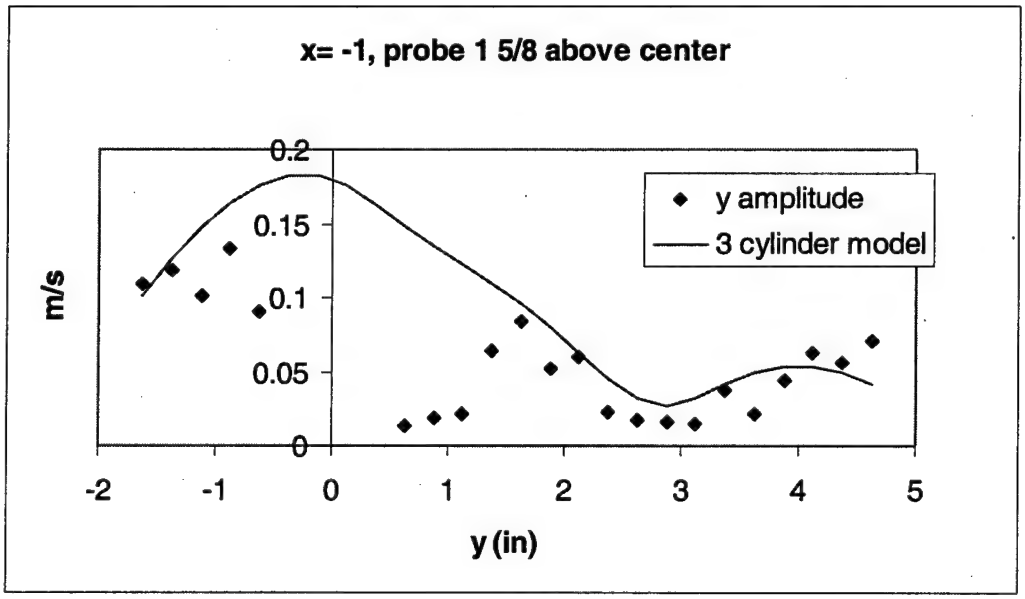

Figure 74. Three cylinder model for y amplitude with hotwire off center, x=-1

The modeled amplitudes in Figure 72 and Figure 74 show some of the characteristics of the data, but the data are largely ambiguous. While this may seem justification to discard the model outright, first consider that the three-cylinder model uses the amplitude and phase of all three cylinders to calculate the resulting phase. The phase prediction for x and, to a lesser extent, the phase prediction for y are clear representations of the data. If there were no merit to the amplitude model, the accuracy of these two predictions would be surprising.

While it was stated that the x and y amplitude models are just sine and cosine of a common perturbation, this was not strictly true. Different constants k' were used to fit the amplitude data. For the x perturbation, k' = 0.025, and for the y perturbation k' = 0.18. This is not very concerning, given the poor match between the model and the amplitude data. As the amplitudes of the real and virtual cylinders were all considered to be the same, changing the amplitude by a constant amount had no effect on the phase data prediction. The phase shift constants (ϕ_{shift}) were 4.0 rad for x and 3.5 rad for y.

6. Conclusions

For the data with the cylinder nearest the center of the tunnel, a single cylinder model provided a reasonable prediction of the y phase and x and y amplitudes at a point upstream. For data with the cylinder away from the center of the tunnel, the effects of reflections off the endwalls are clearly seen, and are not predicted by a single cylinder model.

The model that incorporates reflections as virtual cylinders has many of the same characteristics as the data, but does not follow it exactly. Again, locations near the center of the tunnel are predicted quite well. Further from the tunnel center the model has many of the same characteristics of the data, but does not accurately predict.

In general, the agreement between the three-cylinder model and the data shows that the flow can be modeled at least to an extent using elements of potential theory. One major departure from potential theory was the power n used to create a working model. Potential theory predicts perturbation decay as 1/r where r is distance from the source. The model used here fell off as $1/r^{0.04}$, and the y amplitude data required an increasing constant with distance from the cylinder, indicating that there was virtually no decay in y amplitude with x distance from the cylinder.

The off-centerline data provided an indication that perhaps a more unifying model can be created. An unambiguous match between the x and y phase models and the data they represented was produced using a single circulatory disturbance.

In this experiment, the manner of taking data probably interfered somewhat with mapping the flowfield, but perhaps serendipitously contributed to an understanding of the nature of the flow. The hotwire was stationary, and the cylinder was moved, in the y direction on a slider, and with the tunnel sidewalls in the x direction. The x direction movement did not seem to create a problem, but y direction movement did. When endwall reflections were discovered in the data, the model was complicated by not only the addition of virtual cylinders but by the fact that when the real cylinder moved, so did the virtual cylinders. If movement of the hotwire to more than just one other location in the tunnel had been possible, a more complete picture of the flowfield might have been developed. If, on the other hand, the cylinder location had been fixed in y and the hotwire moved, the effect of the endwall reflections might not have been as significant, and the virtual cylinder model not developed.

Direct comparison with much of the research of Fabian, Jumper, and Falk [6-9, 11-14] was not possible because of the necessity of using a much lower speed flow. While this is unfortunate, significant steps were taken toward modeling the flowfield upstream of a disturbance using potential theory. When this model has been refined through further experimentation, an accurate prediction of the flowfield upstream a disturbance should be possible, enabling a better understanding of the interaction between blade rows in an engine.

7. Recommendations

Vibrations in the flow at approximately 8 kHz prevented usable data at tunnel speeds comparable to Fabian's work [5]. Higher tunnel speeds produce much stronger shedding and may yield less ambiguous results. Further troubleshooting is recommended to identify the source of the vibration in the tunnel and eliminate it. Once eliminated, it would be useful to replicate some of the configurations used in this research to verify that the results reported herein are compatible with data taken at higher speeds.

Endwall reflections had a more significant effect on the unsteady velocities of the tunnel than was anticipated. This issue was compounded by the cylinder that moved closer to one endwall and farther from the other for each new data point. In order to avoid this compounded effect, a new hotwire configuration that will allow the cylinder to remain stationary in the center of the tunnel while the hotwire moves in the y direction should be used. This would most likely yield a better map of the flowfield. Again, replication of a few of the points of this study with the new hotwire configuration could establish the validity of the model used here.

Finally, data needs to be taken with multiple cylinders in the flow. This would more closely replicate the earlier work by Fabian and Jumper. If a correct model is obtained based on the principle of superposition of flows, it should readily extend itself to a new configuration with multiple cylinders and even to blade row interactions in an engine.

Appendix A MATLAB Code

Text of Matlab code used in processing of data is shown in full.

1. Ensemble average, filter, and convert hotwire voltage to velocity

```
%%%Ensemble Averaging Program %%%%%%%%%%%%%%%%%%%%%%%%%%%%
%Capt David R. Hopper
%Student, Air Force Institute of Technology
%
%This code takes a file of data runs appended together and averages
%them together into a single data set. It then applies a 4th order
%Butterworth filter with a cutoff frequency of 18 kHz. Hanning
%prefilter conditioning is applied to minimized the effects of filtering
%truncated data files. The voltage data
%from the hotwire are converted to velocities and resolved into velocity
%in the x and y directions.
%This code is based on a data set of 4 columns. The code can be quickly
%modified to plot FFTs of the data before and after filtering. Another
%similar modification allows the user to save the converted data
%to a file. Standard outputs are plots of effective wire velocities over
%the sample period, and x and y velocities over the sample period. If
%desired, the user can also output velocities in cylindrical coordinates.
%
%
%
%Last Modified 01 Feb 00
%%%%%%%%%%%%%%%%%%%%%%%%%%%%%%%%%%%%%%%%%%%%%%%%%%%%%%%%%%%

clear
%%%%%%%%%%%%%% VARIABLES %%%%%%%%%%%%%%%%%%%%%%%%%%%%
%
samples=128;        %number of samples per run
sfrq=60000;         %sample (scan) rate
%
off1=4.5;off2=4.5;                  %hotwire offset voltages (change for every data set)
g1=32;g2=32;                        %hotwire gains (change for every data set)
% power law %%
a1=6.739252;a2=3.149863;            %hotwire calibration constants
b1=1.167309;b2=2.399051;            %(change for new wire)
n1=.61;n2=.492509;
% polynomial law %%
c01=-104.053108;c02=375.339020;             %hotwire calibration constants
c11=3.124151;c12=-197.851456;       %(change for new wire)
c21=7.141727;c22=28.108604;
c31=0;c32=0;
% yaw %%
```

```
alph1=45*pi/180;alph2=45*pi/180;                    %yaw angles of wire 1 and wire 2
k12=.294;k22=.149;                                                    %yaw factors (squared)
% temperature compensation %%
t0=20.33;          %calibration temperature (C)
tover=317;         %overheat temperature (C)
m=.2;                        %temperature loading factor
%t1=20;            %use only for temperature calibration of probe (comment out
%                                    %t1 line in temp conversion below)
%Cylindrical Coordinate Transformation
xloc=-1; %locations in consistent units--only used to calculate angle
yloc=-1/2;
%
%%%%%%%%%%%%%% END VARIABLES %%%%%%%%%%%%%%%%%%

    %Prompts the user for the filename of data sets to be averaged.  The
    %number of samples per run is set at 128 and the sample frequency at 120
    %kHz.  The program will find the size of the input vector and calculate
    %the number of runs.
    file=input('What is the name of the data file?    ','s');
    filenm=dlmread(file,'\t');
    [length,z]=size(filenm);
    runs=length/samples;
    for p=1:samples
      t(p,1)=((p-1)*1/sfrq);    %time vector
    end

    %Sums the runs into a single set of data
    sum1=zeros([samples,4]);
    for i=1:runs
      for j=1:samples
        sum1(j,:)=sum1(j,:)+filenm(((i-1)*samples+j),:);
      end
    end

    %Averages the data set over the number of runs
    for k=1:samples
      avg(k,:)=sum1(k,:)/runs;
    end

    %using this instead of the preceding two loops allows a look at only the
    %first run in a data set
    %for k=1:samples
    %  avg(k,:)=filenm(k,:);
    %end

    if 0
    %Take the fft of the unfiltered data and plot
    y(:,1)=fft(avg(:,4),samples);    %pressure
    y(:,2)=fft(avg(:,2),samples);    %wire 1
    y(:,3)=fft(avg(:,3),samples);    %wire 2
    mag(:,:)=abs(y(:,:));
    f=((0:samples-1)*sfrq/samples);  %frequency vector
    f=f';                            %transpose frequency vector
    figure(2)
```

```
clf
subplot(3,1,1),plot(f,mag(:,1))
set(gca,'xtick',[5100]);
xlabel('FFT of Pressure Signal')
title(file)
subplot(3,1,2),plot(f,mag(:,2))
set(gca,'xtick',[23500]);
xlabel('FFT of Wire 1')
axis([0 sfrq 0 10]);
subplot(3,1,3),plot(f,mag(:,3))
set(gca,'xtick',[25000]);
xlabel('FFT of Wire 2')
axis([0 sfrq 0 10]);
end

%Hanning prefilter conditioning
w1mean=mean(avg(:,2));
w2mean=mean(avg(:,3));
for i=1:samples
  avg(i,2)=(avg(i,2)-w1mean)*.5*(1-cos(2*pi*i/samples))+w1mean;
  avg(i,3)=(avg(i,3)-w2mean)*.5*(1-cos(2*pi*i/samples))+w2mean;
end

if 1
%filter the data using a 4th order lowpass Butterworth filter
[b,a]=butter(4,6000/(sfrq/2));
avg(:,2)=filtfilt(b,a,avg(:,2));
avg(:,3)=filtfilt(b,a,avg(:,3));
end

%Hanning postfilter conditioning/throw away first and last 10 points
w1mean=mean(avg(:,2));
w2mean=mean(avg(:,3));
for i=11:samples-10
  newv(i-10,2)=(avg(i,2)-w1mean)/(.5*(1-cos(2*pi*i/samples)))+w1mean;
  newv(i-10,3)=(avg(i,3)-w2mean)/(.5*(1-cos(2*pi*i/samples)))+w2mean;
  newv(i-10,4)=avg(i,4);
  newv(i-10,1)=avg(i,1);
  newt(i-10,1)=t(i-10,1);
end
clear avg t y mag
avg(:,:)=newv(:,:);
t(:,1)=newt(:,1);
samples=samples-20;

%Plots pressure signal (column 4) and voltages from wires (columns
        %2 and 3).
 if 1
   figure(6)
                clf
                subplot(3,1,1),plot(t(:,1),avg(:,4))
                xlabel('Pressure')
                title(file)
                subplot(3,1,2),plot(t(:,1),avg(:,2),'b-',t(:,1),mean(avg(:,2)),'r:')
```

```
            xlabel('wire 1 avg voltage')
            subplot(3,1,3),plot(t(:,1),avg(:,3),'b-',t(:,1),mean(avg(:,3)),'r:')
            xlabel('wire 2 avg voltage')
        end

if 0
%Take the fft of the filtered data and plot
y(:,1)=fft(avg(:,4),samples);    %pressure
y(:,2)=fft(avg(:,2),samples);    %wire 1
y(:,3)=fft(avg(:,3),samples);    %wire 2
mag(:,:)=abs(y(:,:));
f=((0:samples-1)*sfrq/samples);  %frequency vector
f=f';                    %transpose frequency vector
figure(3)
clf
subplot(3,1,1),plot(f,mag(:,1))
set(gca,'xtick',[5100]);
xlabel('FFT of Pressure Signal')
title(file)
subplot(3,1,2),plot(f,mag(:,2))
set(gca,'xtick',[10200]);
xlabel('FFT of Wire 1')
axis([0 sfrq 0 5]);
subplot(3,1,3),plot(f,mag(:,3))
set(gca,'xtick',[10200]);
xlabel('FFT of Wire 2')
axis([0 sfrq 0 5]);
end

%Converts voltages from the wires to effective velocities and voltages
%from the pressure transducer to pressures.  Converts effective
%velocities to wire-axis velocities, then to U and V components of
%velocity.

%%%%%%%%%%%%%%%%%
%troubleshooting only
%solve for bridge voltage without converting to velocity
if 0
        for i=1:samples
    avg(i,2)=((avg(i,2)-0)/g1)+off1;          %correct for offsets and gain
    avg(i,3)=((avg(i,3)-0)/g2)+off2;
        end
end
%end troubleshoot
%%%%%%%%%%%%%%%%%%

if 1  %convert to velocity and plot
  for i=1:samples
    avg(i,2)=((avg(i,2)-0)/g1)+off1;          %correct for offsets and gain
    avg(i,3)=((avg(i,3)-0)/g2)+off2;
  end

  %%%%%% Temperature Correction %%%%%%%%%%%%%%%%%%
  %corrects bridge voltages for temperature
```

```
if 0 %set to 1 to enable temperature correction
tw=t0+tover; %derive from overheat
t1=30*mean(avg(:,1));  %calculate ambient temperature from probe data
%calculate film temperatures
        t1=(tw+t1)/2;
        t0=(tw+t0)/2;

if t1>t0
  for i=1:samples
    avg(i,2)=avg(i,2)*(((tw-t0)/(tw-t1))^(.5*(1+m)));
    avg(i,3)=avg(i,3)*(((tw-t0)/(tw-t1))^(.5*(1+m)));
  end

elseif t1<t0
  for i=1:samples
    avg(i,2)=avg(i,2)*(((tw-t0)/(tw-t1))^(.5*(1-m)));
    avg(i,3)=avg(i,3)*(((tw-t0)/(tw-t1))^(.5*(1-m)));
  end

else
        avg(:,2)=avg(:,2);avg(:,3)=avg(:,3);
end
end %temperature correction
%%%%%%%%%%% End Temperature Correction %%%%%%%%%%%

%%%%%%%%%%%%%%% POWER LAW %%%%%%%%%%%%%%%
if 0 %set to 1 to use power law calibration
        for i=1:samples
    %convert to calibrated velocity using power law
          ucal(i,1)=((avg(i,2)^2-a1)/b1)^(1/n1);
          ucal(i,2)=((avg(i,3)^2-a2)/b2)^(1/n2);
        end
end
%%%%%%%%%%% END POWER LAW %%%%%%%%%%%%%%%%%

%%%%%%%%%%% POLYNOMIAL LAW %%%%%%%%%%%%%%%%%
if 1 %set to 1 to use polynomial law calibration
  for i=1:samples
    %convert to calibrated velocity using polynomial law
    ucal(i,1)=c01+c11*avg(i,2)+c21*avg(i,2)^2+c31*avg(i,2)^3;
    ucal(i,2)=c02+c12*avg(i,3)+c22*avg(i,3)^2+c32*avg(i,3)^3;
  end
end
%%%%%%%%% END POLYNOMIAL LAW %%%%%%%%%%%%%%%%%

%Take calibrated velocities from power law or polynomial law, convert
%to effective velocities, and then convert to velocity in the wire 1
%and wire 2 directions.
for i=1:samples
  ueff(i,1)=sqrt((ucal(i,1)^2)*(1+k12)*(cos(pi/4))^2);
  ueff(i,2)=sqrt((ucal(i,2)^2)*(1+k22)*(cos(3*pi/4))^2);
  %wire 2 component of velocity
        u(i,2)=sqrt((ueff(i,1)^2-k12*ueff(i,2)^2)/(1-k12*k22));
  %wire 1 component of velocity
```

```
        u(i,1)=sqrt((ueff(i,2)^2)-k22*u(i,2)^2);
  end

        if 1
        figure(4)          %plot wire 1 and wire 2 and pressure signal
        clf
        subplot(3,1,1),plot(t(:,1),avg(:,4))
        xlabel('Voltage from pressure transducer vs. time (s)')
        title(file)
        subplot(3,1,2),plot(t(:,1),u(:,1))
        xlabel('Wire 1 Velocity (m/s) vs. time (s)')
        subplot(3,1,3),plot(t(:,1),u(:,2))
        xlabel('Wire 2 Velocity (m/s) vs. time (s)')
  end

end %velocity conversion

%Calculate x and y velocities and substitute for values in 'avg.'
%This section converts directly from wire 1/wire 2 velocities to
%velocities in the lab x and y directions.  The assumption is that
%the probe is placed into the test section so that probe x and y
%coincide with lab x and y.
if 1
        for i=1:samples
          avg(i,2)=u(i,1)*cos(alph1)+u(i,2)*cos(alph2);
          avg(i,3)=u(i,1)*sin(alph1)-u(i,2)*sin(alph2);
        end
end
%%%%%%%% X and Y velocity plot %%%%%%%%%%%%%%%%%%
% set to 1
if 1
        %Plots pressure signal (column 4) and x and y velocities (columns
        %2 and 3).
        figure(1)
        clf
        subplot(3,1,1),plot(t(:,1),avg(:,4))
        xlabel('Pressure')
        title(file)
        subplot(3,1,2),plot(t(:,1),avg(:,2),'b-',t(:,1),mean(avg(:,2)),'r:')
        xlabel('X Velocity (m/s) vs. time (s)')
        subplot(3,1,3),plot(t(:,1),avg(:,3),'b-',t(:,1),mean(avg(:,3)),'r:')
        xlabel('Y Velocity (m/s) vs. time (s)')

        if 1
        %Take the fft of the x and y velocities and plot
        y(:,1)=fft(avg(:,4),samples);    %pressure
        y(:,2)=fft(avg(:,2),samples);    %x
        y(:,3)=fft(avg(:,3),samples);    %y
        mag(:,:)=abs(y(:,:));
        f=((0:samples-1)*sfrq/samples);  %frequency vector
        f=f';                            %transpose frequency vector
        figure(5)
        clf
        subplot(3,1,1),plot(f,mag(:,1))
```

```
        set(gca,'xtick',[4000]);
        xlabel('FFT of Pressure Signal')
        title(file)
        subplot(3,1,2),plot(f,mag(:,2))
        set(gca,'xtick',[5000 10000 15000 20000 25000]);
        xlabel('FFT of x velocity')
        axis([0 sfrq 0 5]);
        subplot(3,1,3),plot(f,mag(:,3))
        set(gca,'xtick',[5000 10000 15000 20000 25000]);
        xlabel('FFT of y velocity')
        axis([0 sfrq 0 5]);
        end
end %x and y velocity plot

%%%%%%%%% Cylindrical Coordinate Transform and Plot %%%%%%%%%
  %set to 1
  if 0
    theta=atan2(yloc,xloc);
    for i=1:samples
      vcyl(i,1)=avg(i,2)*cos(theta)+avg(i,3)*sin(theta);
      vcyl(i,2)=-avg(i,2)*sin(theta)+avg(i,3)*cos(theta);
      avg(i,2)=vcyl(i,1);
      avg (i,3)=vcyl(i,2);
    end

    %Plots pressure signal (column 4) and x and y velocities (columns
                %2 and 3).
                figure(1)
                clf
                subplot(3,1,1),plot(t(:,1),avg(:,4))
                xlabel('Pressure')
                title(file)
                subplot(3,1,2),plot(t(:,1),avg(:,2),'b-',t(:,1),mean(avg(:,2)),'r:')
                xlabel('r Velocity (m/s) vs. time (s)')
                subplot(3,1,3),plot(t(:,1),avg(:,3),'b-',t(:,1),mean(avg(:,3)),'r:')
                xlabel('theta Velocity (m/s) vs. time (s)')

                if 1
                %Take the fft of the x and y velocities and plot
                y(:,1)=fft(avg(:,4),samples);    %pressure
                y(:,2)=fft(avg(:,2),samples);    %r
                y(:,3)=fft(avg(:,3),samples);    %theta
                mag(:,:)=abs(y(:,:));
                f=((0:samples-1)*sfrq/samples);  %frequency vector
                f=f';                            %transpose frequency vector
                figure(5)
                clf
                subplot(3,1,1),plot(f,mag(:,1))
                set(gca,'xtick',[4000]);
                xlabel('FFT of Pressure Signal')
                title(file)
                subplot(3,1,2),plot(f,mag(:,2))
                set(gca,'xtick',[5000 10000 15000 20000 25000]);
                xlabel('FFT of r velocity')
```

```
axis([0 sfrq 0 20]);
subplot(3,1,3),plot(f,mag(:,3))
set(gca,'xtick',[5000 10000 15000 20000 25000]);
xlabel('FFT of theta velocity')
axis([0 sfrq 0 20]);
end

 end
%%%%%% end cylindrical coordinate transform and plot %%%%%%%%%

if 1
%Prompts the user to save the averaged data as a file.
newfile1=input('Please enter the filename for the averaged data    ','s');
dlmwrite(newfile1,avg,'\t');
end
```

2. Find sinusoidal approximation to data through minimization

```
%%%Curve Fit Minimization Program %%%%%%%%%%%%%%%%
%Capt David R. Hopper
%Student, Air Force Institute of Technology
%
%This MATLAB code takes a file of averaged data and calls a function
%jfunc which finds a minimum difference squared between the data and a
%two-frequency sinusoidal approximation.
%
%
%
%Last Modified 01 Feb 00
%%%%%%%%%%%%%%%%%%%%%%%%%%%%%%%%%%%%%%%%%%%%%%%%

clear all
global file filenm samples t nn mean2 J wf1

%Prompts the user for the filename of data set.  The
%sample frequency is set at 120 kHz.
%The program will find the size of the input vector and calculate its
%size.
file=input('What is the name of the averaged data file?    ','s');
filenm=dlmread(file,'\t');
sfrq=60000;                %sample (scan) rate
[samples,z]=size(filenm);

for p=1:samples
  t(p,1)=((p-1)*1/sfrq);
end



%Call the function jfunc 3 times (once for each column of data) in the
%minimization routine fminsearch.  Fminsearch uses the Nelder-Mead simplex
%(direct search) method.

%%%% Minimization %%%%%%%%%%

for nn=4:-1:2  %4 is pressure, 3 is y velocity, 2 is x velocity
  compare=300;
        mean2=mean(filenm(:,nn));
        mean3(nn)=mean2;
  options=optimset('maxfunevals',4000,'maxiter',2000);

  for p=1:2        %how many times to run with different random guesses

        %initial guesses through random number generation
        %pressure                x velocity          y velocity
        x0(1,4)=.1*rand;         x0(1,2)=.05*rand;          x0(1,3)=.1*rand;
```

```
        x0(2,4)=2*pi*rand;      x0(2,2)=2*pi*rand;      x0(2,3)=2*pi*rand;
        x0(3,4)=.05*rand;       x0(3,2)=.01*rand;       x0(3,3)=.01*rand;
        x0(4,4)=2*pi*rand;      x0(4,2)=2*pi*rand;      x0(4,3)=2*pi*rand;
        x0(5,4)=2600*2*pi;      %x0(5,2)=x0(5,4);       x0(5,3)=x0(5,4);
        %x0(6,4)=2*x0(5,4);     x0(6,2)=2*x0(5,4);      x0(6,3)=2*x0(5,4);

        if nn==4
  x(:,nn)=fminsearch('jfuncp',x0(:,nn),options);
else
  x(:,nn)=fminsearch('jfuncv',x0(:,nn),options);
end

        %make all amps and freqs positive; all phases between 0 and 2pi
        %%amplitude
        if x(1,nn)<0
        x(2,nn)=x(2,nn)+pi;      %if amplitude comes out negative, add
        x(1,nn)=-(x(1,nn));      %180 phase and make ampl. positive
        end
        if x(3,nn)<0
          x(4,nn)=x(4,nn)+pi;
          x(3,nn)=-(x(3,nn));
        end
        %%frequency
if nn==4
if x(5,nn)<0
          x(5,nn)=-x(5,nn);              %if frequency comes out negative,
          x(2,nn)=-x(2,nn);              %take the opposite of freq. and phase
        end
        %if x(6,nn)<0
        %  x(6,nn)=-x(6,nn);
        %  x(4,nn)=-x(4,nn);
%end
        end

%%phase
        while x(2,nn)<0
                x(2,nn)=x(2,nn)+2*pi;  %add or subtract 360 to
              end                              % bring phase into range
              while x(2,nn)>=2*pi
                x(2,nn)=x(2,nn)-2*pi;
              end
              while x(4,nn)<0
                x(4,nn)=x(4,nn)+2*pi;
              end
              while x(4,nn)>=2*pi
                x(4,nn)=x(4,nn)-2*pi;
              end

J
if J<compare
  compare=J;
  %save variables from minimization
  %round the frequencies to the nearest 50
  %round amplitude and phase to the nearest .001
```

```
    if nn==4
      af1=round(x(1,4)*1000)/1000;          %pressure
      pf1=round(x(2,4)*1000)/1000;
      wf1=round(x(5,4));
      ah1=round(x(3,4)*1000)/1000;
      ph1=round(x(4,4)*1000)/1000;
      %wh1=round(x(6,4));
      wh1=2*wf1;
    end
        if nn==2
      af2=round(x(1,2)*1000)/1000;          %x velocity
      pf2=round(x(2,2)*1000)/1000;
      %wf2=round(x(5,2));
      ah2=round(x(3,2)*1000)/1000;
      ph2=round(x(4,2)*1000)/1000;
      %wh2=round(x(6,2));
      wf2=wf1;
      wh2=2*wf1;
    end
        if nn==3
      af3=round(x(1,3)*1000)/1000;          %y velocity
      pf3=round(x(2,3)*1000)/1000;
      %wf3=round(x(5,3));
      ah3=round(x(3,3)*1000)/1000;
      ph3=round(x(4,3)*1000)/1000;
      %wh3=round(x(6,3));
      wf3=wf1;
      wh3=2*wf1;
    end
  end

  end    %end of p loop

end      %end of nn loop

%%% create 2-frequency waveforms for plotting %%%%%%%%%%%%%
% note that the phase is corrected for the midpoint conversion
for i=1:samples
  wave(i,4)=mean3(4)+(af1*sin(wf1*(t(i,1))+pf1)+...
    ah1*sin(wh1*(t(i,1))+ph1));
  wave(i,2)=mean3(2)+(af2*sin(wf2*(t(i,1))+pf2)+...
    ah2*sin(wh2*(t(i,1))+ph2));
  wave(i,3)=mean3(3)+(af3*sin(wf3*(t(i,1))+pf3)+...
    ah3*sin(wh3*(t(i,1))+ph3));
end

%%% create text strings for plot legends %%%%%%%%%%%%%%%%%%%%
% phases displayed are those at the trigger point
% frequencies displayed are in Hz, not rad/s
presswave=[num2str(af1) 'sin(2pi*' num2str(round(wf1/(2*pi)/50)*50) 't + '...
    num2str(pf1) ')' ' + ' num2str(ah1) 'sin(2pi*'...
    num2str(round(wh1/(2*pi)/50)*50) 't + ' num2str(ph1) ')'];
xwave=[num2str(af2) 'sin(2pi*' num2str(round(wf2/(2*pi)/50)*50) 't + '...
    num2str(pf2) ')' ' + ' num2str(ah2) 'sin(2pi*'...
```

```
    num2str(round(wh2/(2*pi)/50)*50) 't + ' num2str(ph2) ')'];
ywave=[num2str(af3) 'sin(2pi*' num2str(round(wf3/(2*pi)/50)*50) 't + '...
    num2str(pf3) ')' ' + ' num2str(ah3) 'sin(2pi*'...
    num2str(round(wh3/(2*pi)/50)*50) 't + ' num2str(ph3) ')'];
%%%%%%%%%%%%%%%%%%%%%%%%%%%%%%%%%%%%%%%%%%%%%%%%%%%%%%%%%%%%%%%%%%%%%%%%%%%%%%%%%%%%%

%Plots three columns of data (assumes pressure signal is column 4
%and hotwires are columns 2 and 3).
figure(1)
clf
subplot(3,1,1),plot(t(:,1),filenm(:,4),'b-',t(:,1),wave(:,4),'r:')
legend('averaged pressure data',presswave,0)
xlabel('Time (s)')
title(file)
subplot(3,1,2),plot(t(:,1),filenm(:,2),'b-',t(:,1),wave(:,2),'r:')
legend('x velocity data (m/s)',xwave,0)
xlabel('s')
ylabel('m/s')
subplot(3,1,3),plot(t(:,1),filenm(:,3),'b-',t(:,1),wave(:,3),'r:')
legend('y velocity data (m/s)',ywave,0)
xlabel('s')
ylabel('m/s')
```

3. Least squares minimization function for pressure

```
%%% Function JFUNCP %%%%%%%%%%%%%%%%%%%%%%%%%%%%%%%%%%%%
    %Capt David R. Hopper
    %Student, Air Force Institute of Technology
    %
    %
    %This MATLAB subroutine contains a function that will be called by the file
    %minim.m and the difference between the function and a file of data, contained
    %in global variable filenm, will be minimized.
    %
    %
    %
    %
    %Last Modified 01 Feb 00
    %%%%%%%%%%%%%%%%%%%%%%%%%%%%%%%%%%%%%%%%%%%%%%%%%%%%%%%

    function J=jfuncp(x)
    global file filenm samples t nn mean2 J
    af=x(1,1);pf=x(2,1);wf=x(5,1);
    ah=x(3,1);ph=x(4,1);%wh=x(6,1);
    wh=2*wf;
    sum1=0;
      for i=1:(samples)
            wave(i,1)=mean2+(af*sin(wf*t(i,1)+pf)+ah*sin(wh*t(i,1)+ph));
            diff=(filenm(i,nn)-wave(i,1))^2;
            sum1=sum1+diff;
            end

    J=sum1;
```

4. Least squares minimization function for velocity

```
%%% Function JFUNCV %%%%%%%%%%%%%%%%%%%%%%%%%%%%%%%
    %Capt David R. Hopper
    %Student, Air Force Institute of Technology
    %
    %
    %This MATLAB subroutine contains a function that will be called by the file
    %minim.m and the difference between the function and a file of data, contained
    %in global variable filenm, will be minimized.
    %
    %
    %
    %
    %Last Modified 01 Feb 00
    %%%%%%%%%%%%%%%%%%%%%%%%%%%%%%%%%%%%%%%%

    function J=jfuncv(x)
    global file filenm samples t nn mean2 J wf1
    af=x(1,1);pf=x(2,1);%wf=x(5,1);
    ah=x(3,1);ph=x(4,1);%wh=x(6,1);
    wf=wf1;
    wh=2*wf;
    sum1=0;
      for i=1:(samples)
            wave(i,1)=mean2+(af*sin(wf*t(i,1)+pf)+ah*sin(wh*t(i,1)+ph));
            diff=(filenm(i,nn)-wave(i,1))^2;
            sum1=sum1+diff;
            end
    J=sum1;
```

Appendix B Data and Two Frequency Approximations

1. Data at x = -1 in

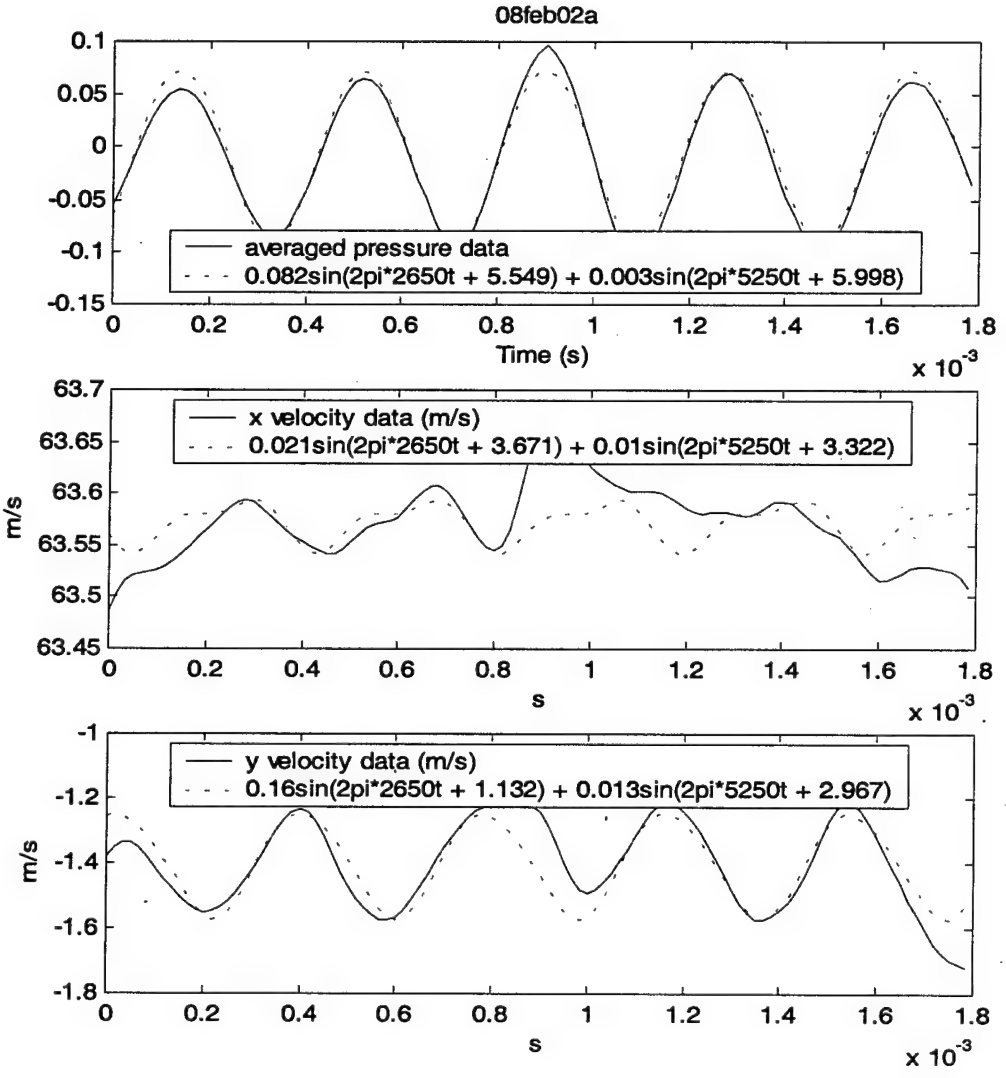

Figure 75. Data and two frequency approximation at x = -1 in, y = -2 in

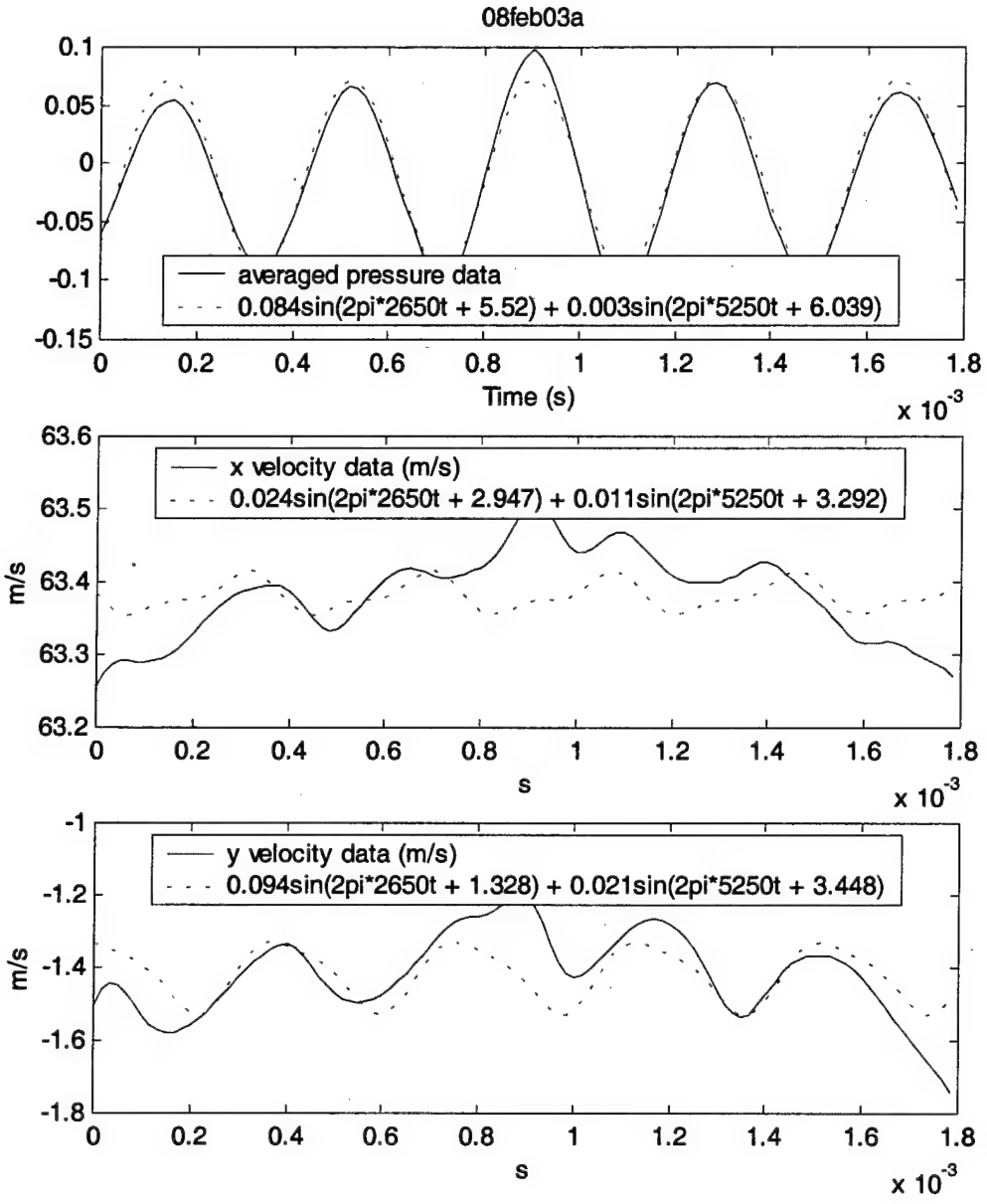

Figure 76. Data and two frequency approximation at x = -1 in, y = -1.75 in

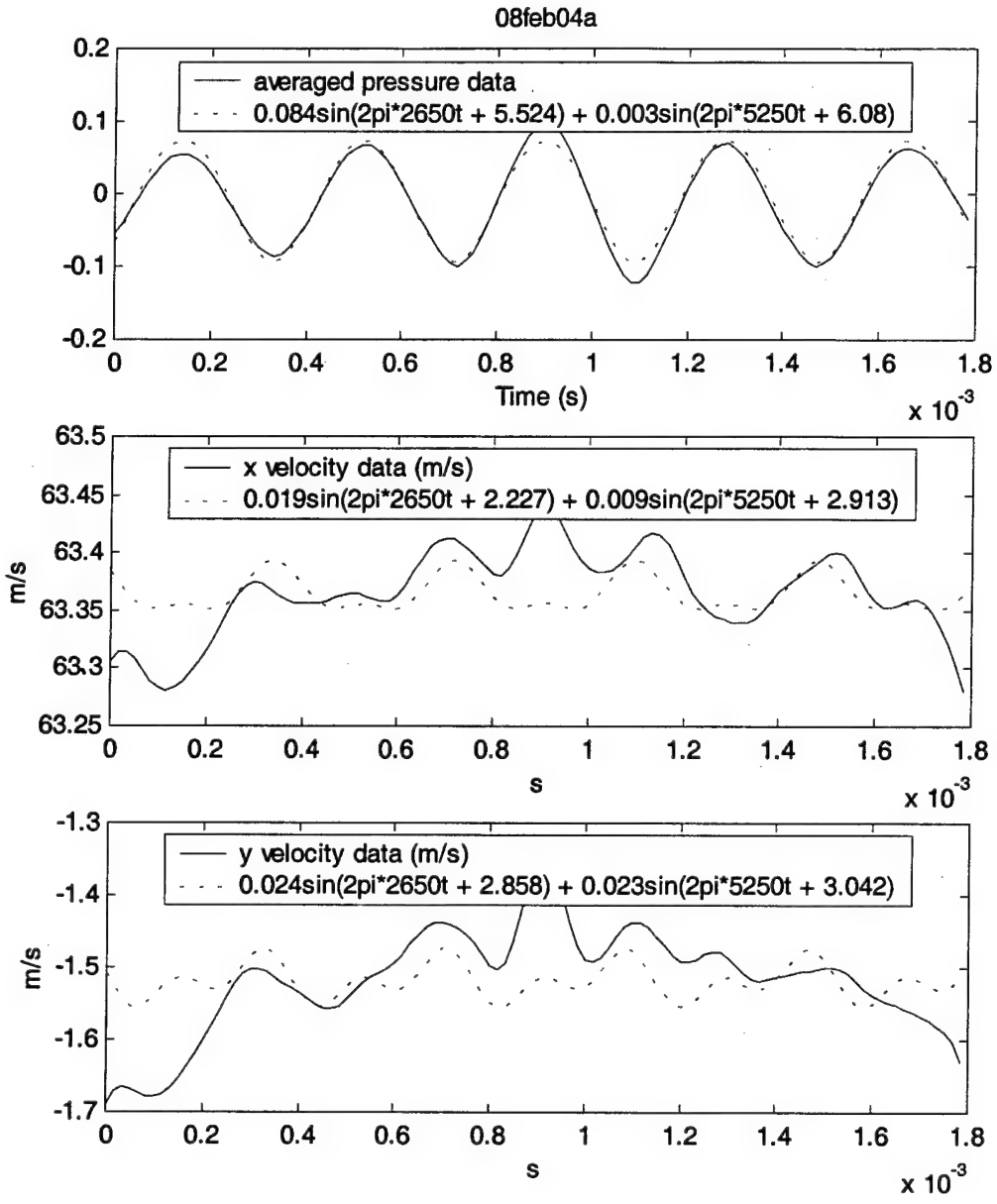

Figure 77. Data and two frequency approximation at x = -1 in, y = -1.5 in

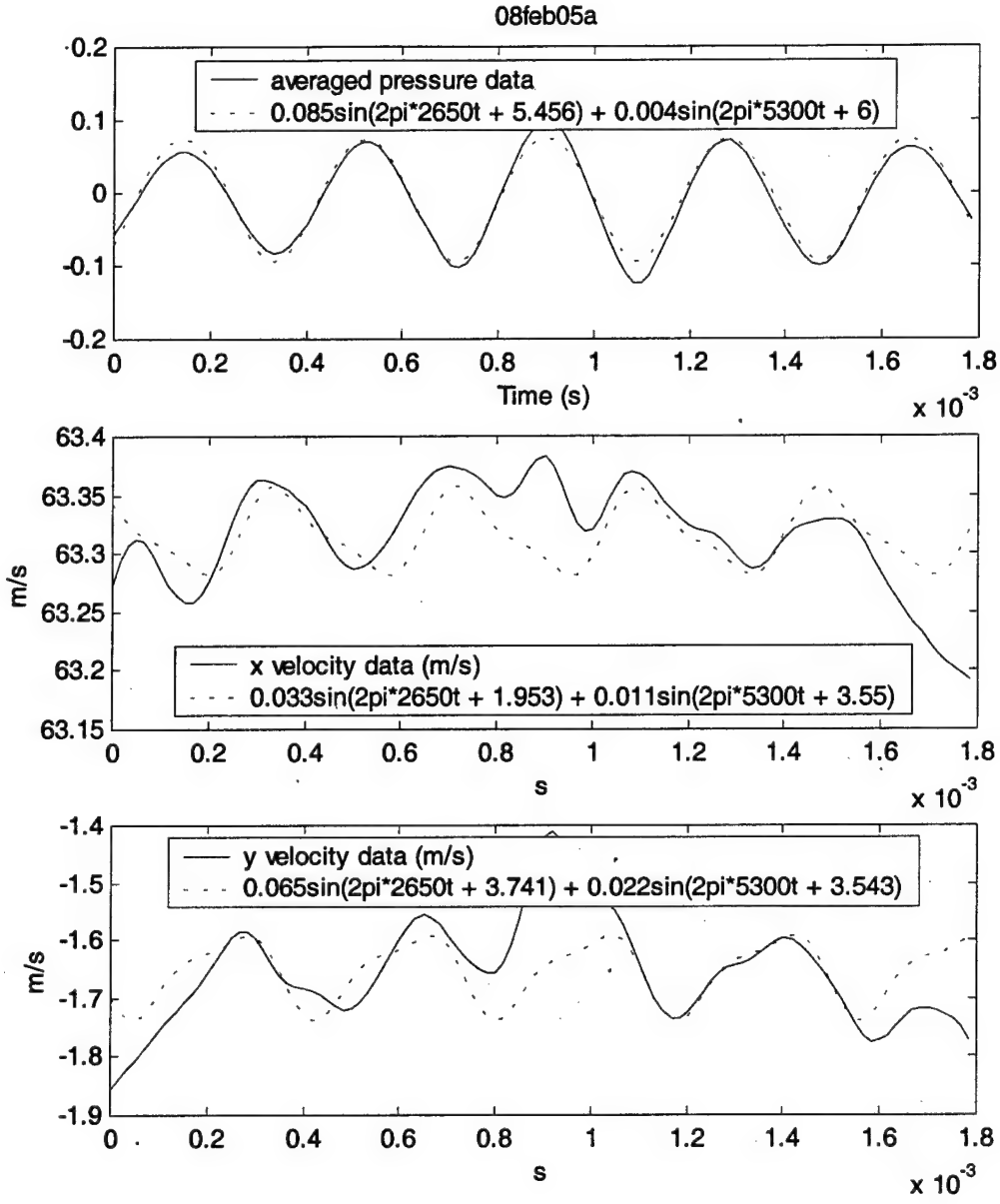

Figure 78. Data and two frequency approximation at x = -1 in, y = -1.25 in

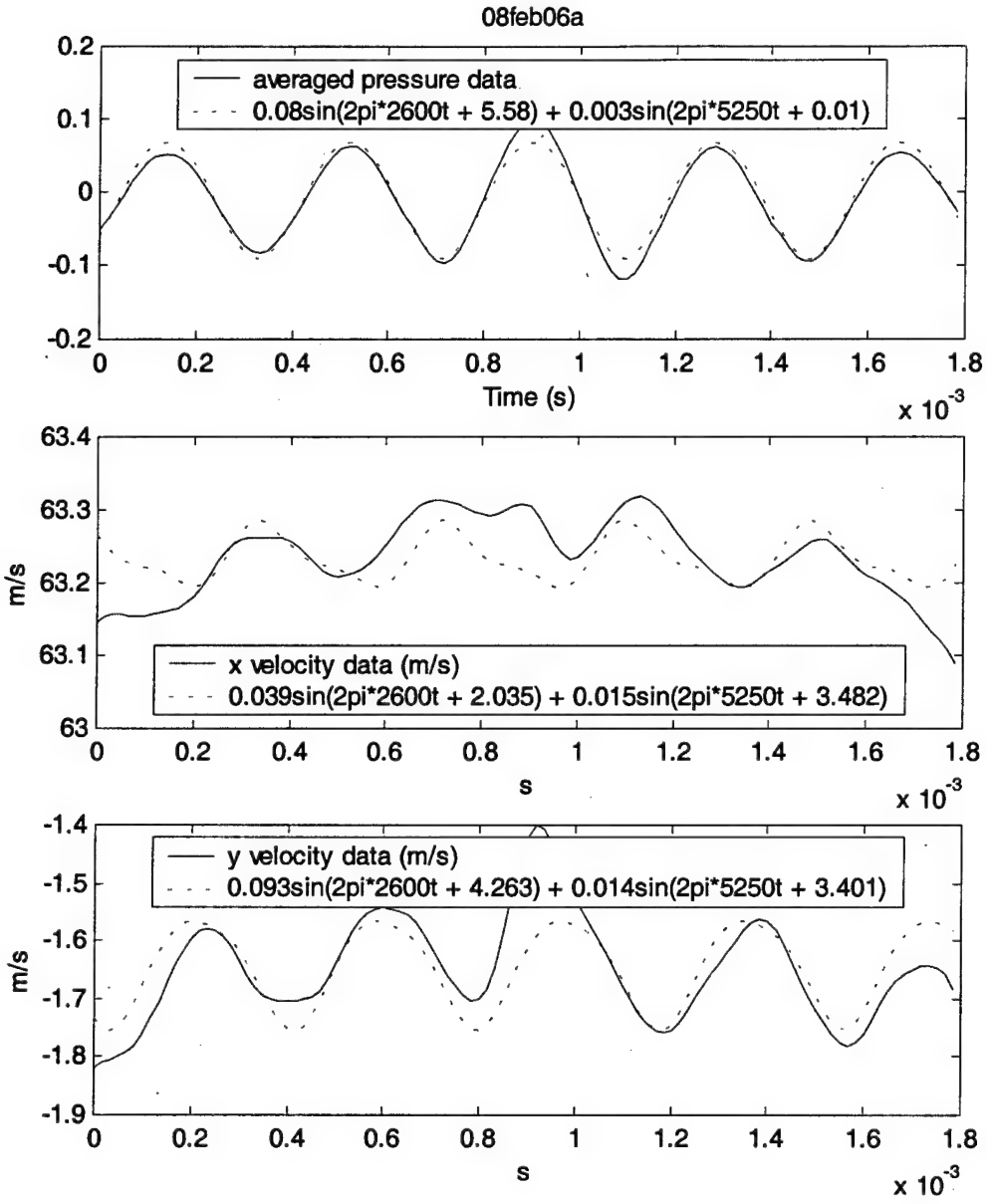

Figure 79. Data and two frequency approximation at x = -1 in, y = -1.125 in

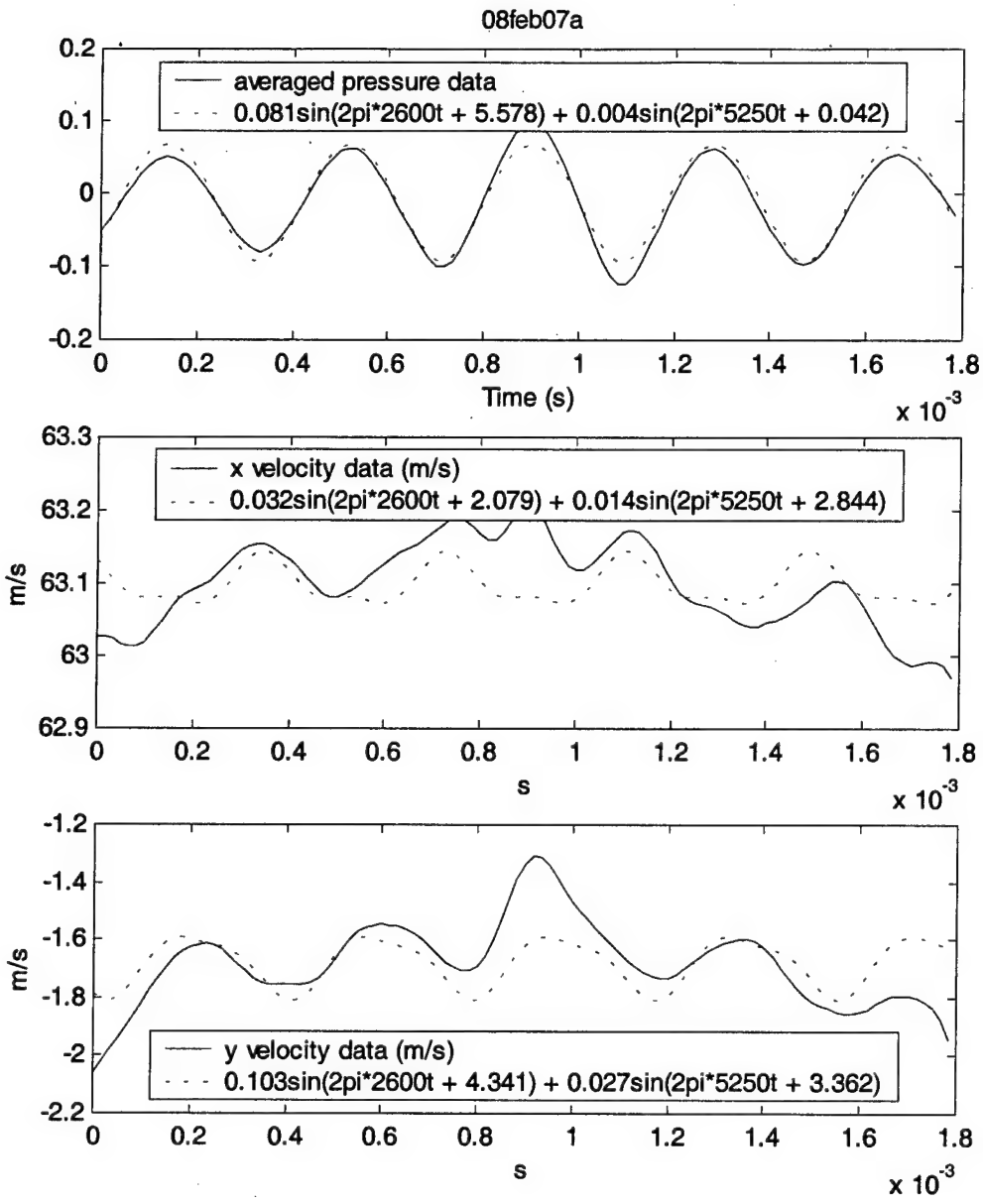

Figure 80. Data and two frequency approximation at x = -1 in, y = -1 in

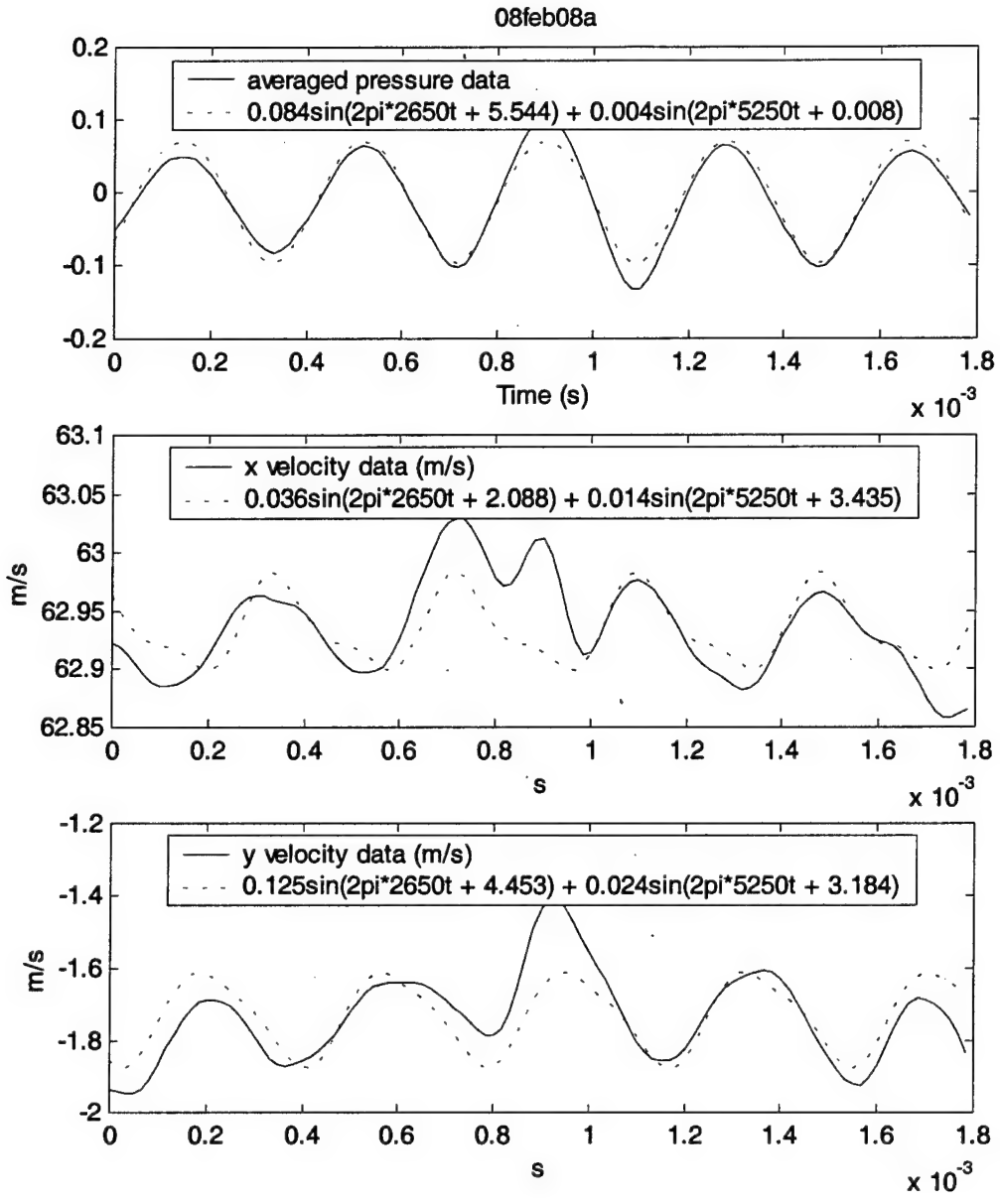

Figure 81. Data and two frequency approximation at x = -1 in, y = -0.875 in

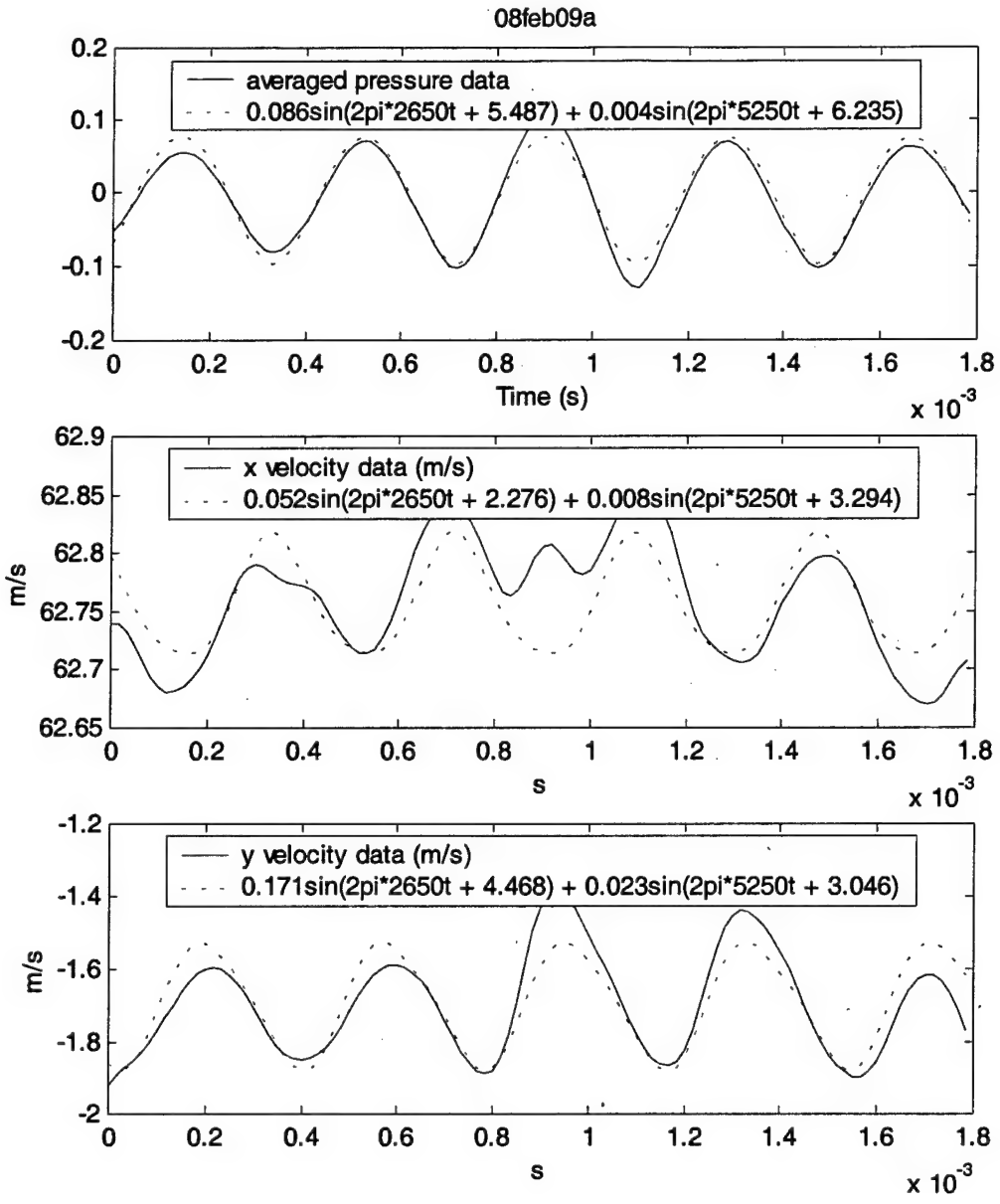

Figure 82. Data and two frequency approximation at x = -1 in, y = -0.75 in

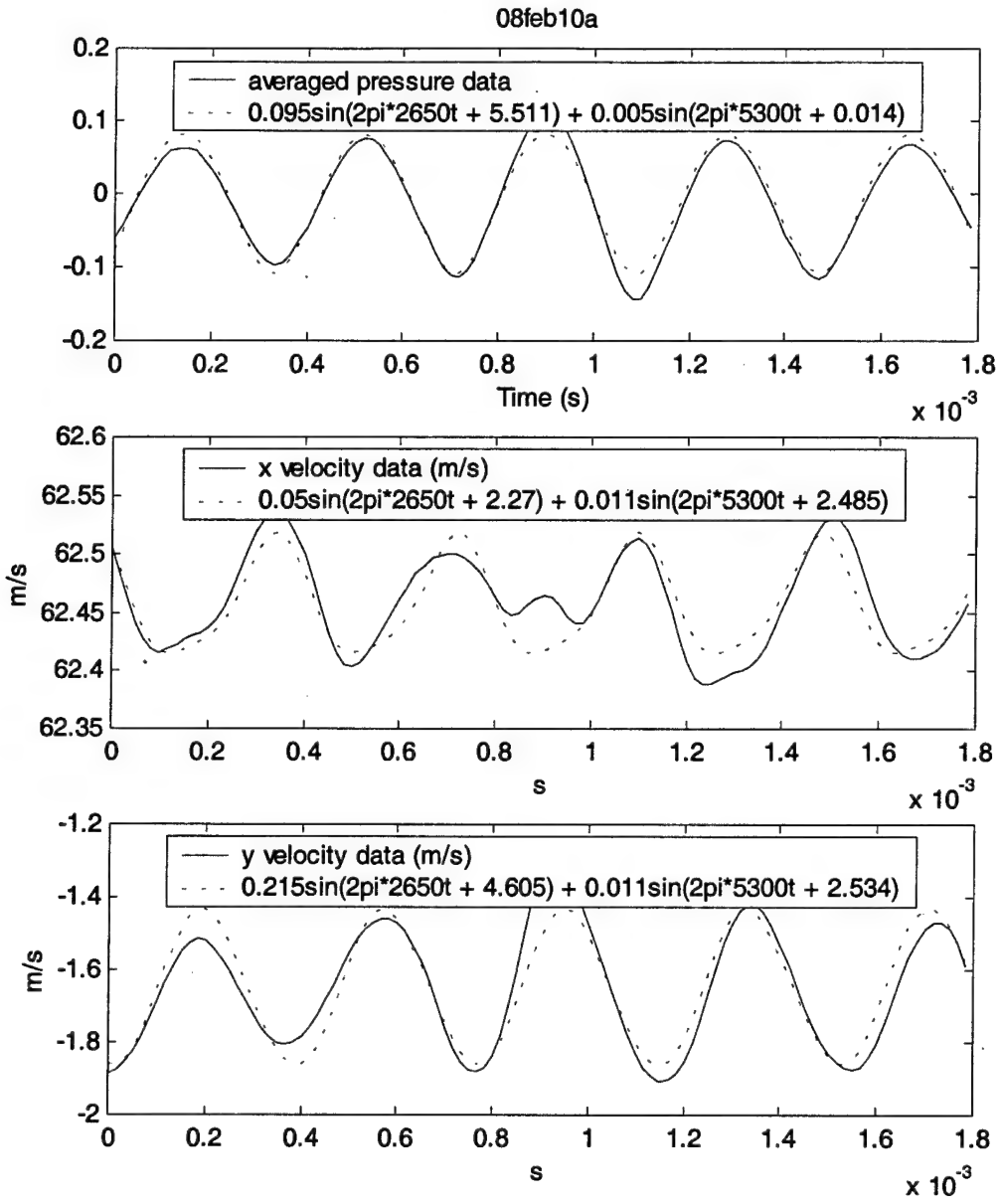

Figure 83. Data and two frequency approximation at x = -1 in, y = -0.625 in

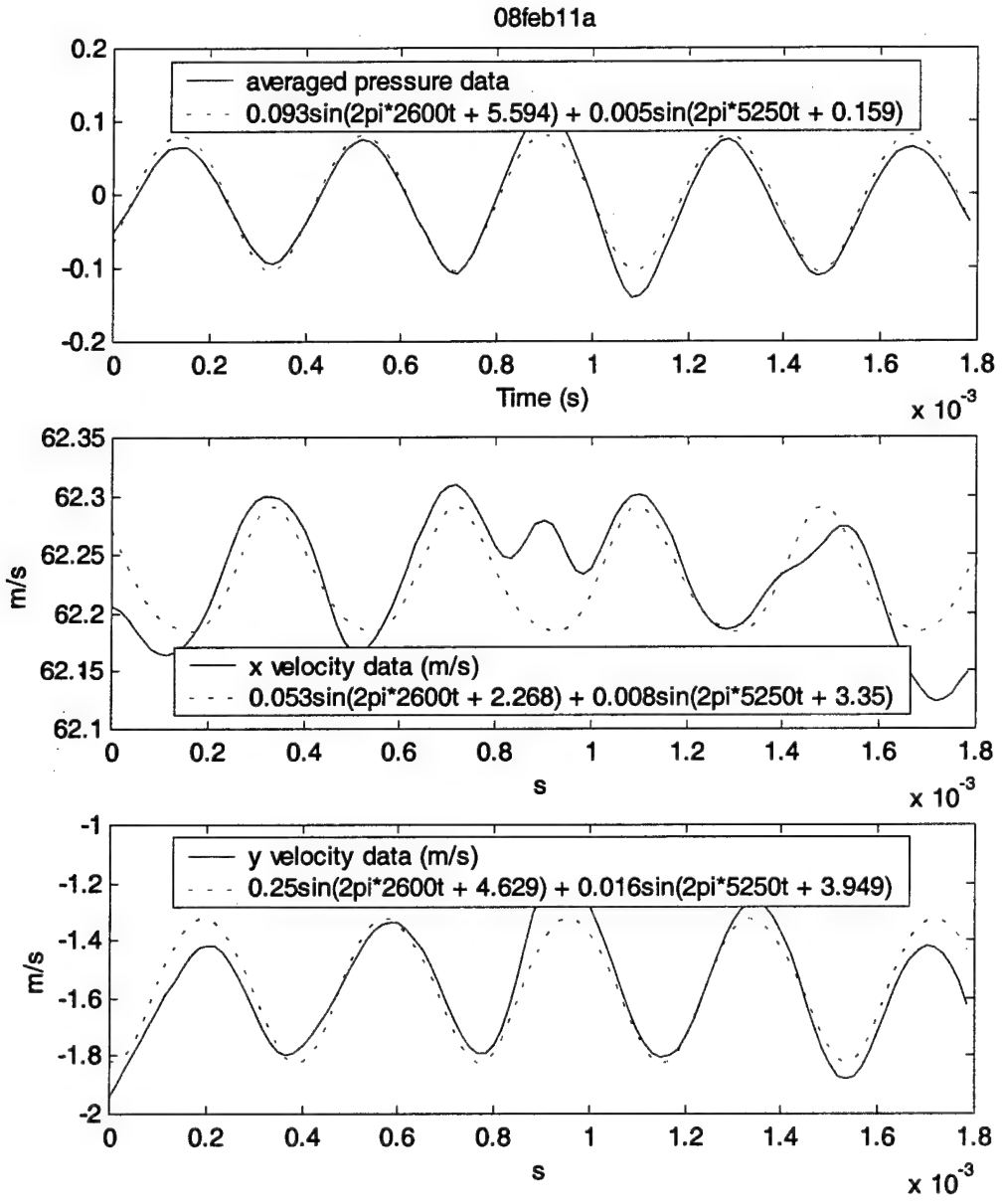

Figure 84. Data and two frequency approximation at x = -1 in, y = -0.5 in

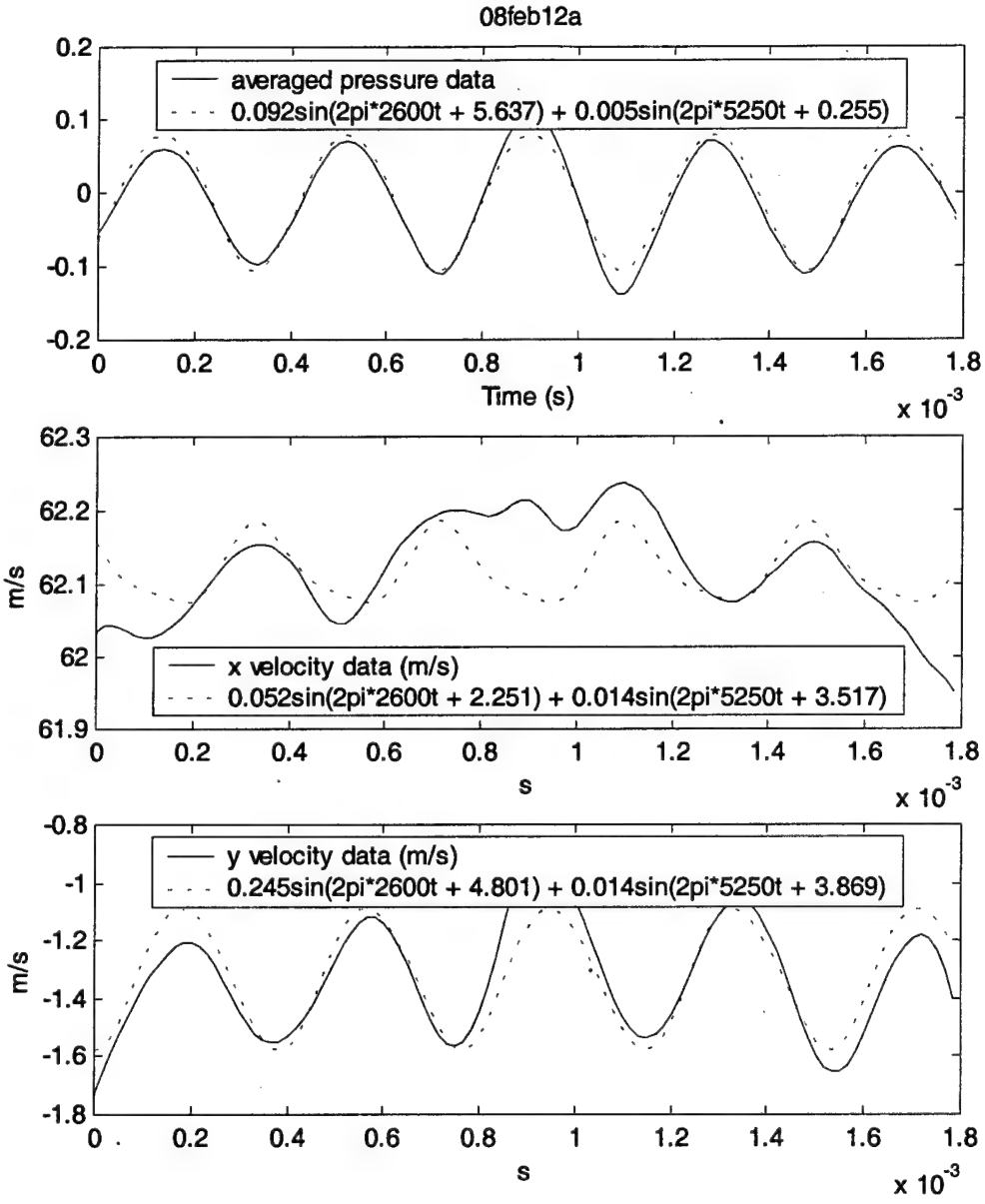

Figure 85. Data and two frequency approximation at x = -1 in, y = -0.375 in

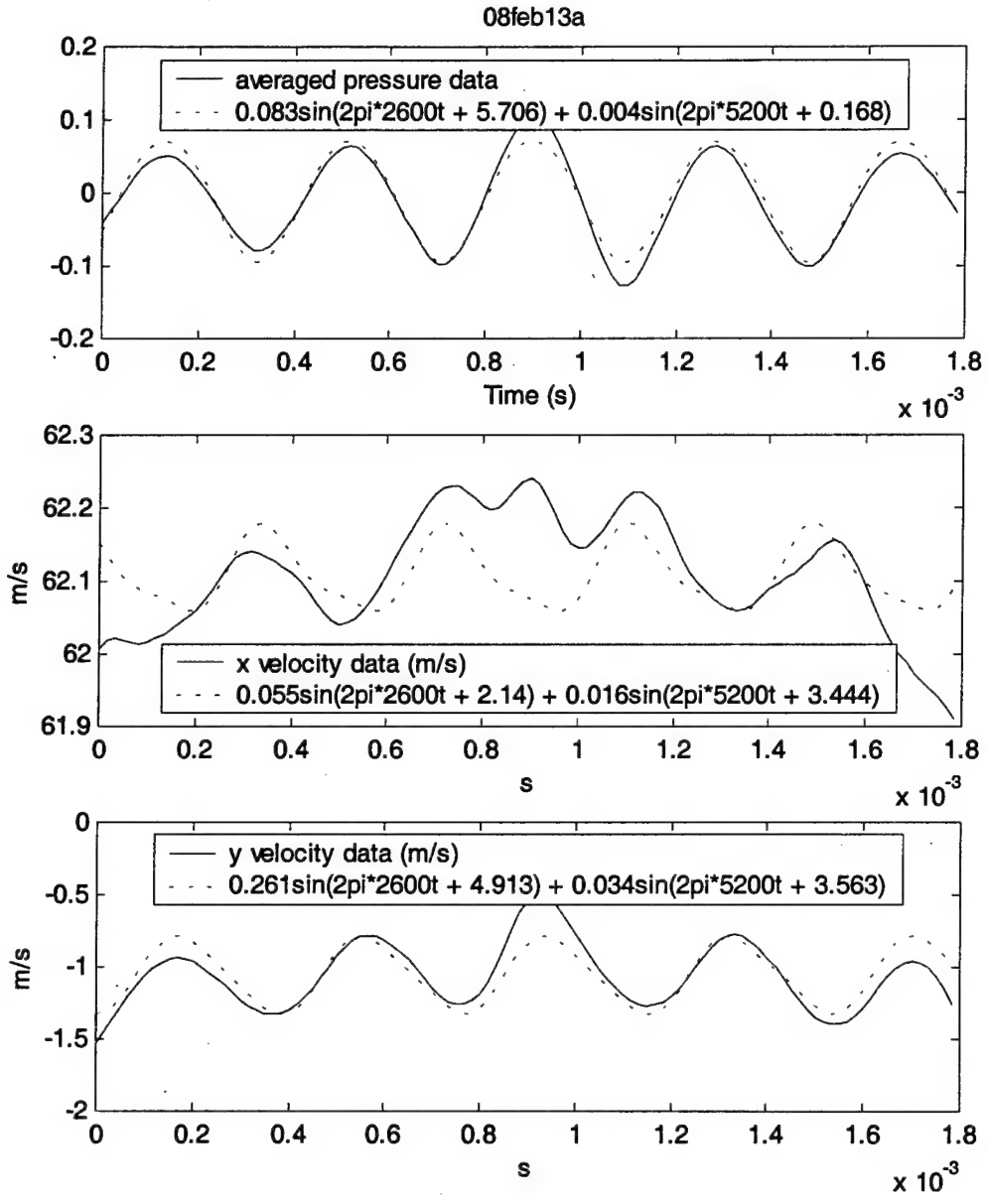

Figure 86. Data and two frequency approximation at x = -1 in, y = -0.25 in

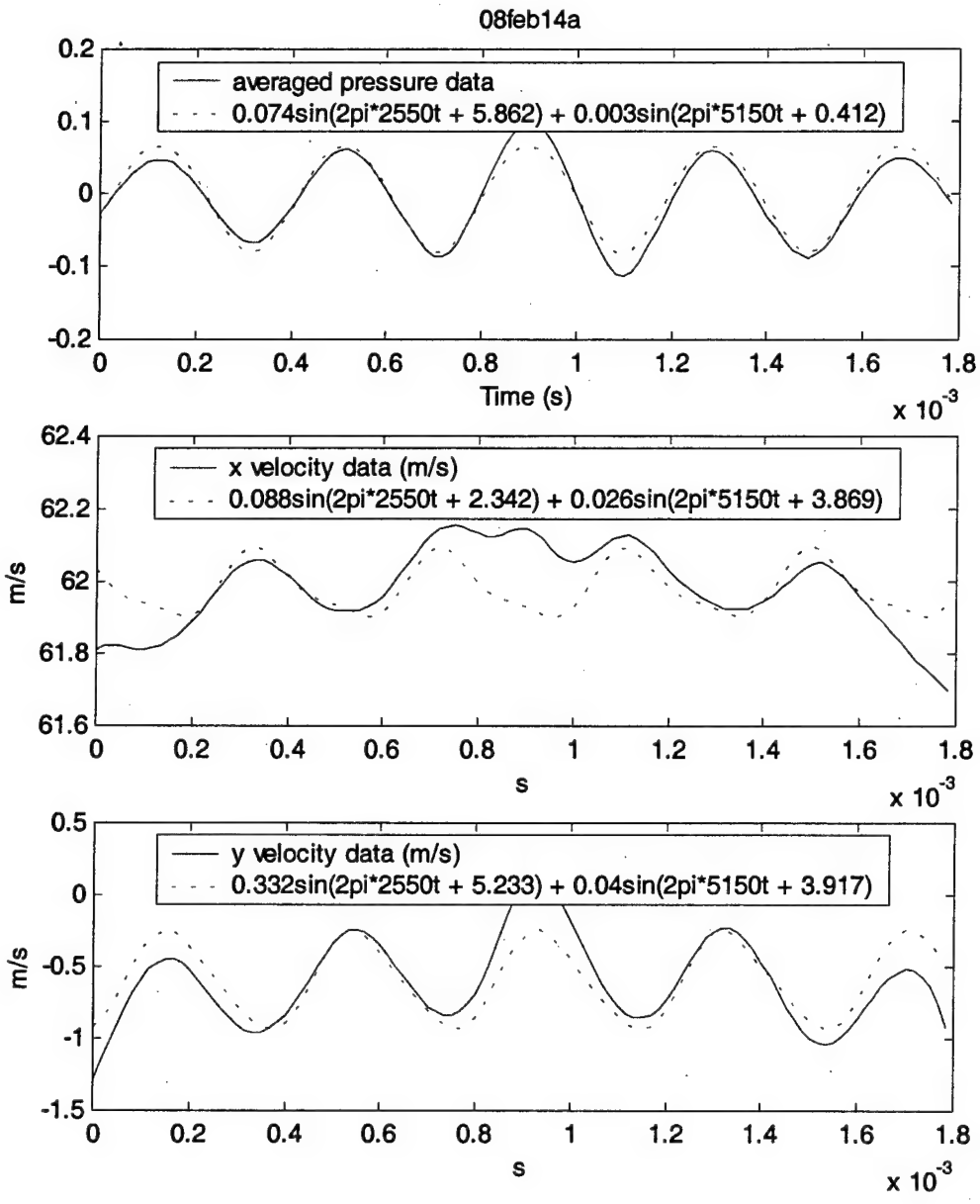

Figure 87. Data and two frequency approximation at x = -1 in, y = -0.125 in

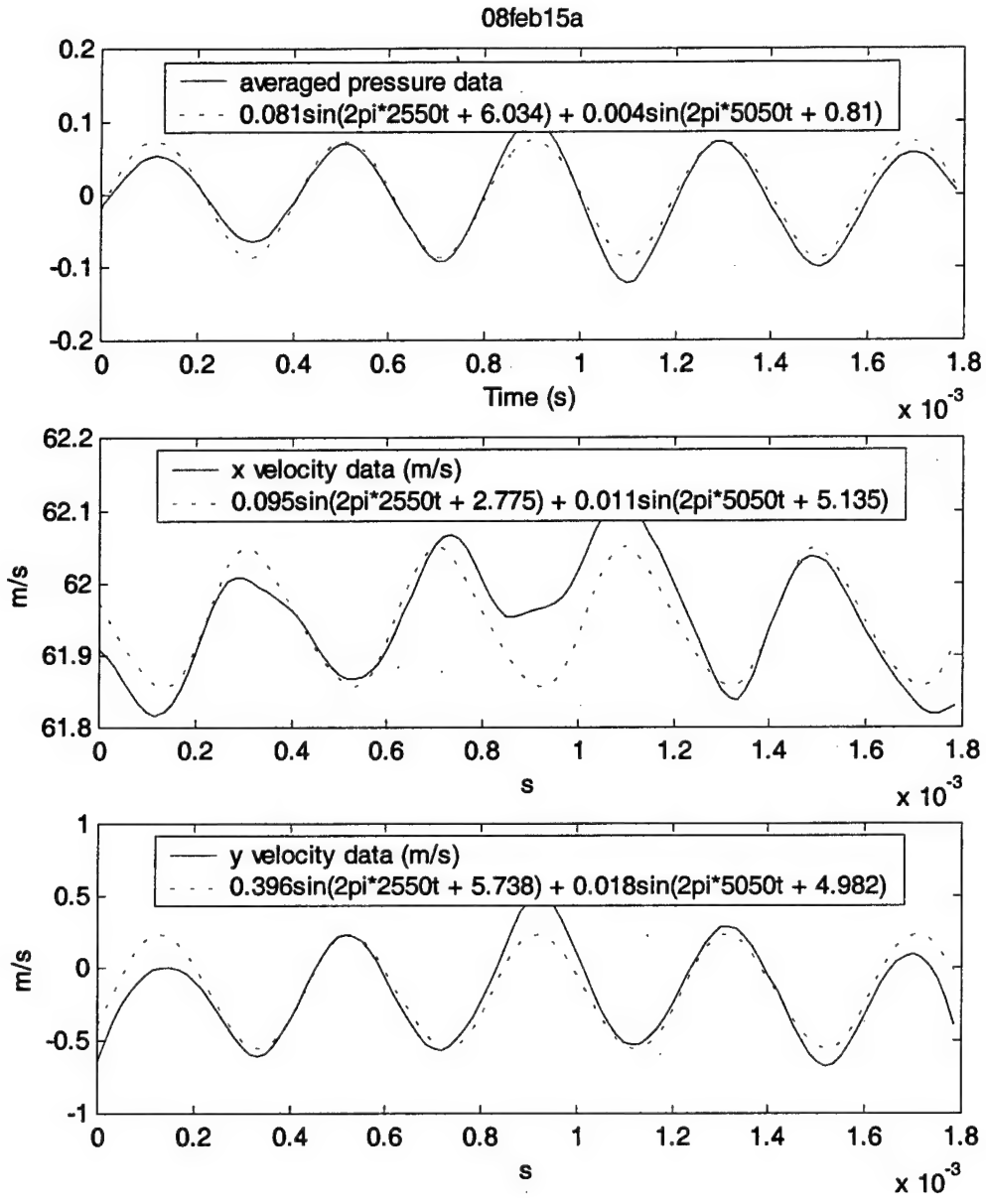

Figure 88. Data and two frequency approximation at x = -1 in, y = 0 in

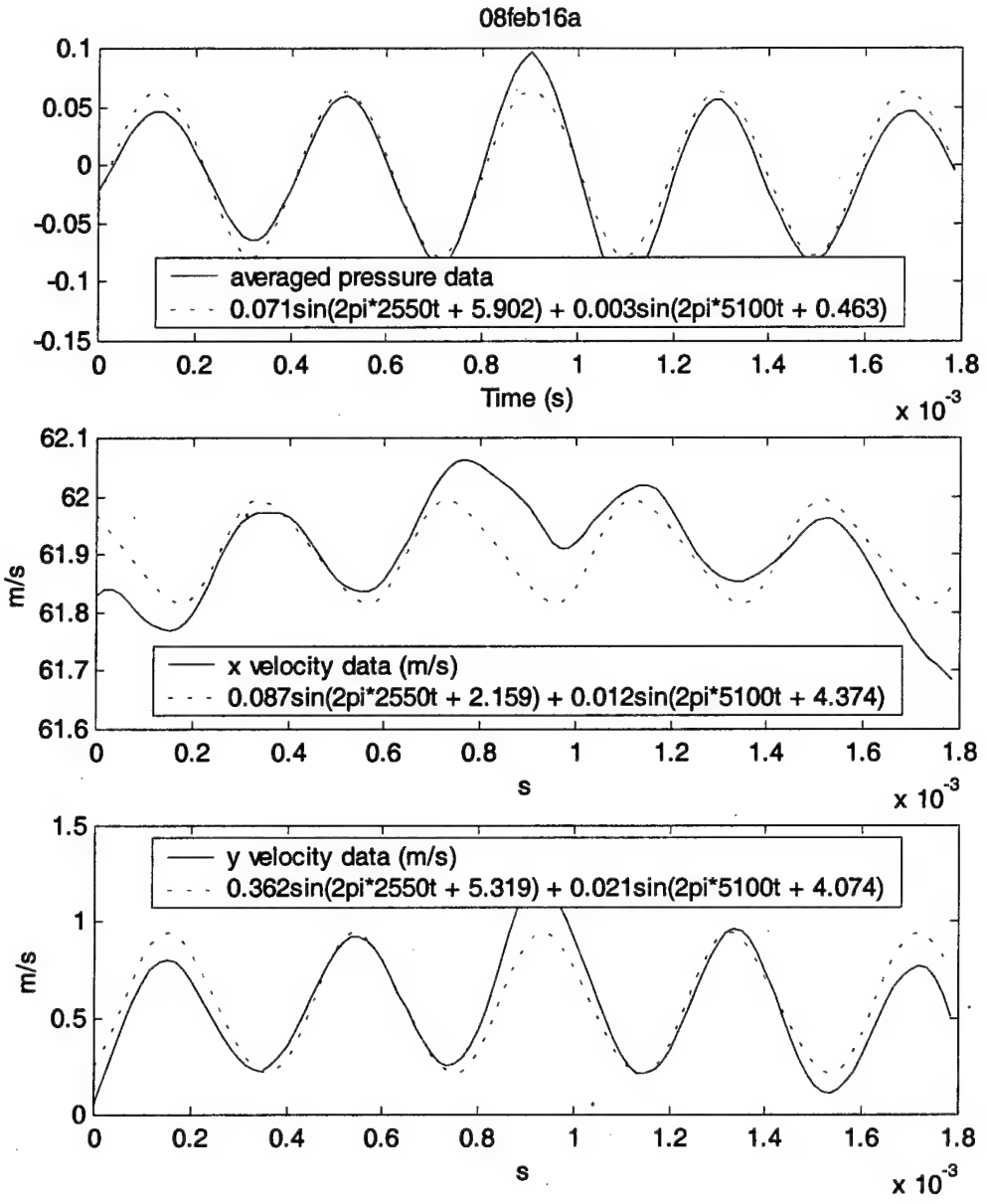

Figure 89. Data and two frequency approximation at x = -1 in, y = 0.125 in

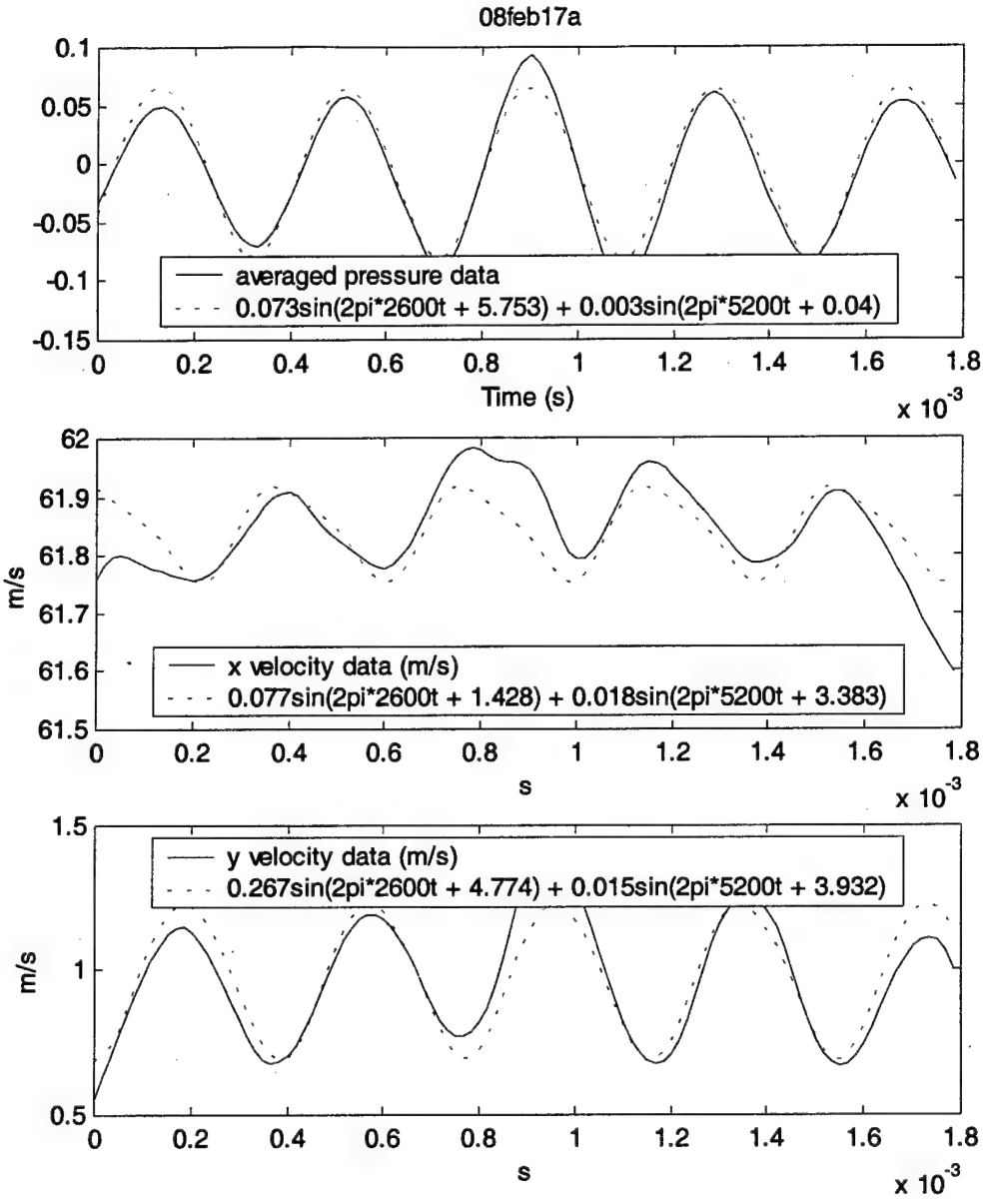

Figure 90. Data and two frequency approximation at x = -1 in, y = 0.25 in

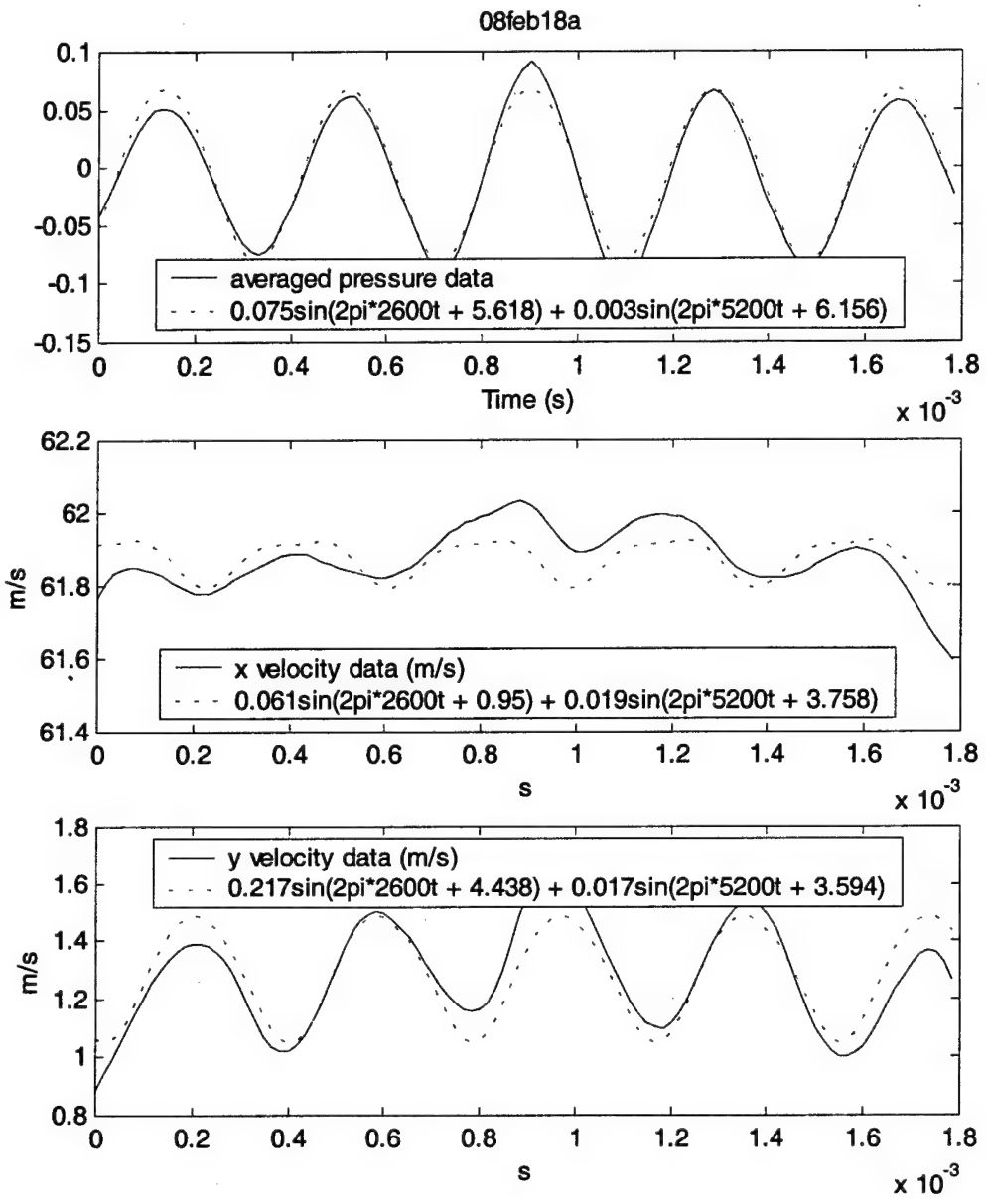

Figure 91. Data and two frequency approximation at x = -1 in, y = 0.375 in

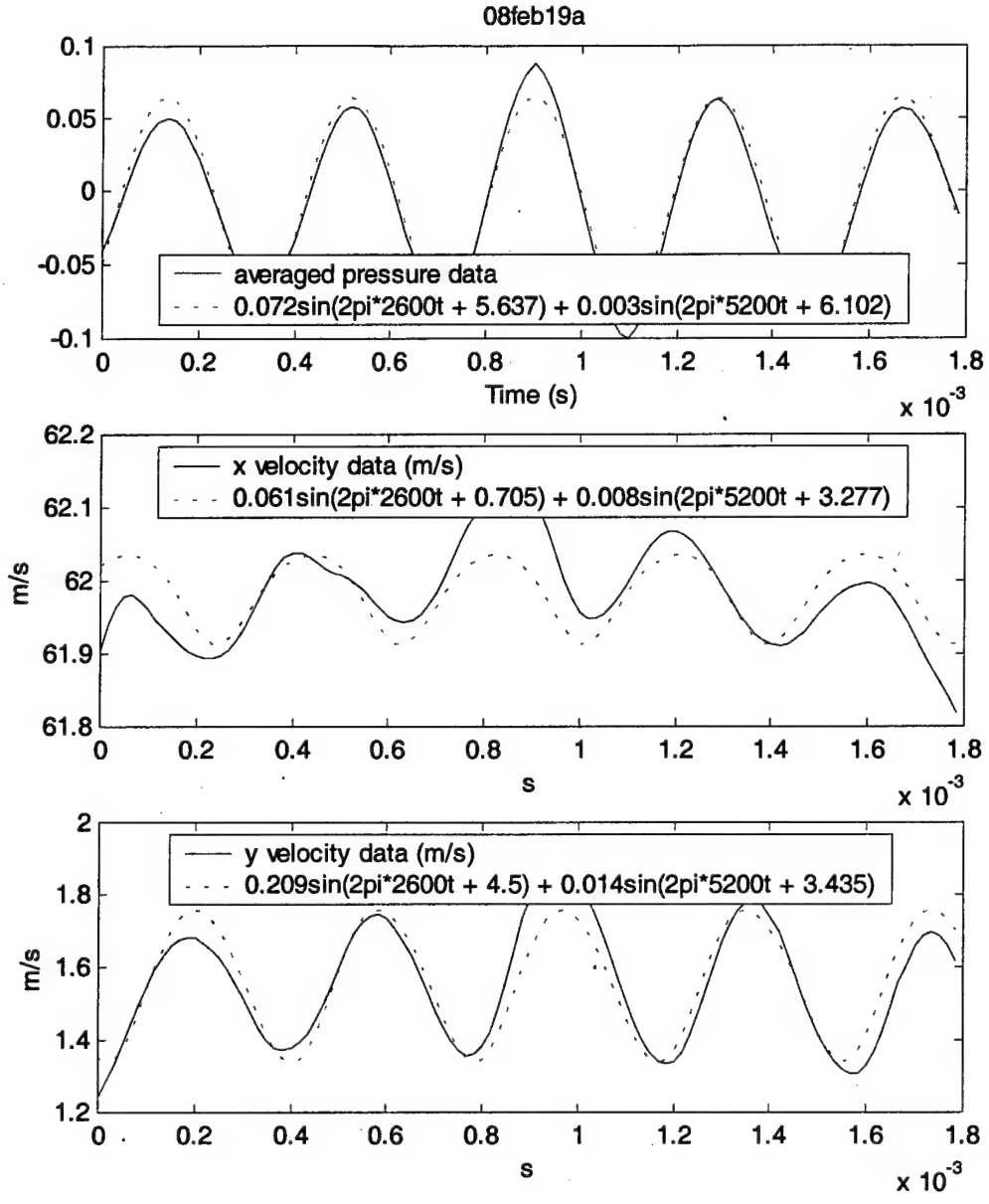

Figure 92. Data and two frequency approximation at x = -1 in, y = 0.5 in

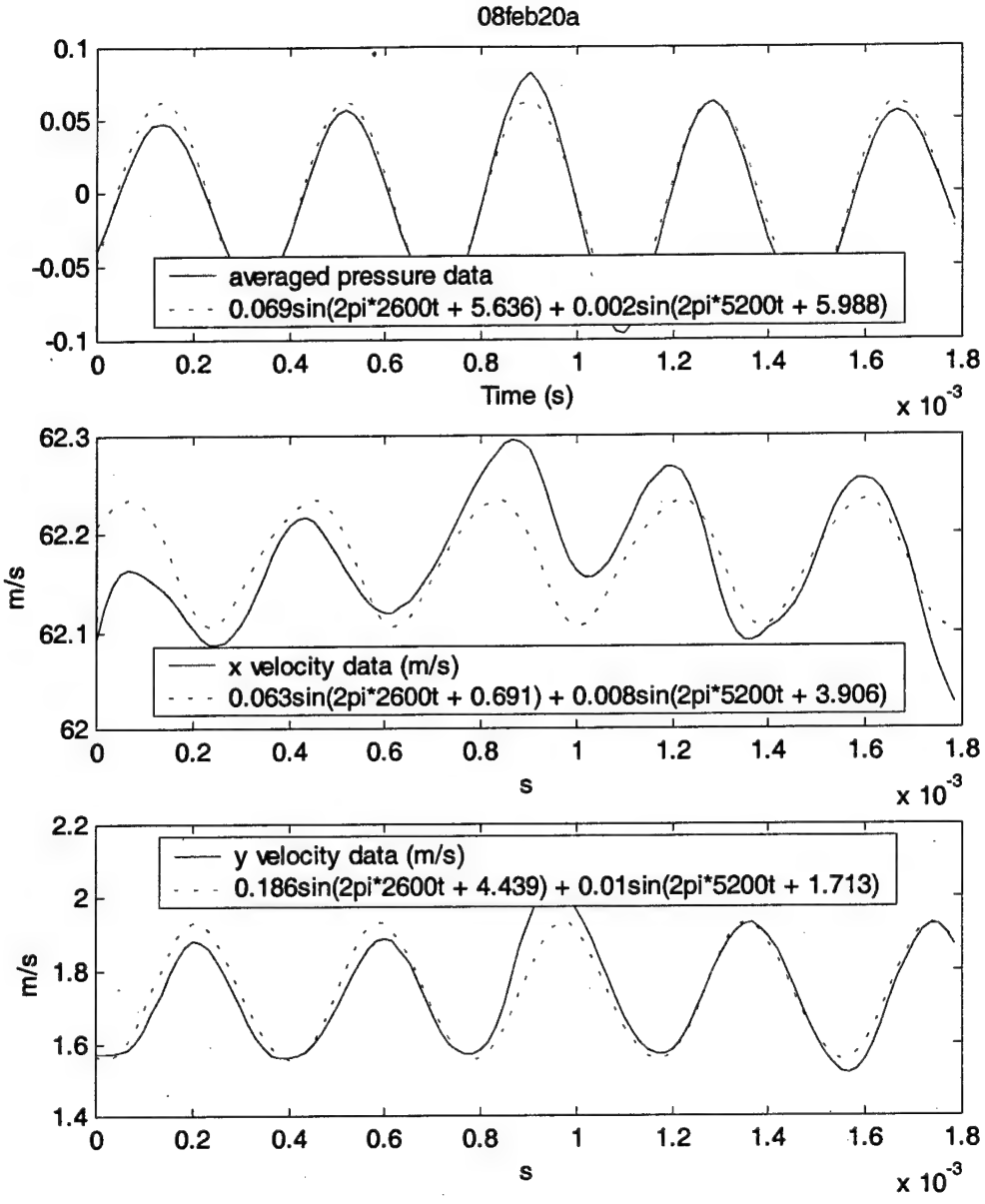

Figure 93. Data and two frequency approximation at x = -1 in, y = 0.625 in

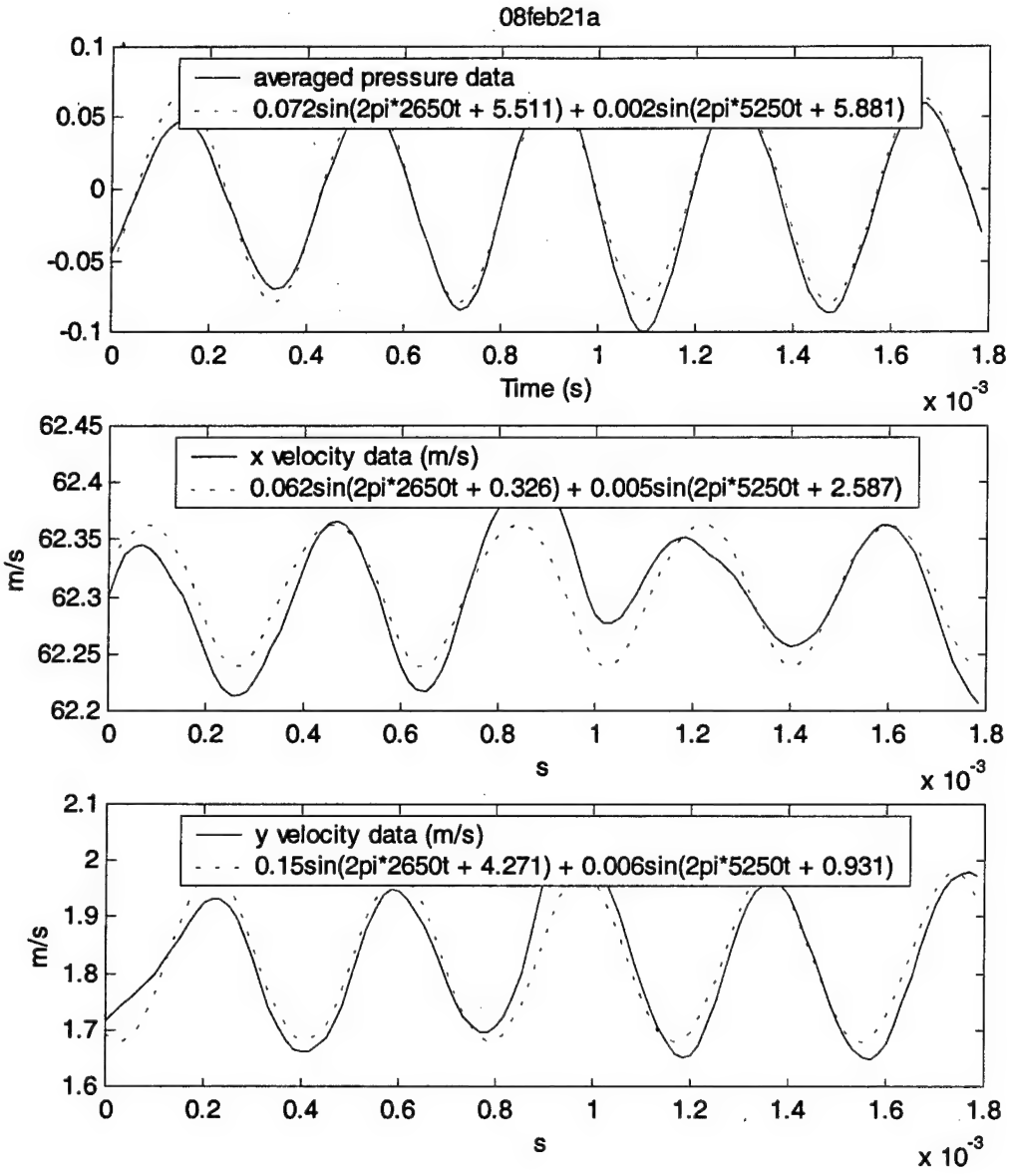

Figure 94. Data and two frequency approximation at x = -1 in, y = 0.75 in

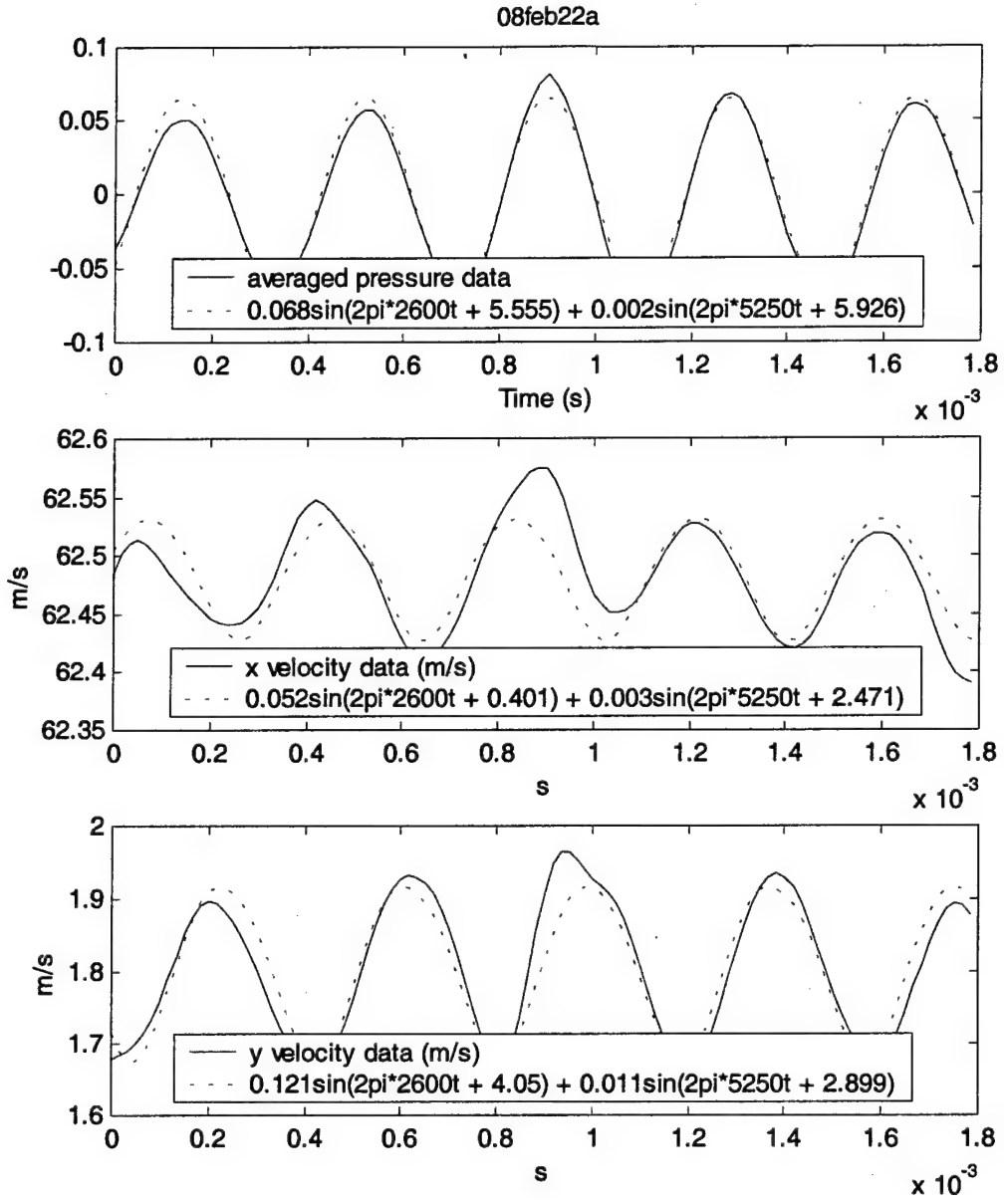

Figure 95. Data and two frequency approximation at x = -1 in, y = 0.875 in

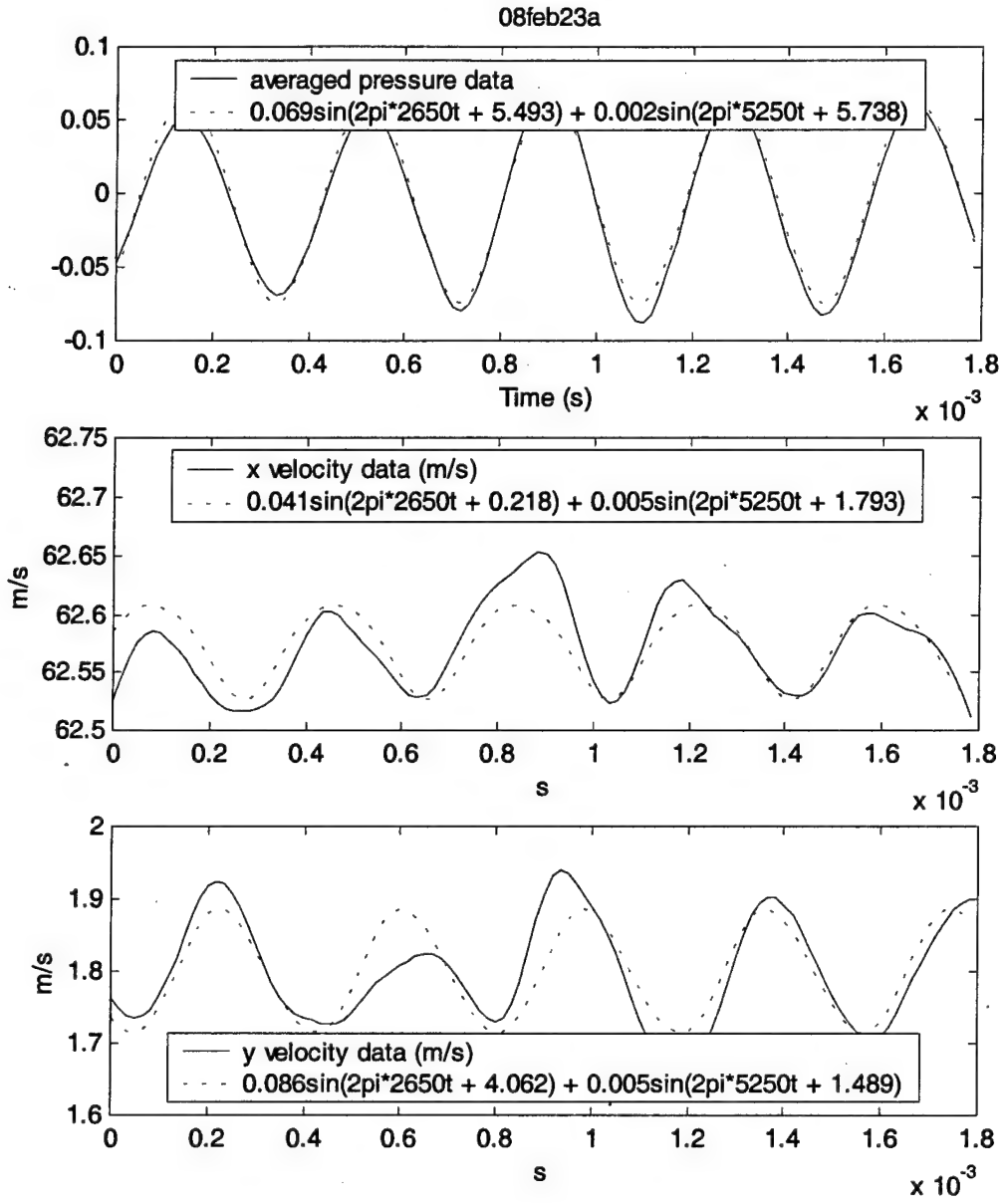

Figure 96. Data and two frequency approximation at x = -1 in, y = 1 in

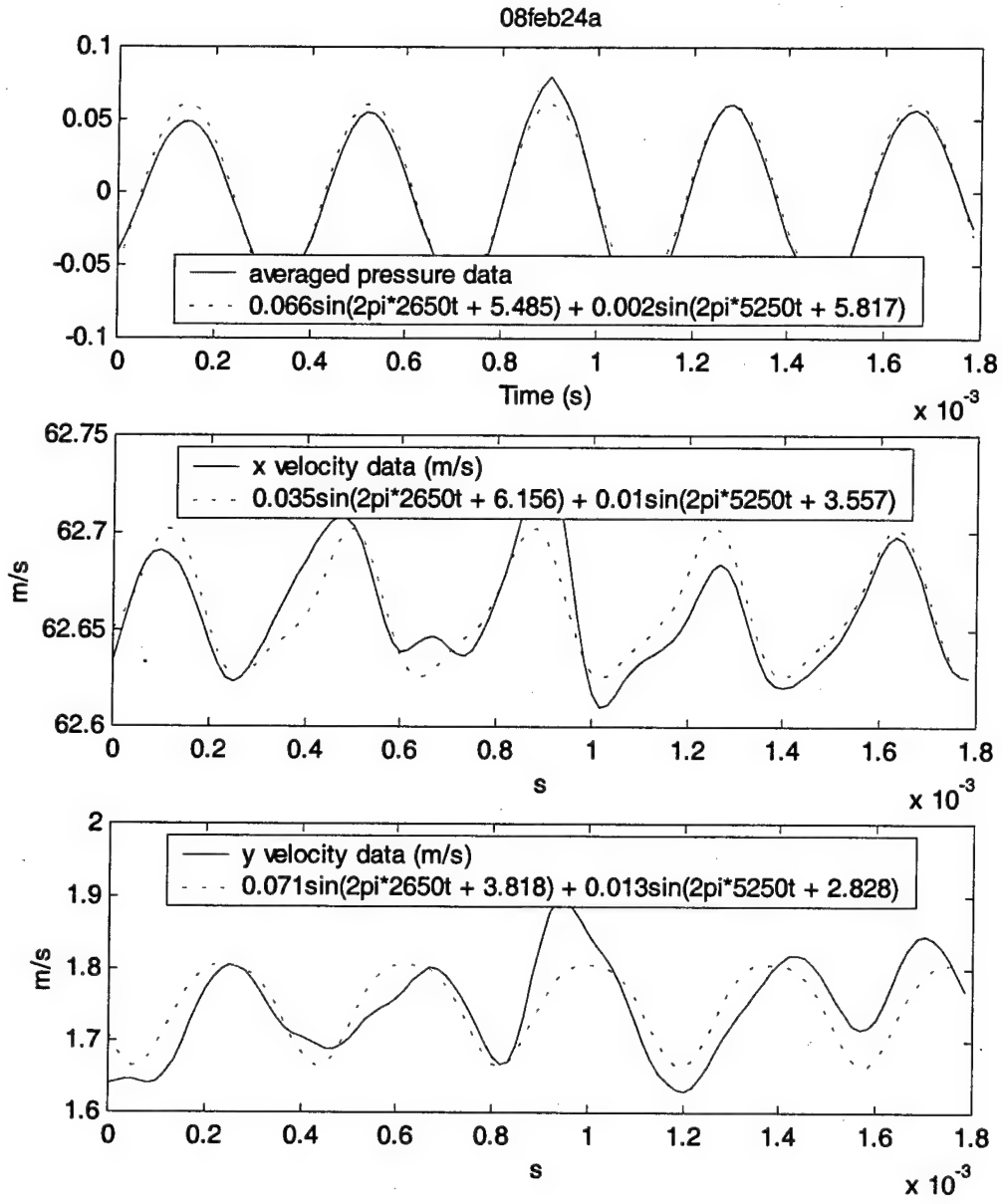

Figure 97. Data and two frequency approximation at x = -1 in, y = 1.125 in

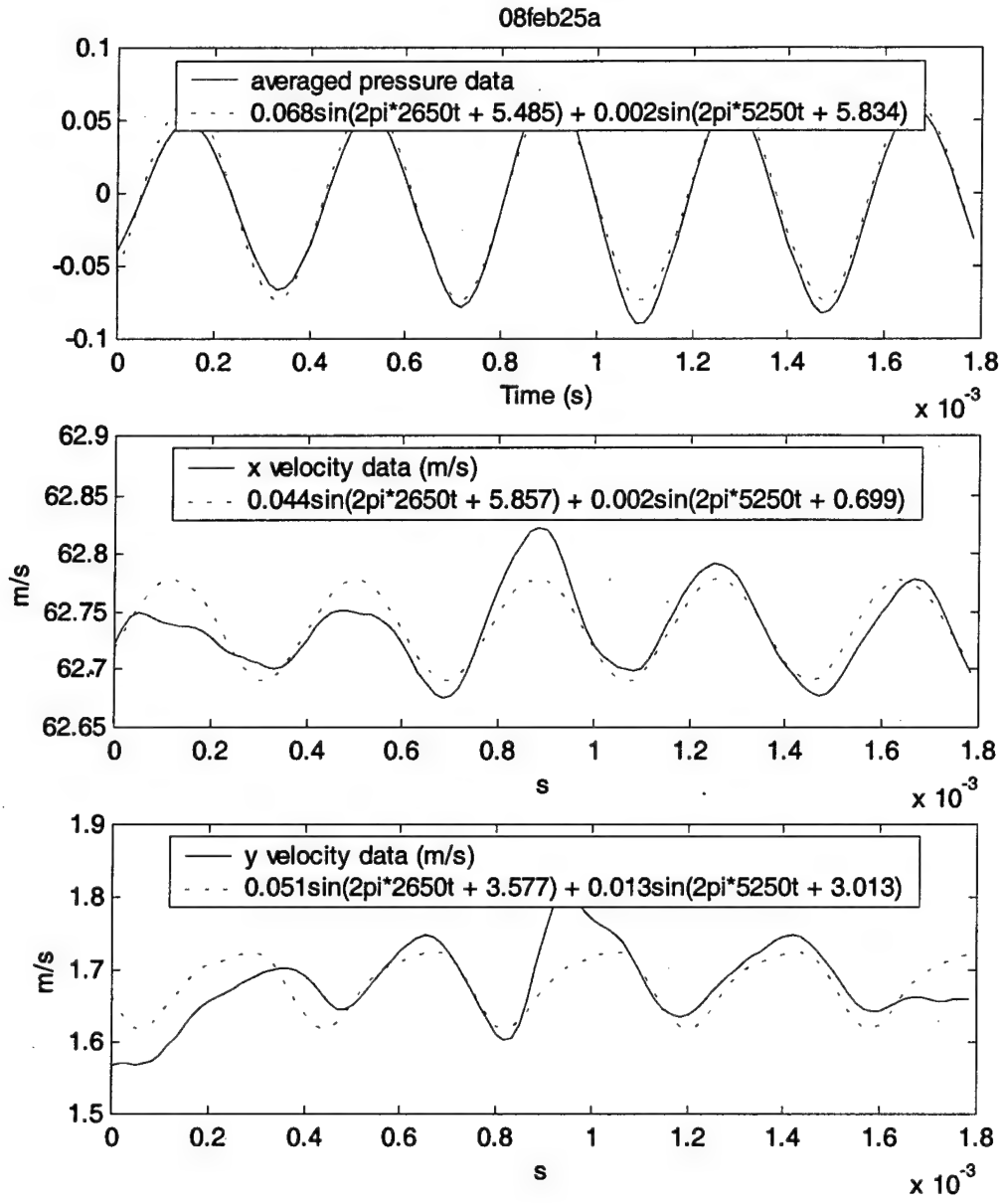

Figure 98. Data and two frequency approximation at x = -1 in, y = 1.25 in

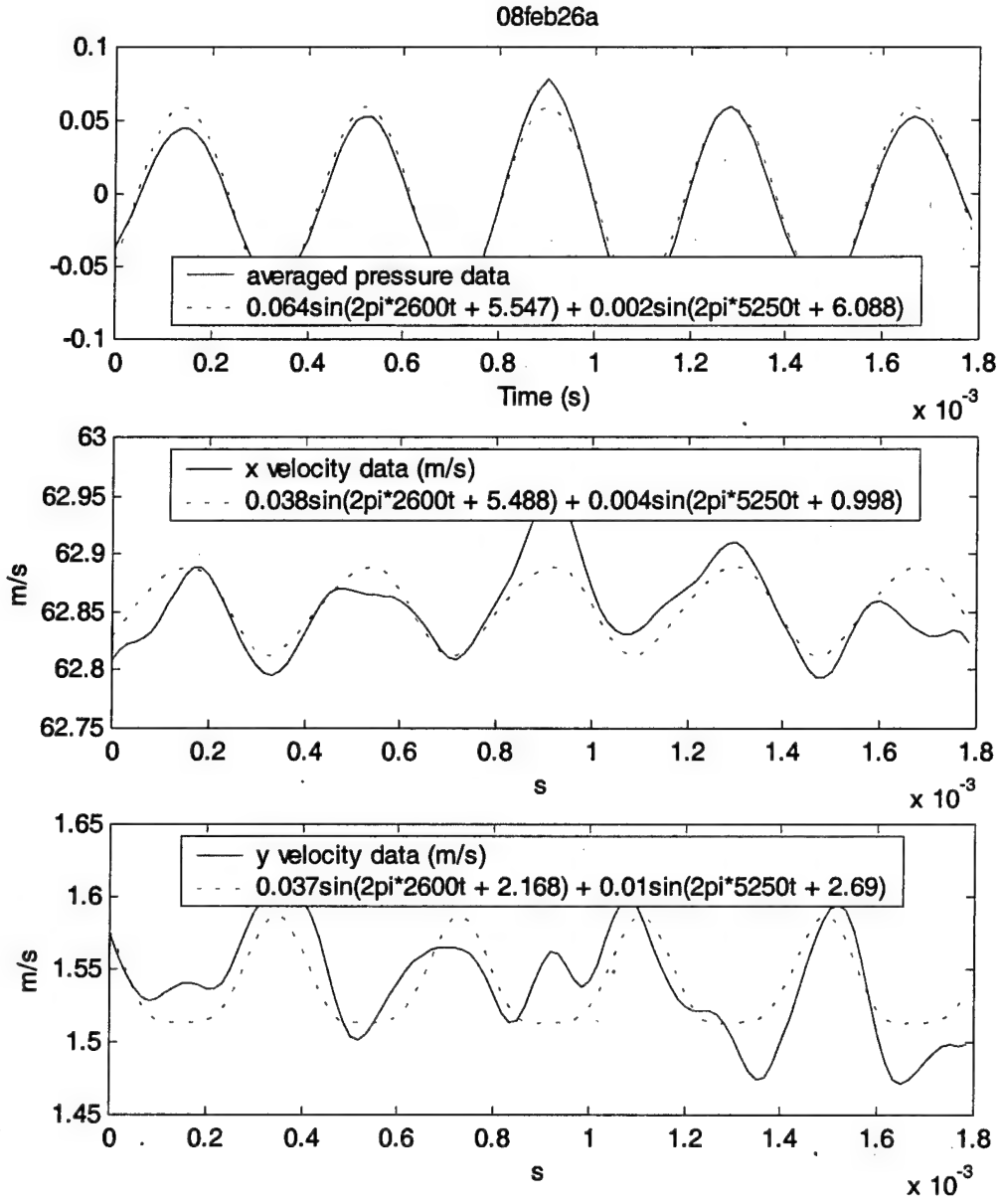

Figure 99. Data and two frequency approximation at x = -1 in, y = 1.5 in

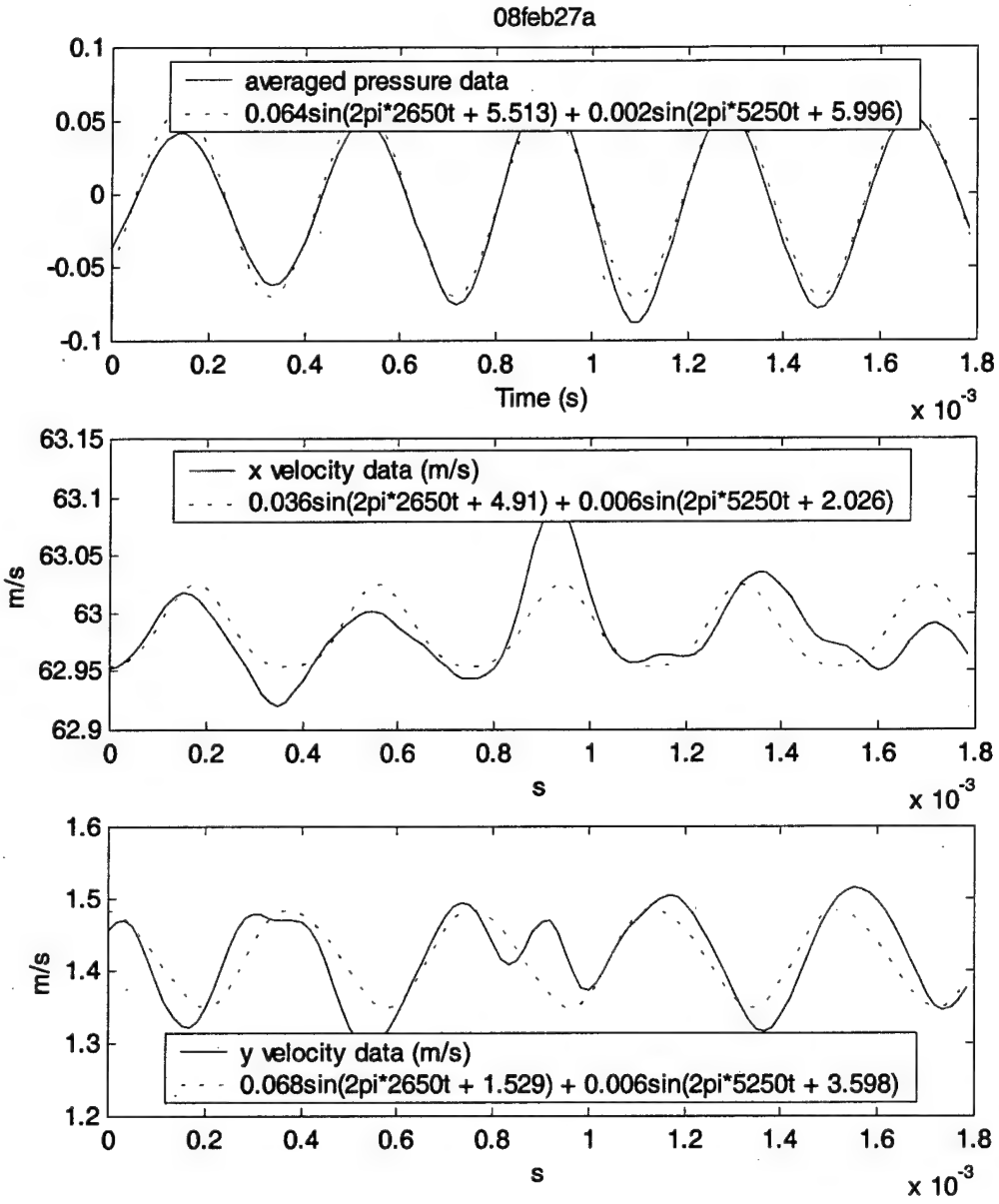

Figure 100. Data and two frequency approximation at x = -1 in, y = 1.75 in

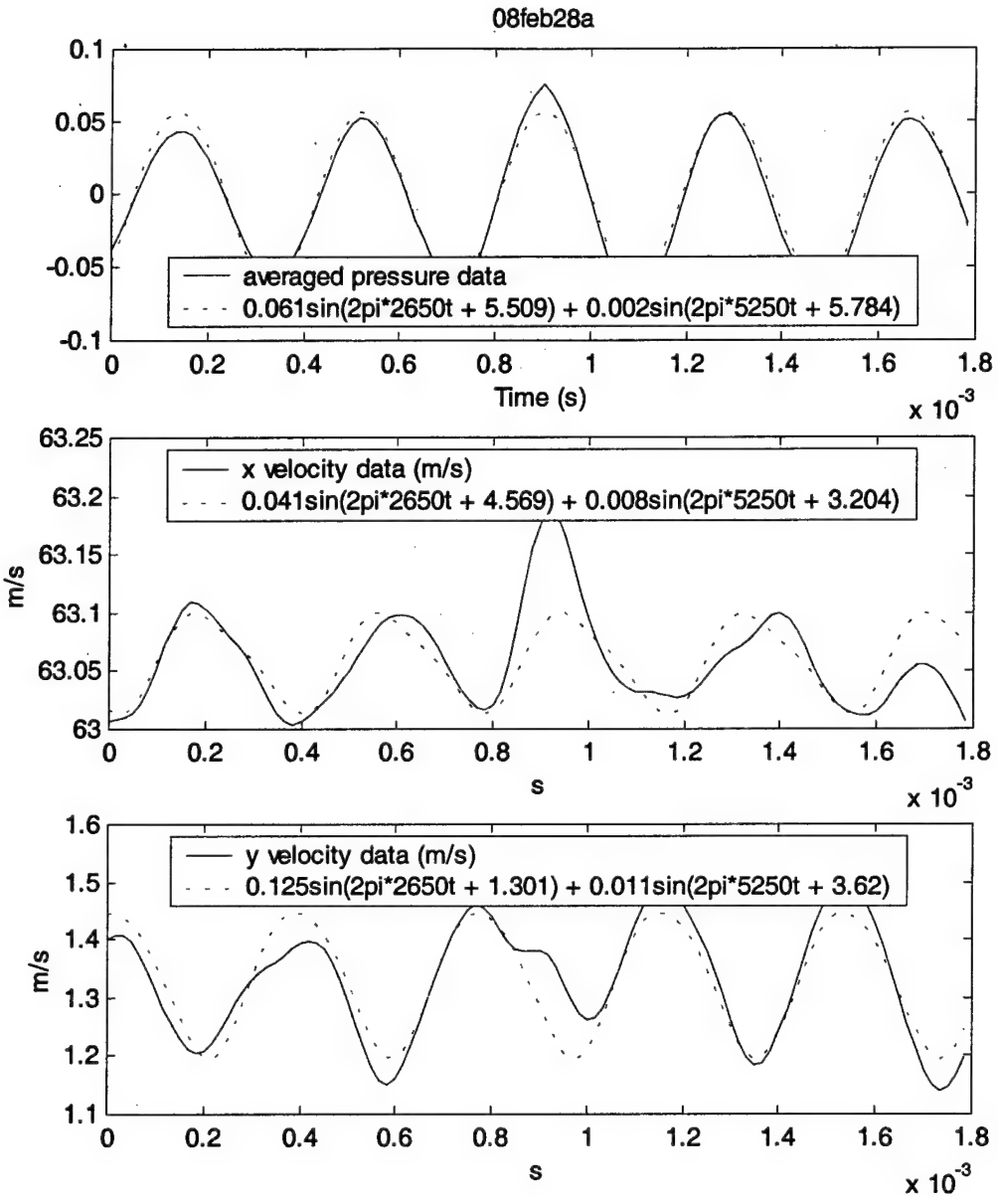

Figure 101. Data and two frequency approximation at x = -1 in, y = 2 in

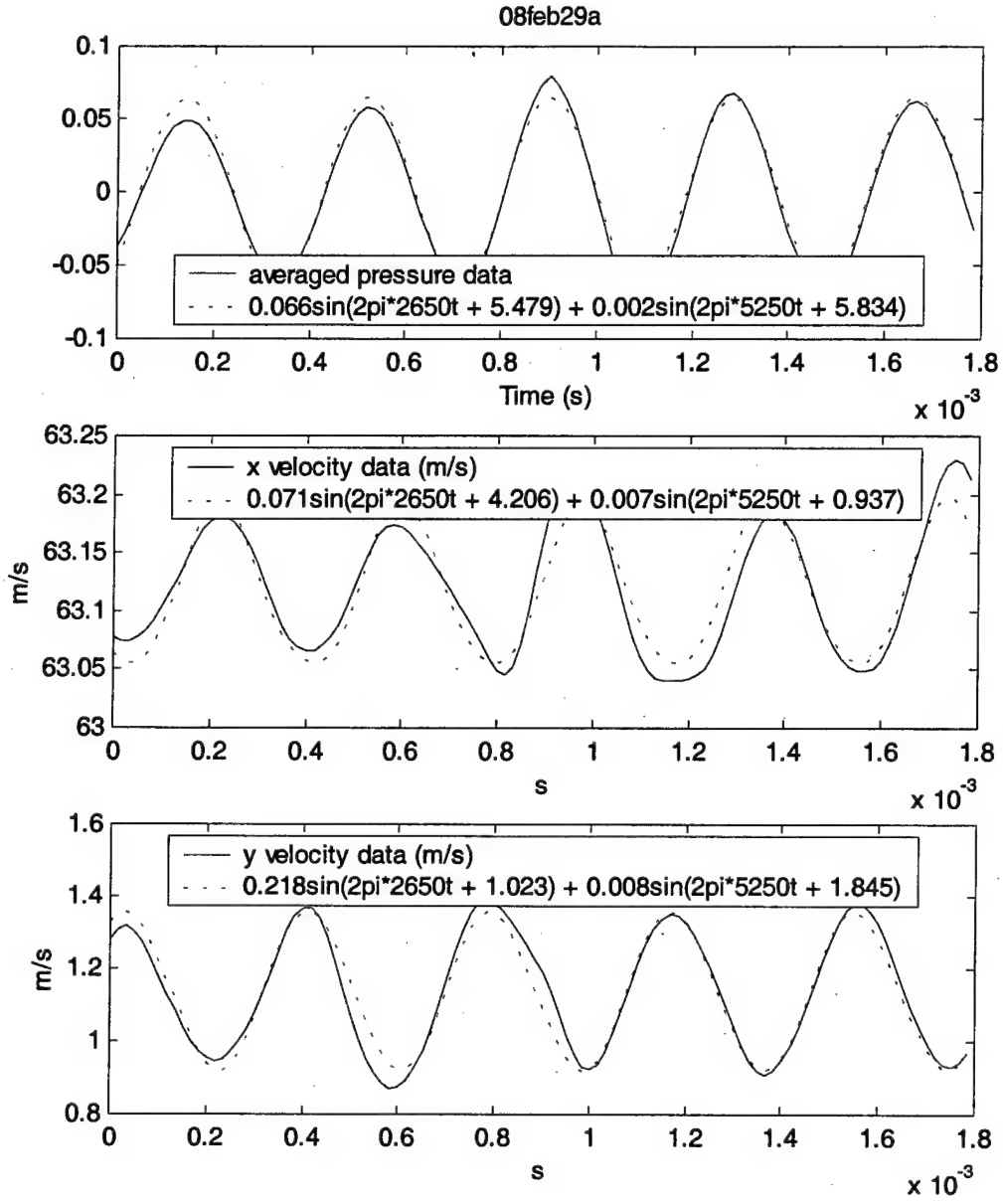

Figure 102. Data and two frequency approximation at x = -1 in, y = 2.5 in

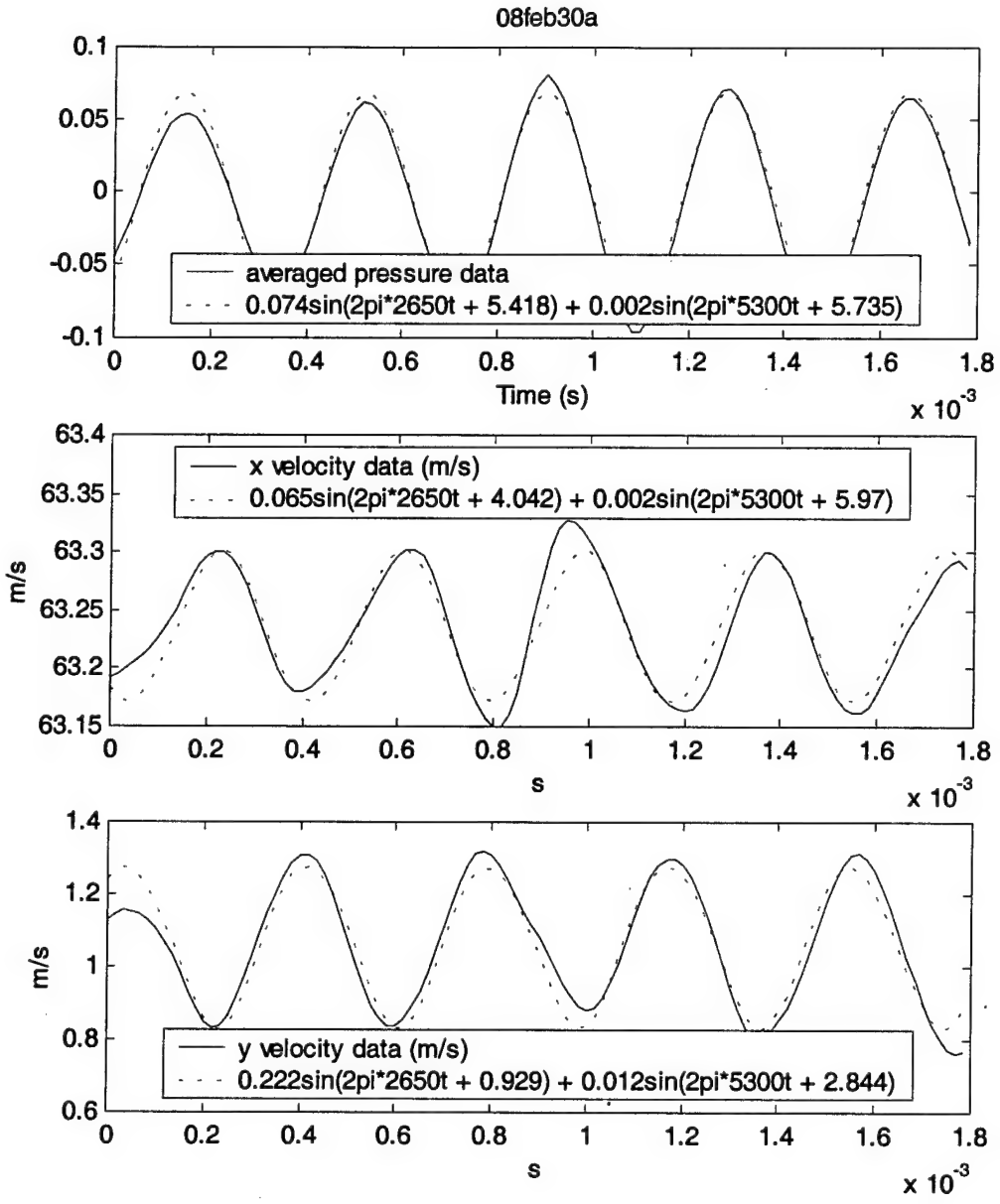

Figure 103. Data and two frequency approximation at x = -1 in, y = 3 in

2. Data at x = -1.5 in

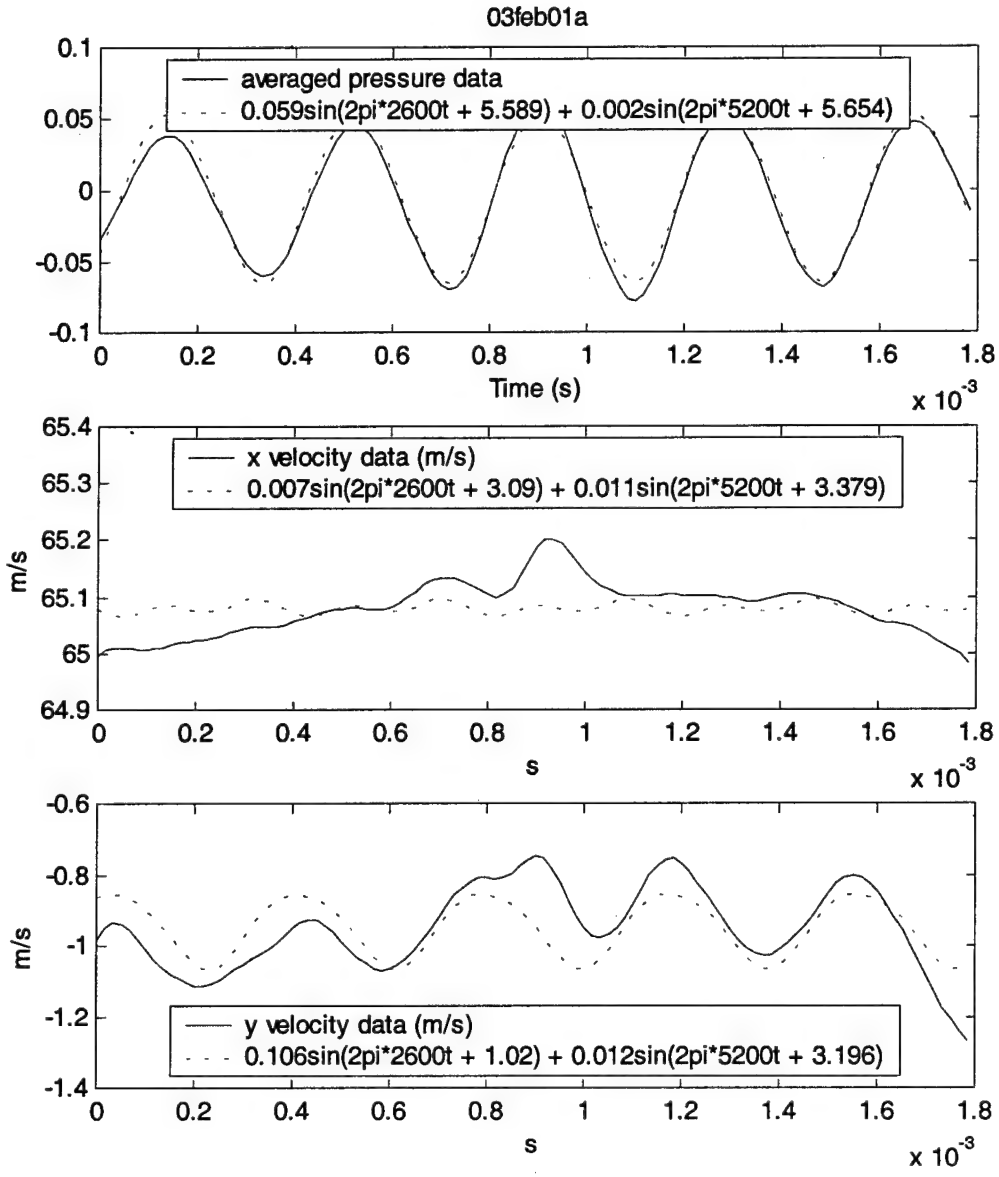

Figure 104. Data and two frequency approximation at x = -1.5 in, y = -2 in

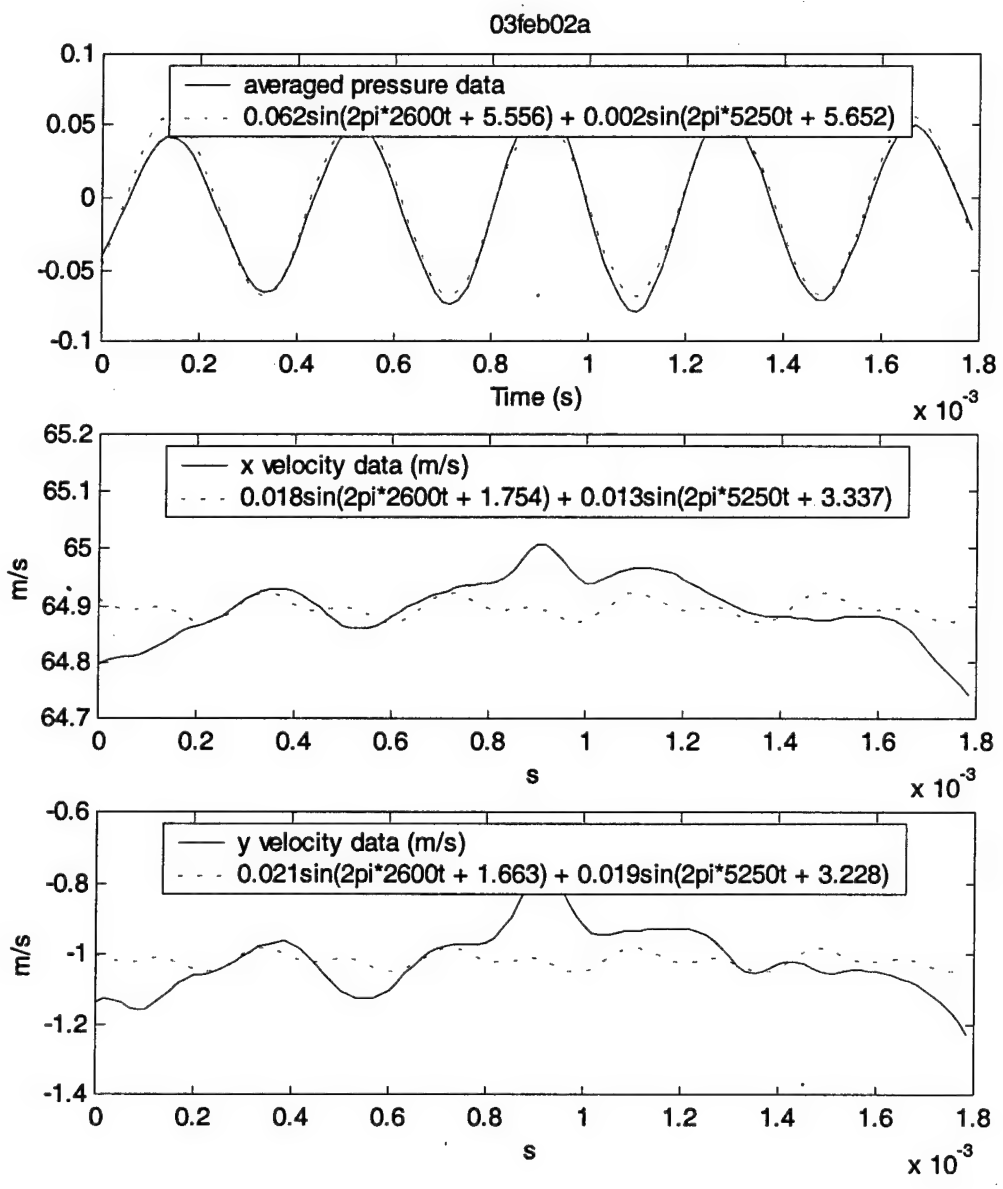

Figure 105. Data and two frequency approximation at x = -1.5 in, y = -1.5 in

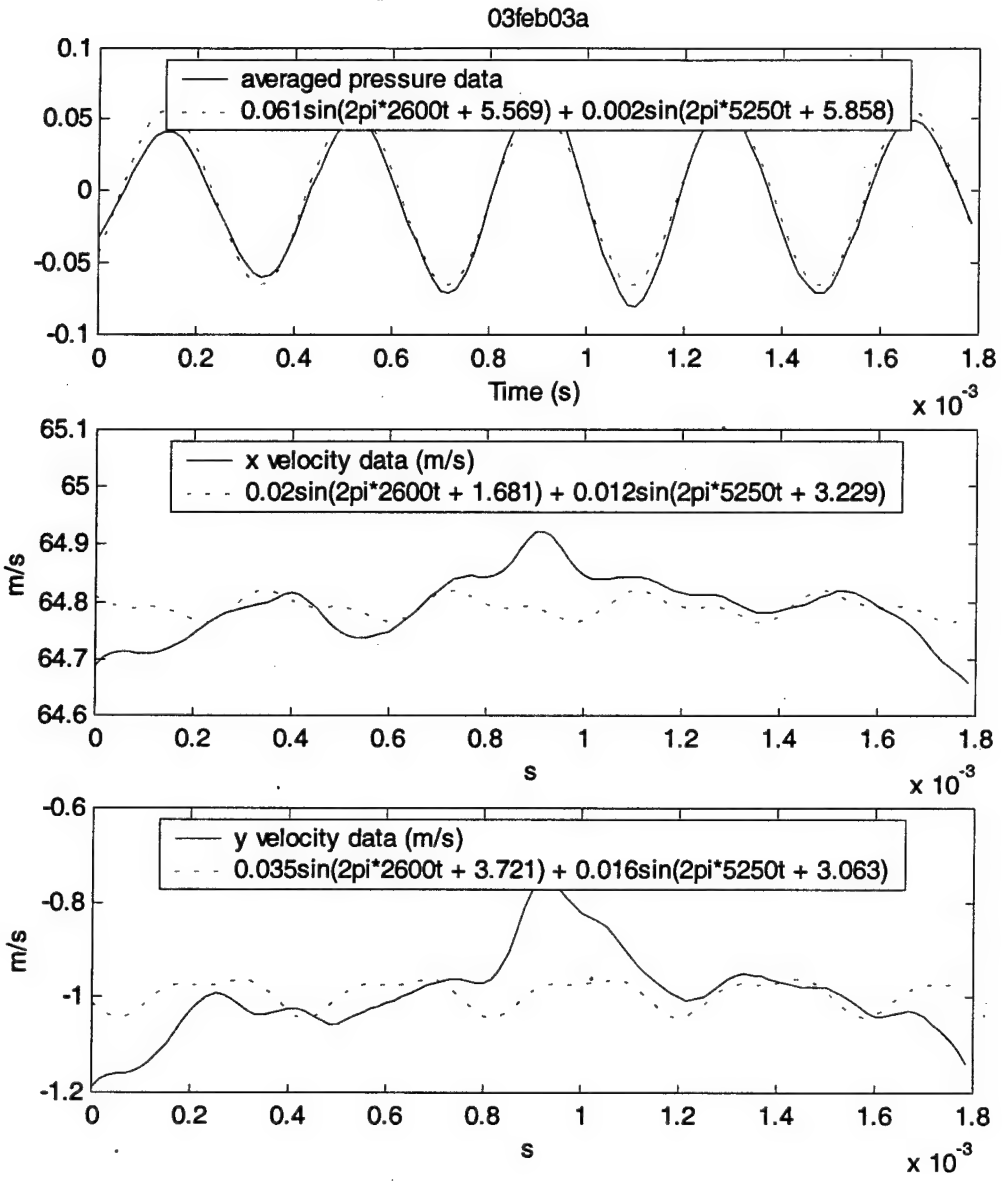

Figure 106. Data and two frequency approximation at x = -1.5 in, y = -1.25 in

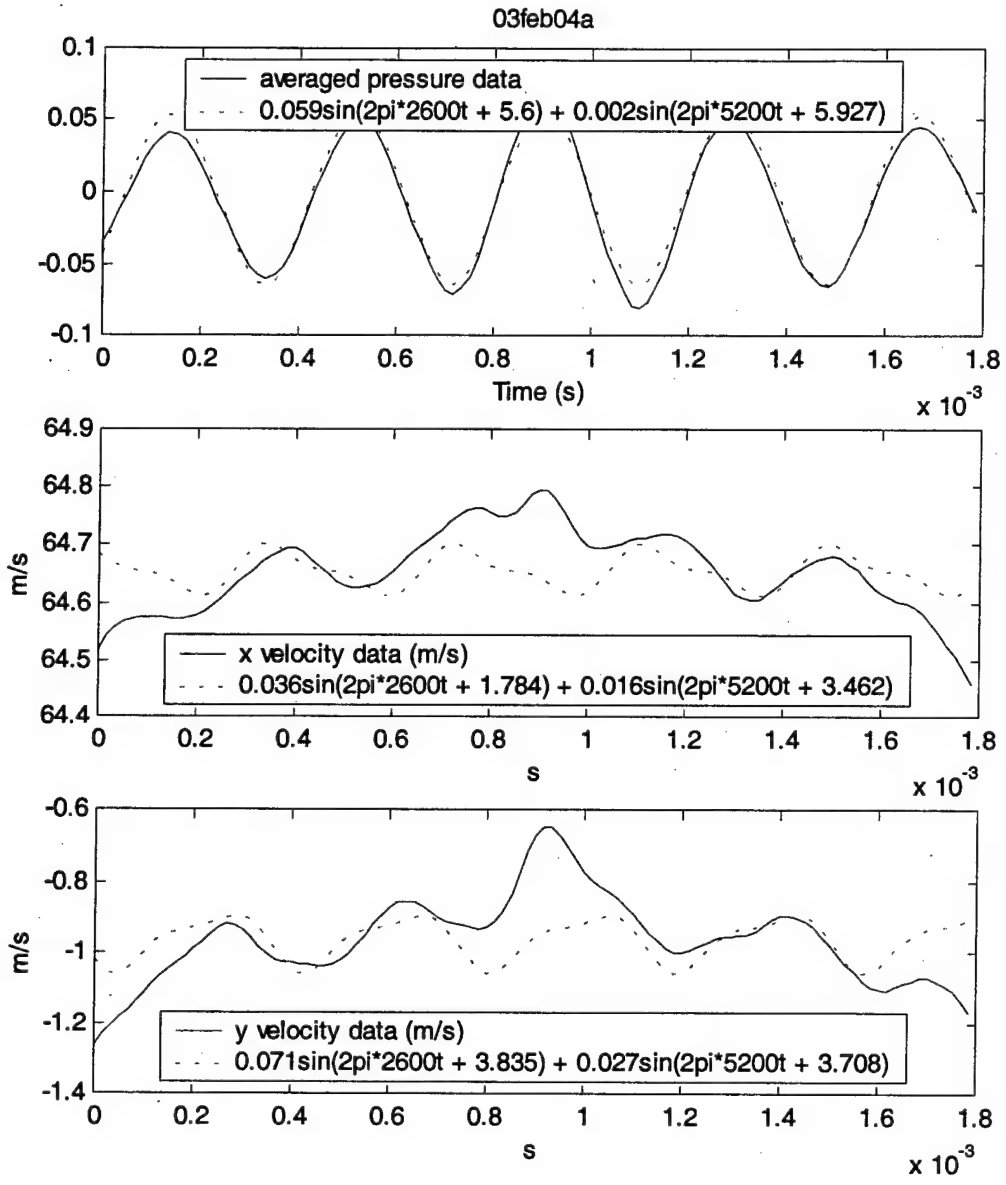

Figure 107. Data and two frequency approximation at x = -1.5 in, y = -1 in

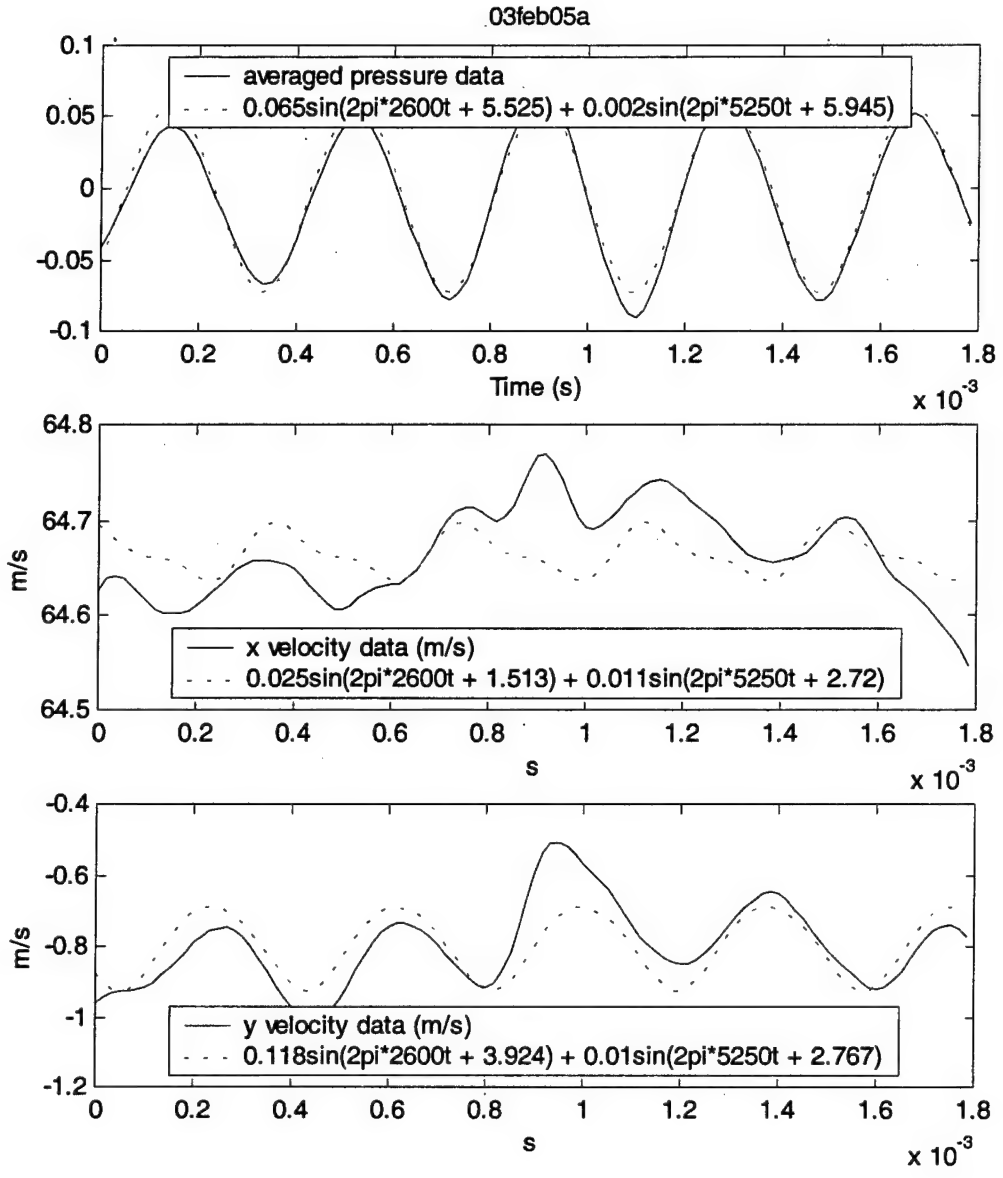

Figure 108. Data and two frequency approximation at x = -1.5 in, y = -0.875 in

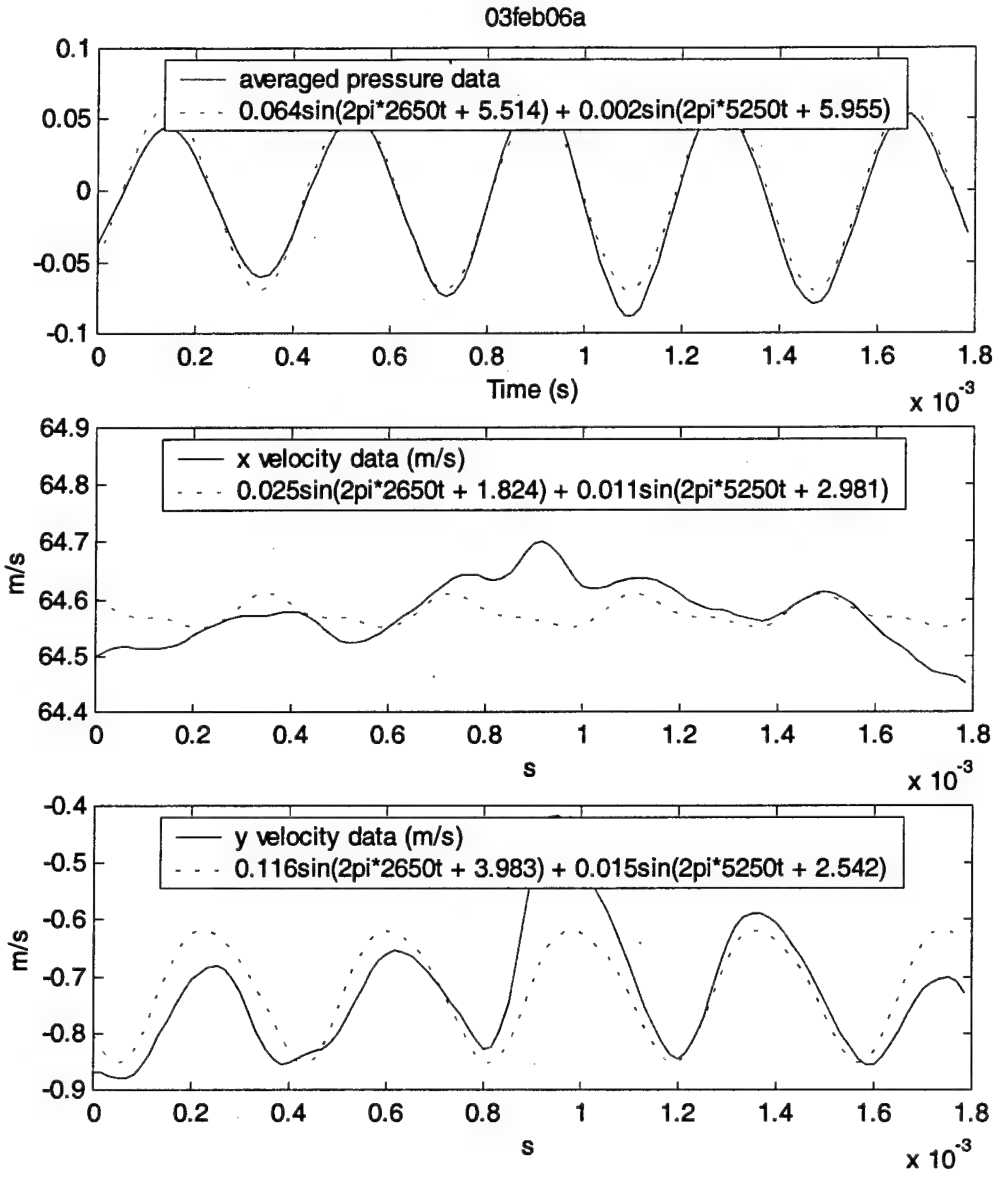

Figure 109. Data and two frequency approximation at x = -1.5 in, y = -0.75 in

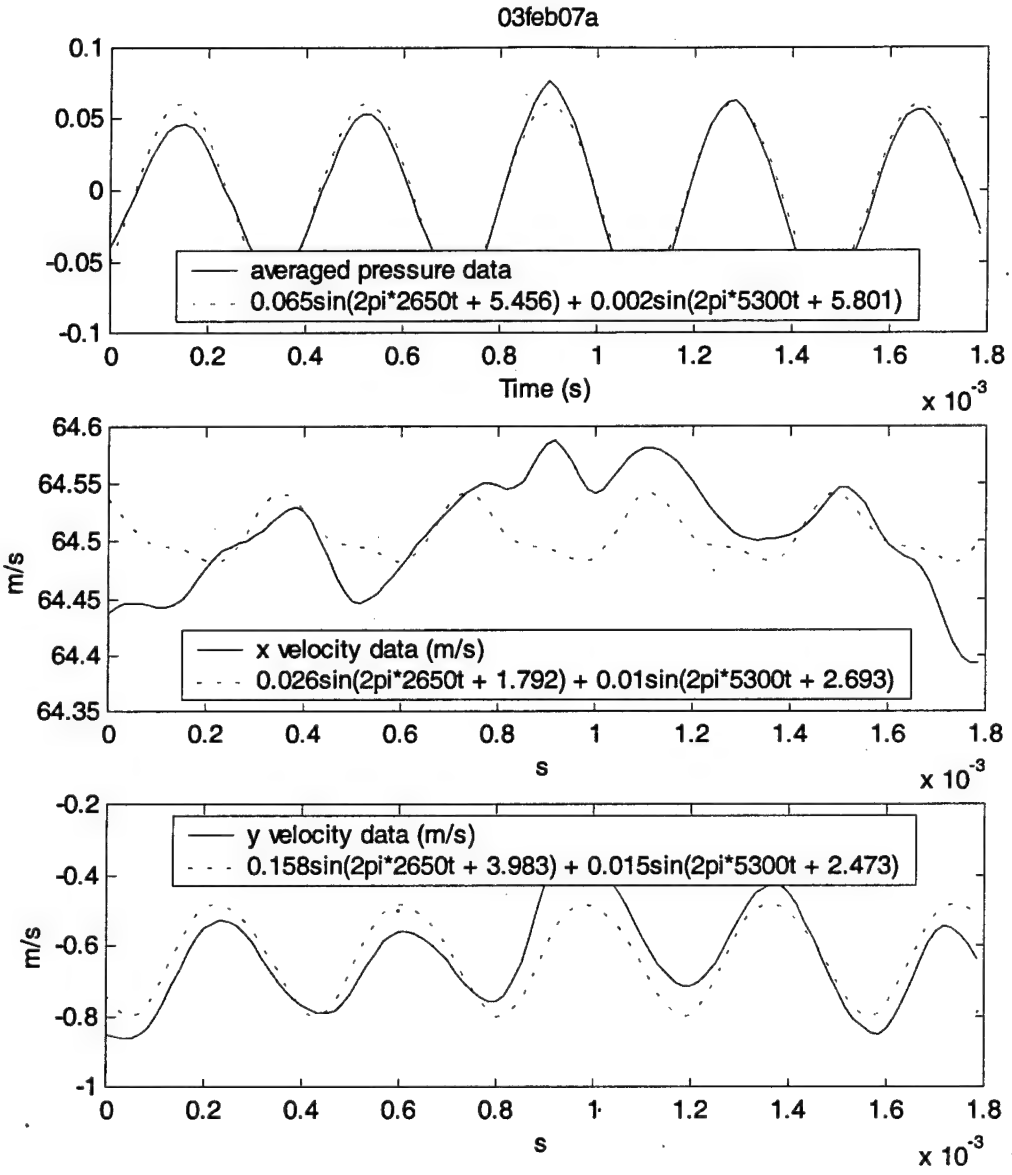

Figure 110. Data and two frequency approximation at x = -1.5 in, y = -0.625 in

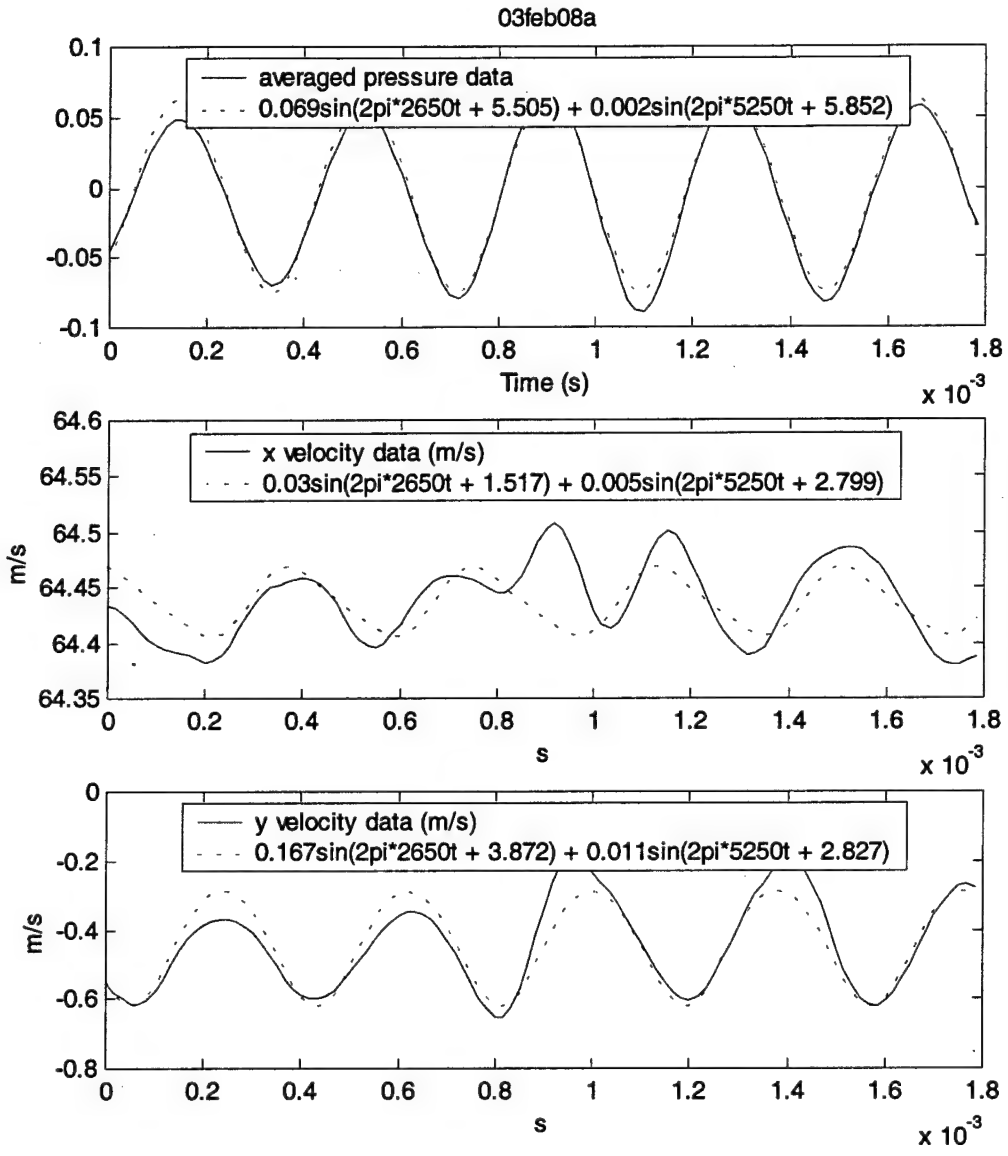

Figure 111. Data and two frequency approximation at x = -1.5 in, y = -0.5 in

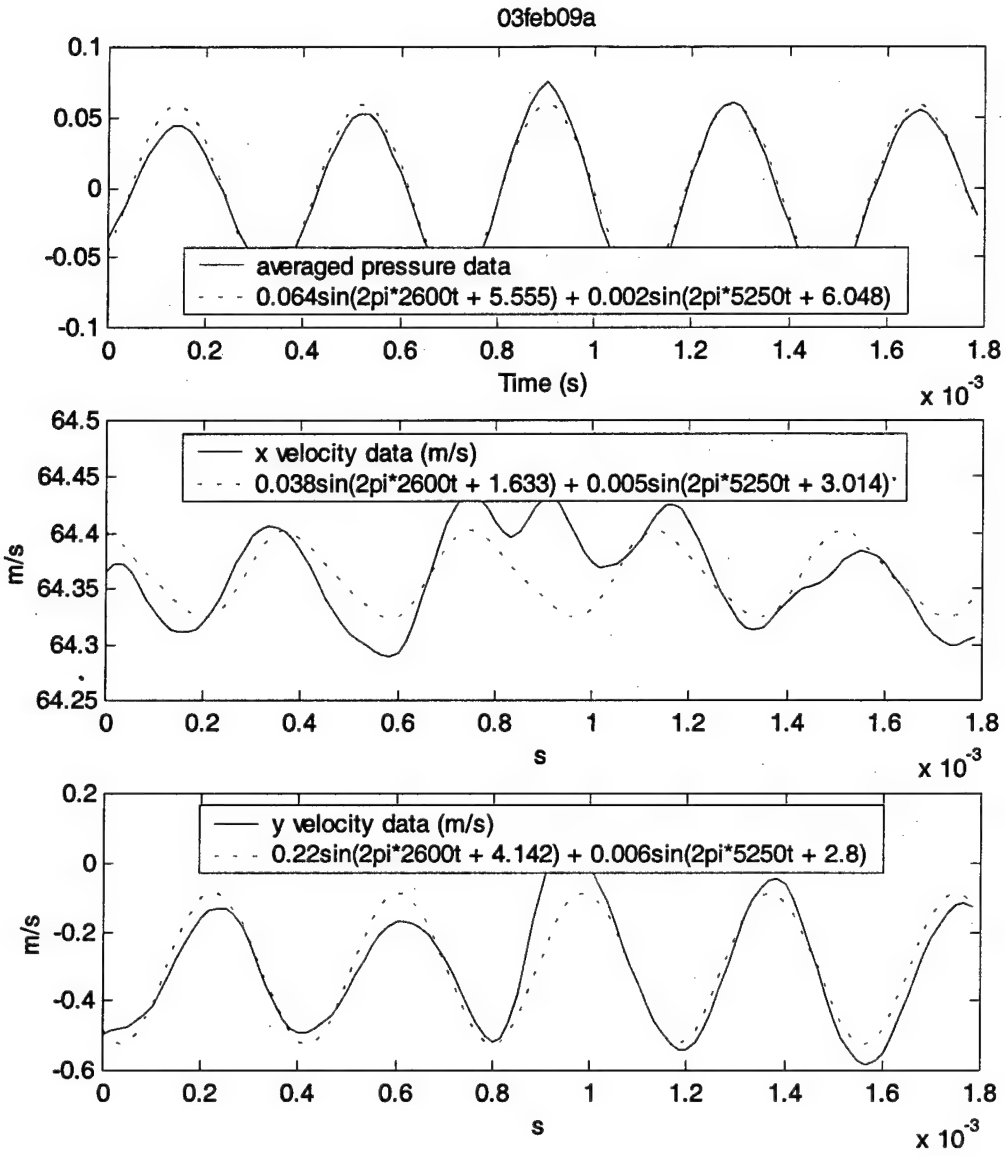

Figure 112. Data and two frequency approximation at x = -1.5 in, y = -0.375 in

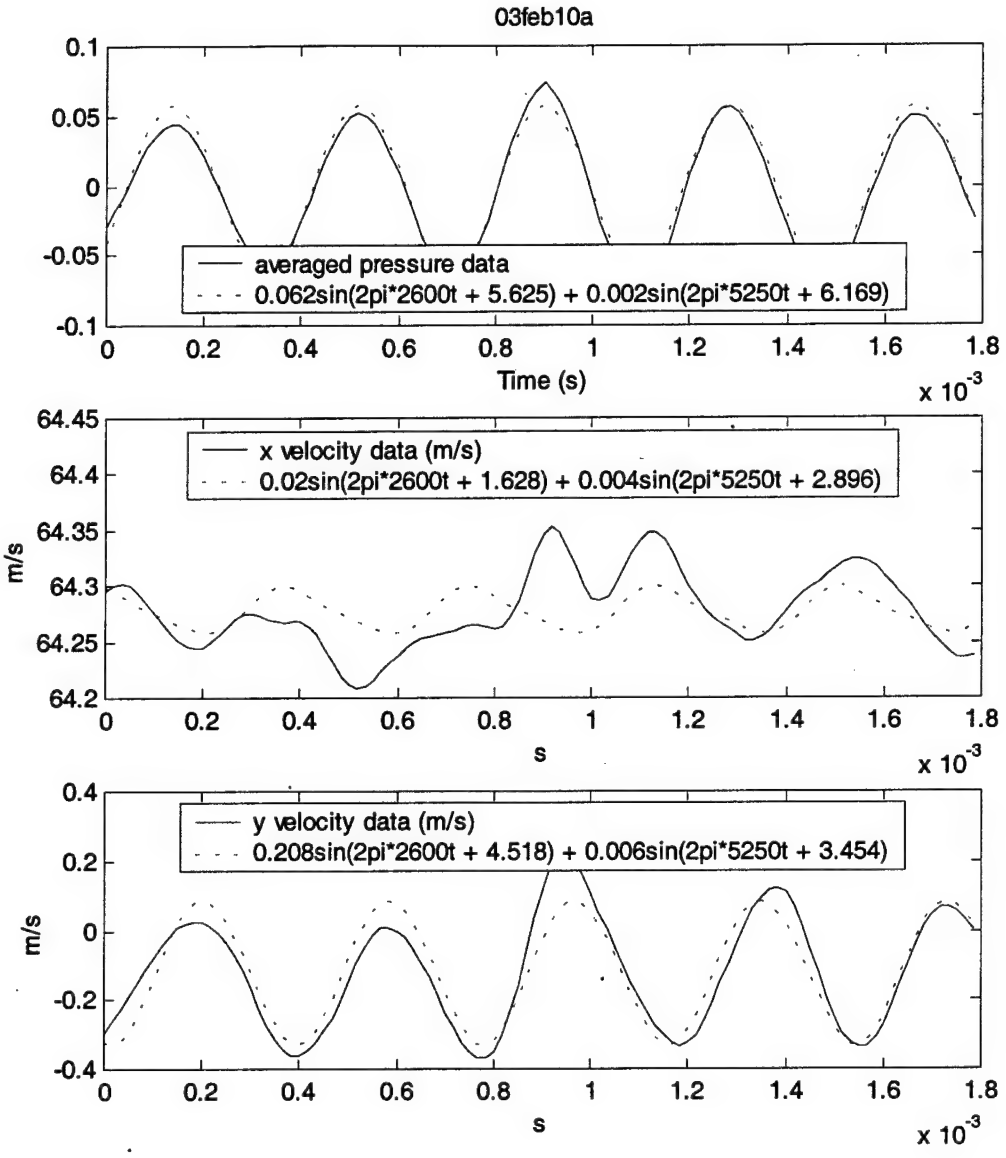

Figure 113. Data and two frequency approximation at x = -1.5 in, y = -0.25 in

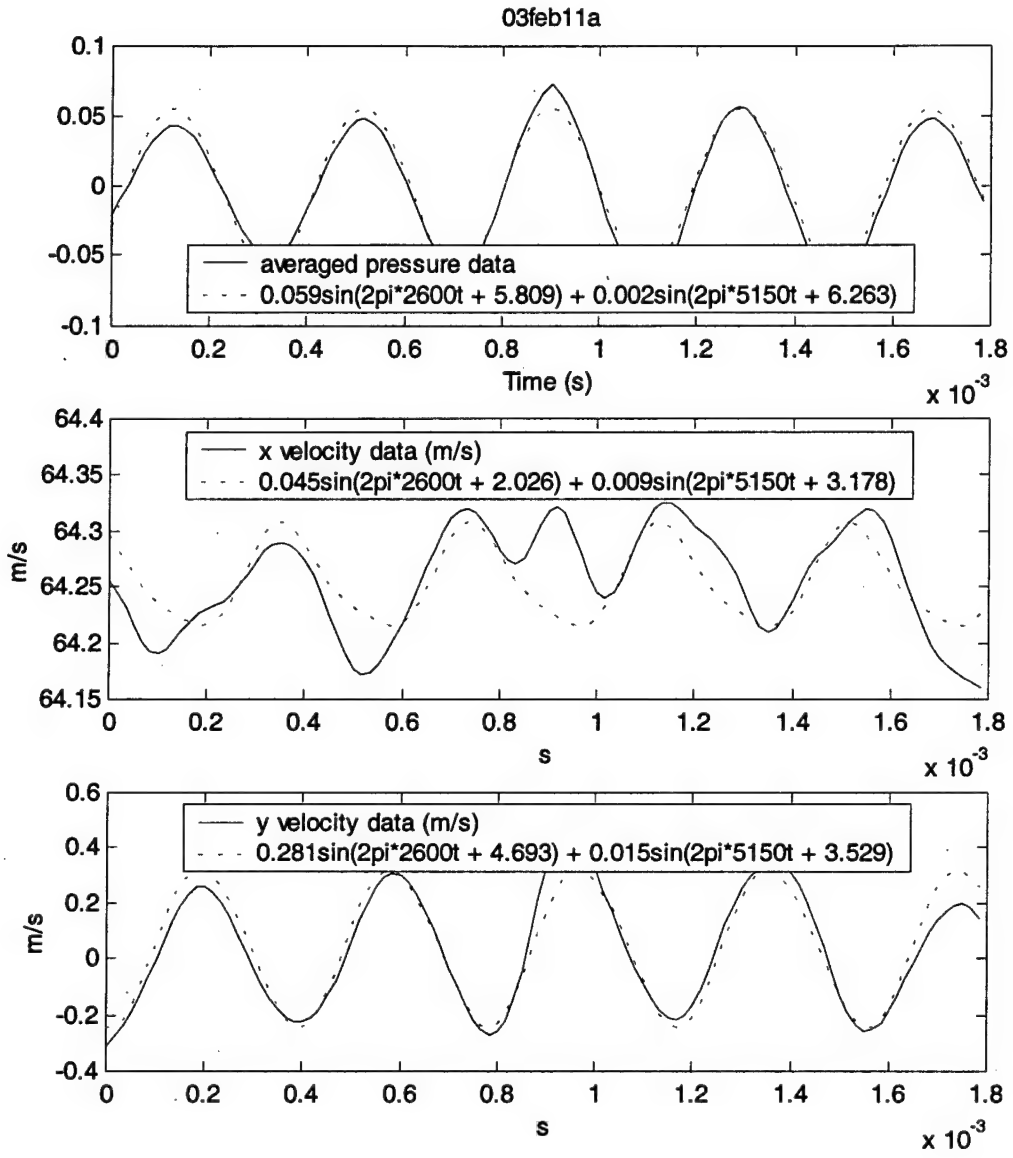

Figure 114. Data and two frequency approximation at x = -1.5 in, y = -0.125 in

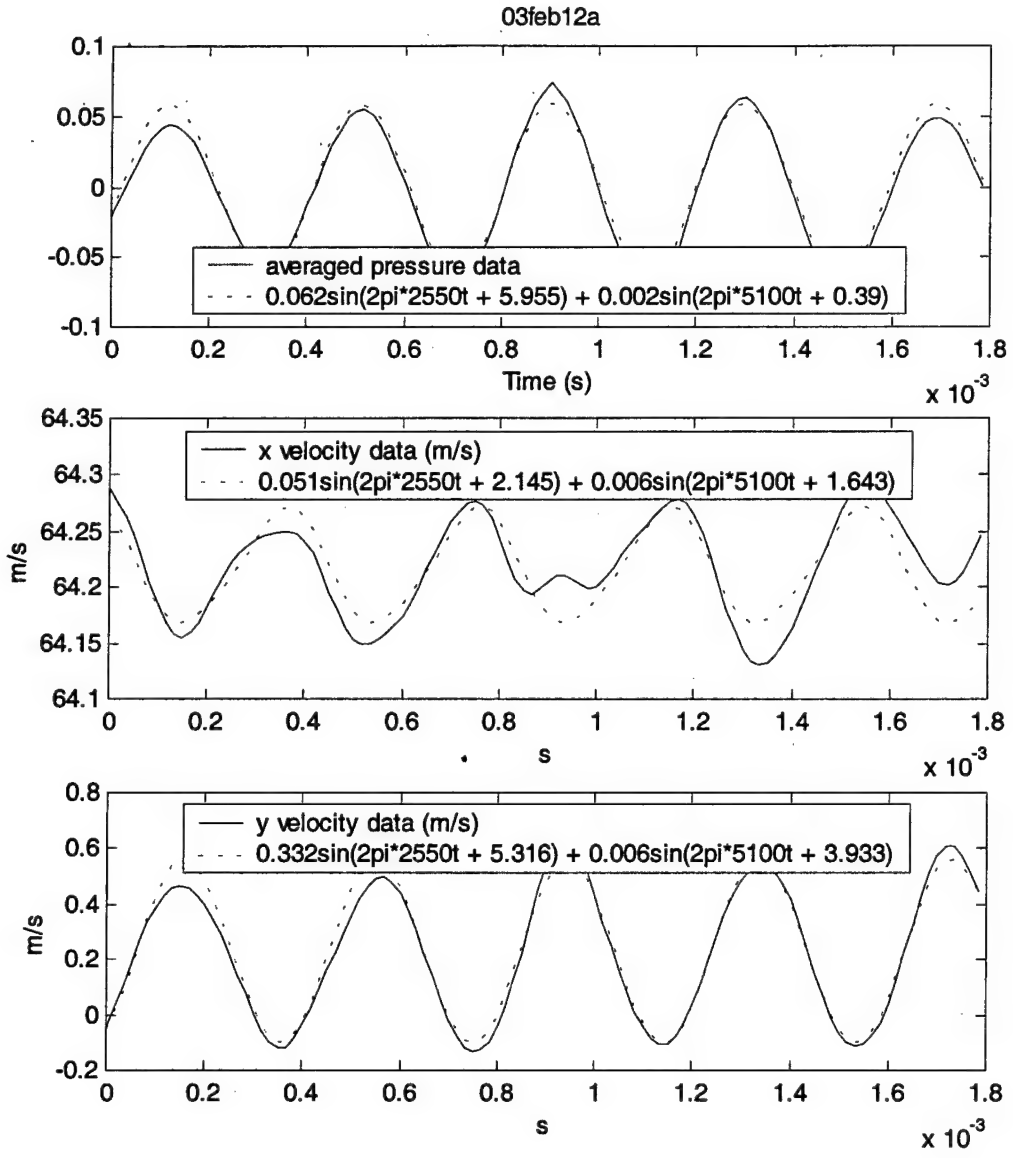

Figure 115. Data and two frequency approximation at x = -1.5 in, y = 0 in

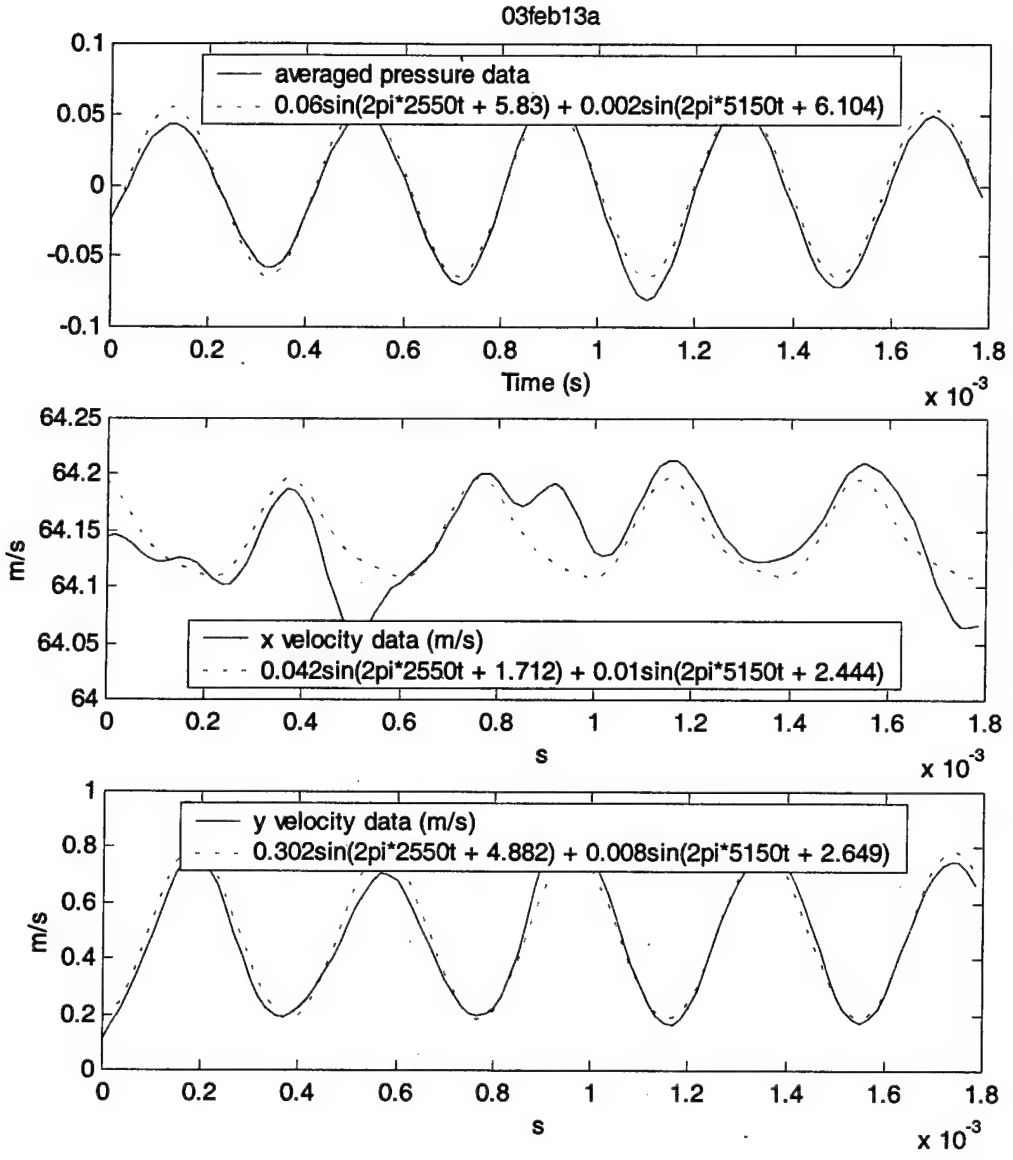

Figure 116. Data and two frequency approximation at x = -1.5 in, y = 0.125 in

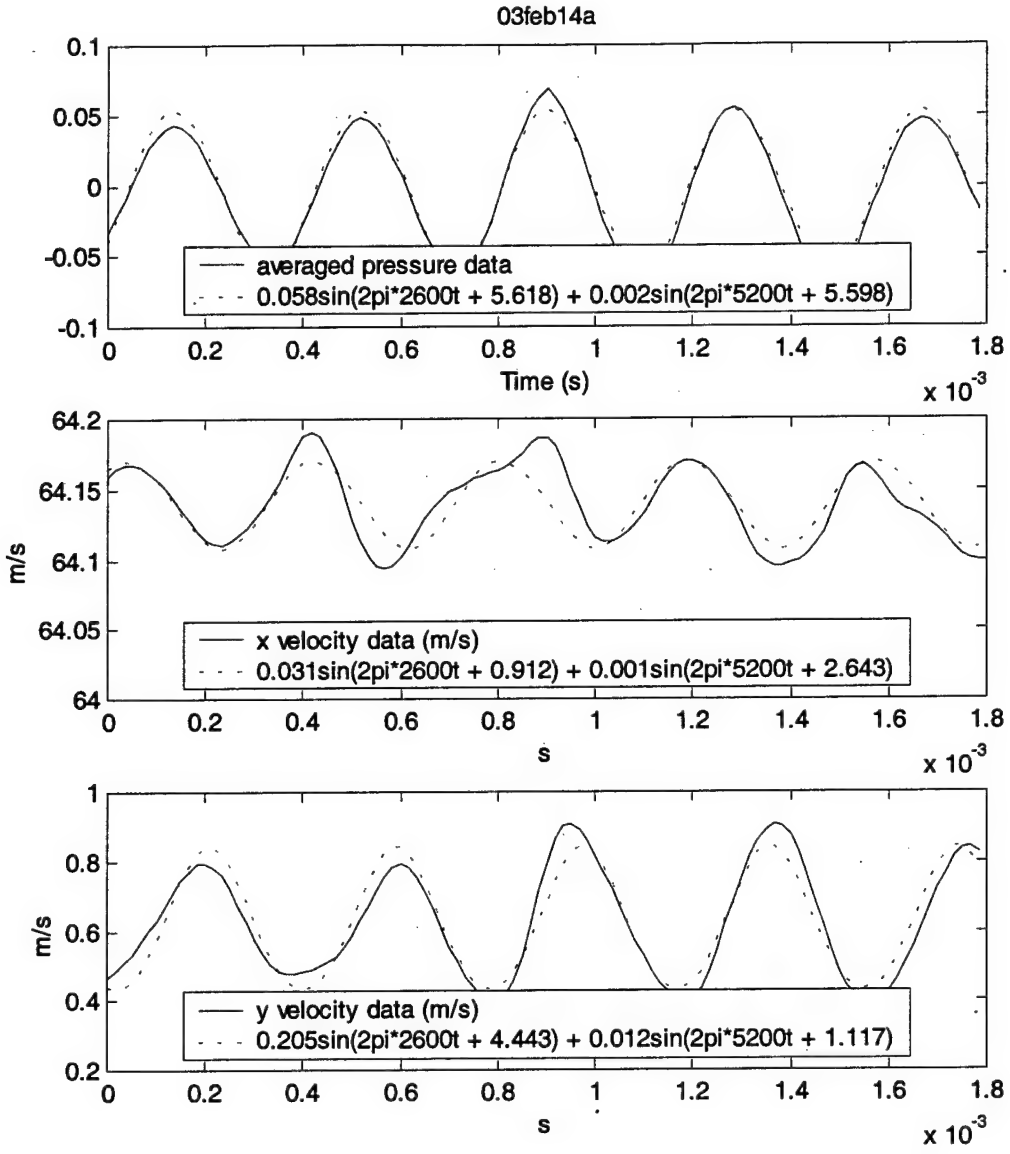

Figure 117. Data and two frequency approximation at x = -1.5 in, y = 0.25 in

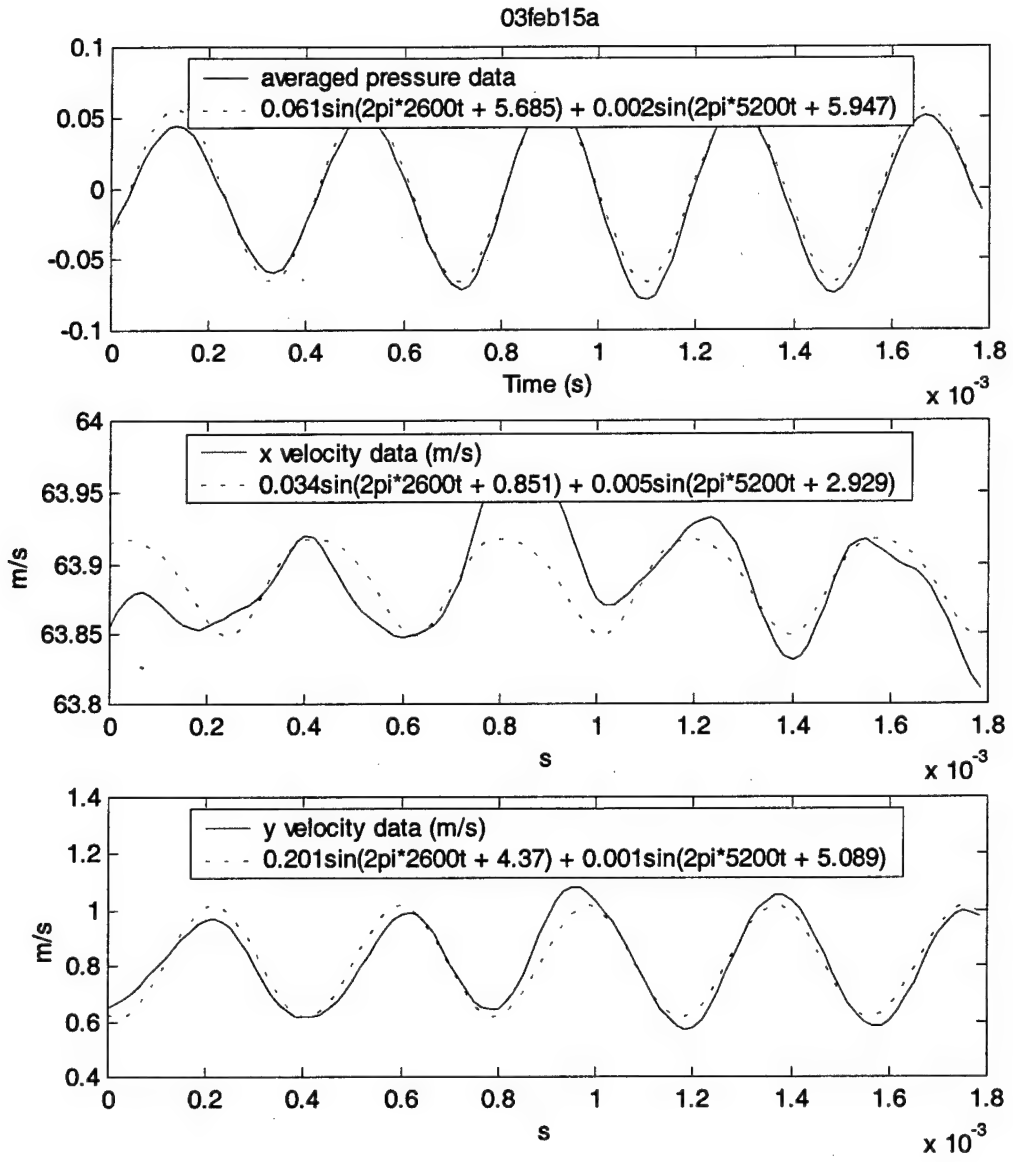

Figure 118. Data and two frequency approximation at x = -1.5 in, y = 0.375 in

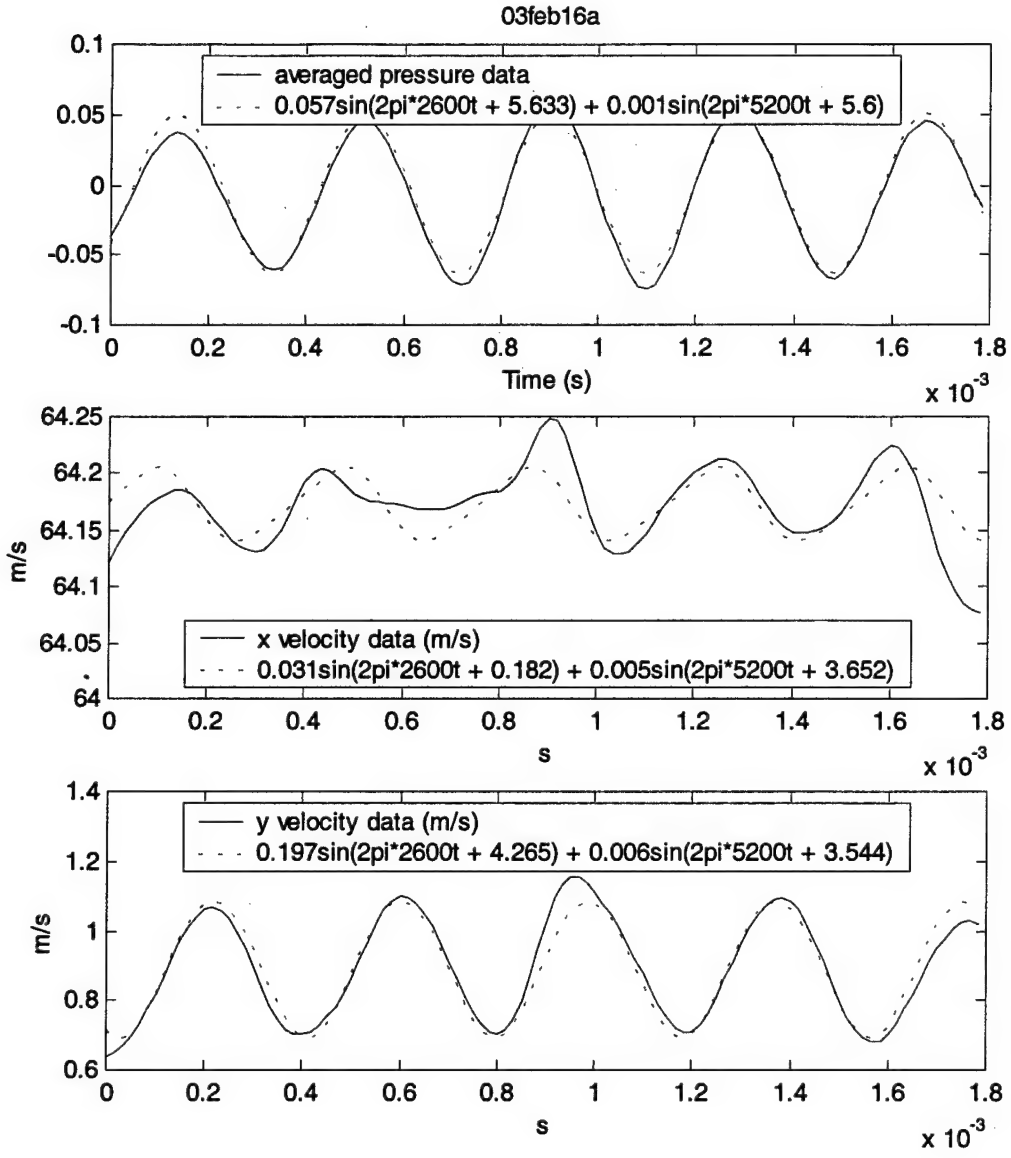

Figure 119. Data and two frequency approximation at x = -1.5 in, y = 0.5 in

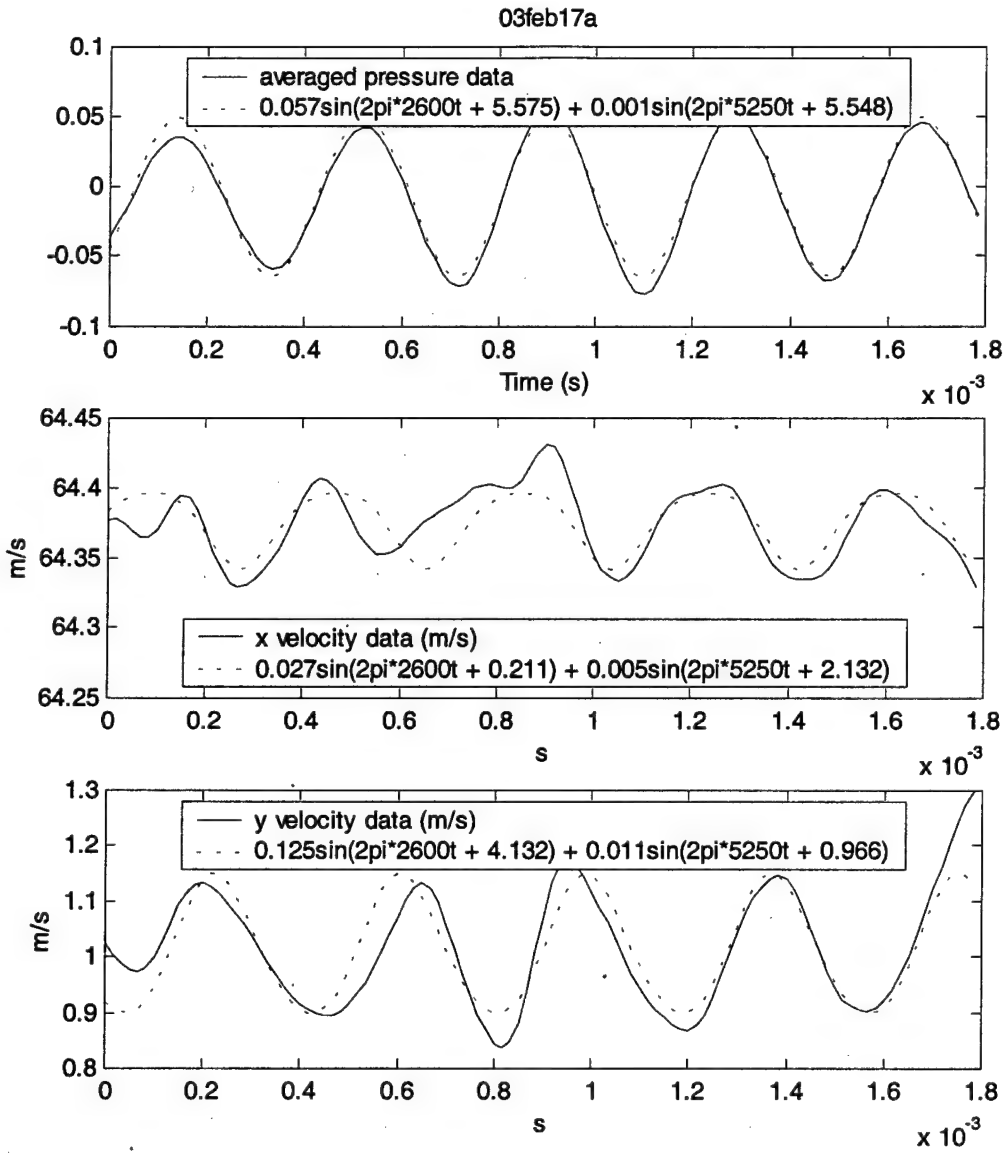

Figure 120. Data and two frequency approximation at x = -1.5 in, y = 0.625 in

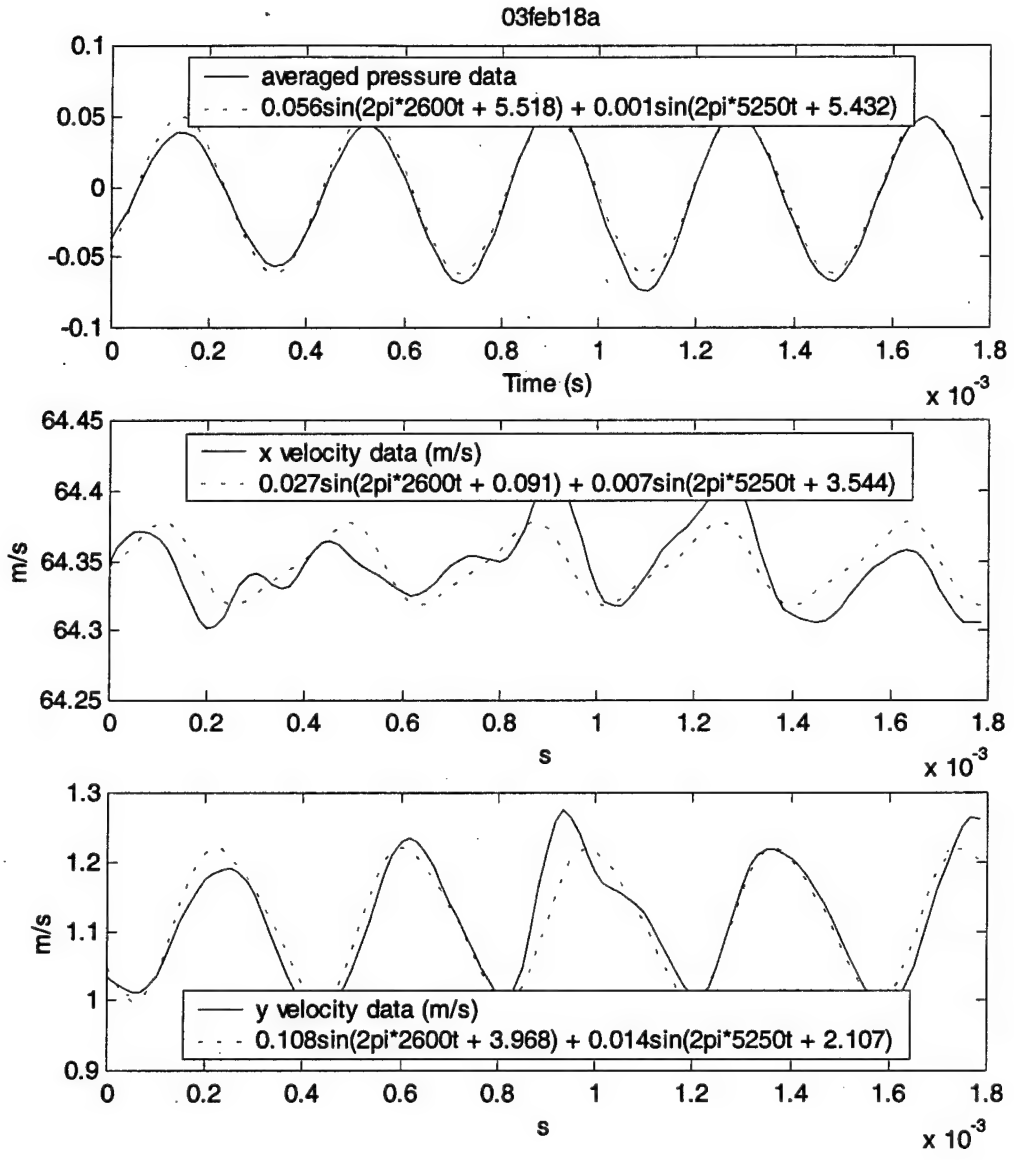

Figure 121. Data and two frequency approximation at x = -1.5 in, y = 0.75 in

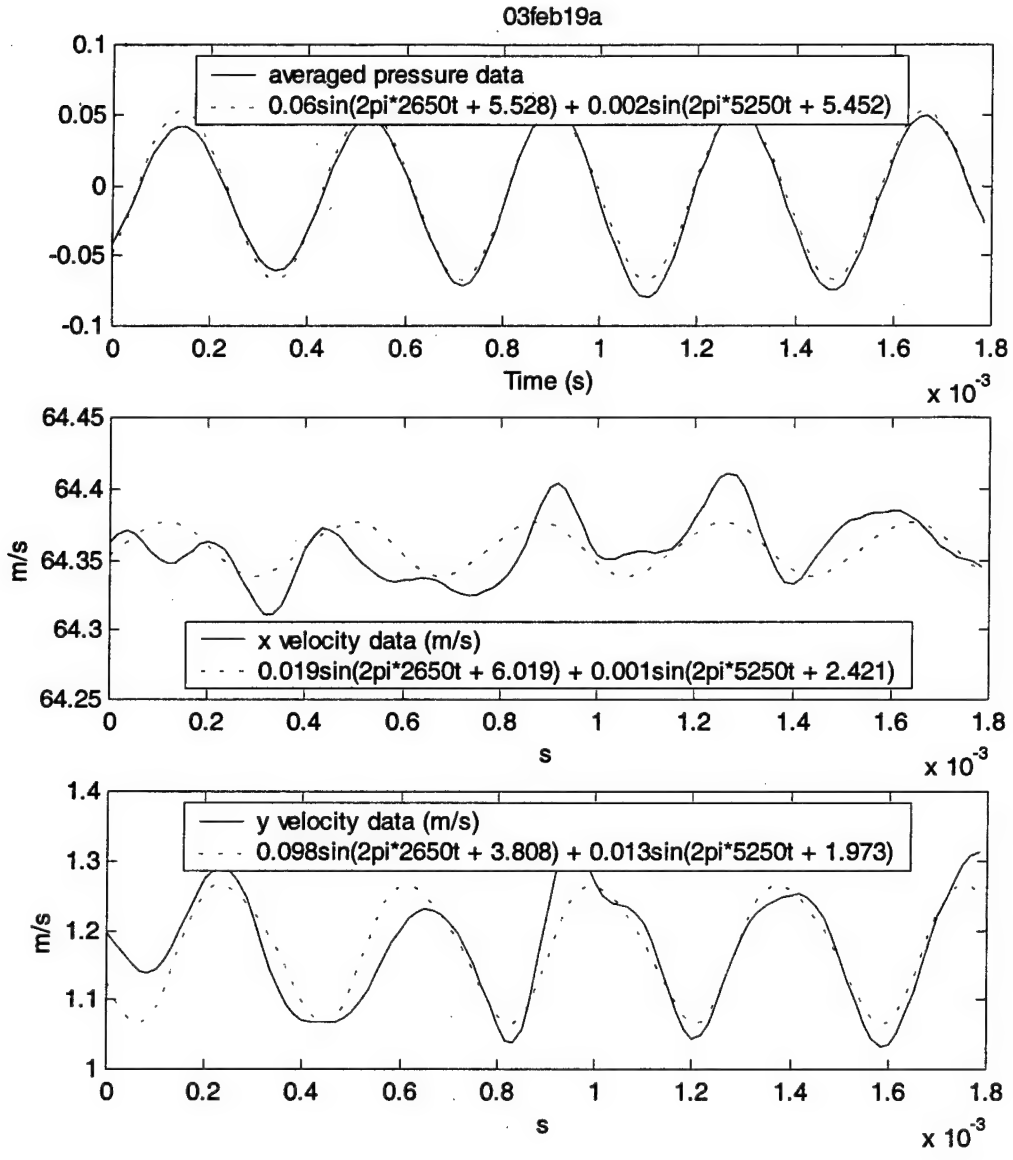

Figure 122. Data and two frequency approximation at x = -1.5 in, y = 0.875 in

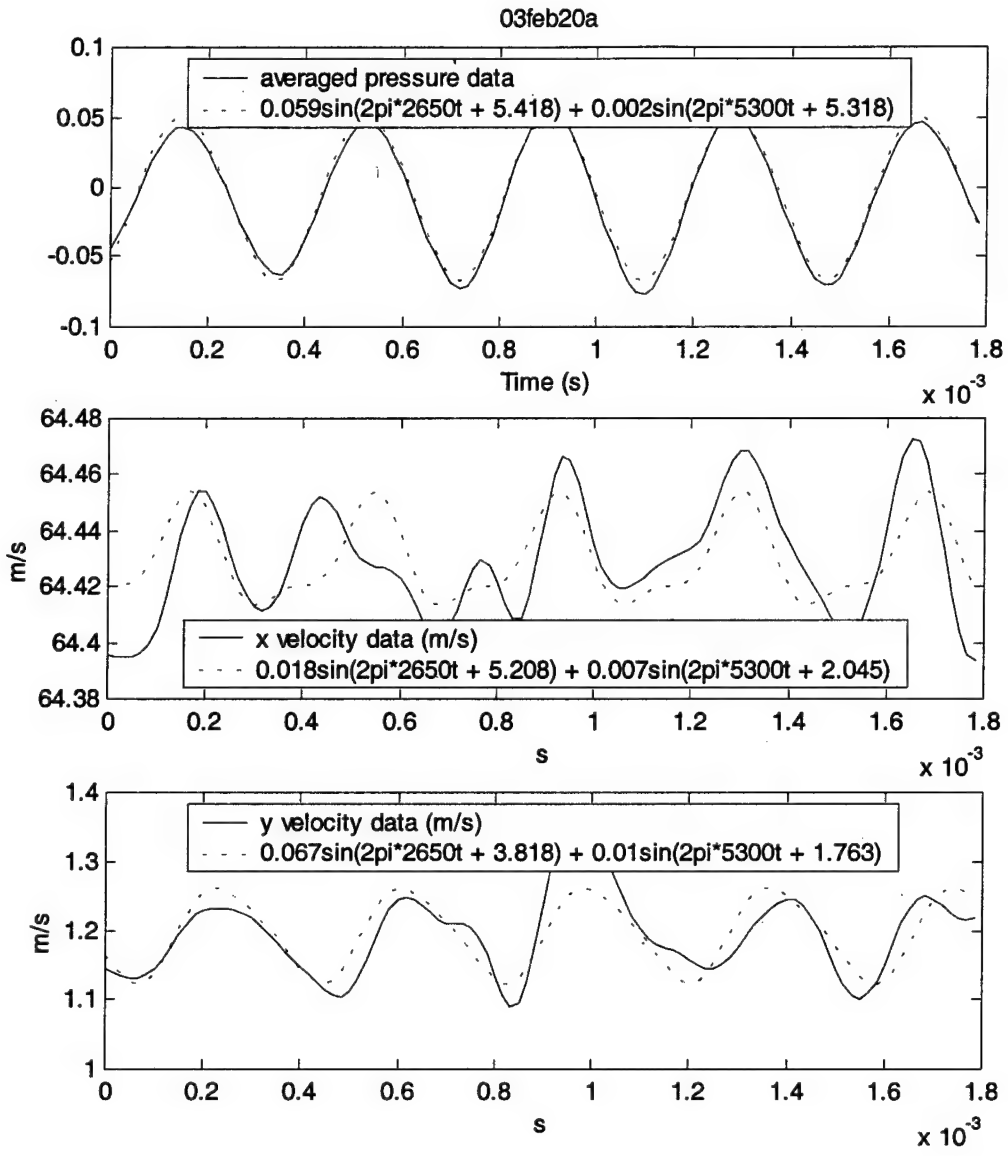

Figure 123. Data and two frequency approximation at x = -1.5 in, y = 1 in

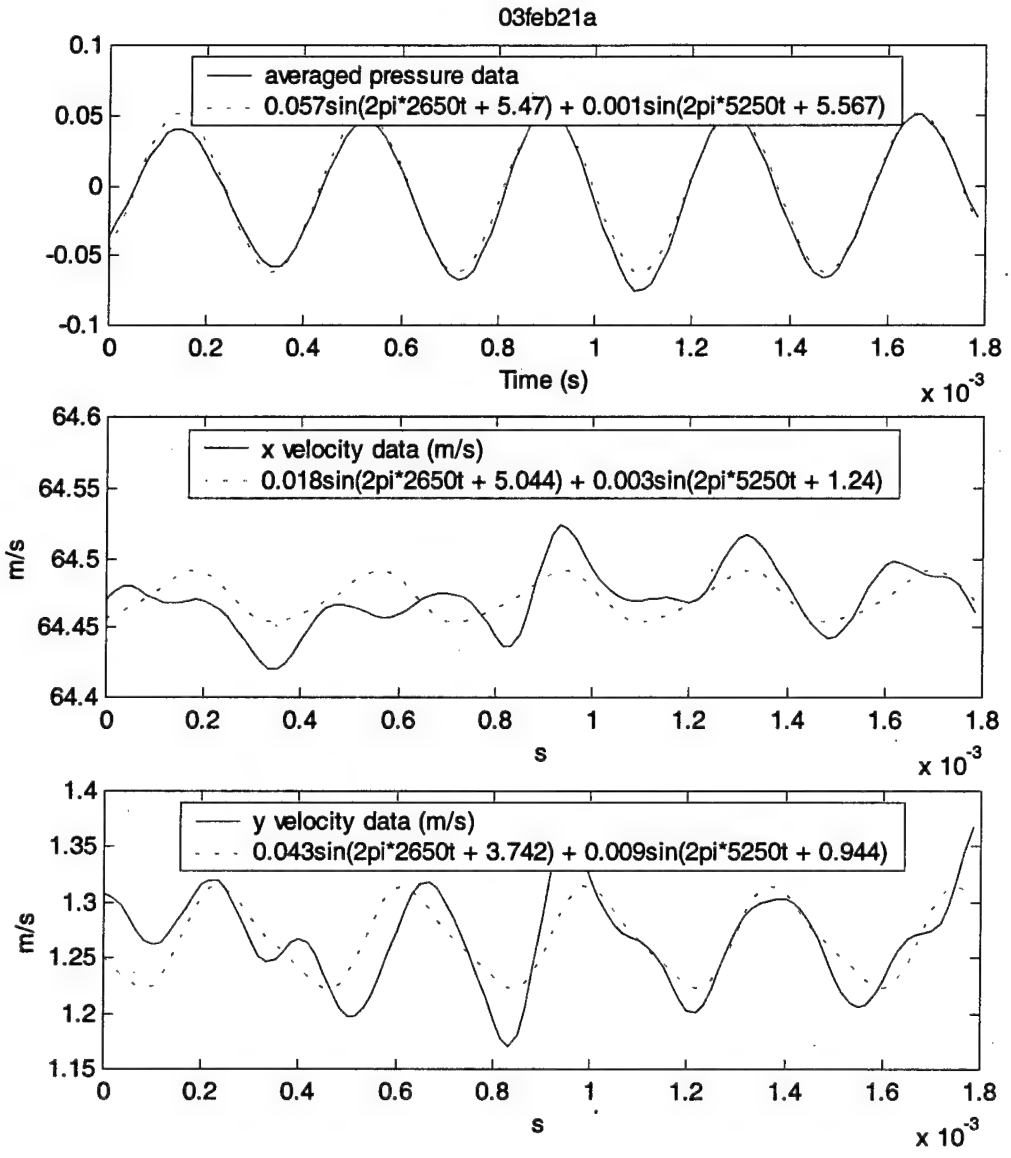

Figure 124. Data and two frequency approximation at x = -1.5 in, y = 1.25 in

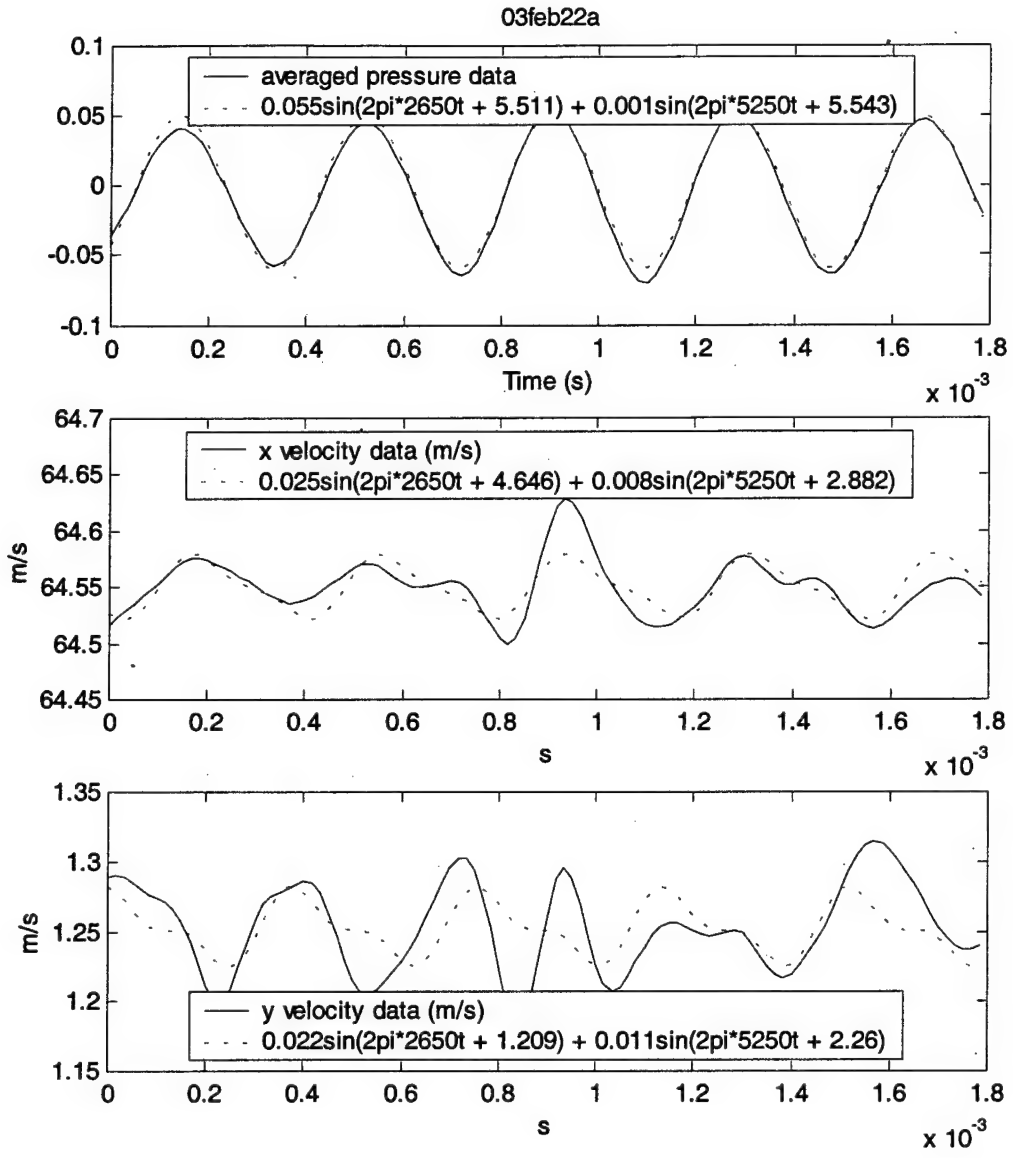

Figure 125. Data and two frequency approximation at x = -1.5 in, y = 1.5 in

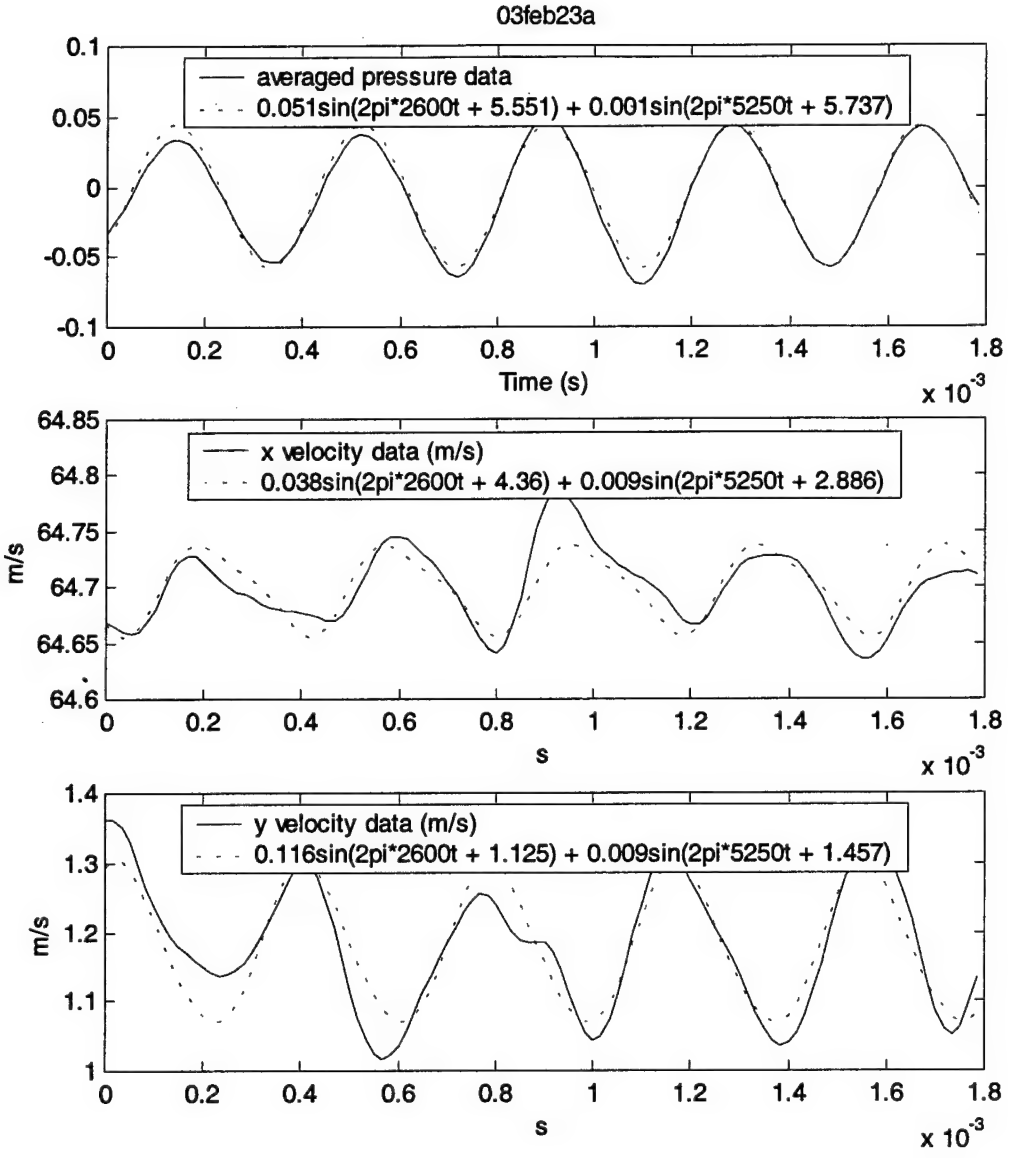

Figure 126. Data and two frequency approximation at x = -1.5 in, y = 2 in

3. Data at x = -1.75 in

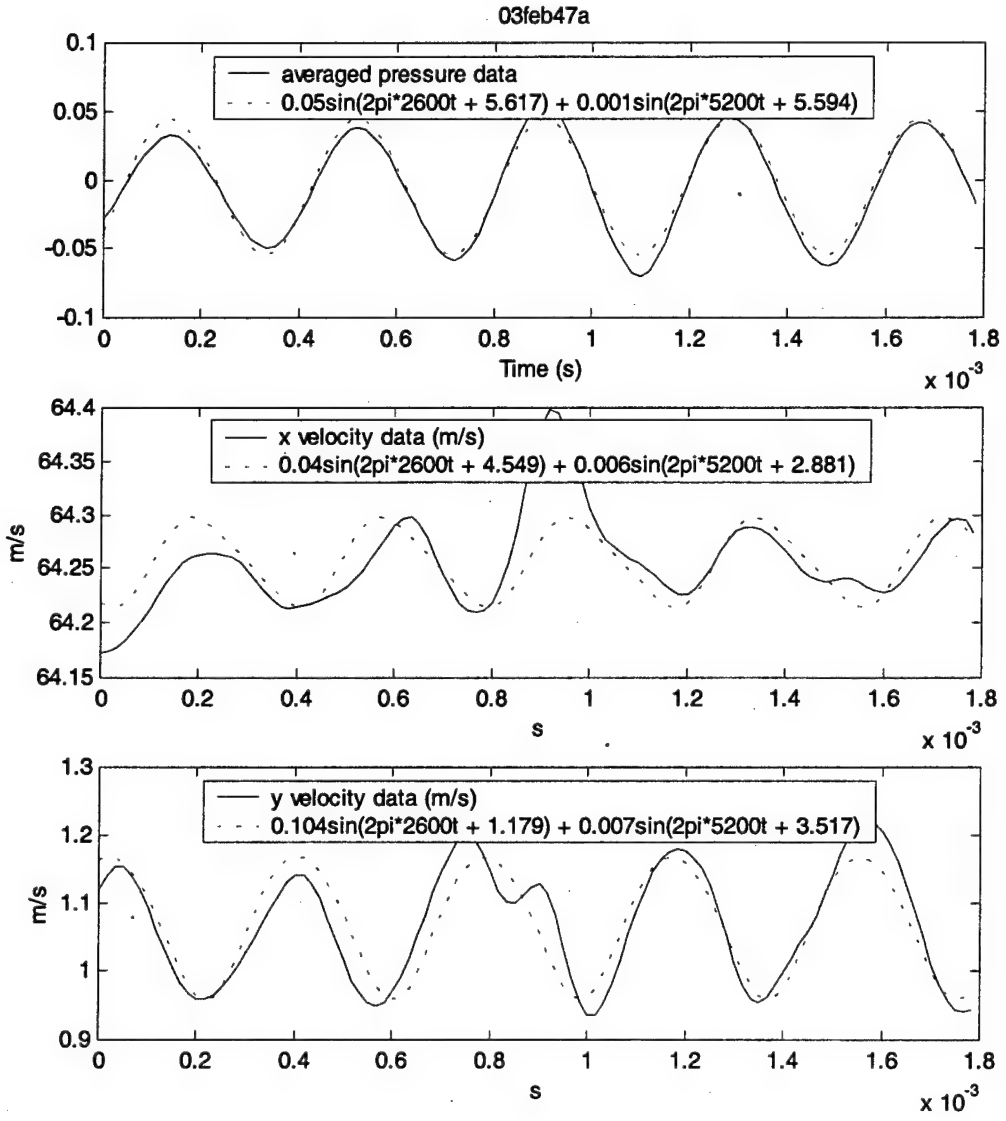

Figure 127. Data and two frequency approximation at x = -1.75 in, y = 2 in

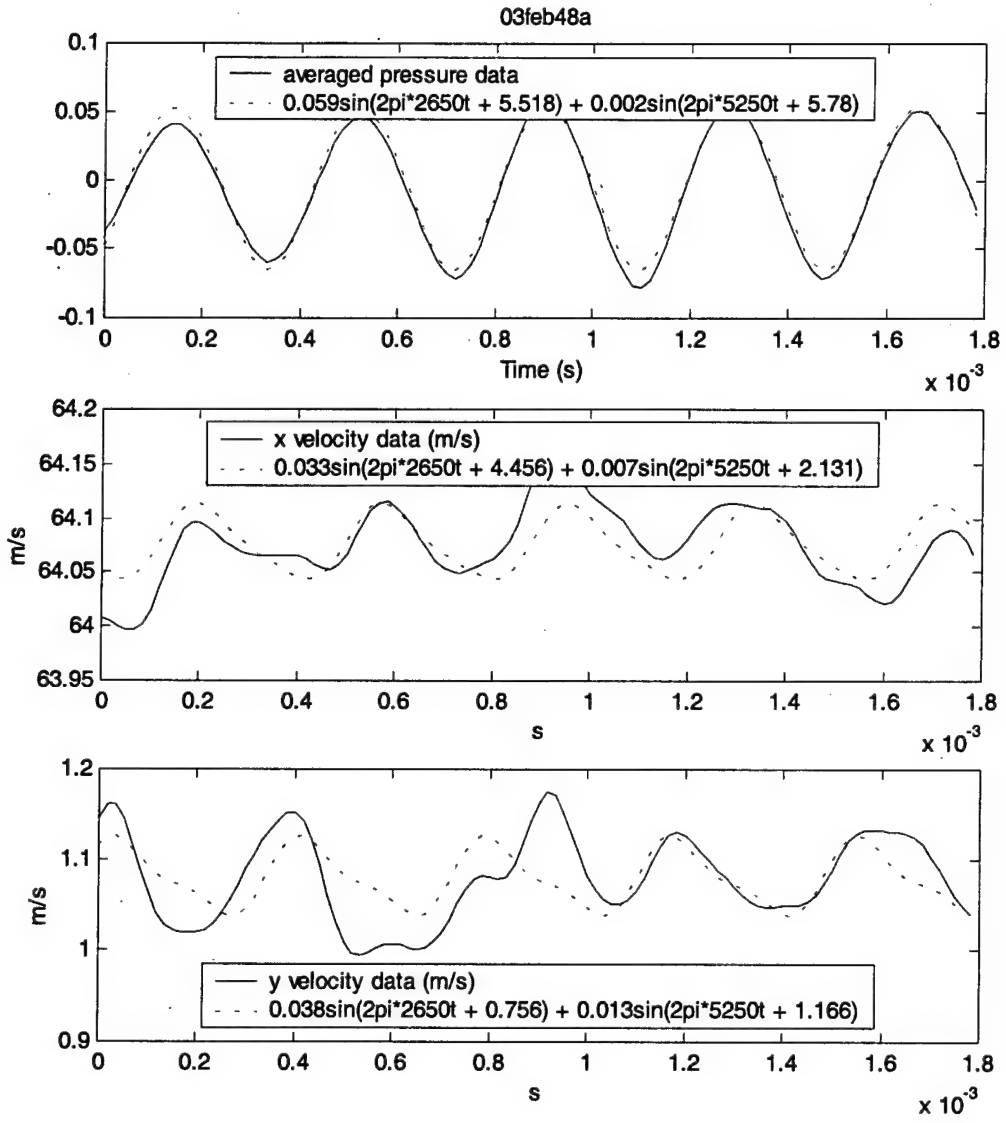

Figure 128. Data and two frequency approximation at x = -1.75 in, y = 1.5 in

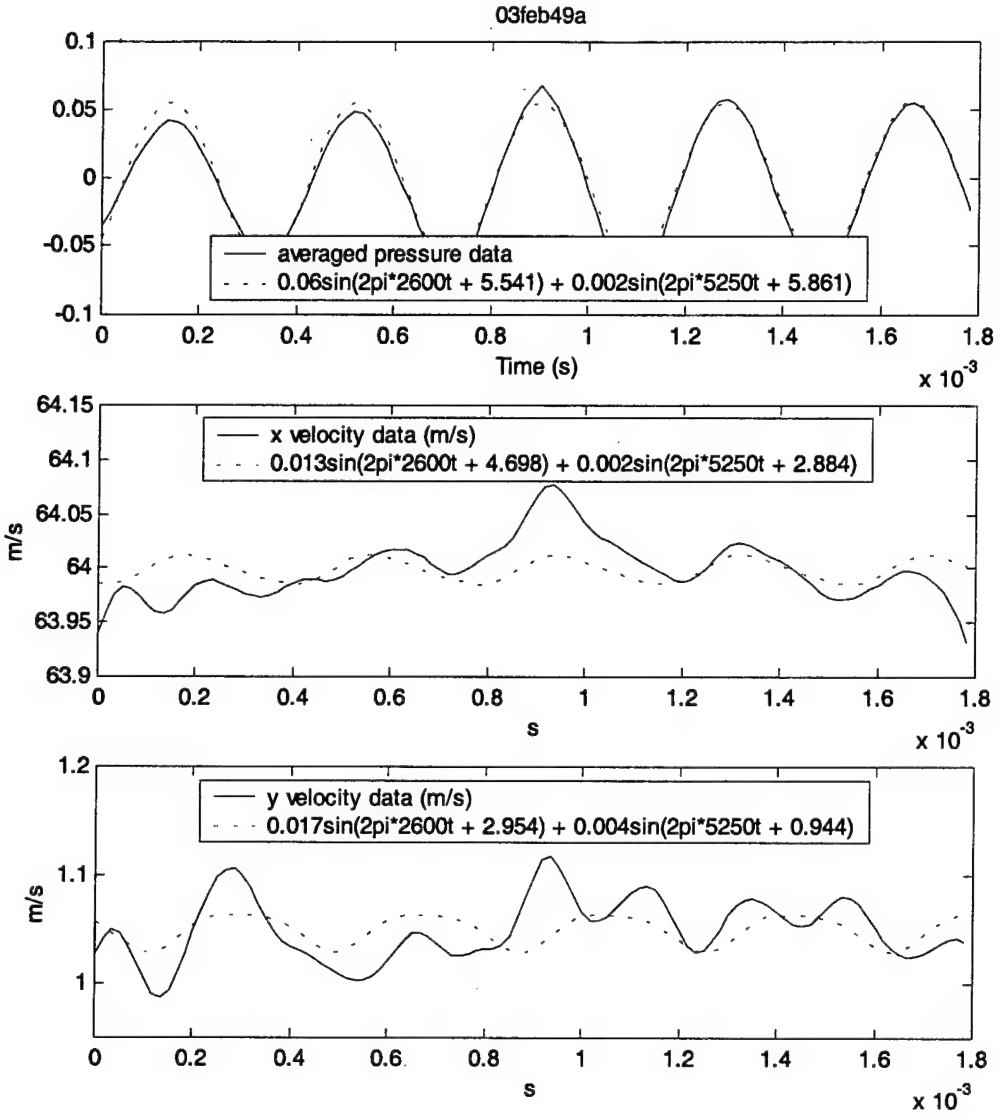

Figure 129. Data and two frequency approximation at x = -1.75 in, y = 1.25 in

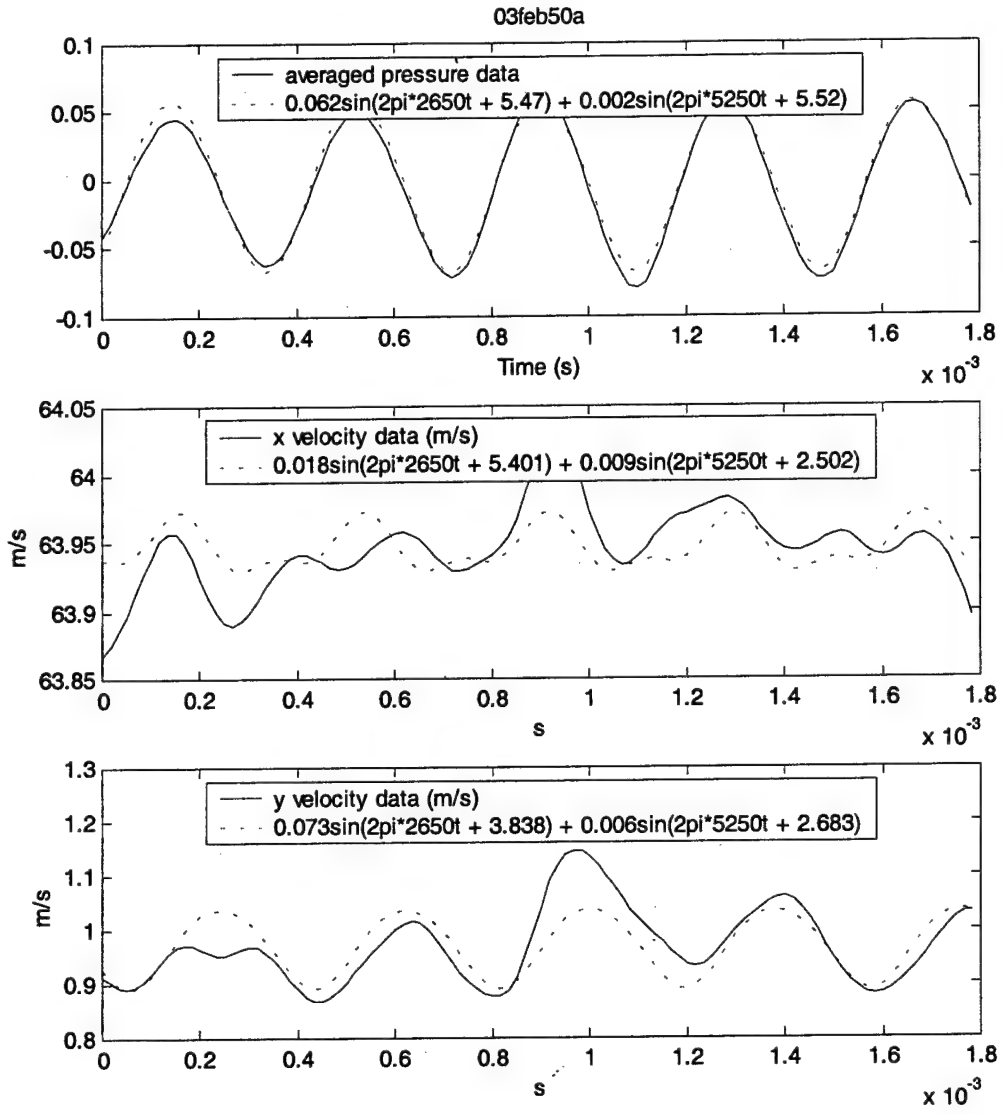

Figure 130. Data and two frequency approximation at x = -1.75 in, y = 1 in

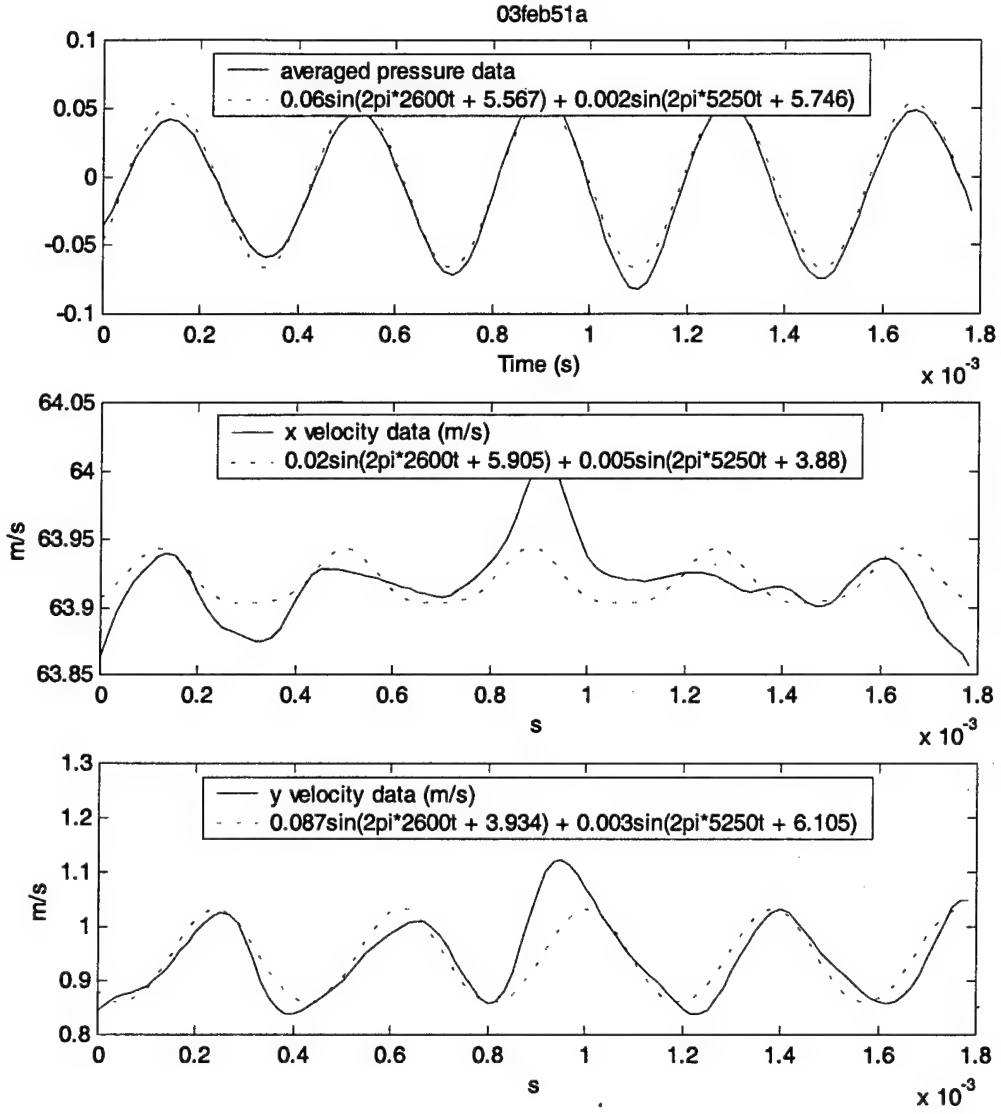

Figure 131. Data and two frequency approximation at x = -1.75 in, y = 0.875 in

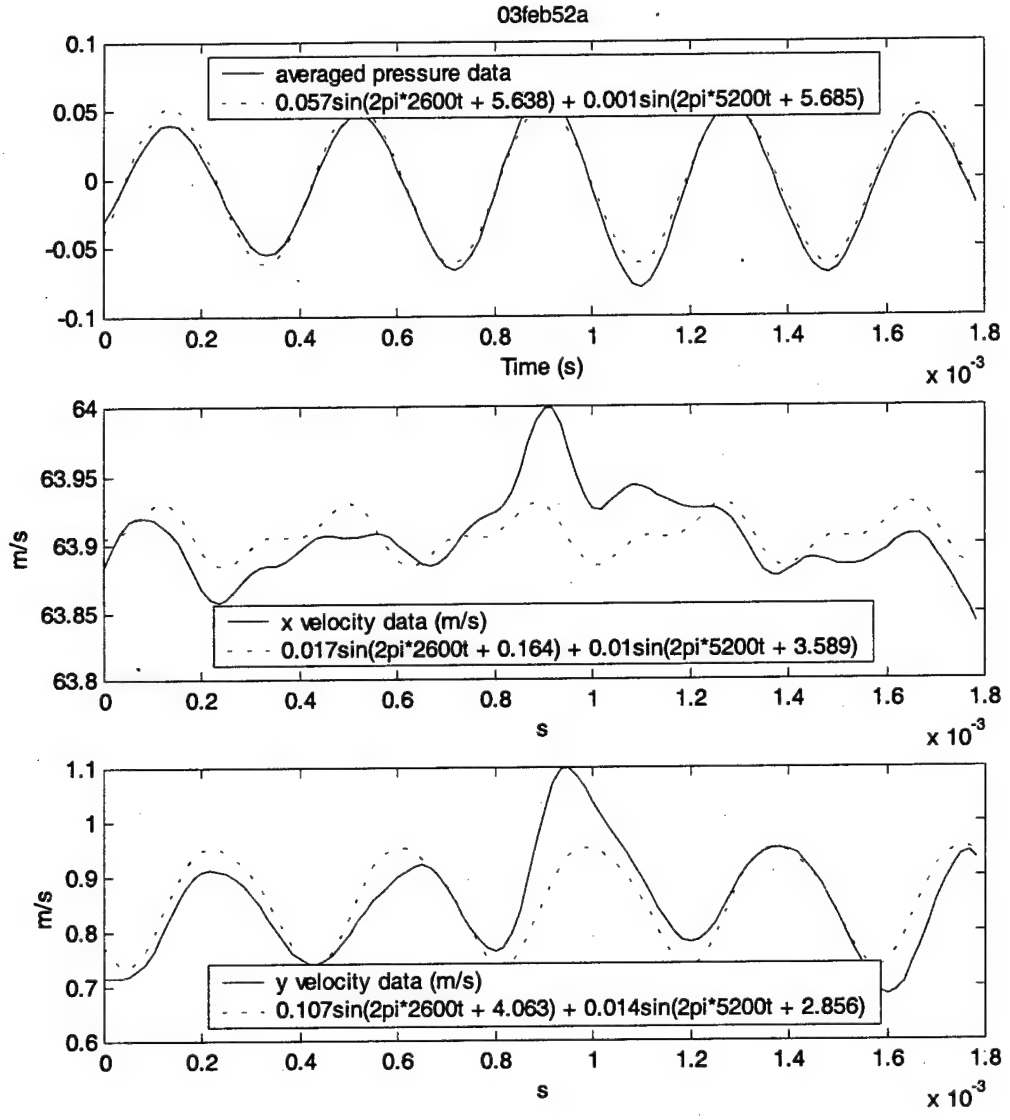

Figure 132. Data and two frequency approximation at x = -1.75 in, y = 0.75 in

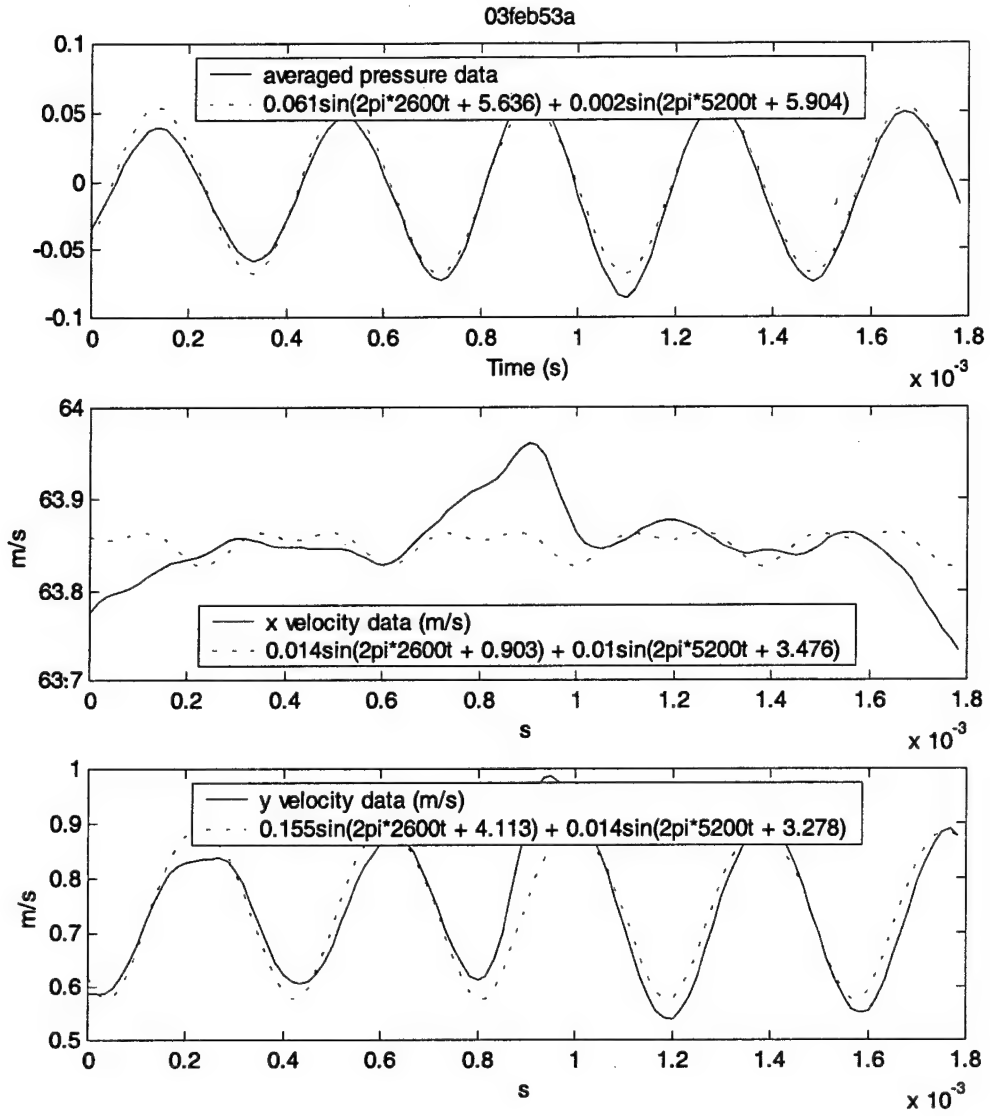

Figure 133. Data and two frequency approximation at x = -1.75 in, y = 0.625 in

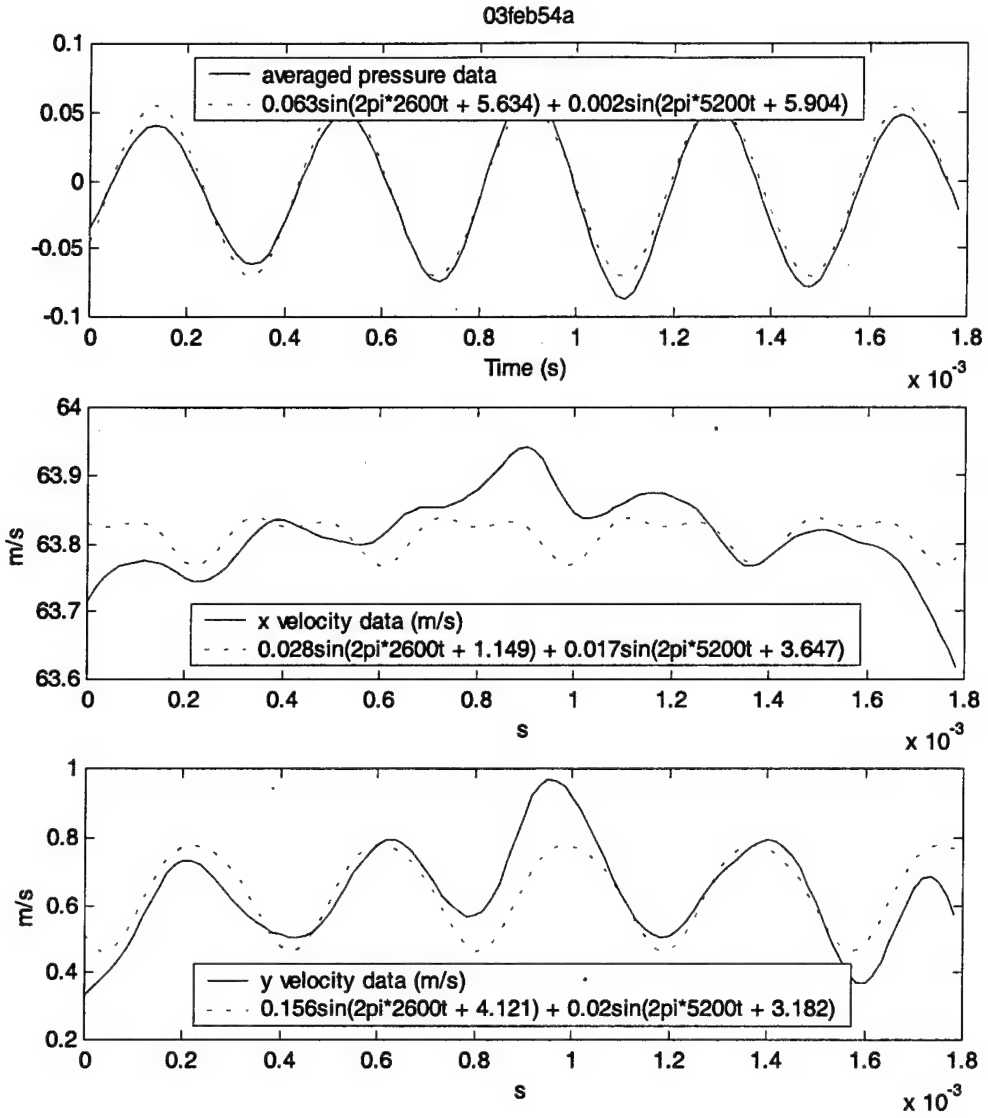

Figure 134. Data and two frequency approximation at x = -1.75 in, y = 0.5 in

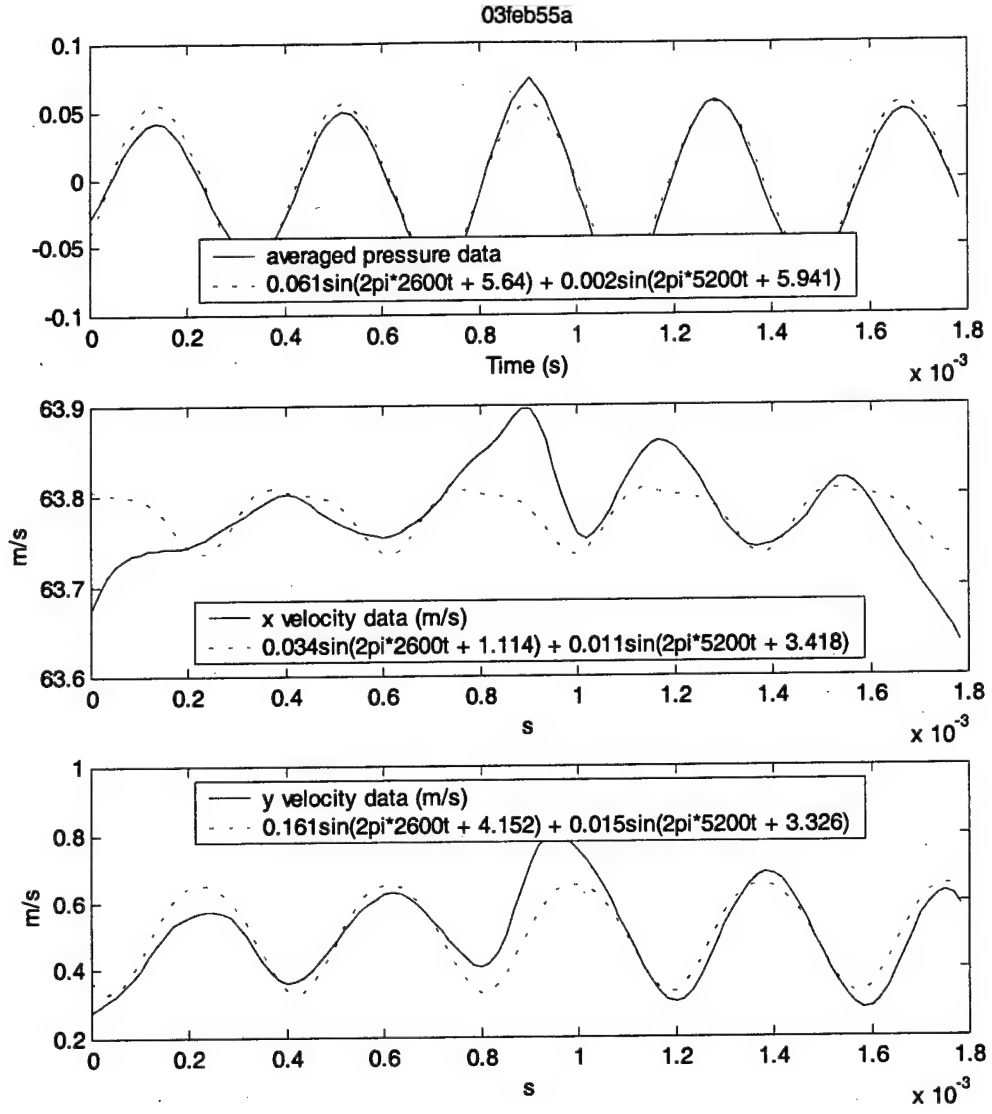

Figure 135. Data and two frequency approximation at x = -1.75 in, y = 0.375 in

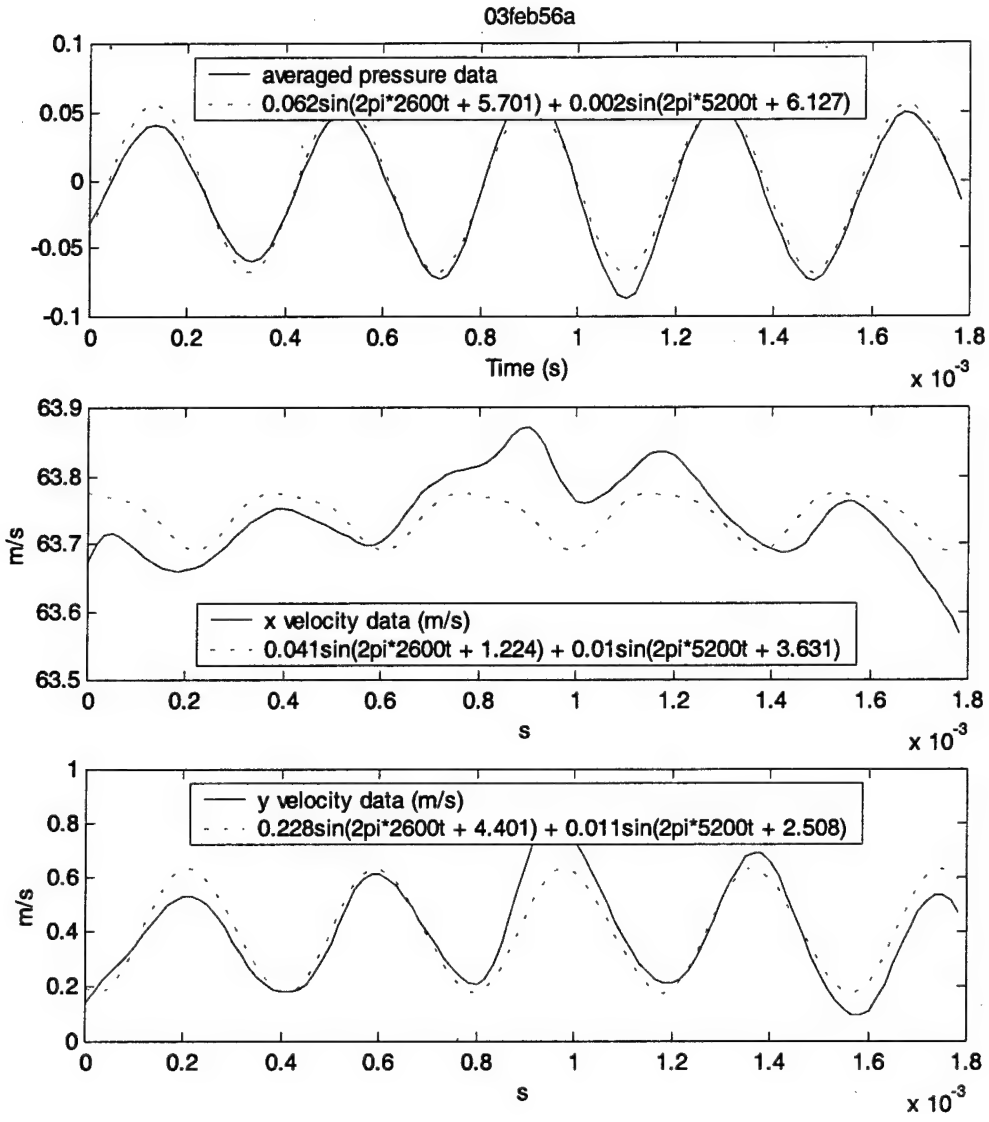

Figure 136. Data and two frequency approximation at x = -1.75 in, y = 0.25 in

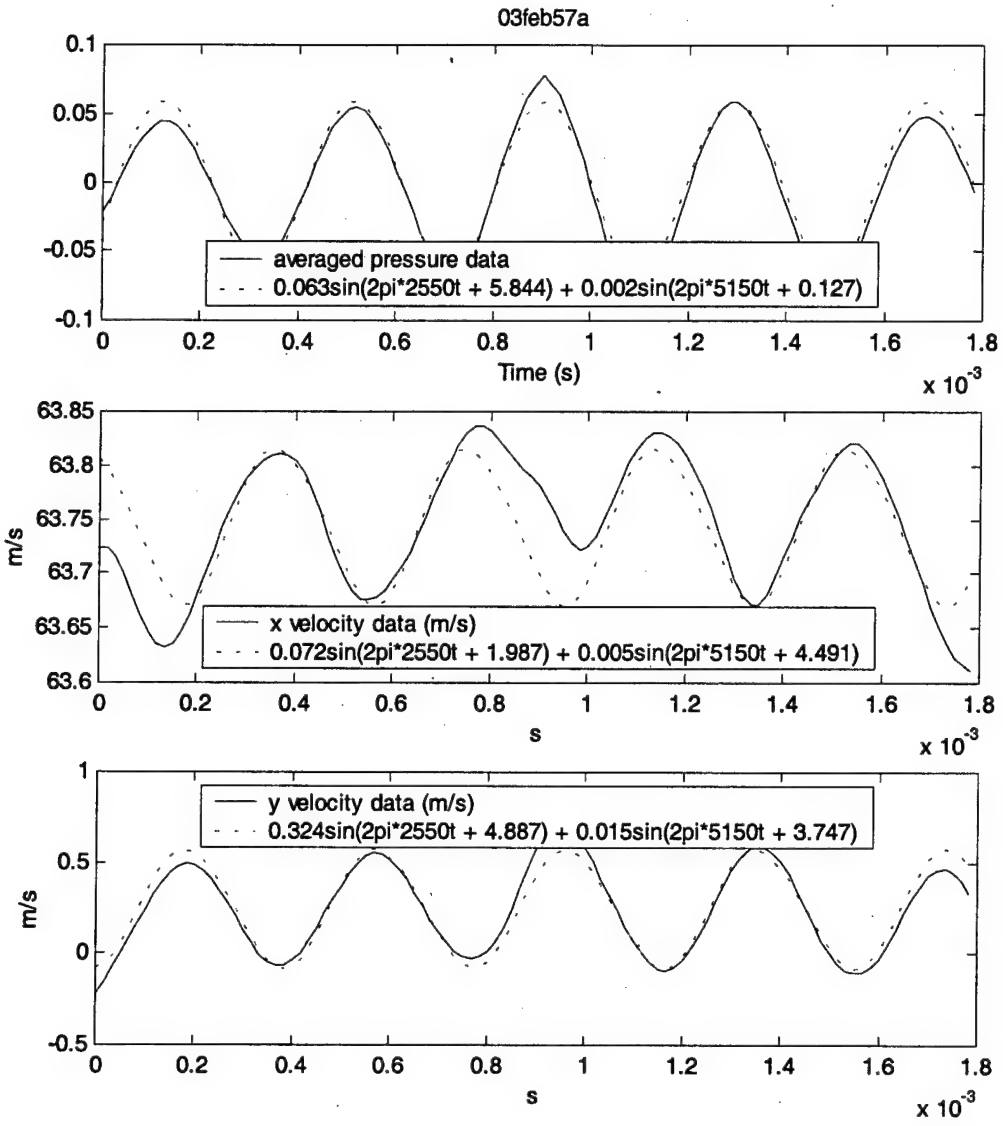

Figure 137. Data and two frequency approximation at x = -1.75 in, y = 0.125 in

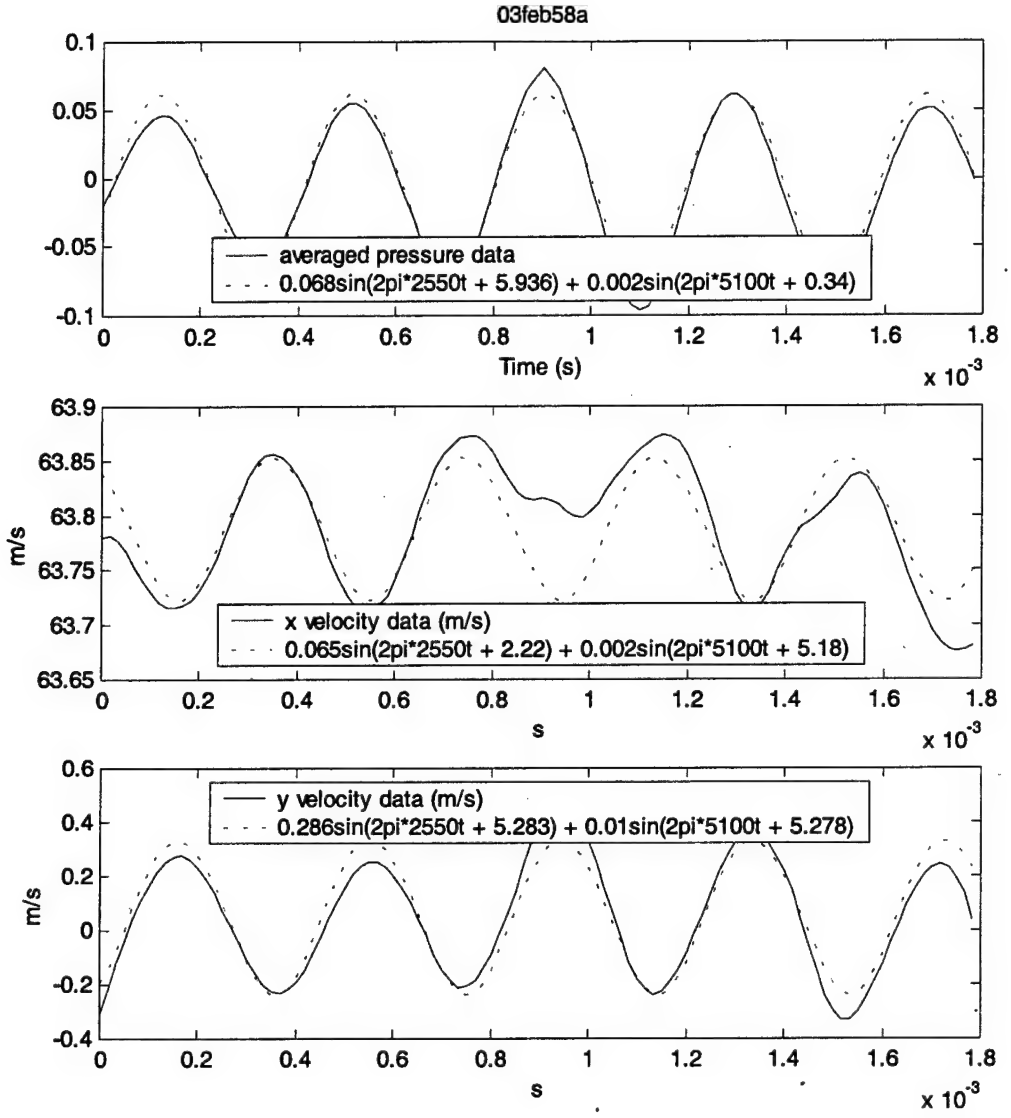

Figure 138. Data and two frequency approximation at x = -1.75 in, y = 0 in

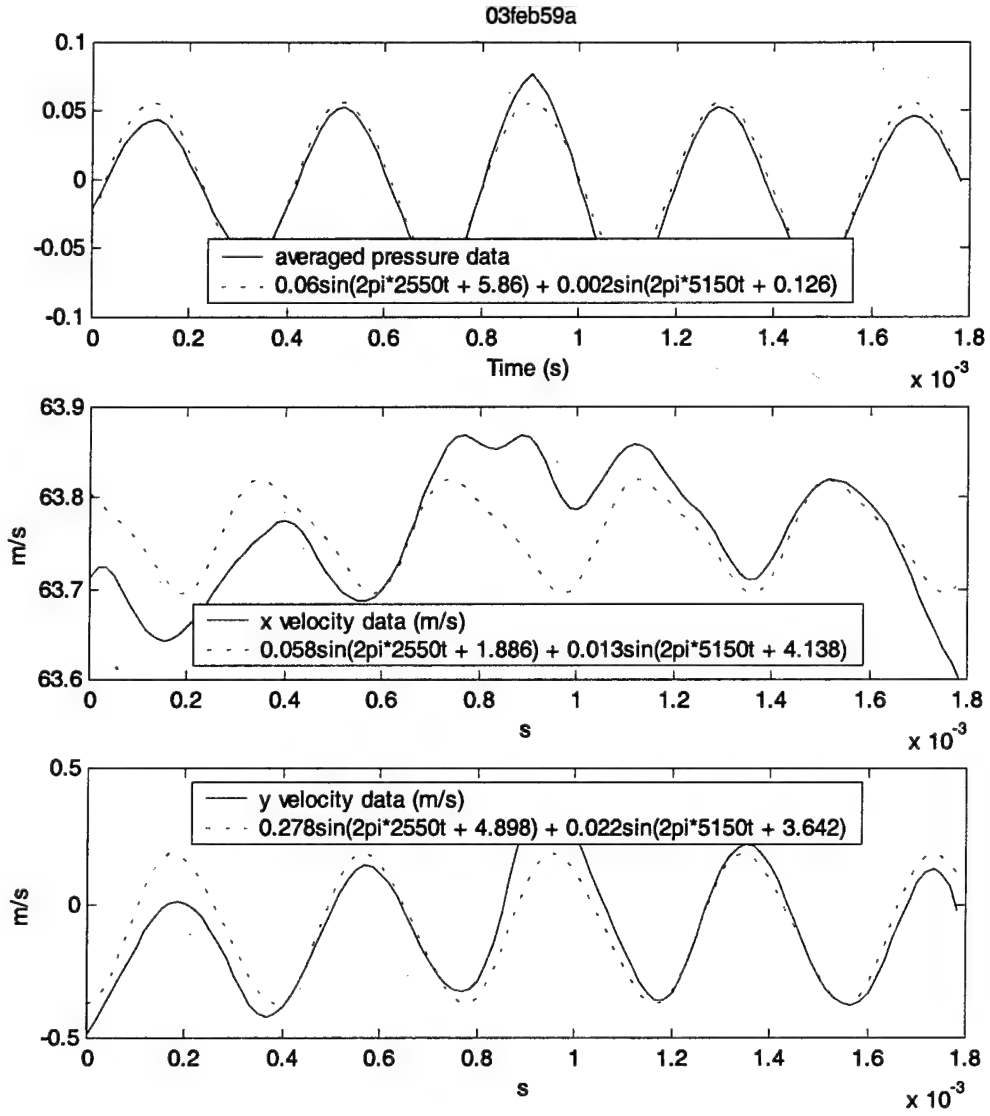

Figure 139. Data and two frequency approximation at x = -1.75 in, y = -0.125 in

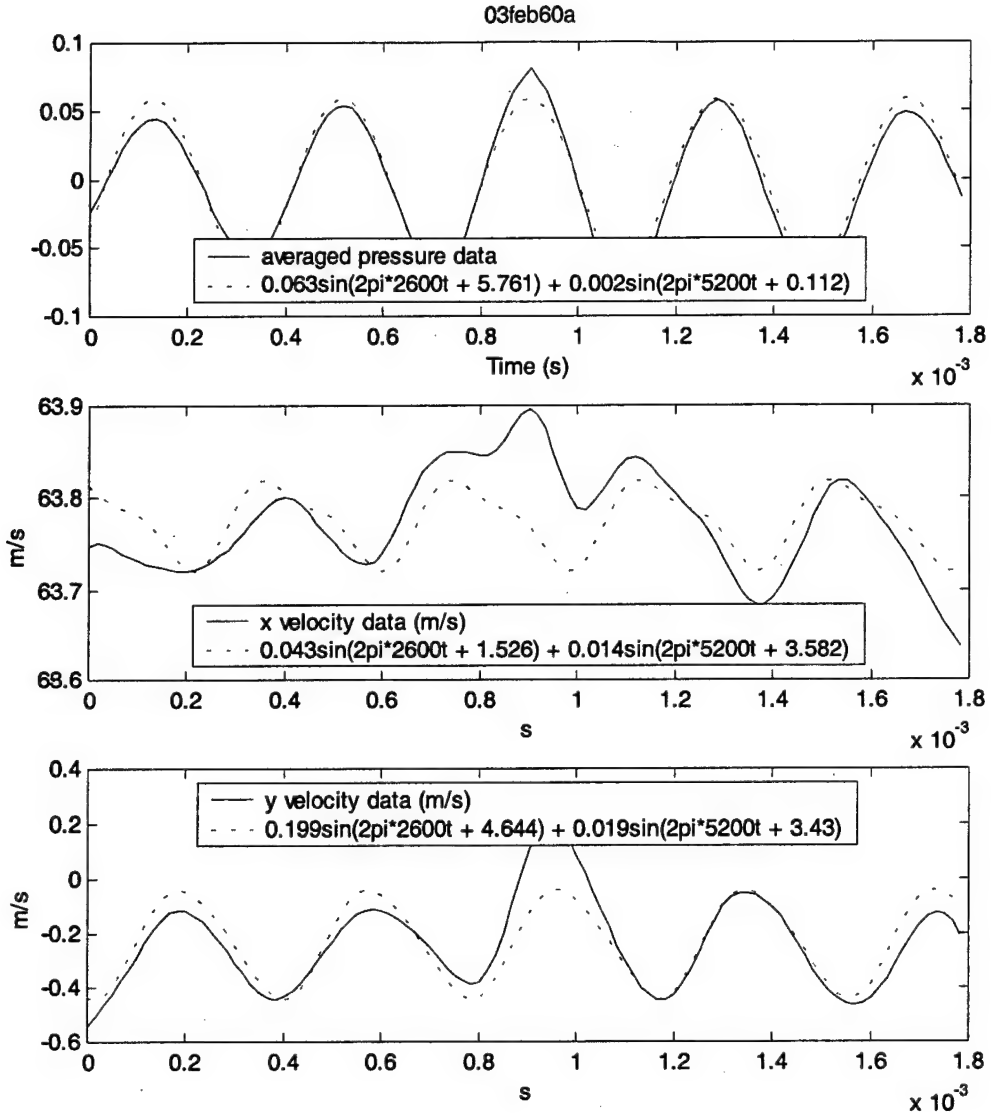

Figure 140. Data and two frequency approximation at x = -1.75 in, y = -0.25 in

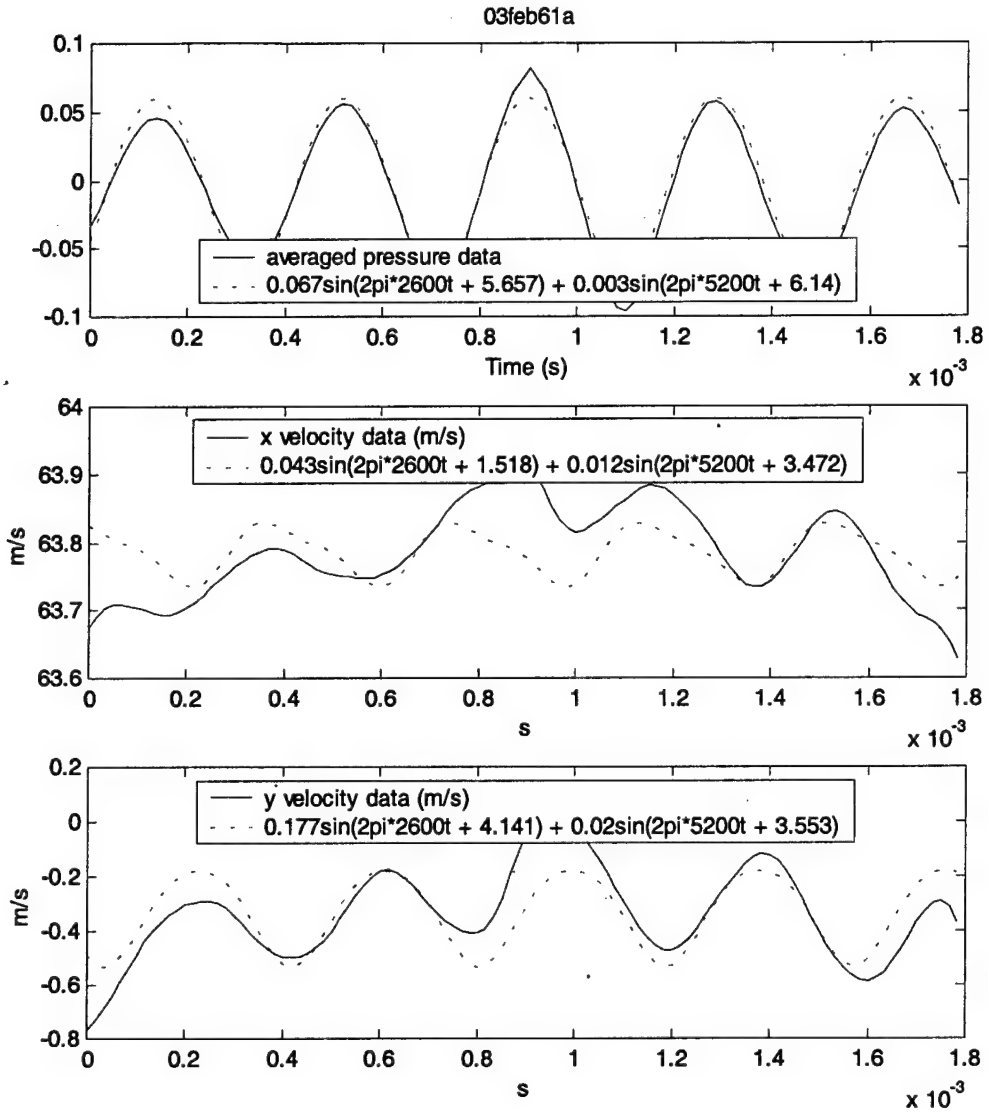

Figure 141. Data and two frequency approximation at x = -1.75 in, y = -0.375 in

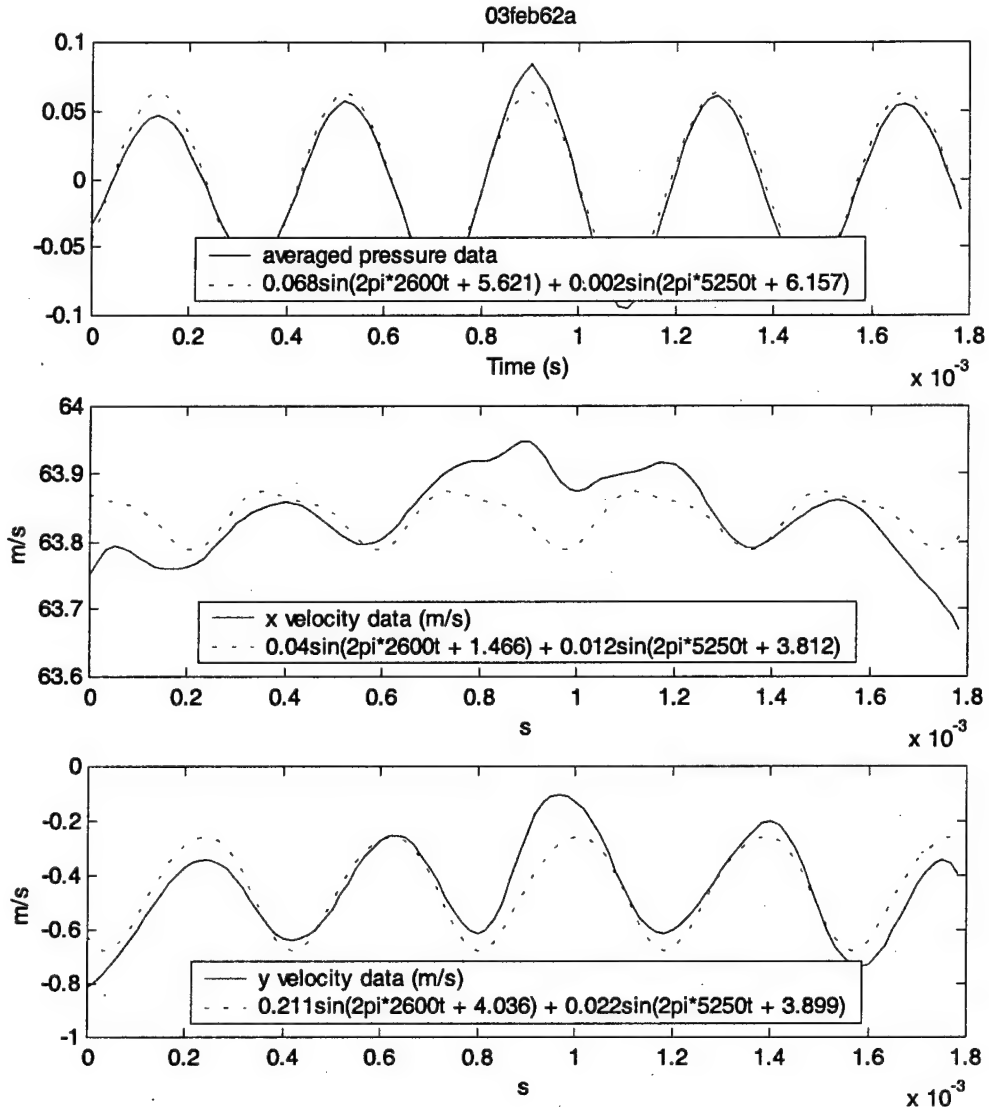

Figure 142. Data and two frequency approximation at x = -1.75 in, y = -0.5 in

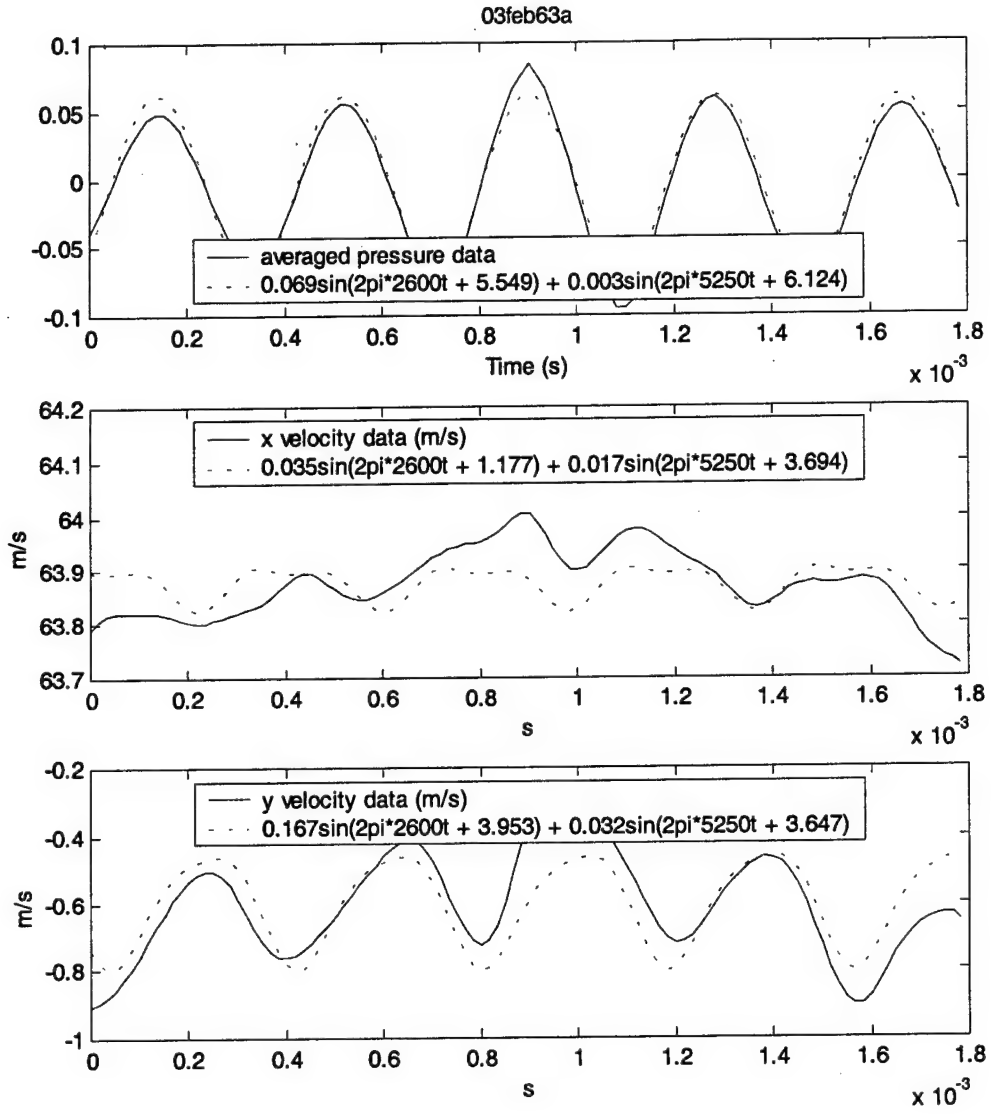

Figure 143. Data and two frequency approximation at x = -1.75 in, y = -0.625 in

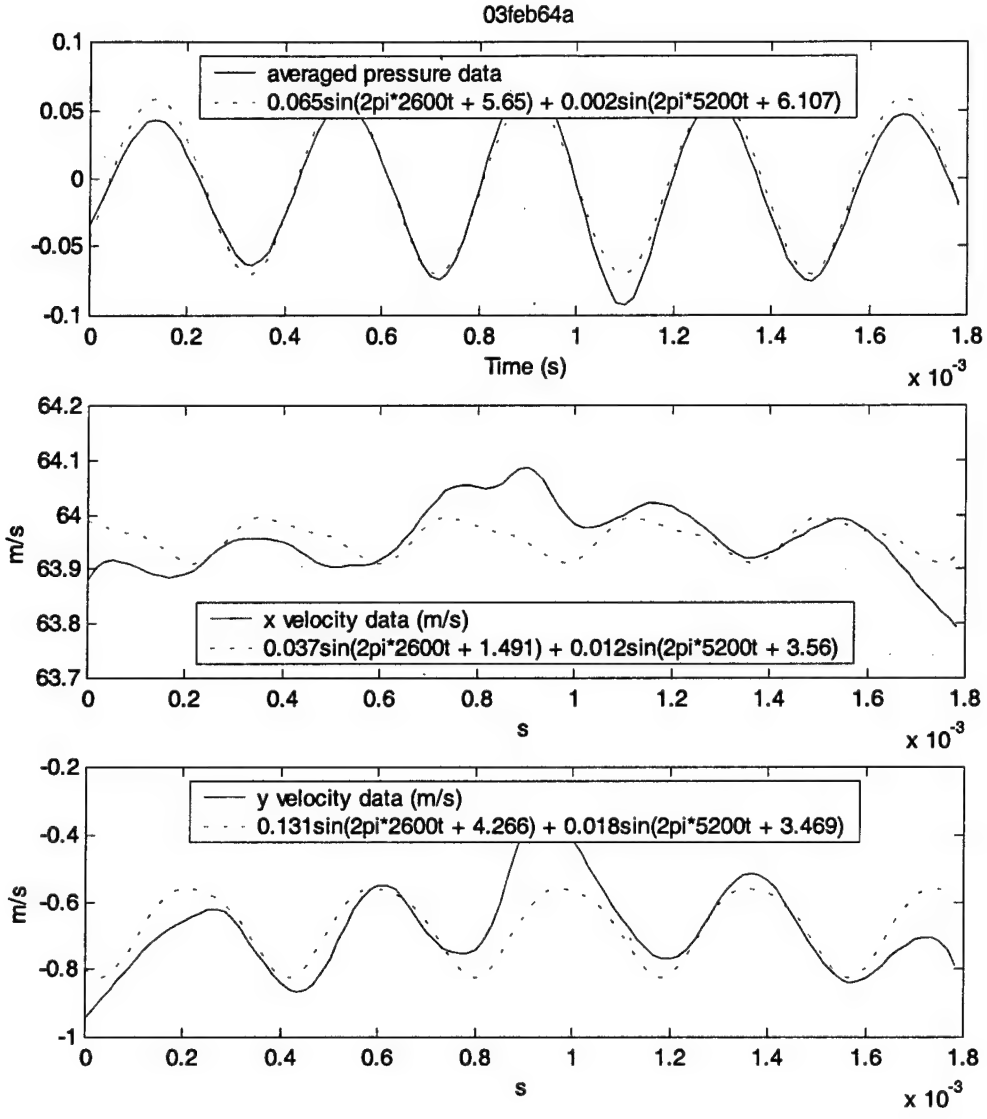

Figure 144. Data and two frequency approximation at x = -1.75 in, y = -0.75 in

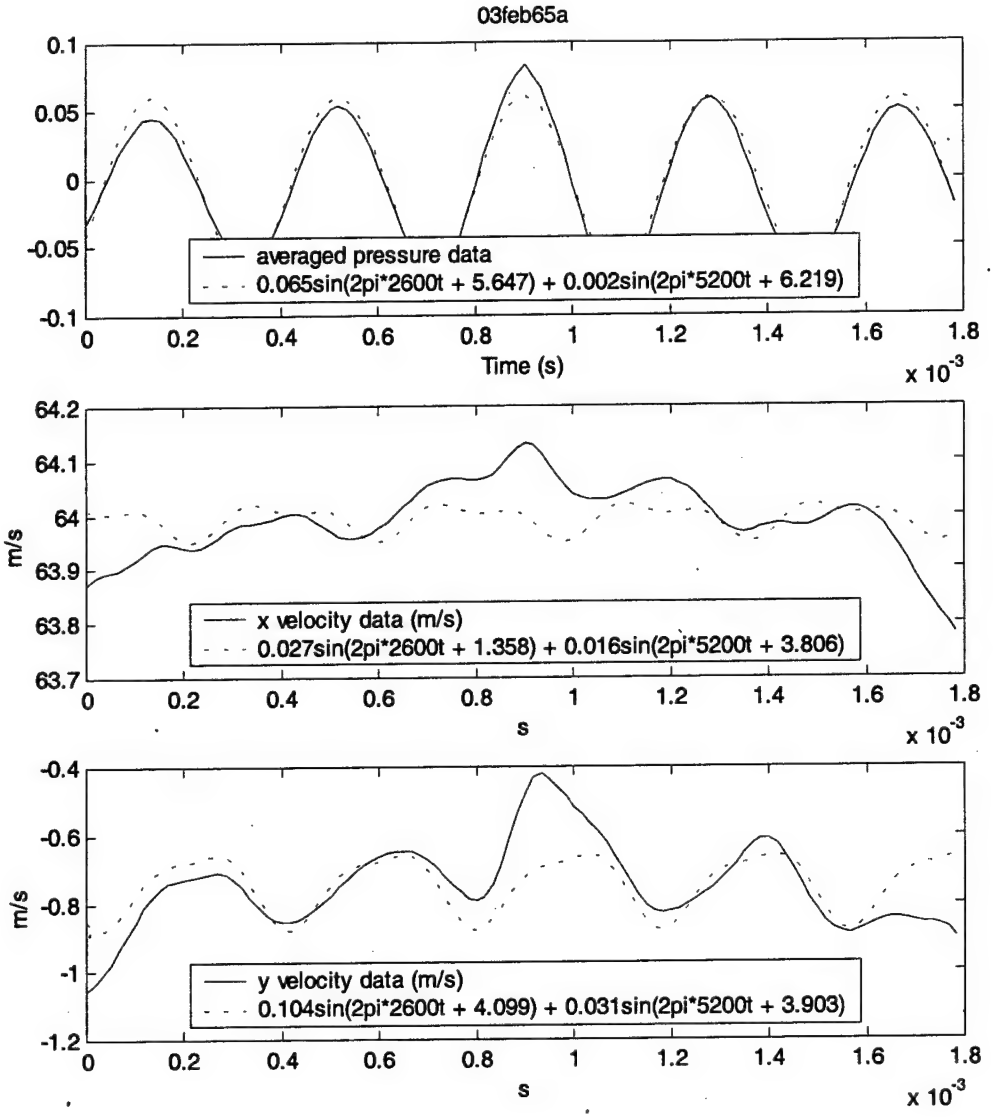

Figure 145. Data and two frequency approximation at x = -1.75 in, y = -0.875 in

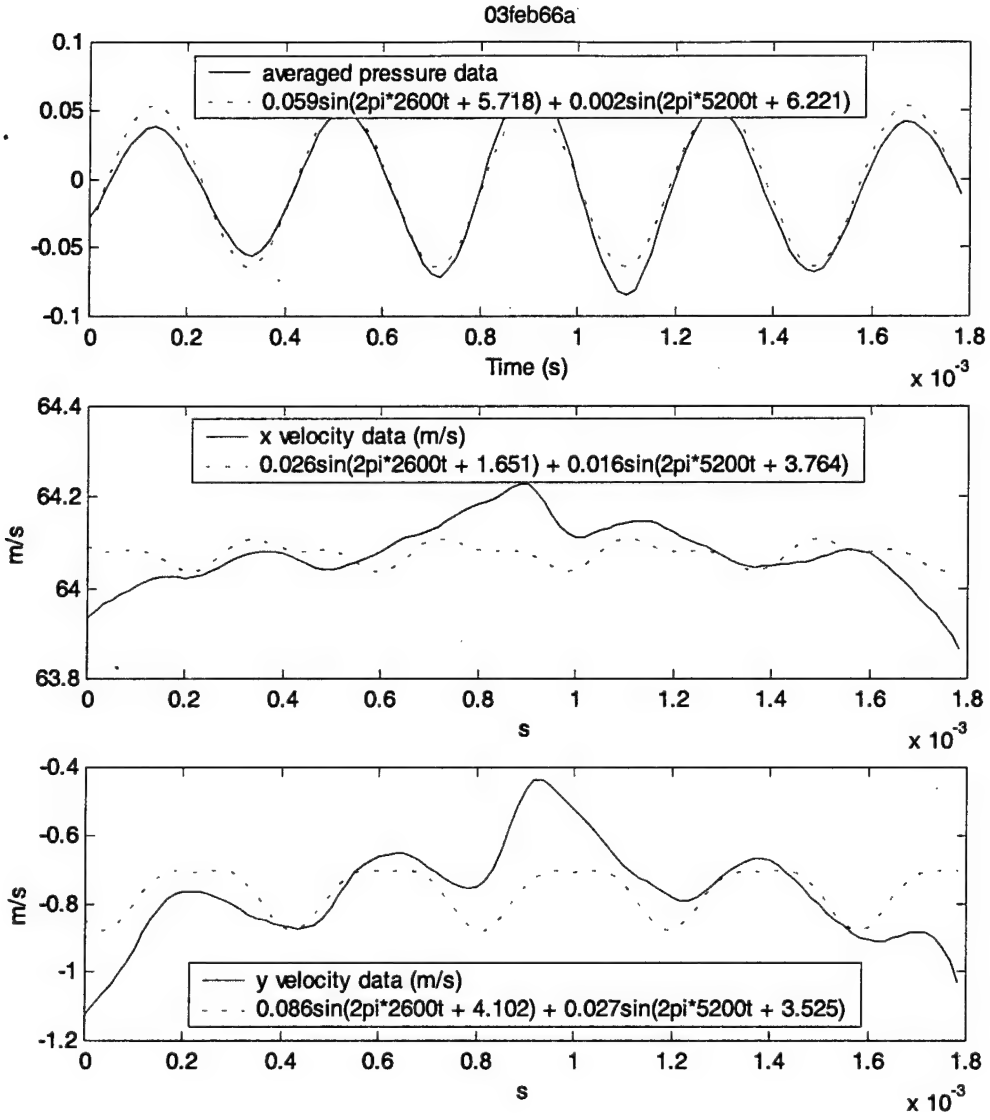

Figure 146. Data and two frequency approximation at x = -1.5 in, y = -1 in

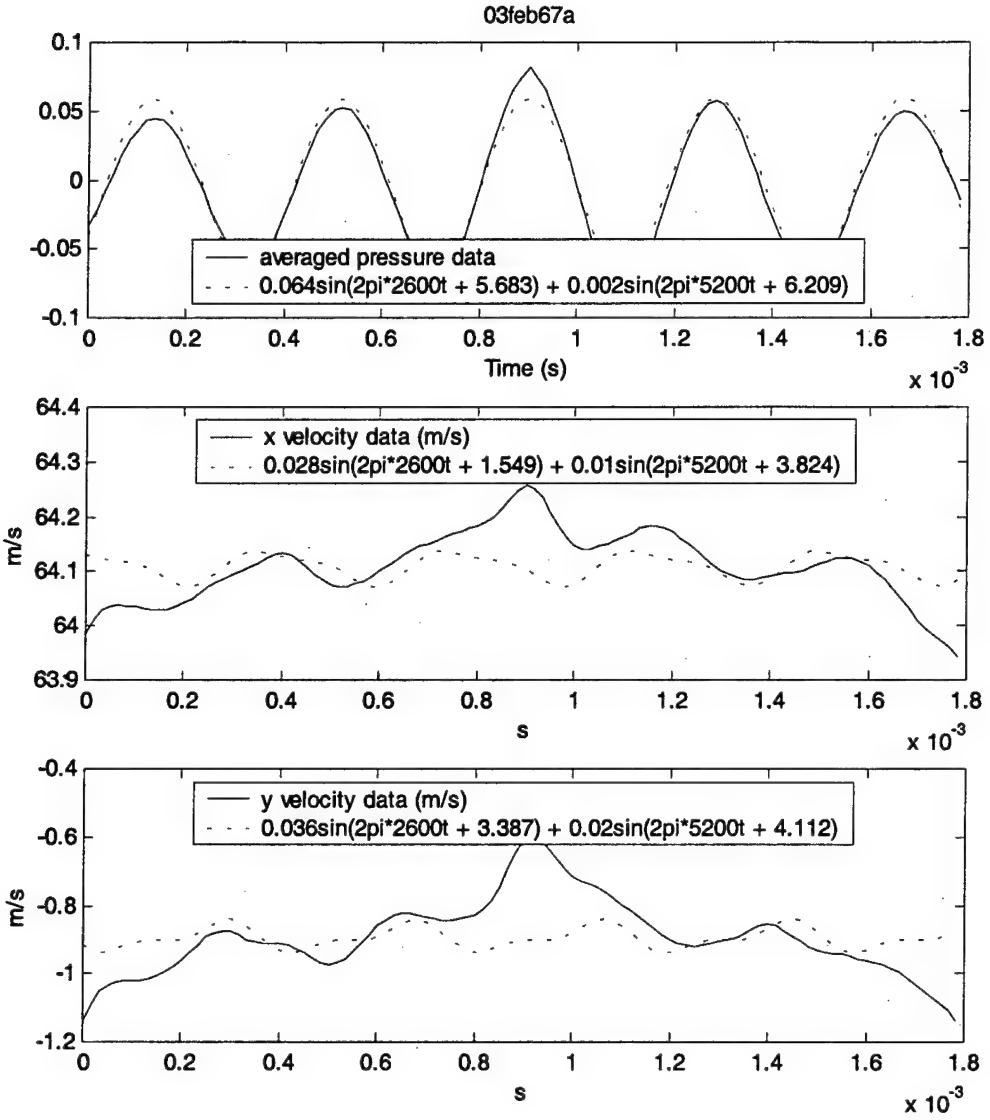

Figure 147. Data and two frequency approximation at x = -1.75 in, y = -1.25 in

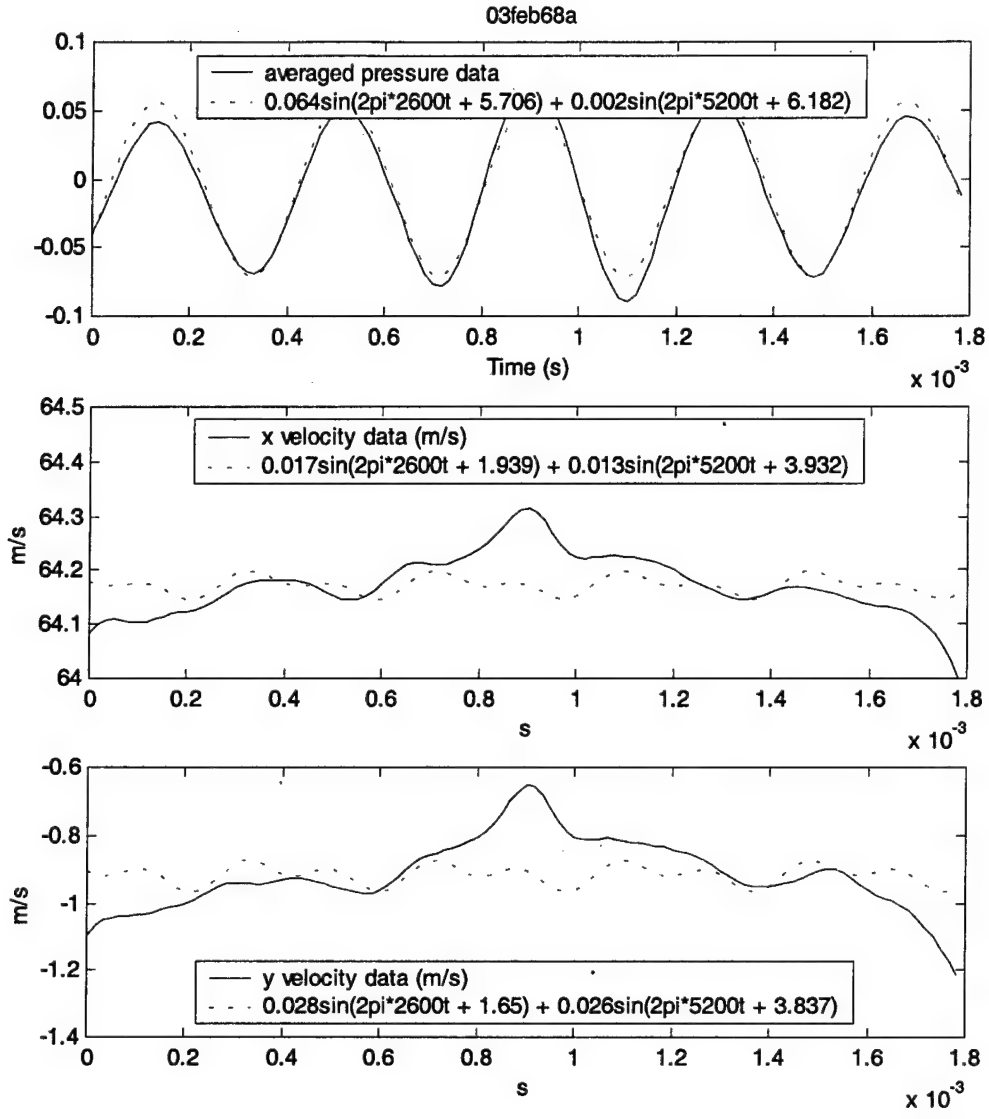

Figure 148. Data and two frequency approximation at x = -1.75 in, y = -1.5 in

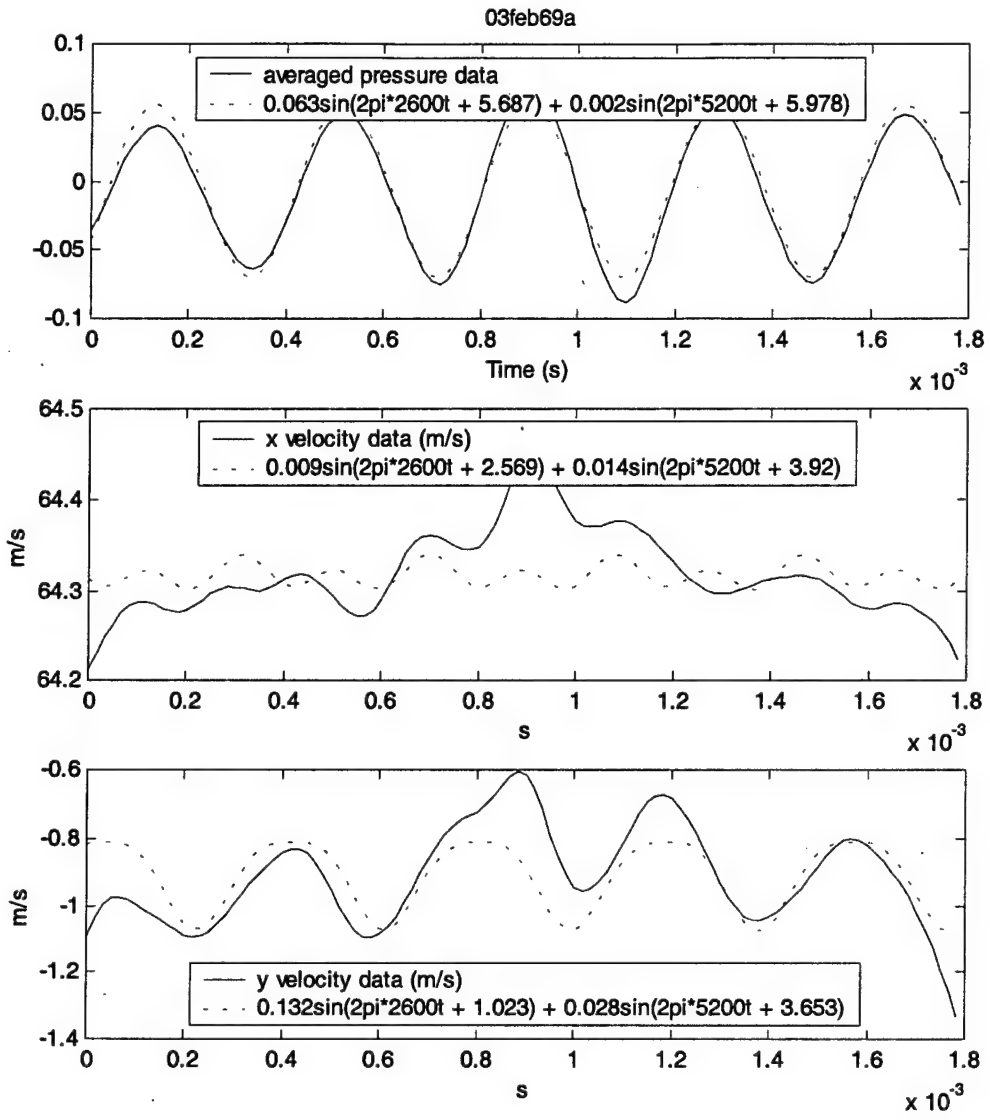

Figure 149. Data and two frequency approximation at x = -1.75 in, y = -2 in

4. Data at x = -2 in

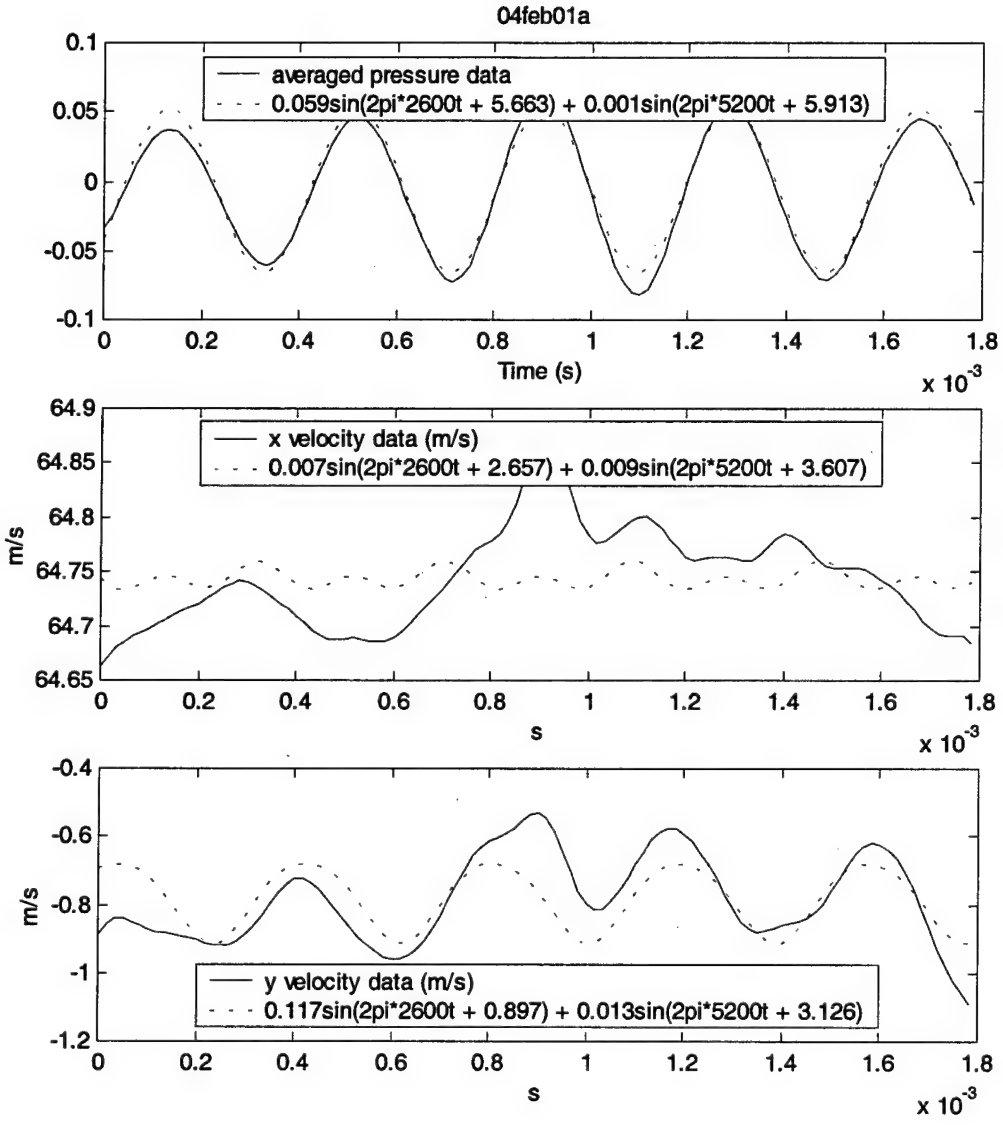

Figure 150. Data and two frequency approximation at x = -2 in, y = -2 in

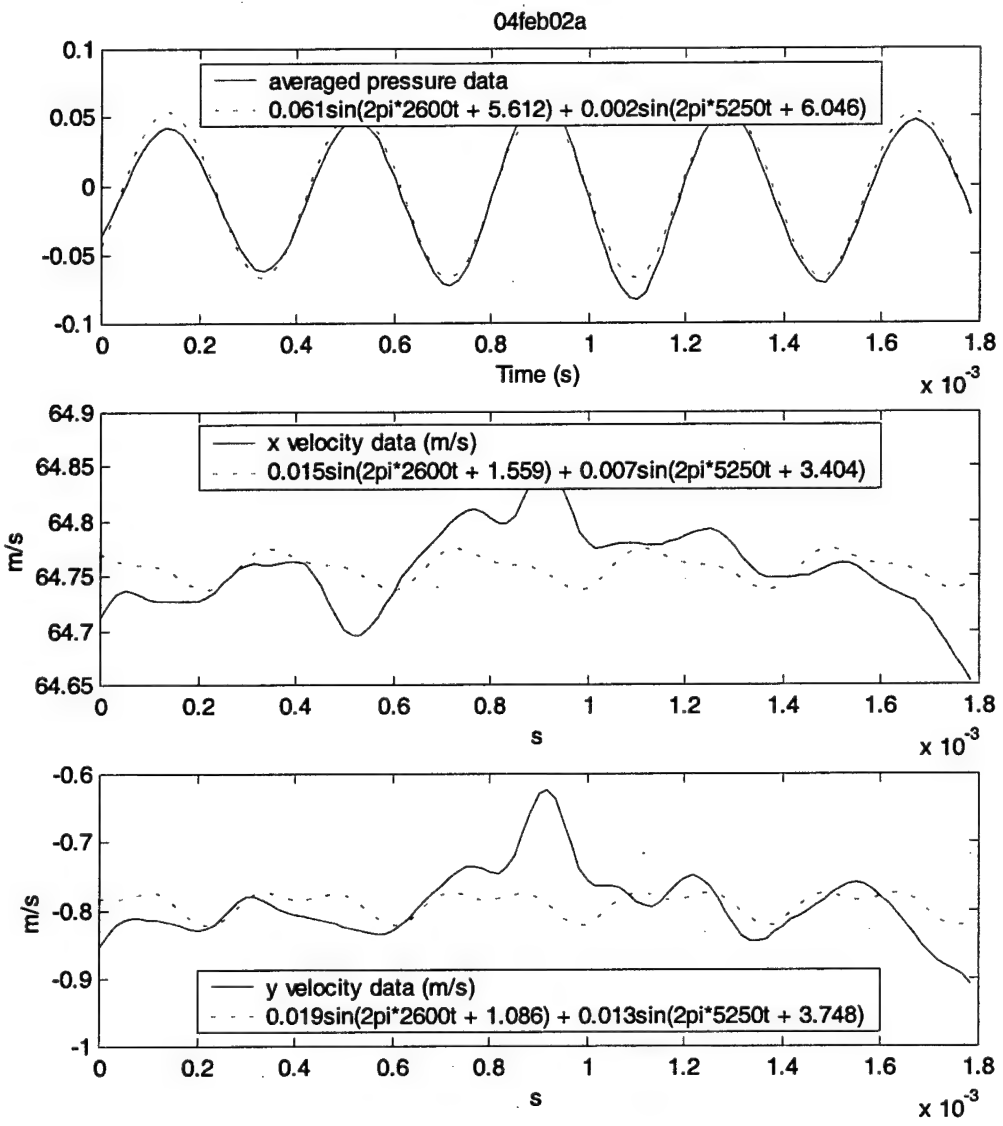

Figure 151. Data and two frequency approximation at x = -2 in, y = -1.5 in

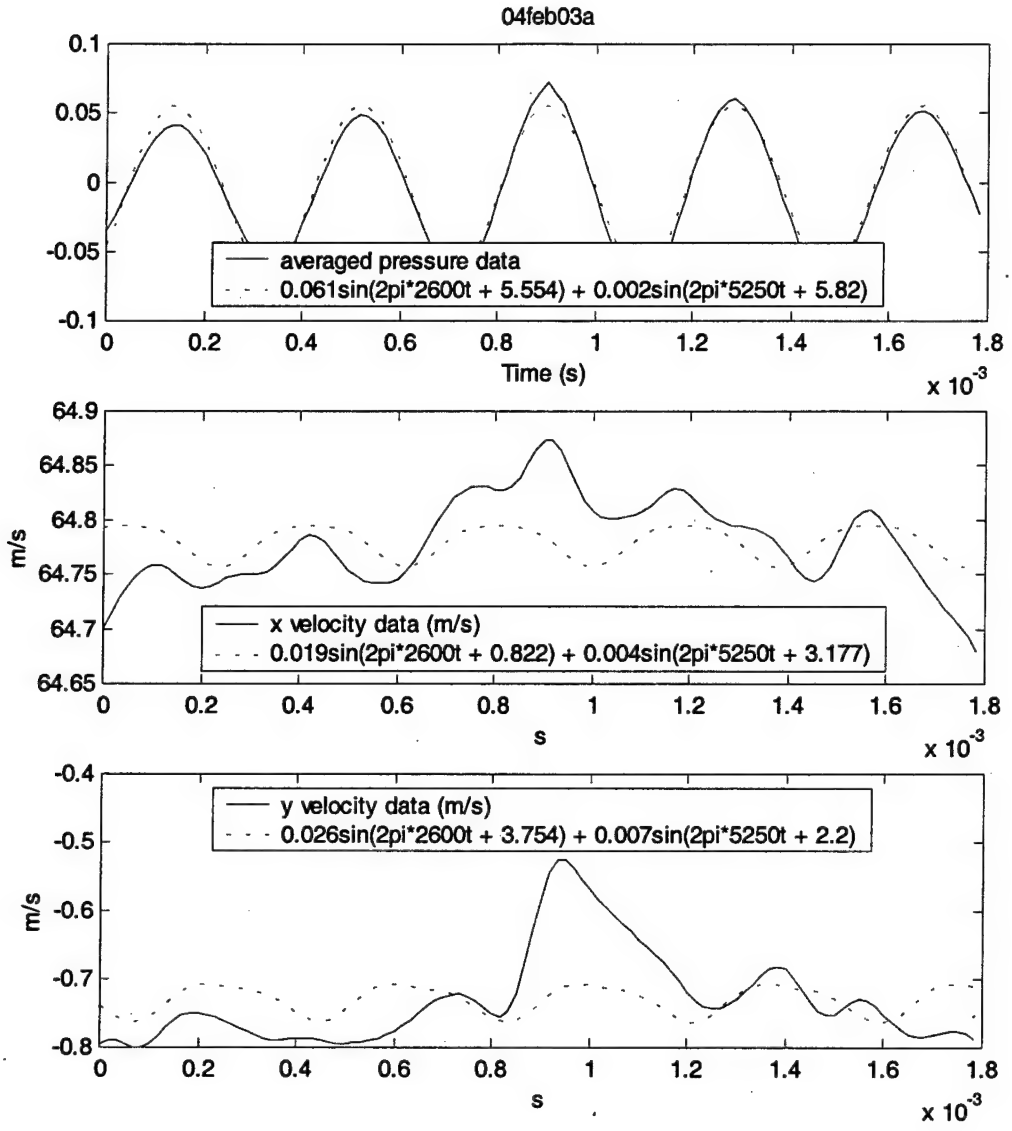

Figure 152. Data and two frequency approximation at x = -2 in, y = -1.25 in

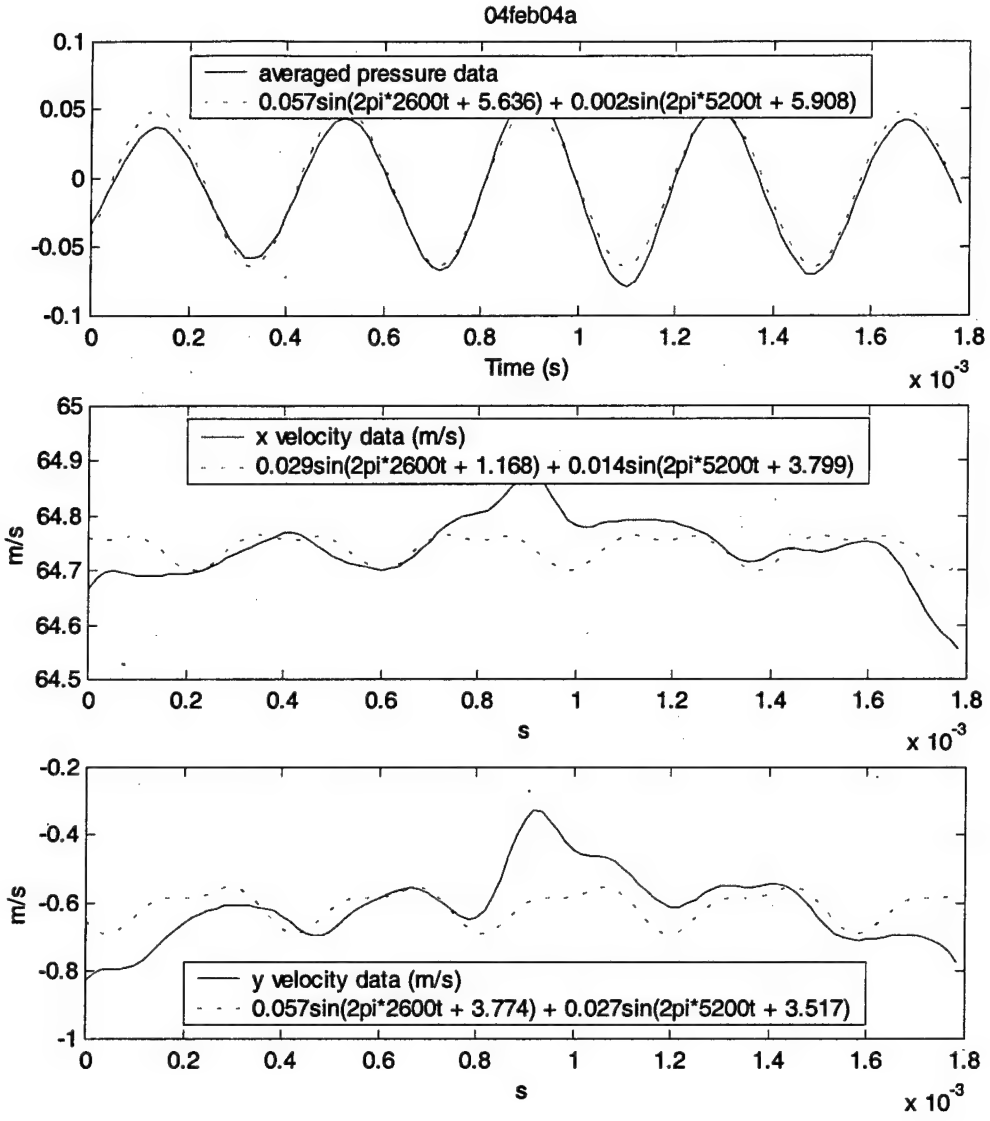

Figure 153. Data and two frequency approximation at x = -2 in, y = -1 in

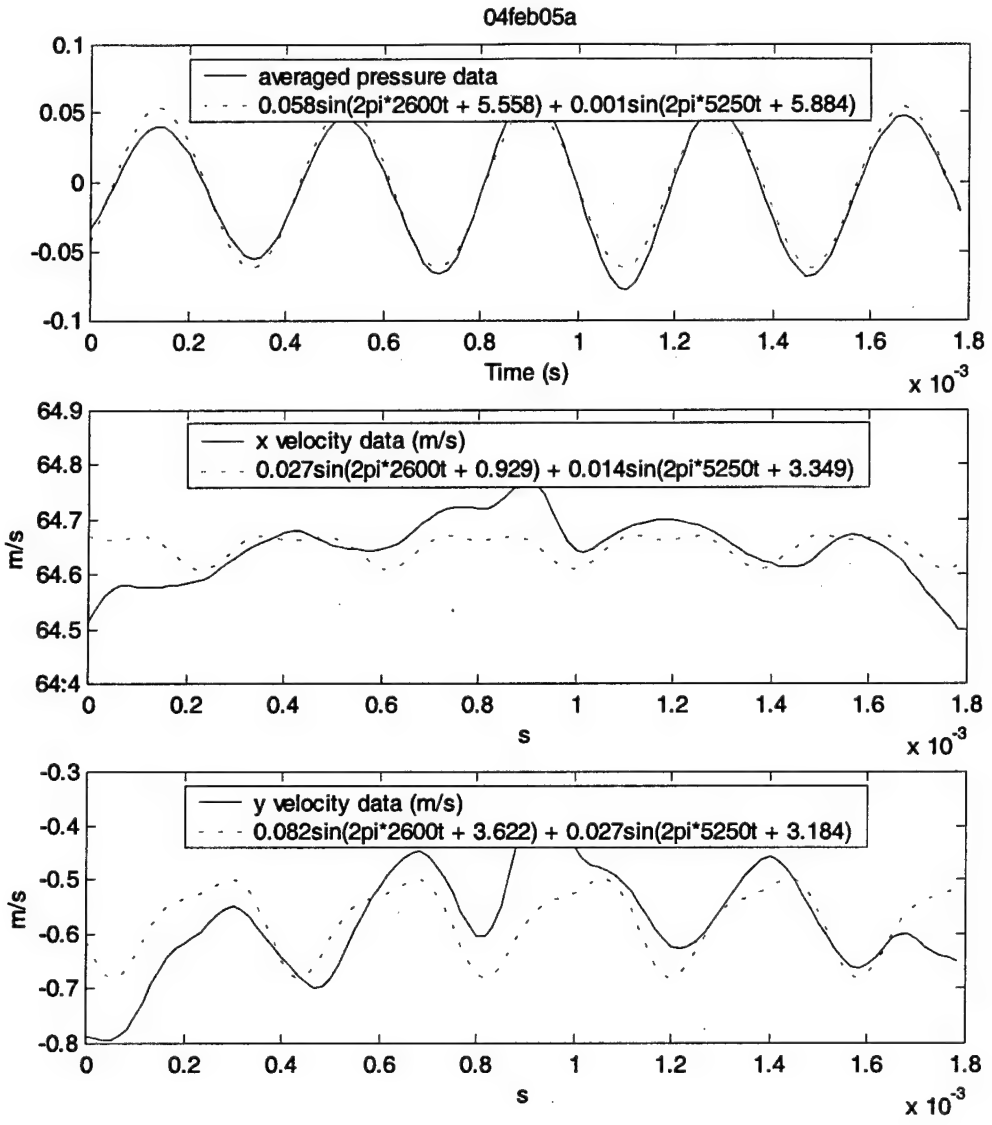

Figure 154. Data and two frequency approximation at x = -2 in, y = -0.875 in

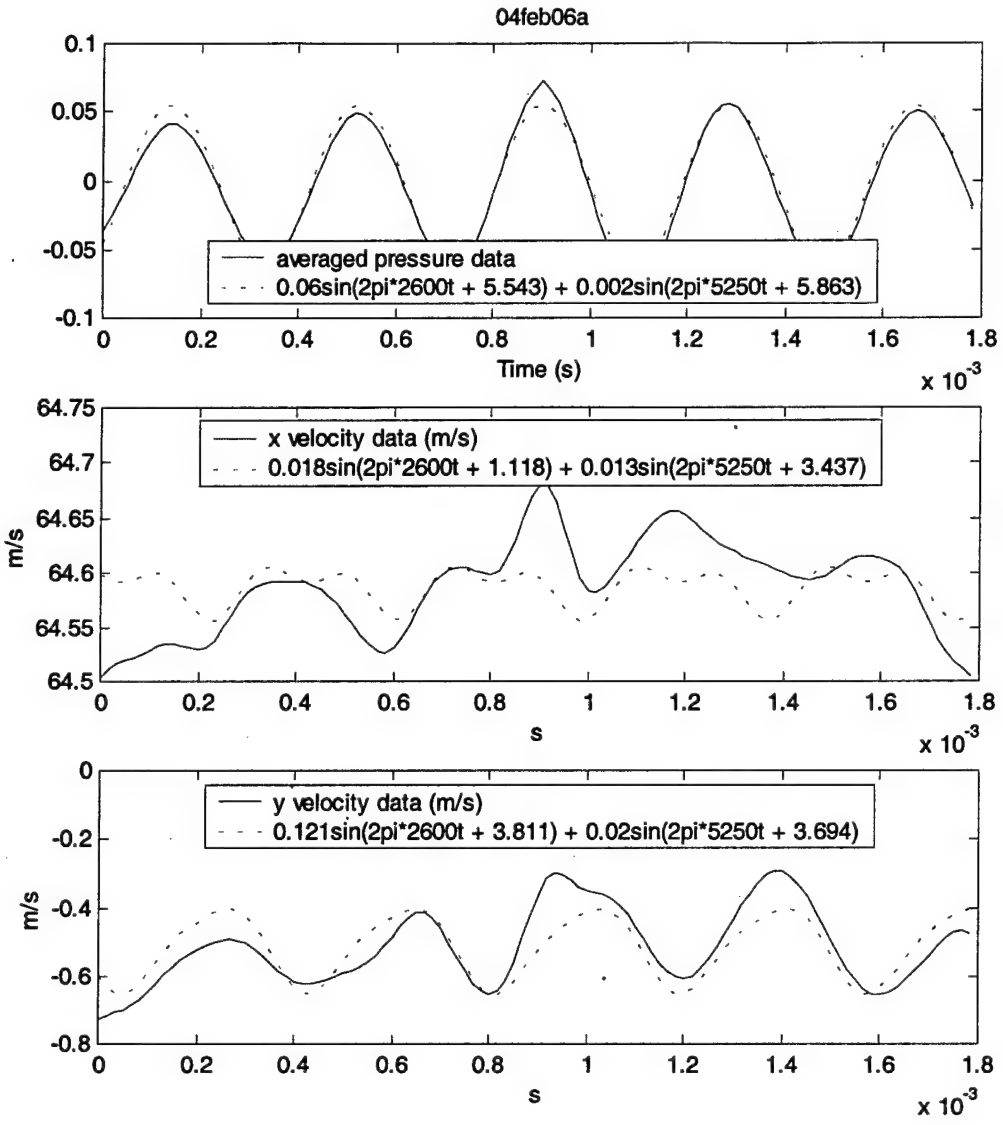

Figure 155. Data and two frequency approximation at x = -2 in, y = -0.75 in

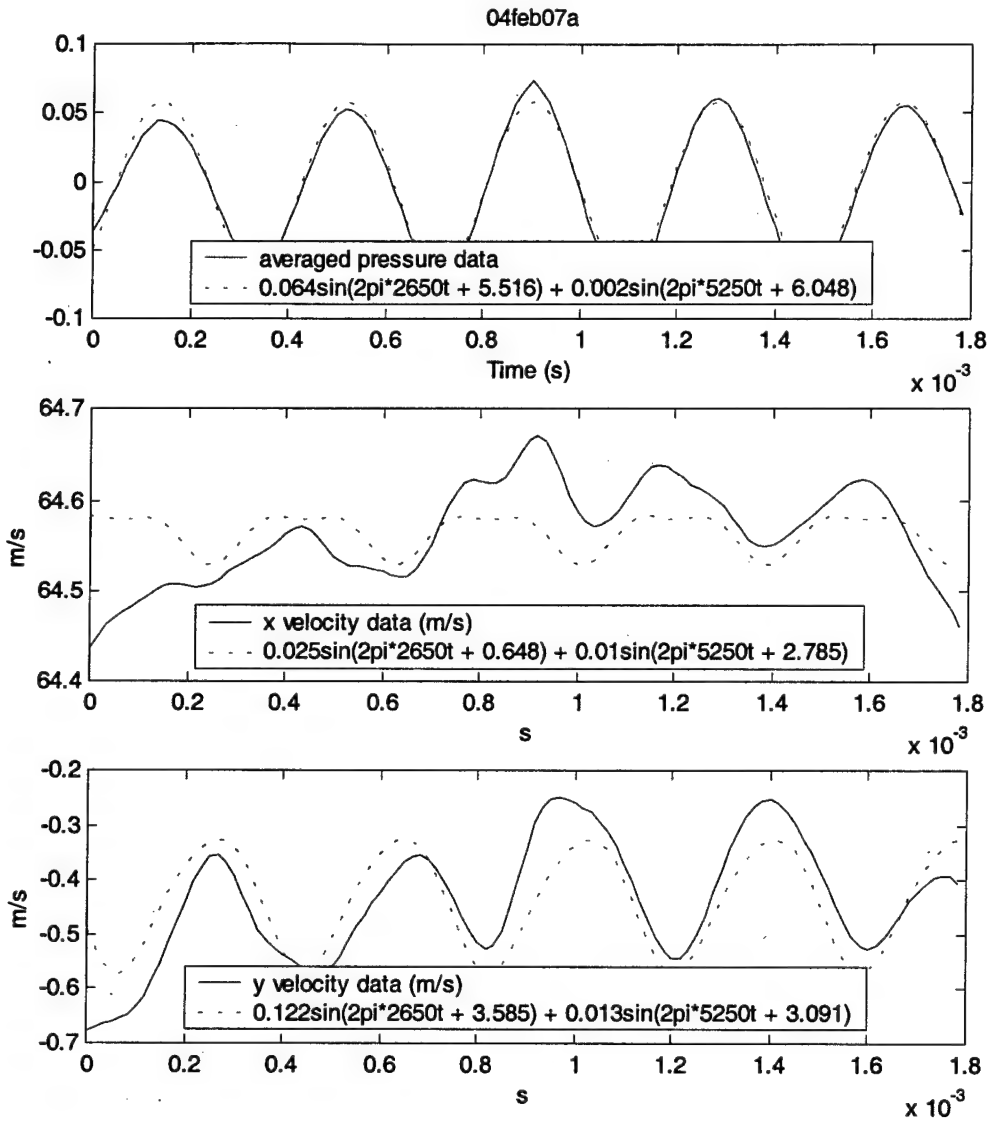

Figure 156. Data and two frequency approximation at x = -2 in, y = -0.625 in

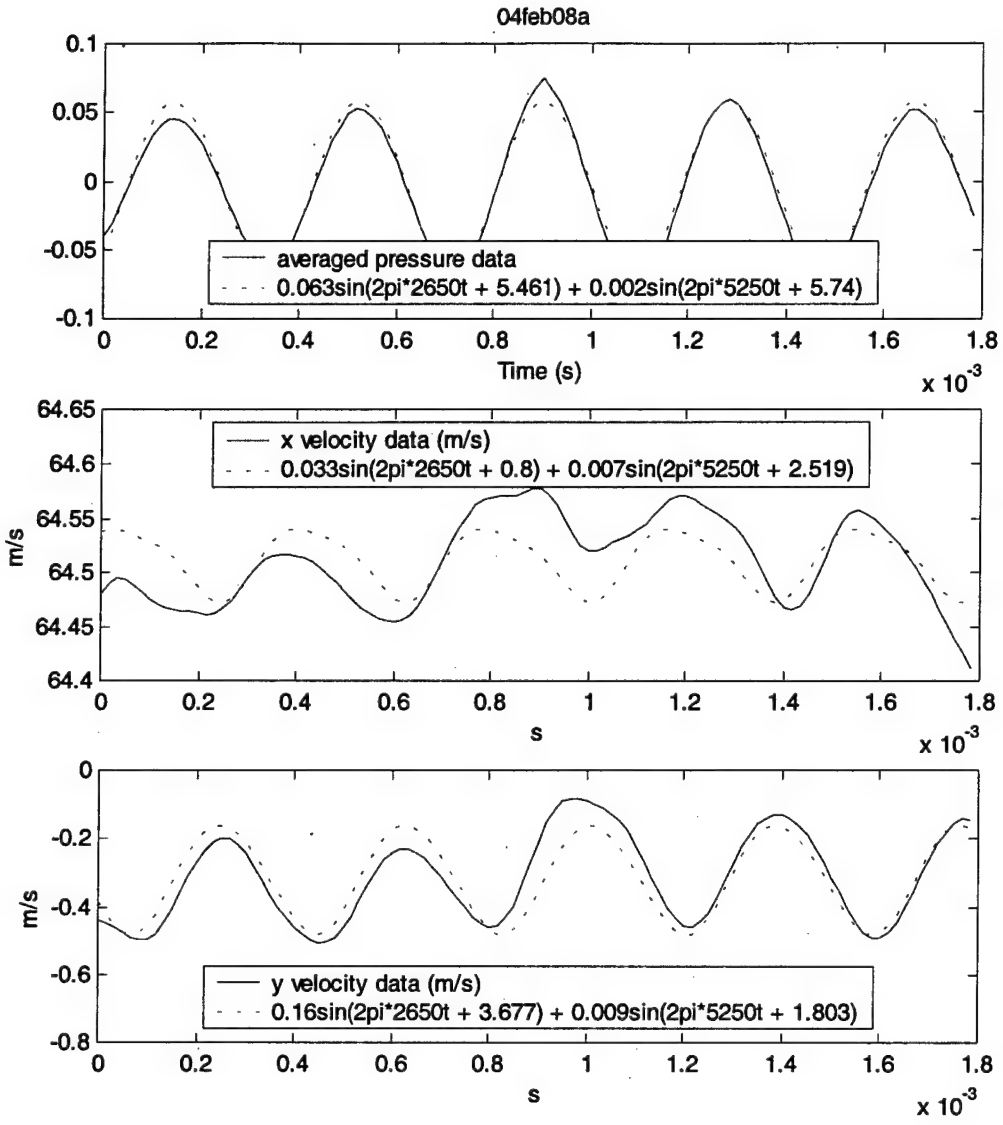

Figure 157. Data and two frequency approximation at x = -2 in, y = -0.5 in

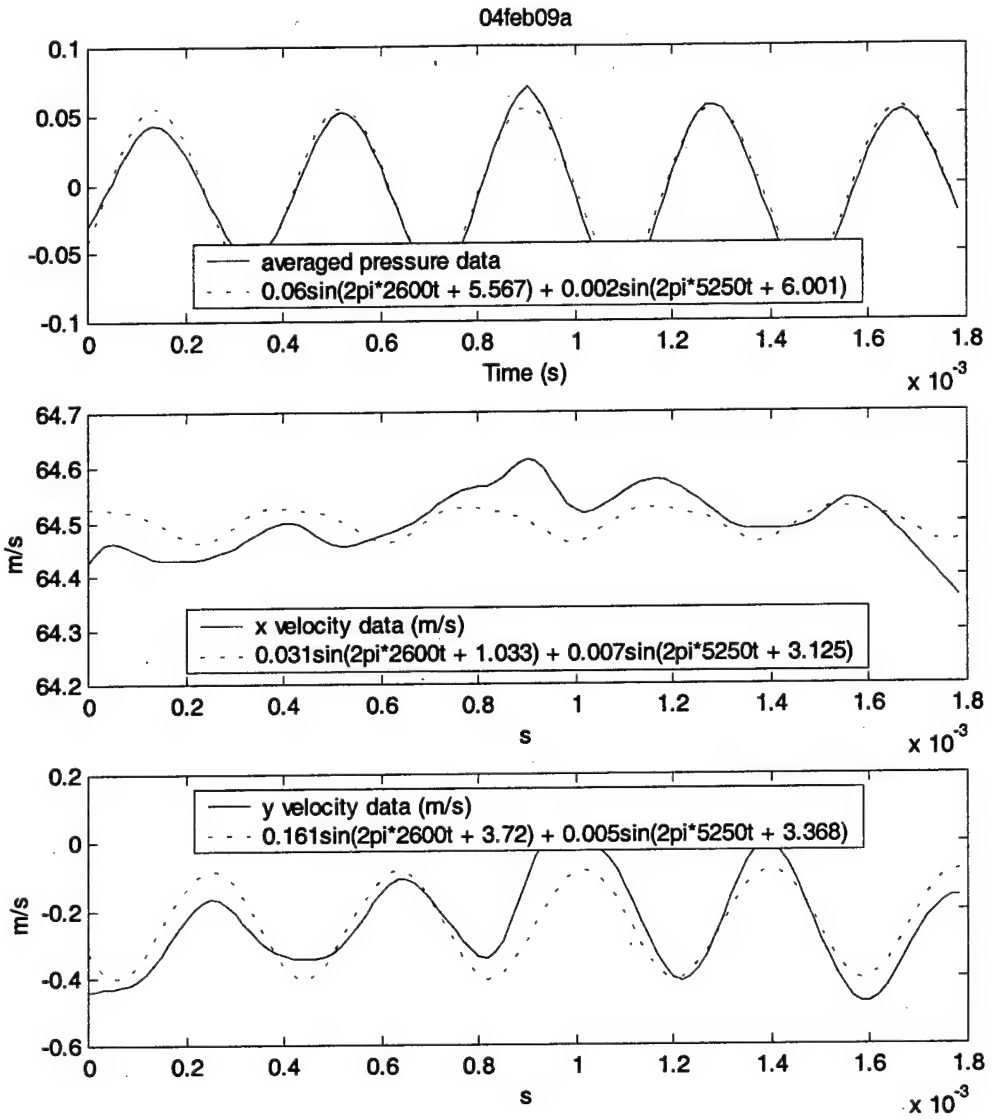

Figure 158. Data and two frequency approximation at x = -2 in, y = -0.375 in

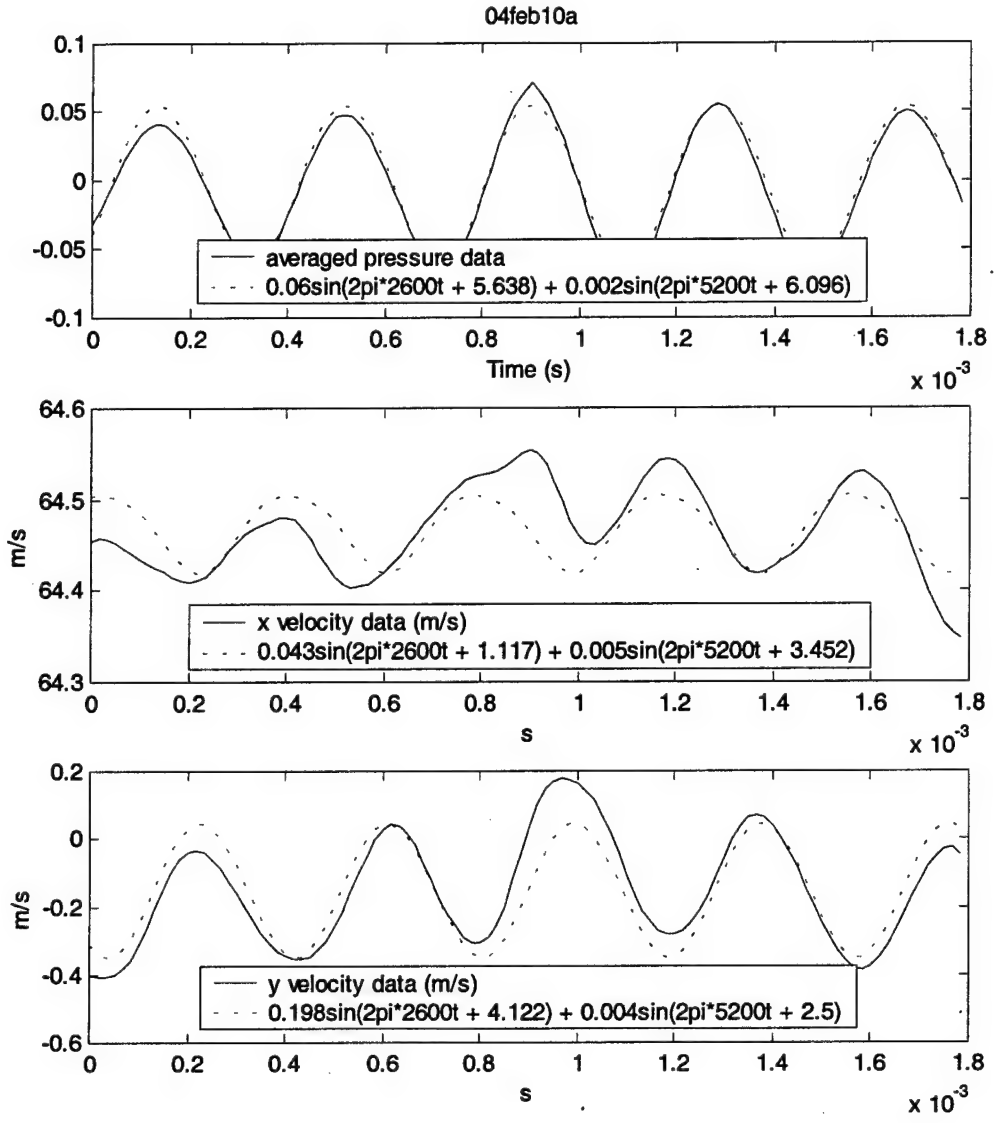

Figure 159. Data and two frequency approximation at x = -2 in, y = -0.25 in

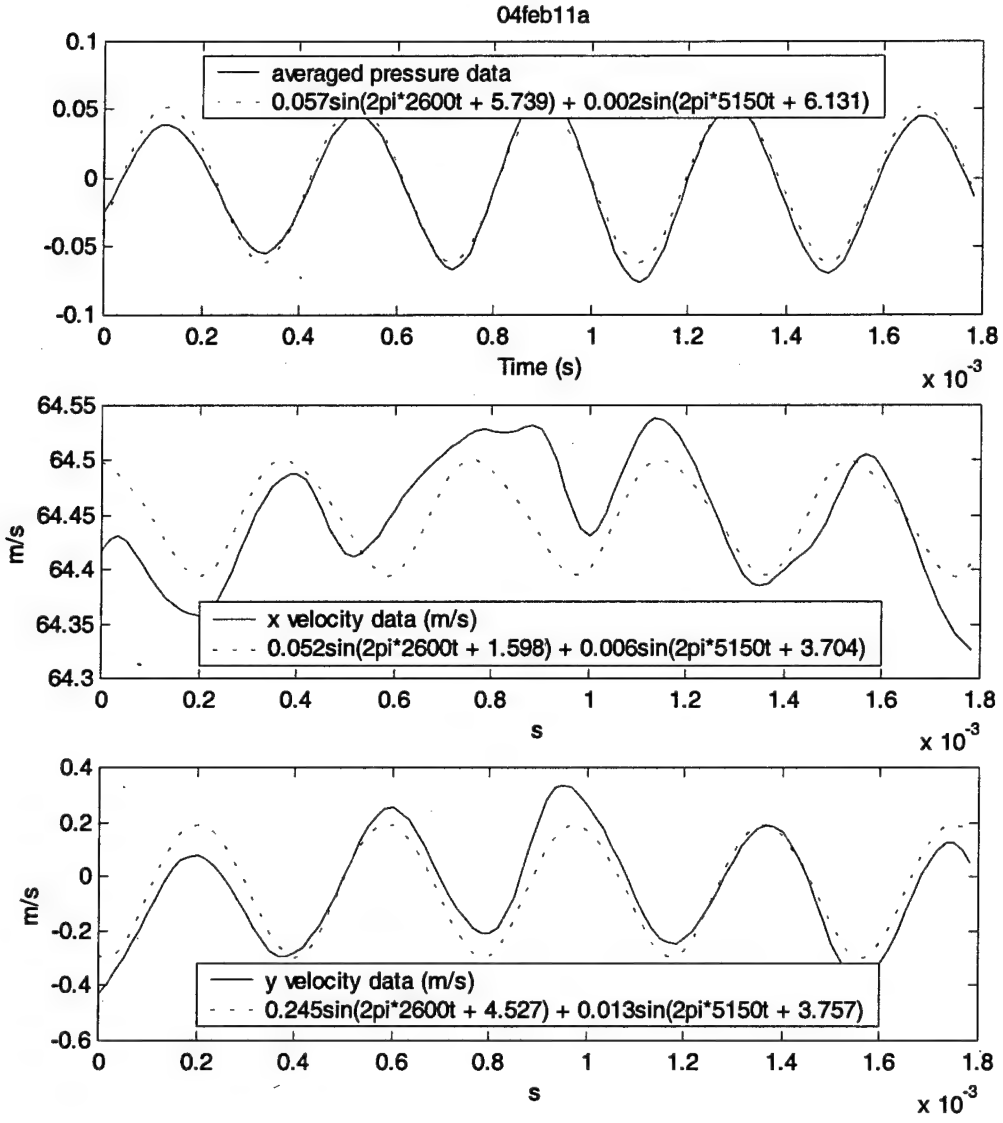

Figure 160. Data and two frequency approximation at x = -2 in, y = -0.125 in

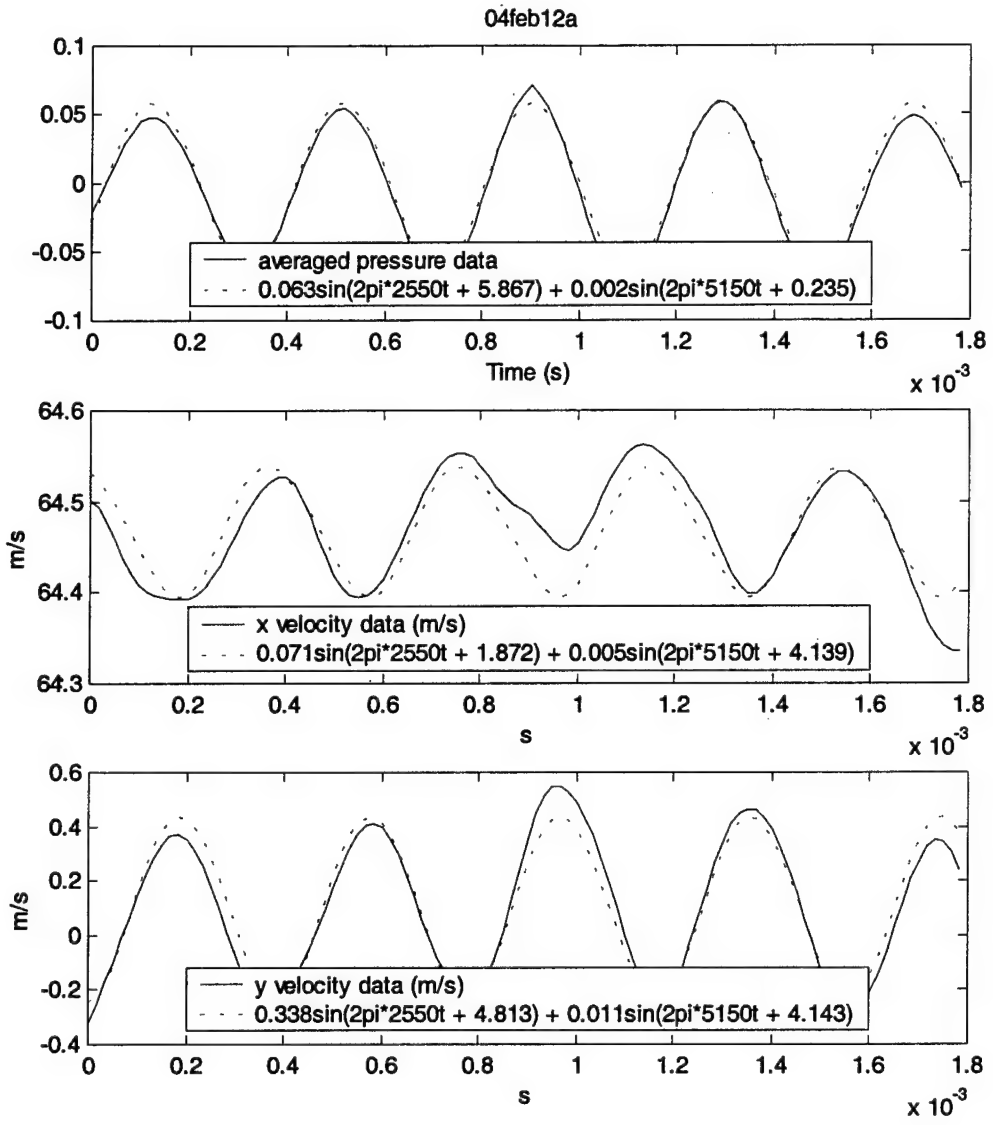

Figure 161. Data and two frequency approximation at x = -2 in, y = 0 in

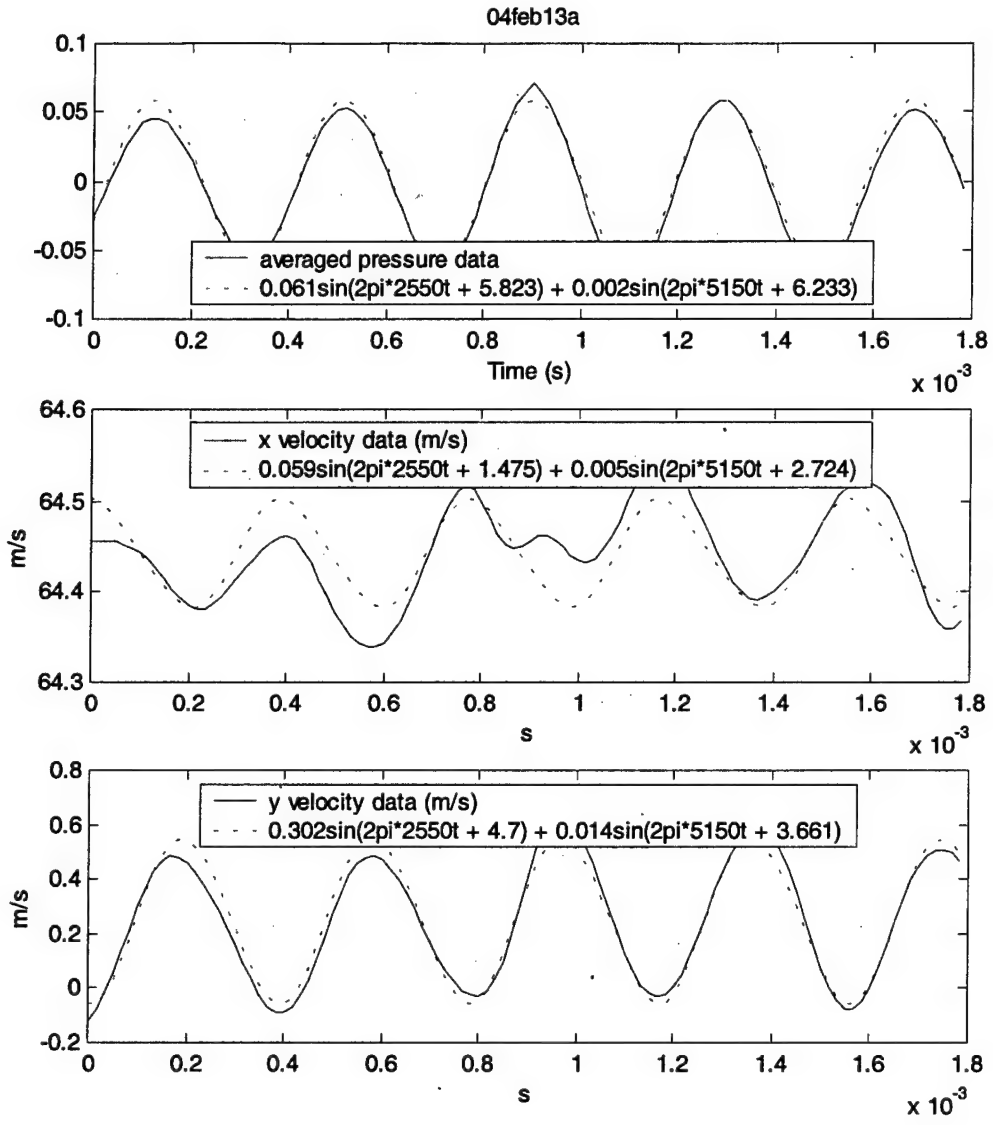

Figure 162. Data and two frequency approximation at x = -2 in, y = 0.125 in

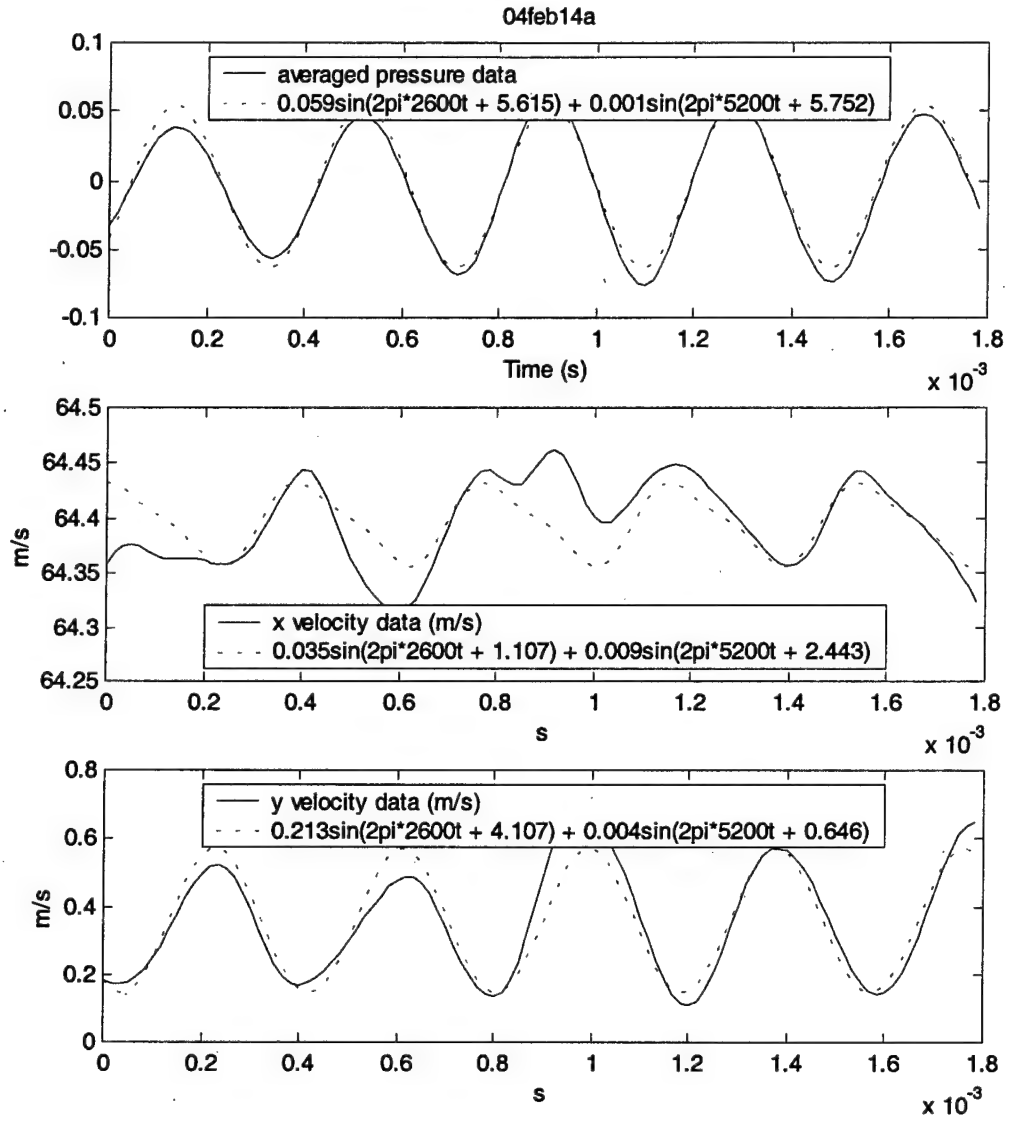

Figure 163. Data and two frequency approximation at x = -2 in, y = 0.25 in

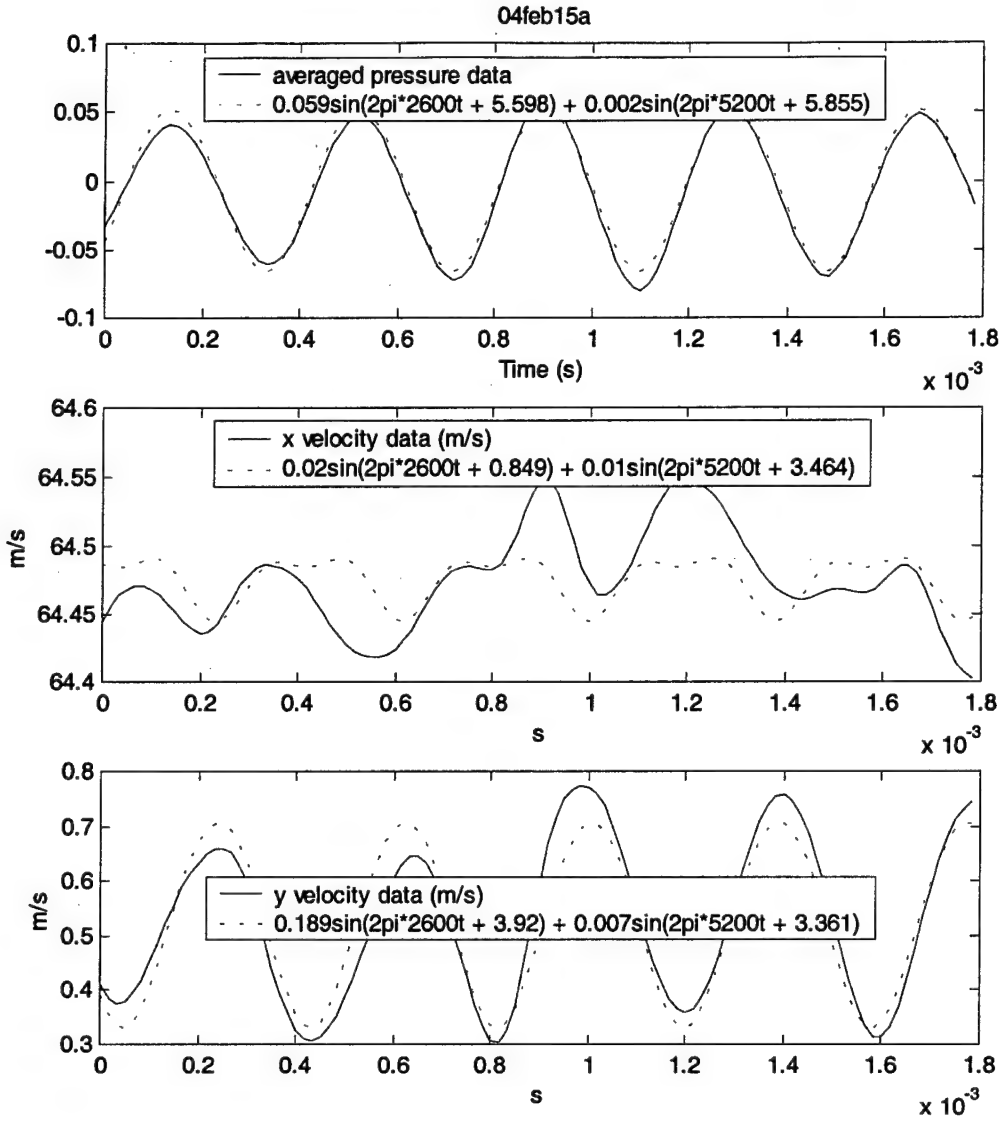

Figure 164. Data and two frequency approximation at x = -2 in, y = 0.375 in

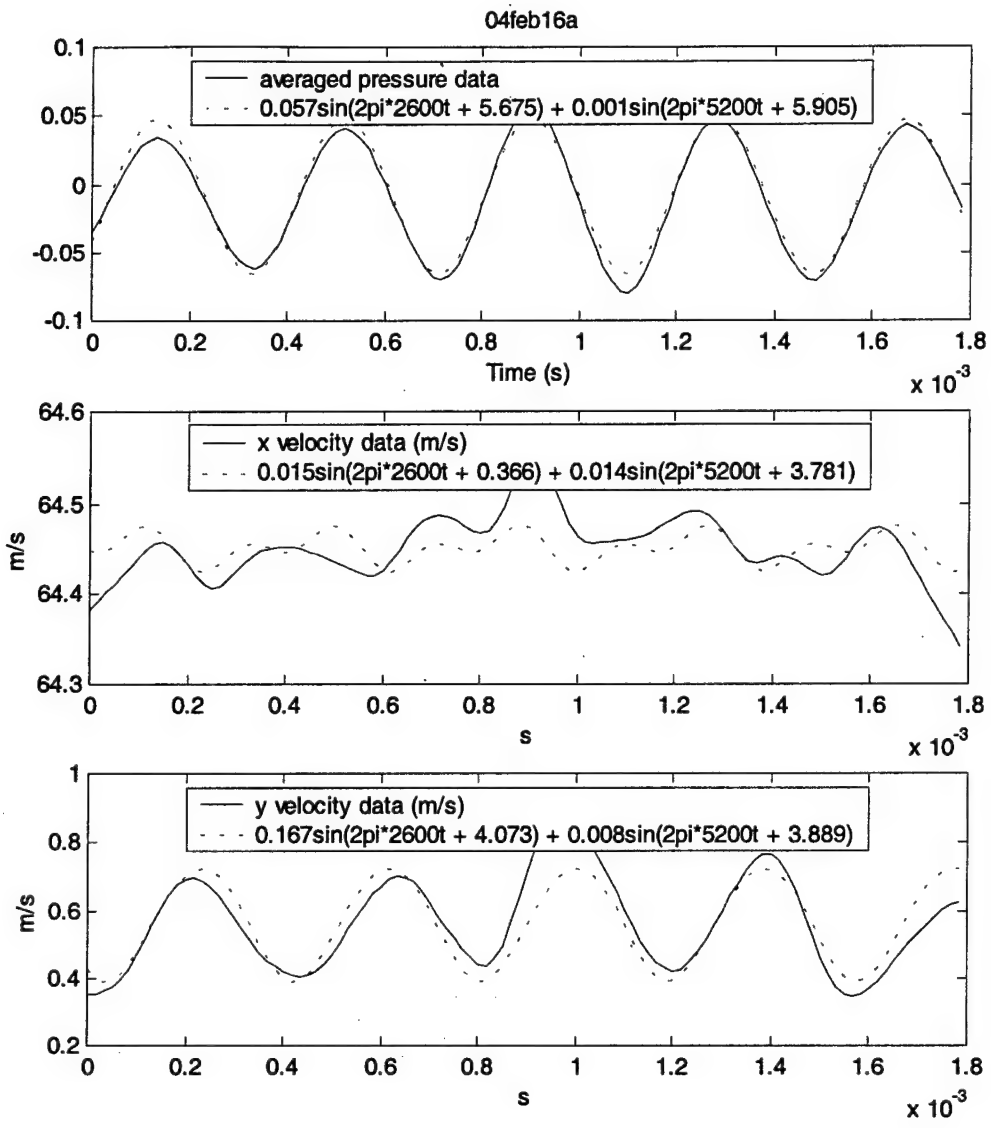

Figure 165. Data and two frequency approximation at x = -2 in, y = 0.5 in

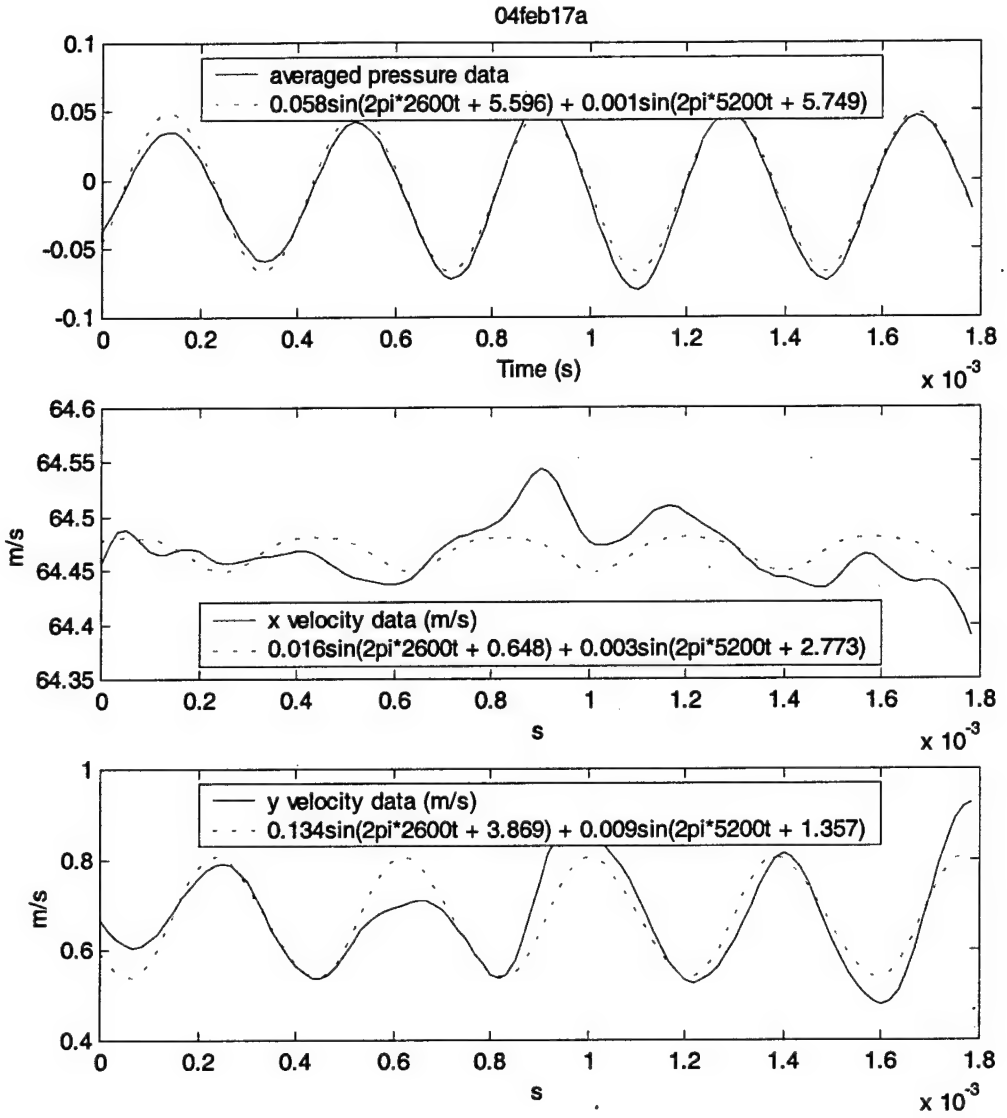

Figure 166. Data and two frequency approximation at x = -2 in, y = 0.625 in

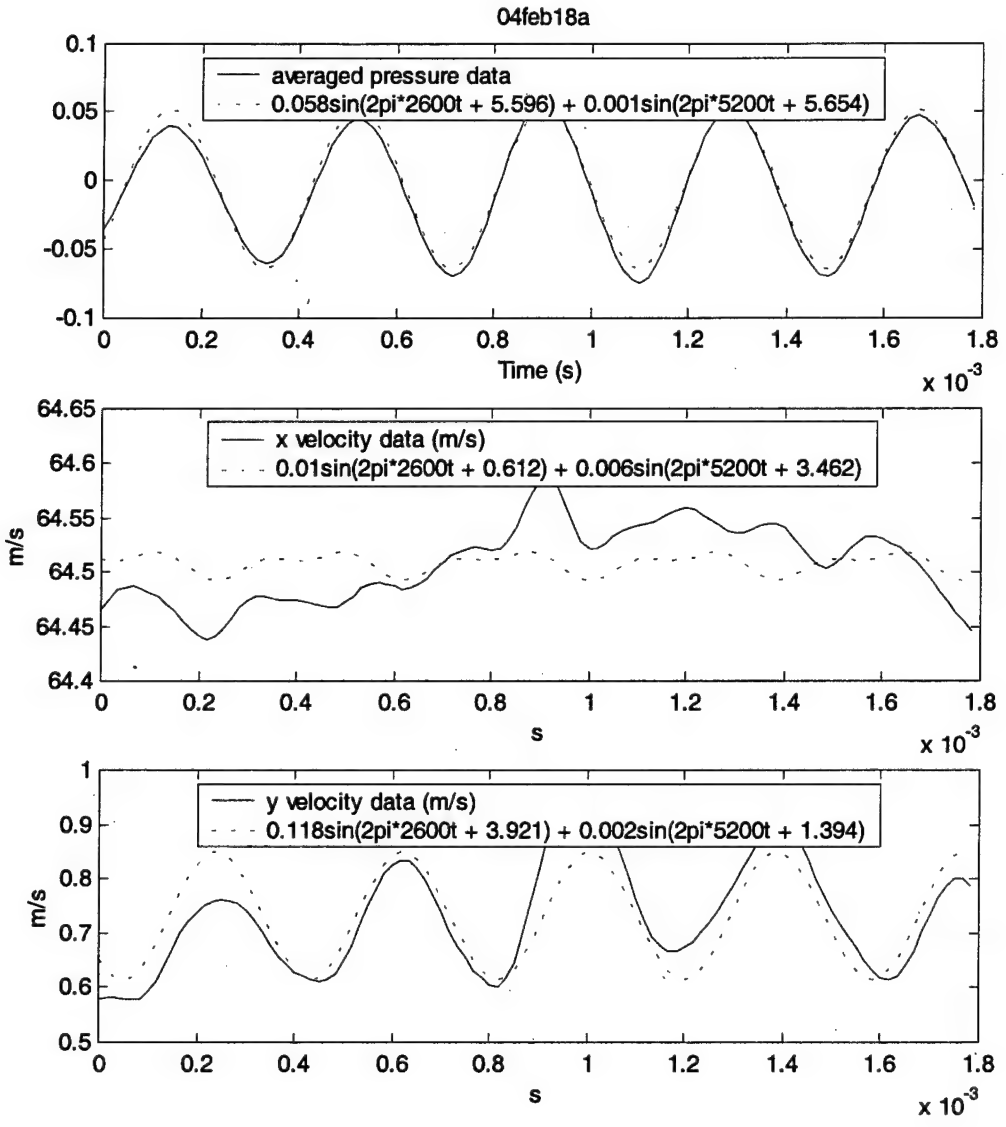

Figure 167. Data and two frequency approximation at x = -2 in, y = 0.75 in

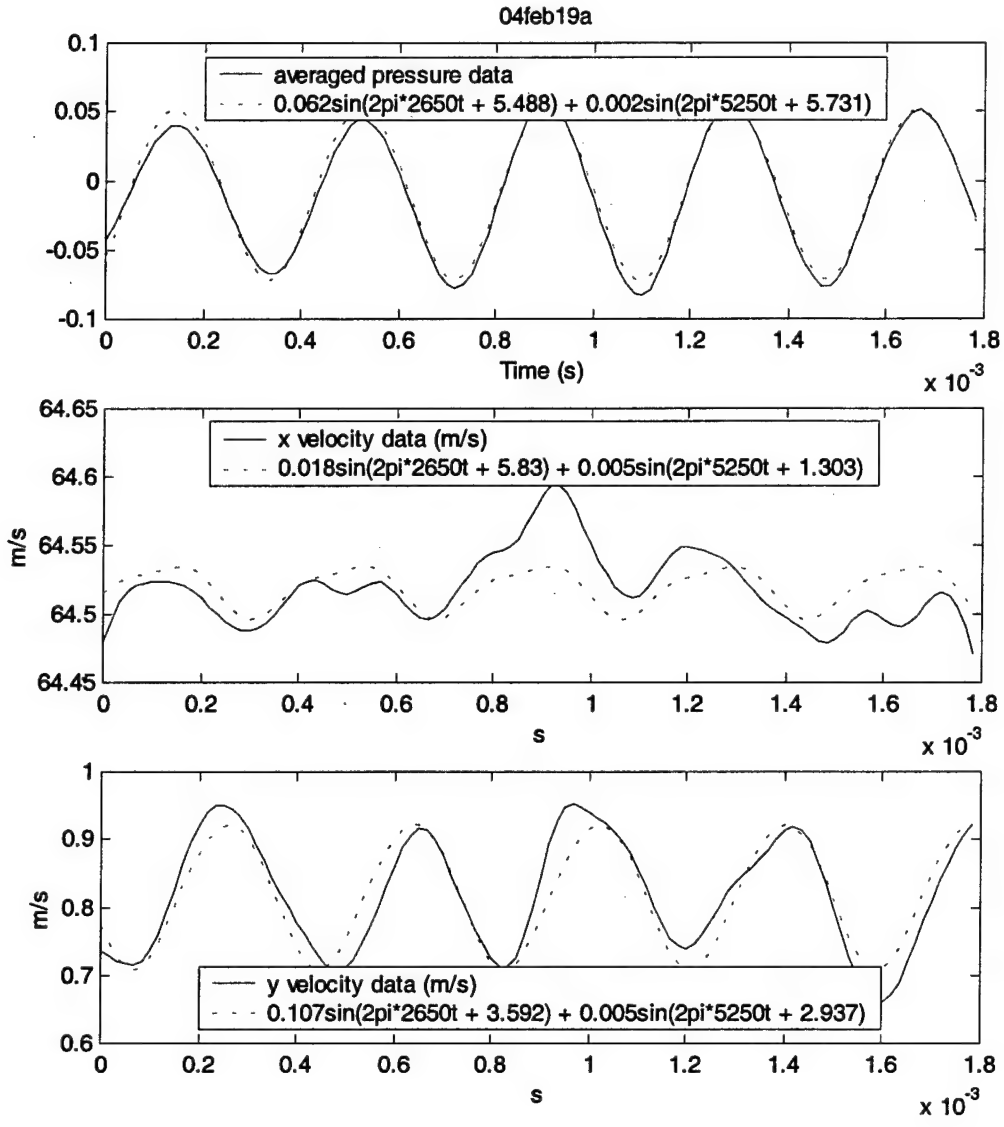

Figure 168. Data and two frequency approximation at x = -2 in, y = 0.875 in

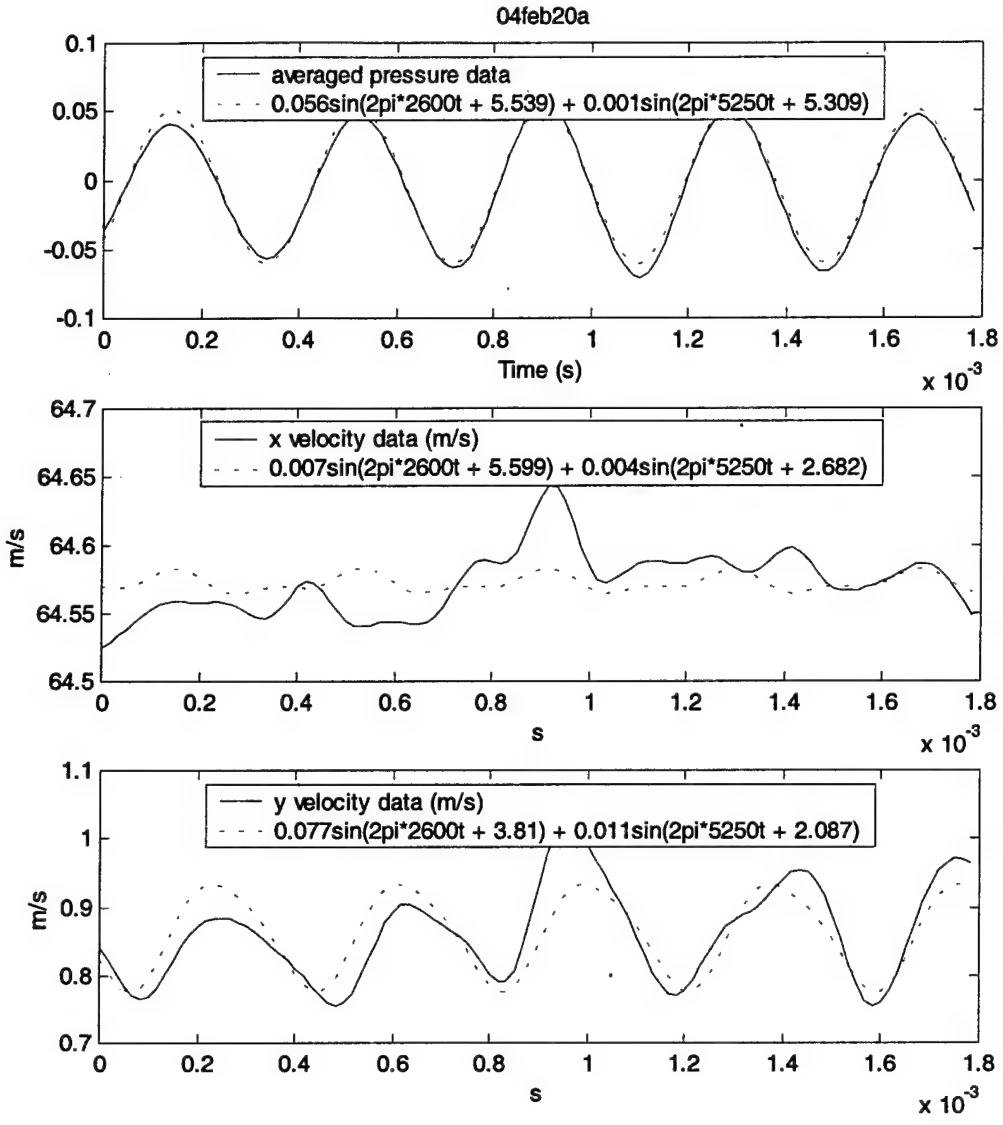

Figure 169. Data and two frequency approximation at x = -2 in, y = 1 in

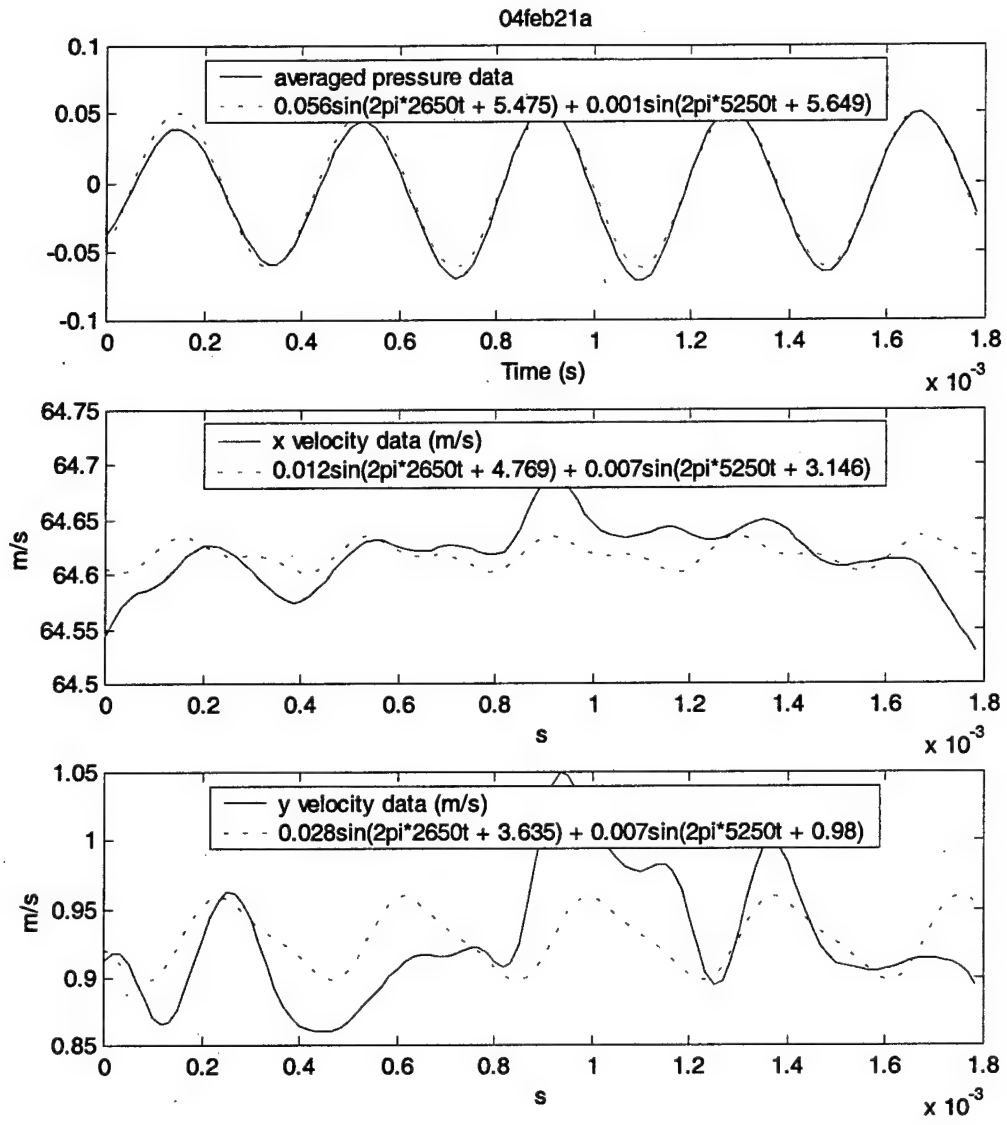

Figure 170. Data and two frequency approximation at x = -2 in, y = 1.25 in

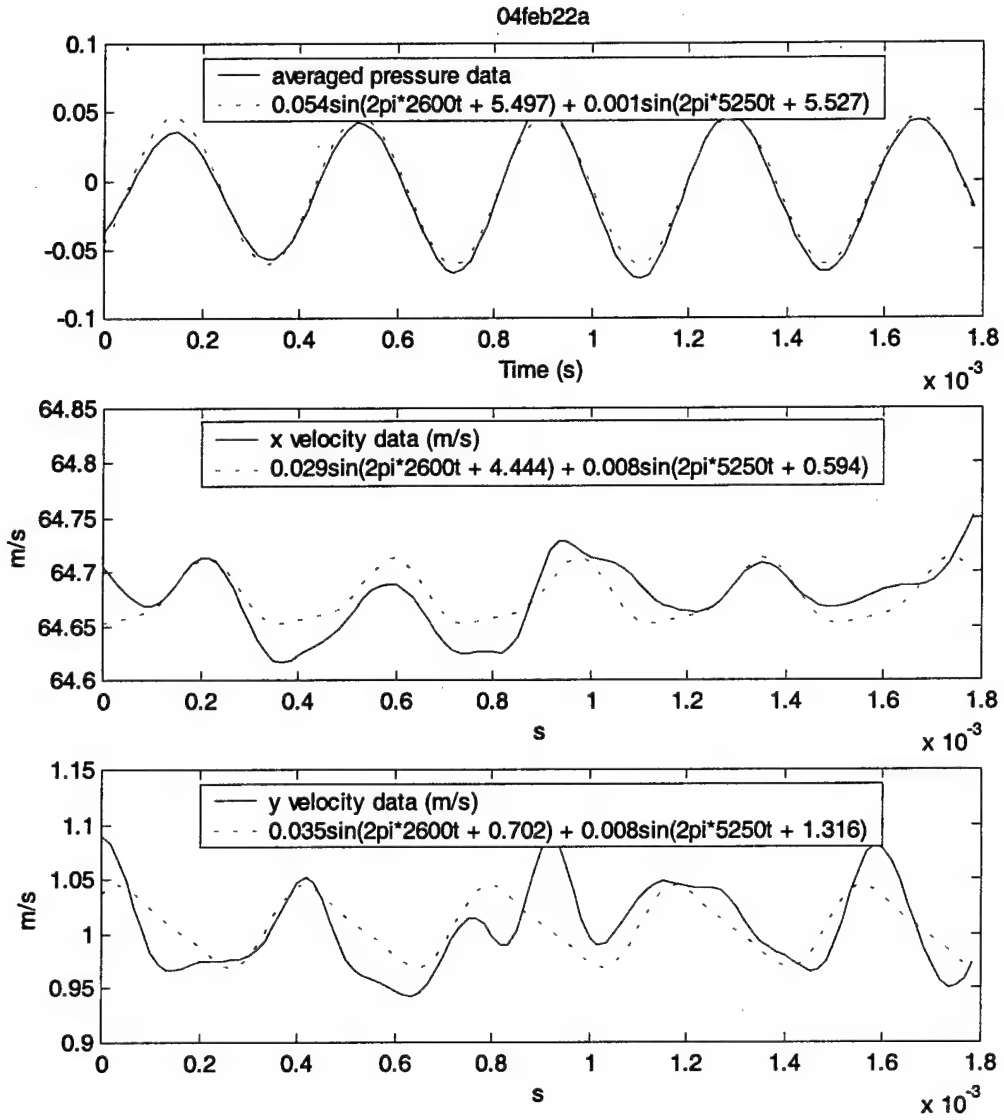

Figure 171. Data and two frequency approximation at x = -2 in, y = 1.5 in

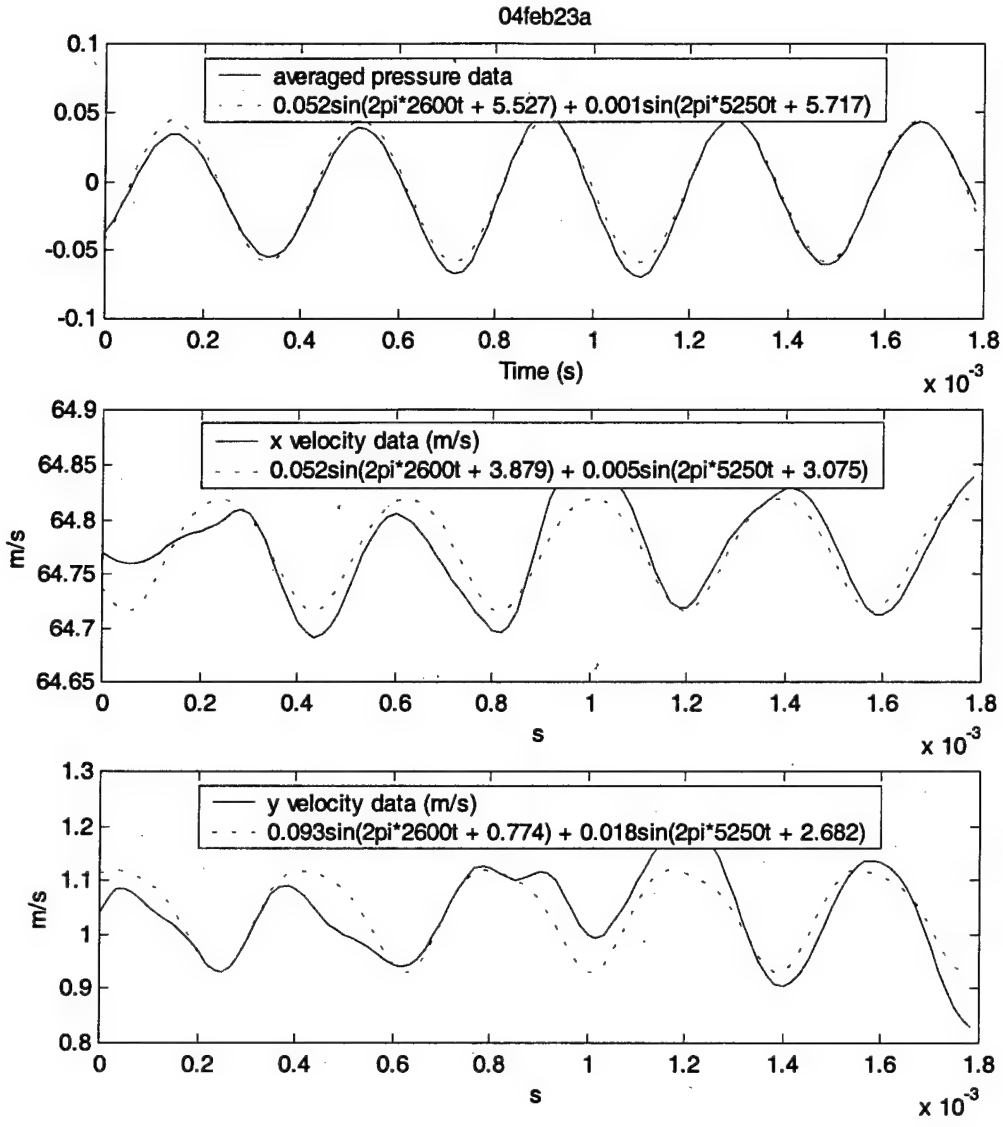

Figure 172. Data and two frequency approximation at x = -2 in, y = 2 in

5. Off-Centerline Data, x = -1 in

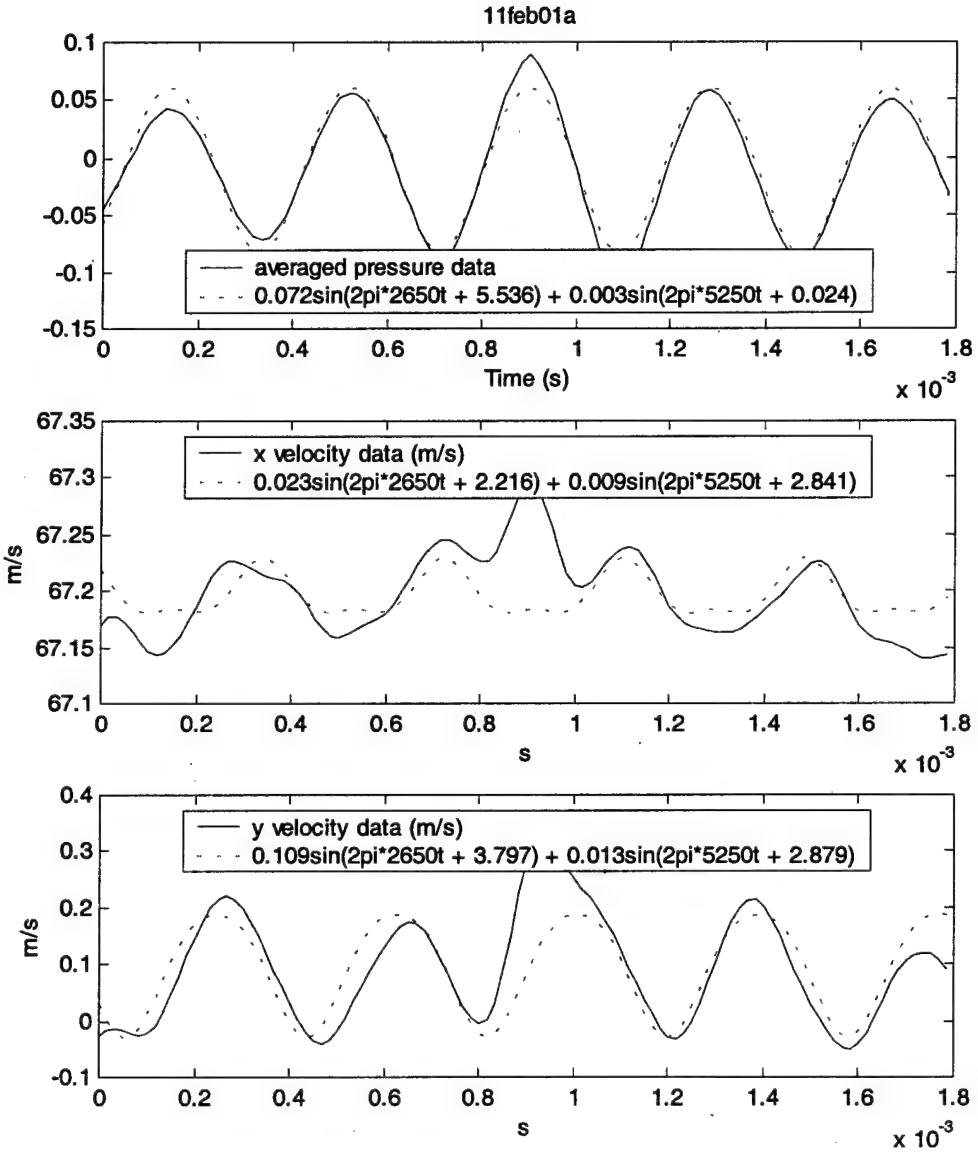

Figure 173. Data and two frequency approximation at x = -1 in, y = -1.625 in

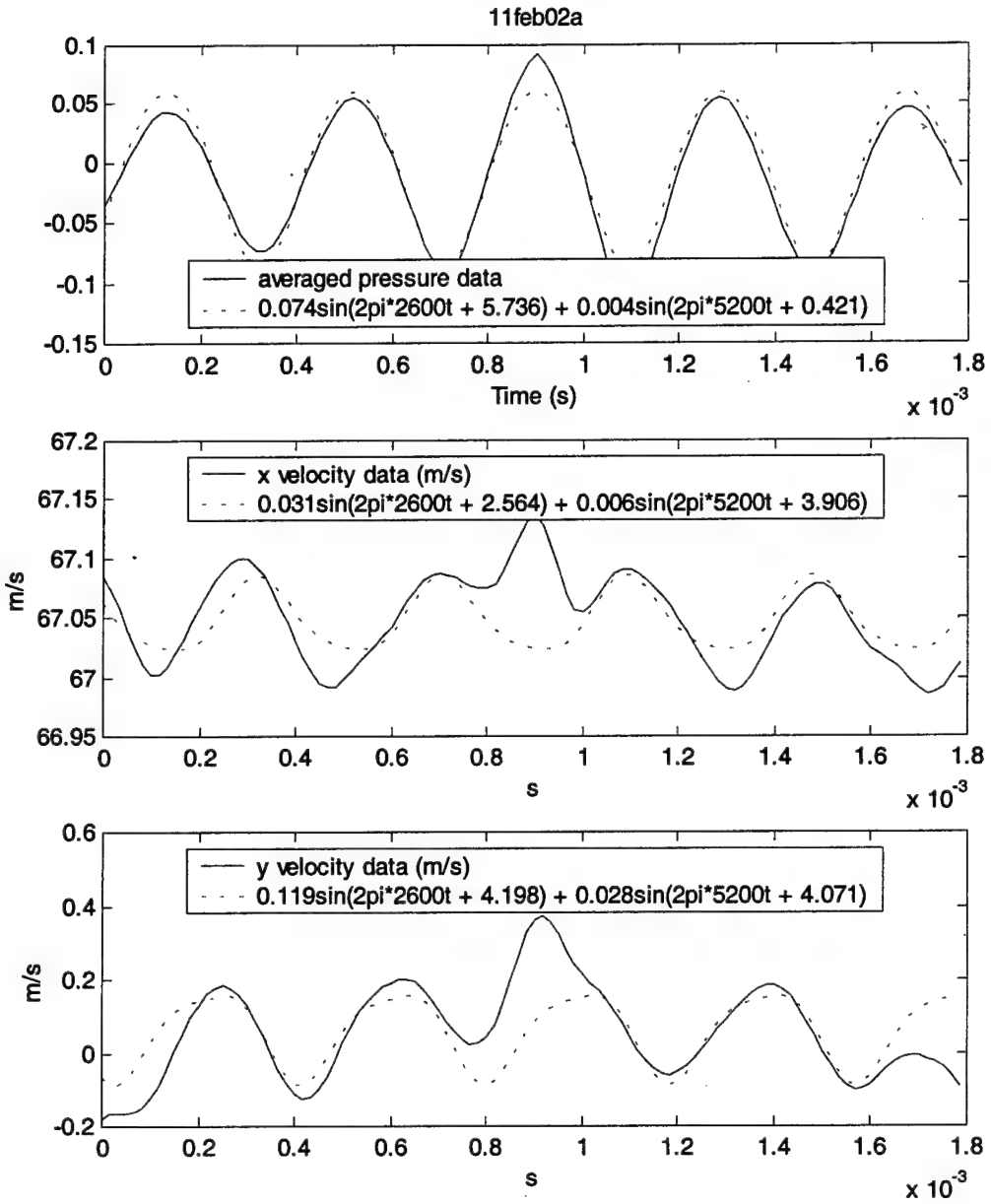

Figure 174. Data and two frequency approximation at x = -1 in, y = -1.375 in

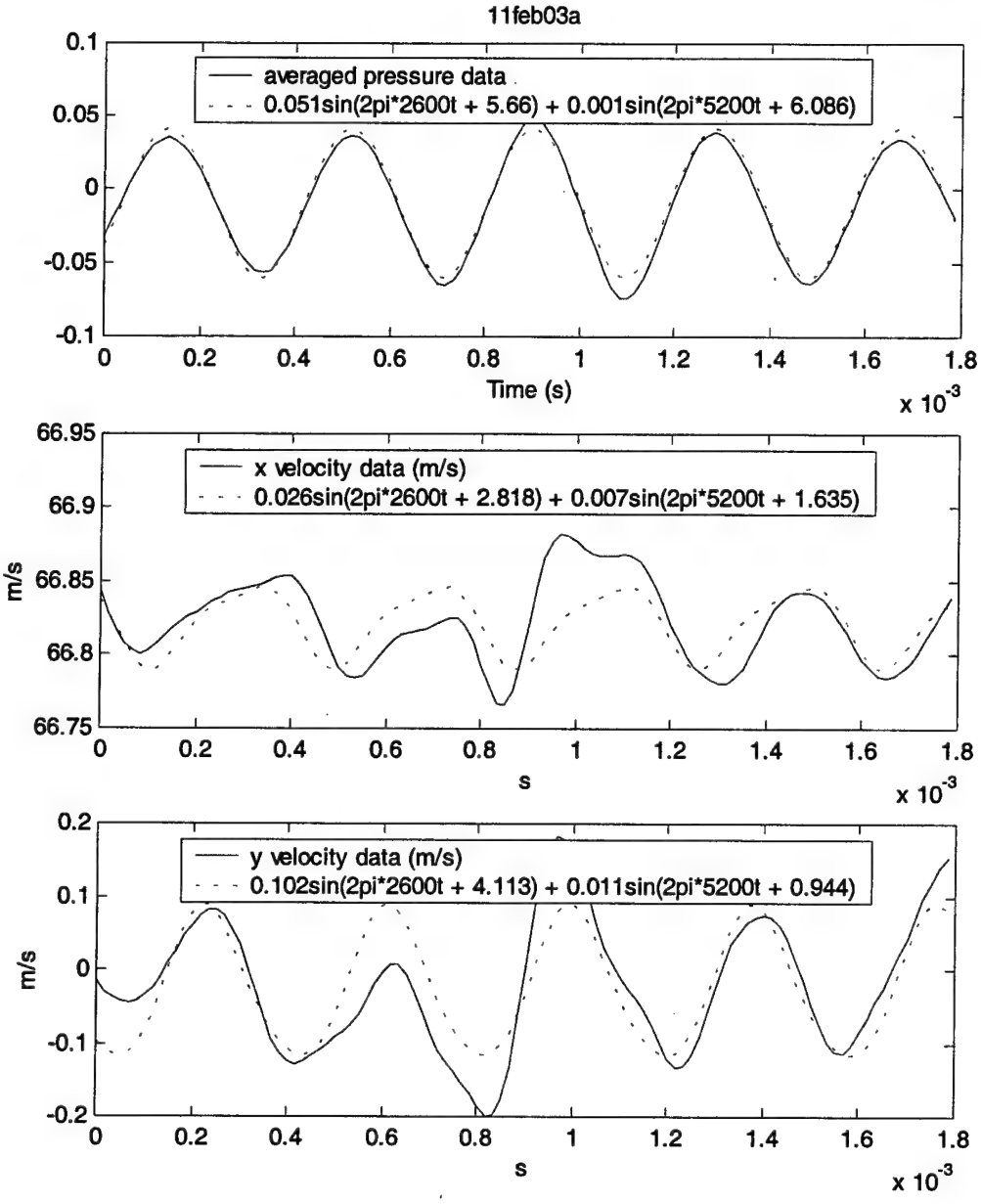

Figure 175. Data and two frequency approximation at x = -1 in, y = -1.125 in

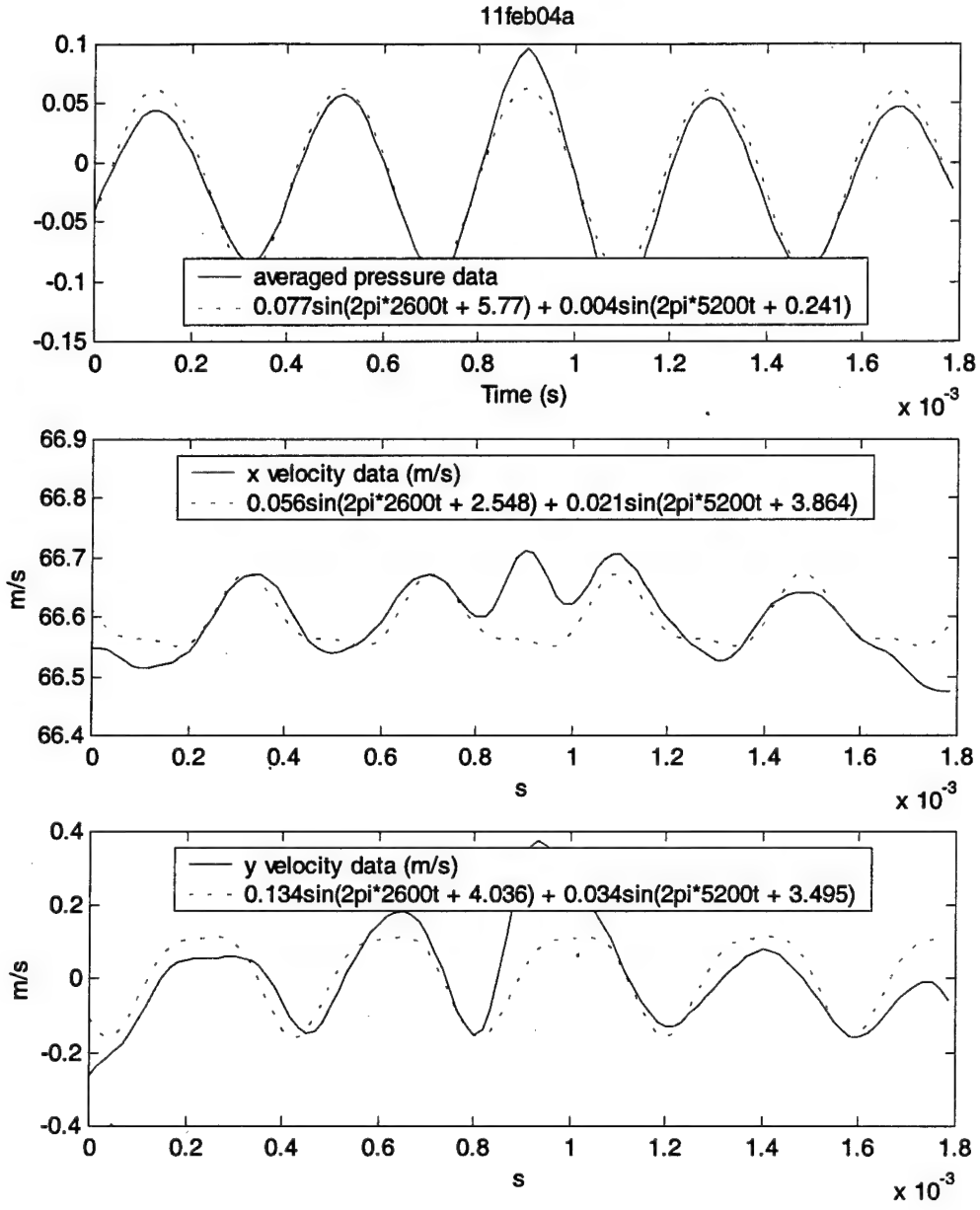

Figure 176. Data and two frequency approximation at x = -1 in, y = -0.875 in

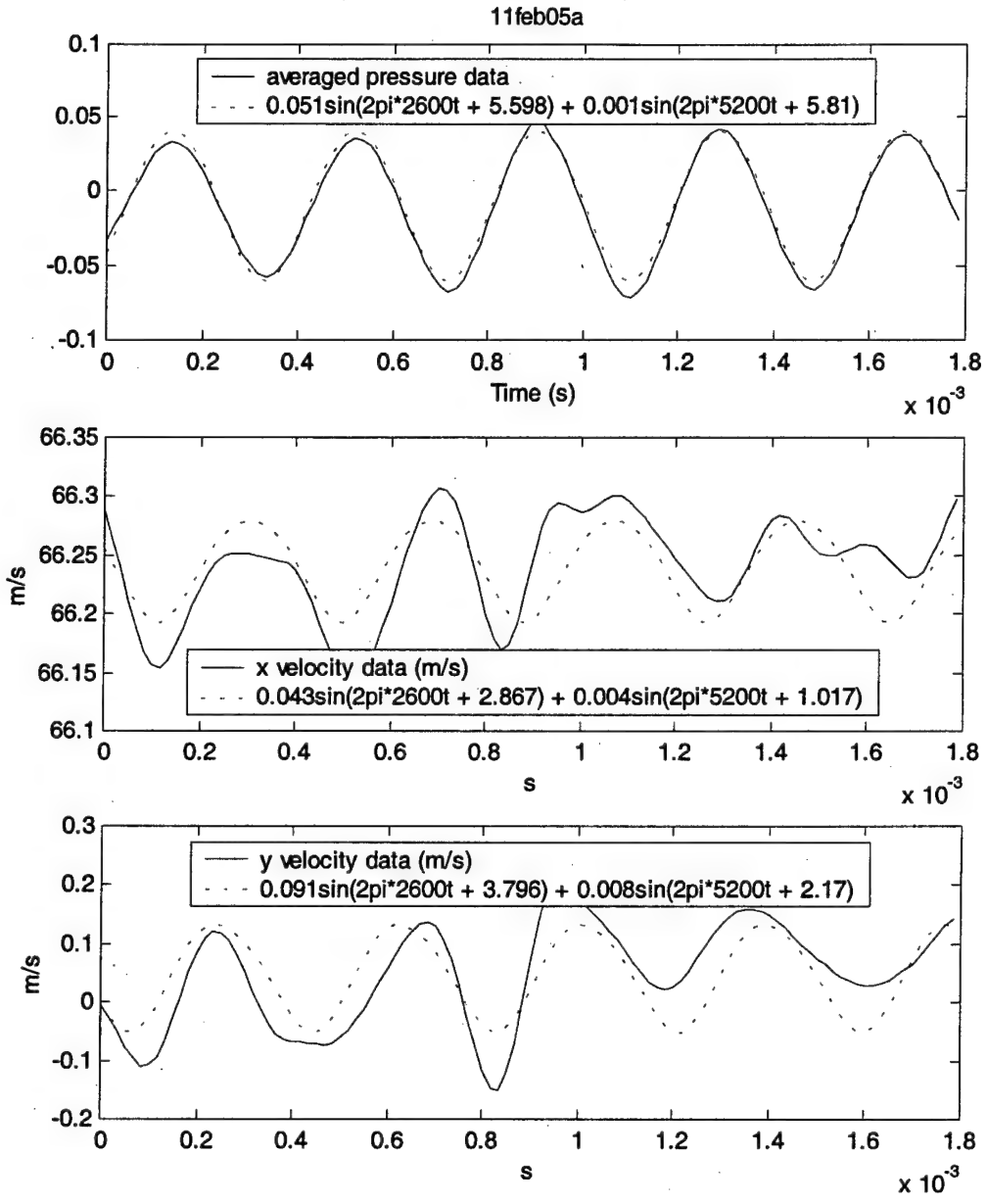

Figure 177. Data and two frequency approximation at x = -1 in, y = -0.625 in

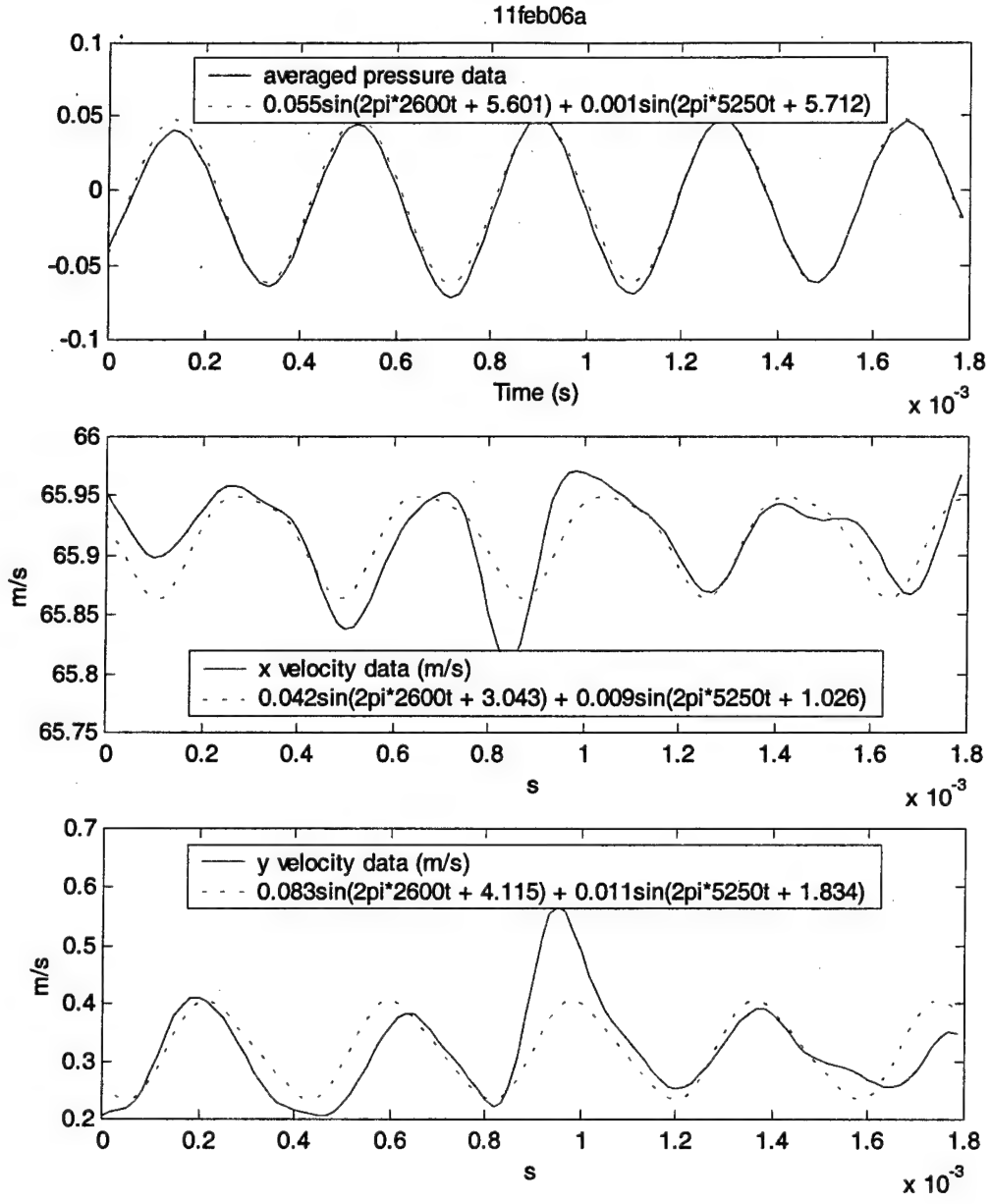

Figure 178. Data and two frequency approximation at x = -1 in, y = -0.375 in

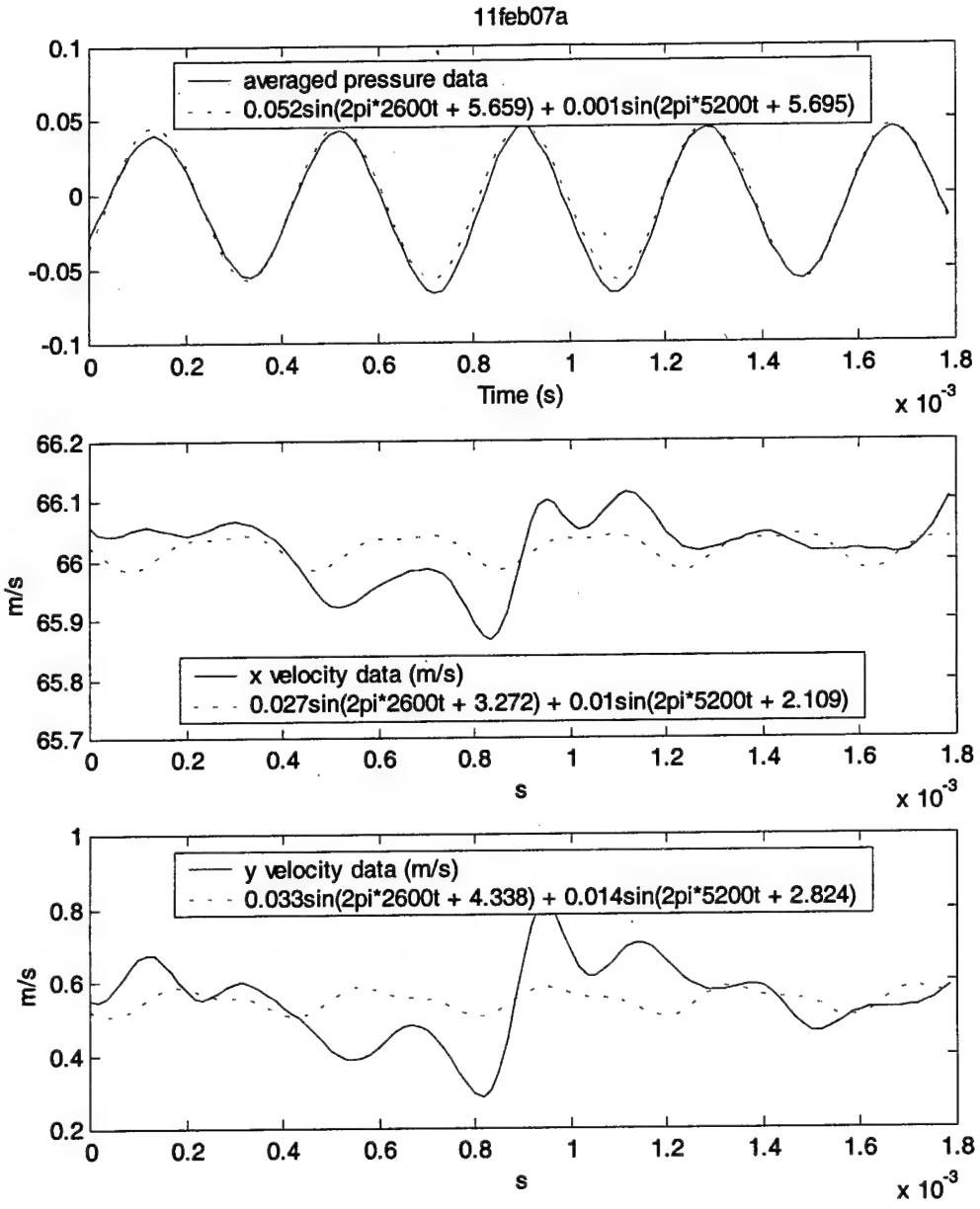

Figure 179. Data and two frequency approximation at x = -1 in, y = -0.125 in

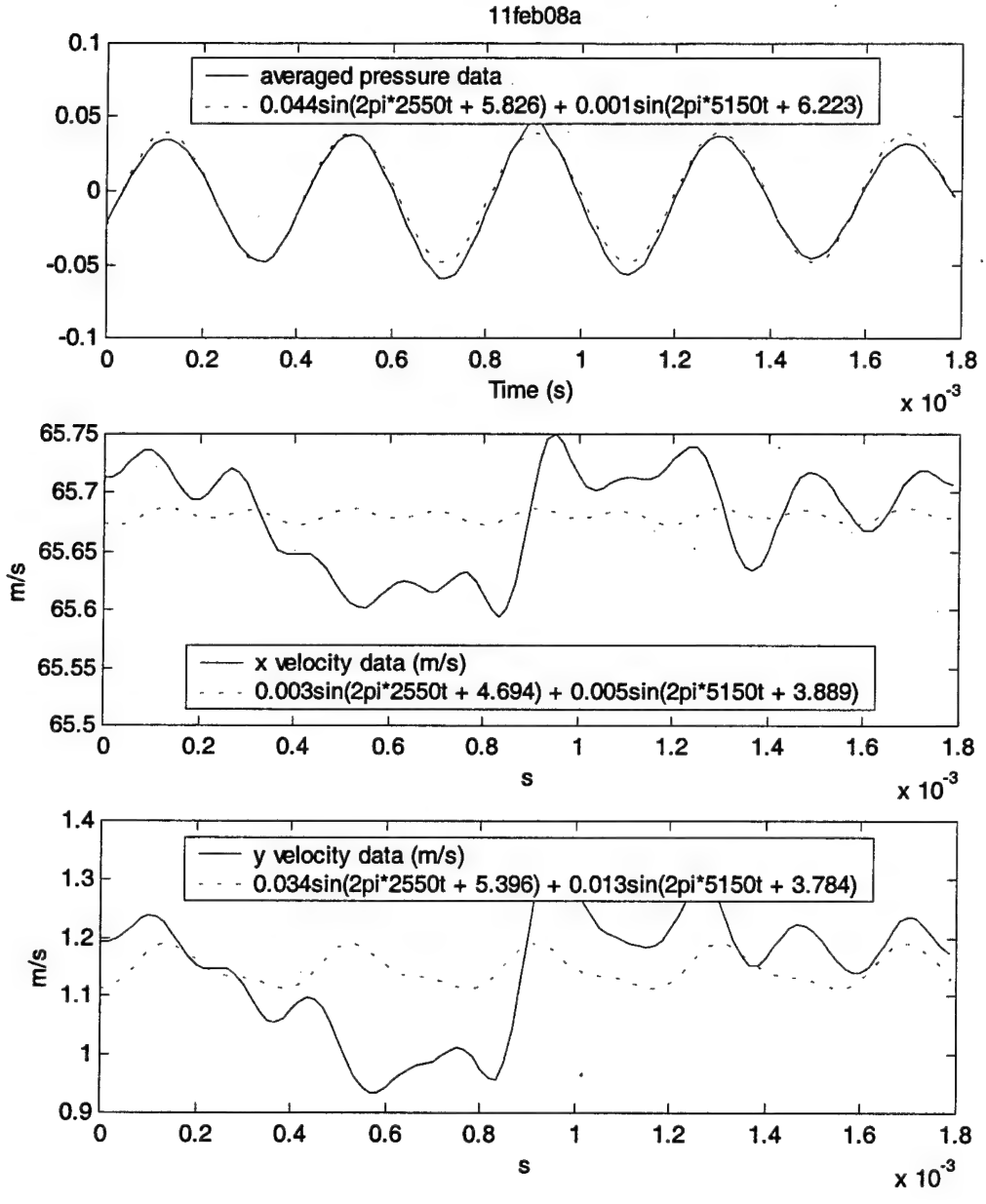

Figure 180. Data and two frequency approximation at x = -1 in, y = 0.125 in

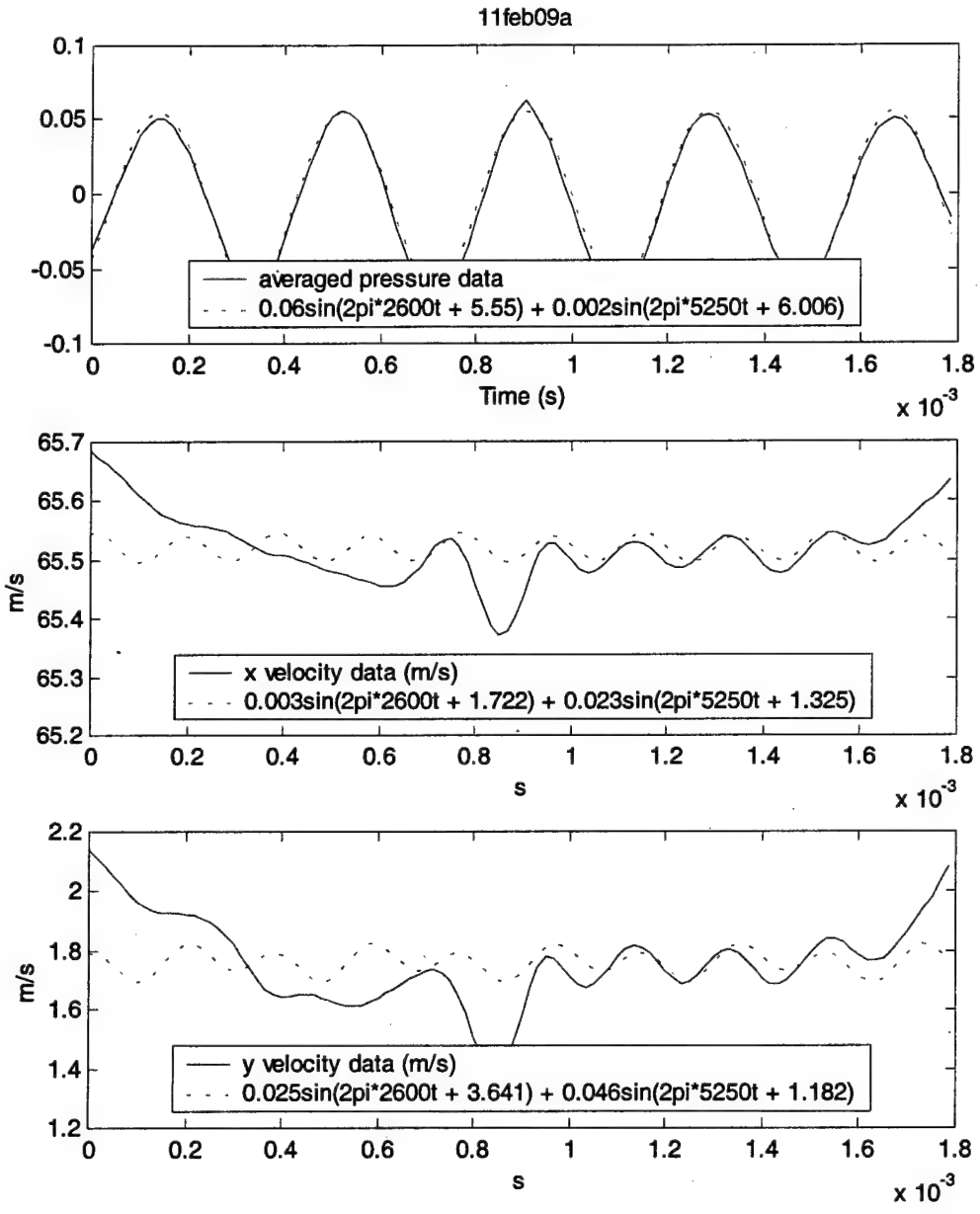

Figure 181. Data and two frequency approximation at x = -1 in, y = 0.375 in

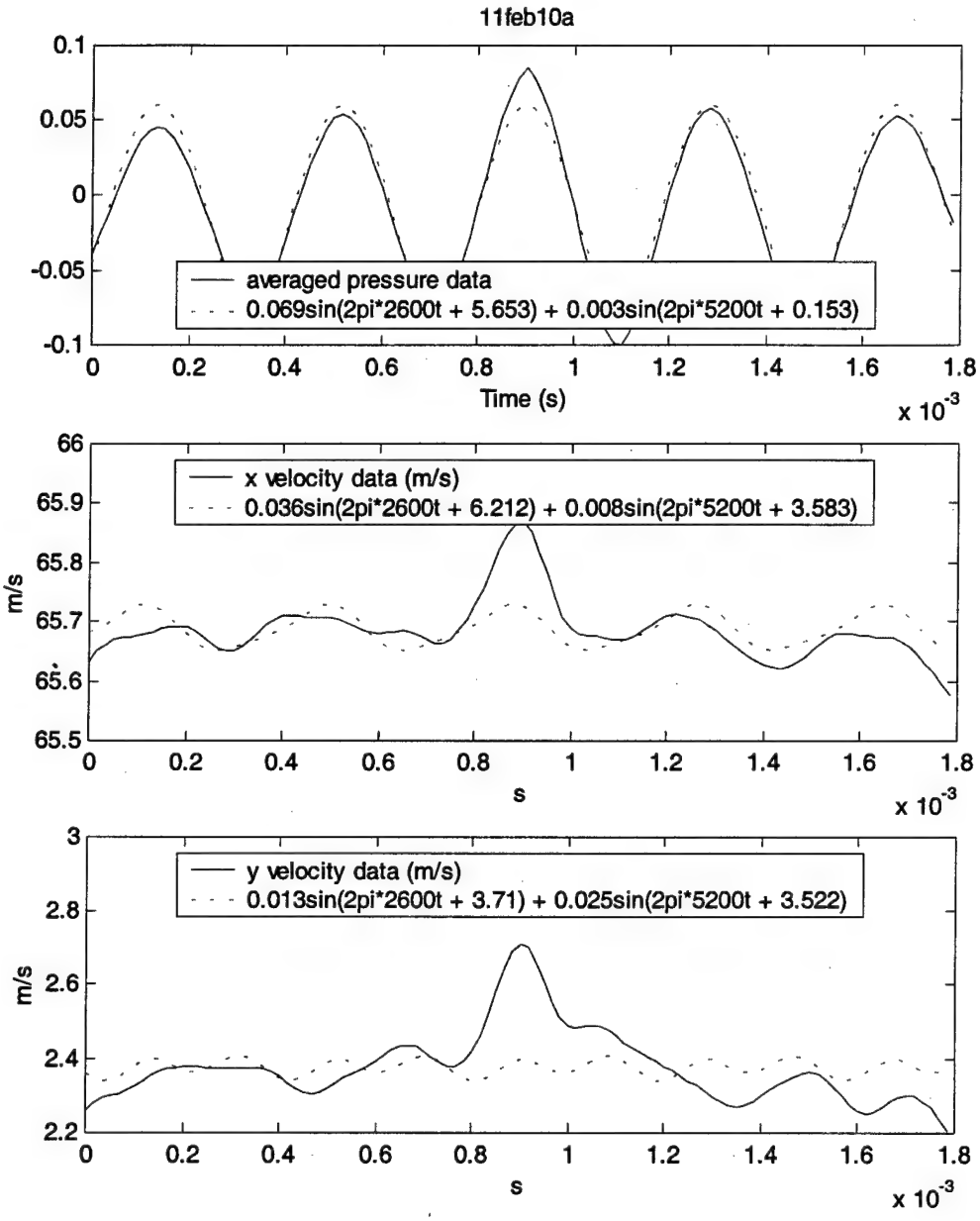

Figure 182. Data and two frequency approximation at x = -1 in, y = 0.625 in

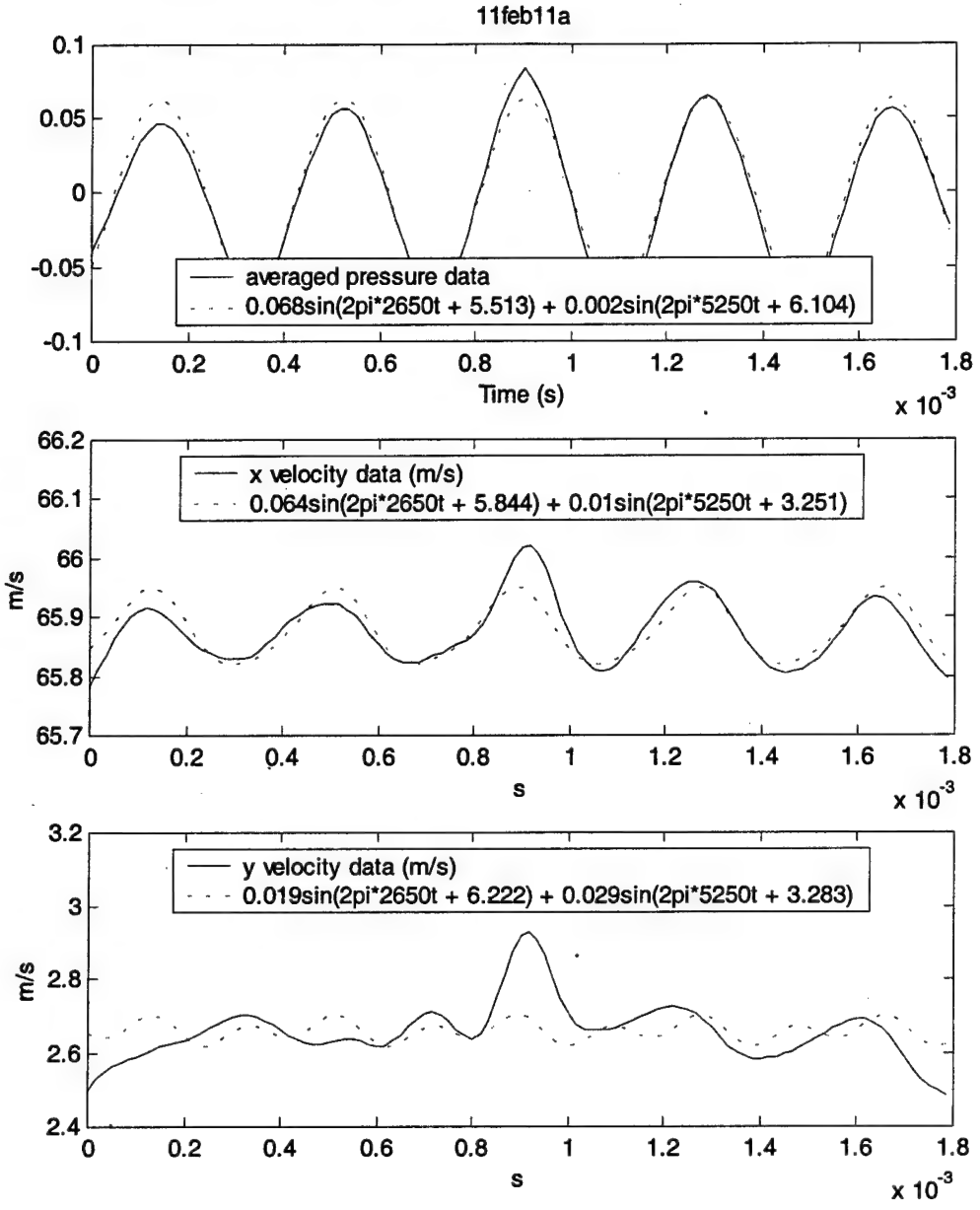

Figure 183. Data and two frequency approximation at x = -1 in, y = 0.875 in

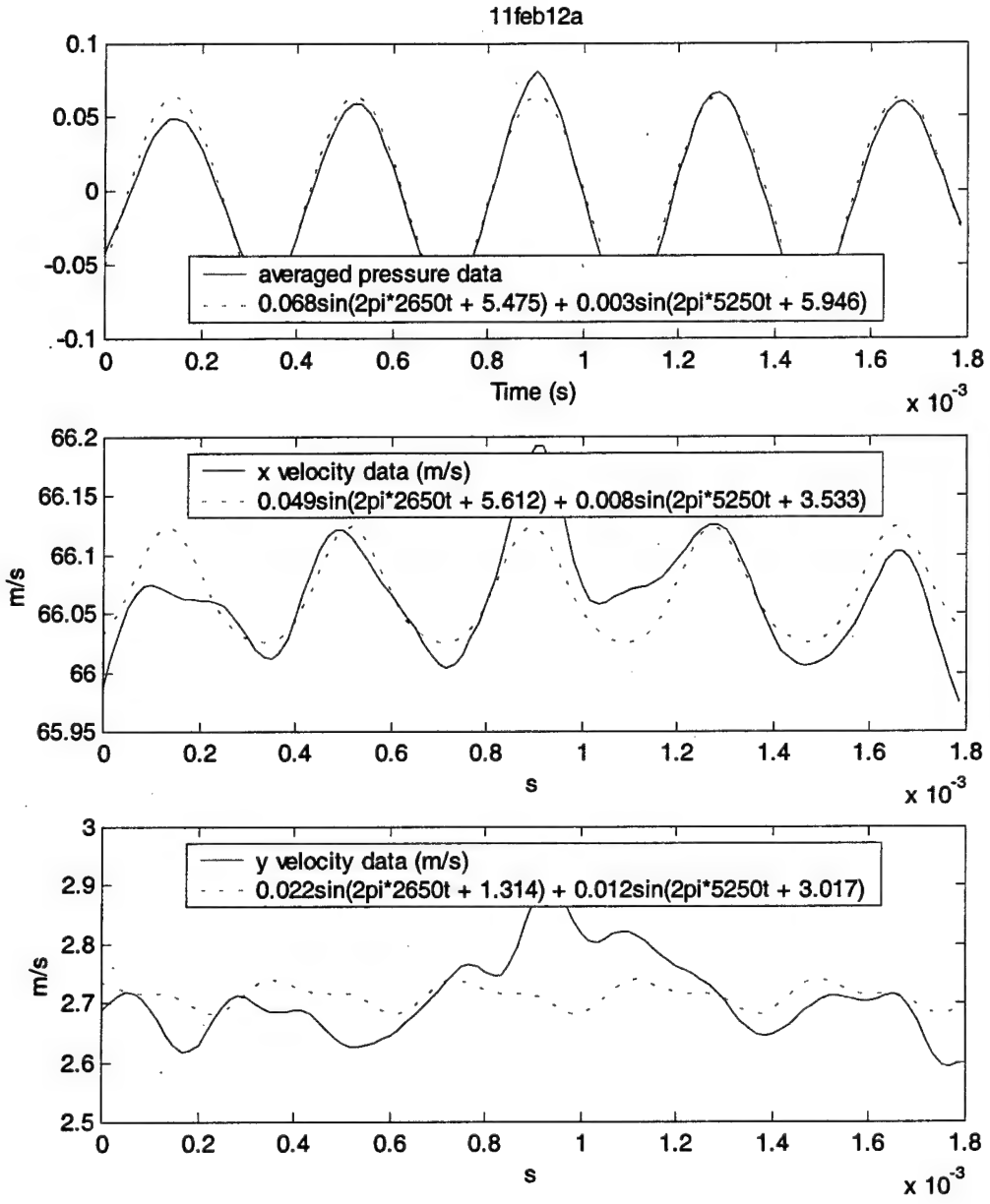

Figure 184. Data and two frequency approximation at x = -1 in, y = 1.125 in

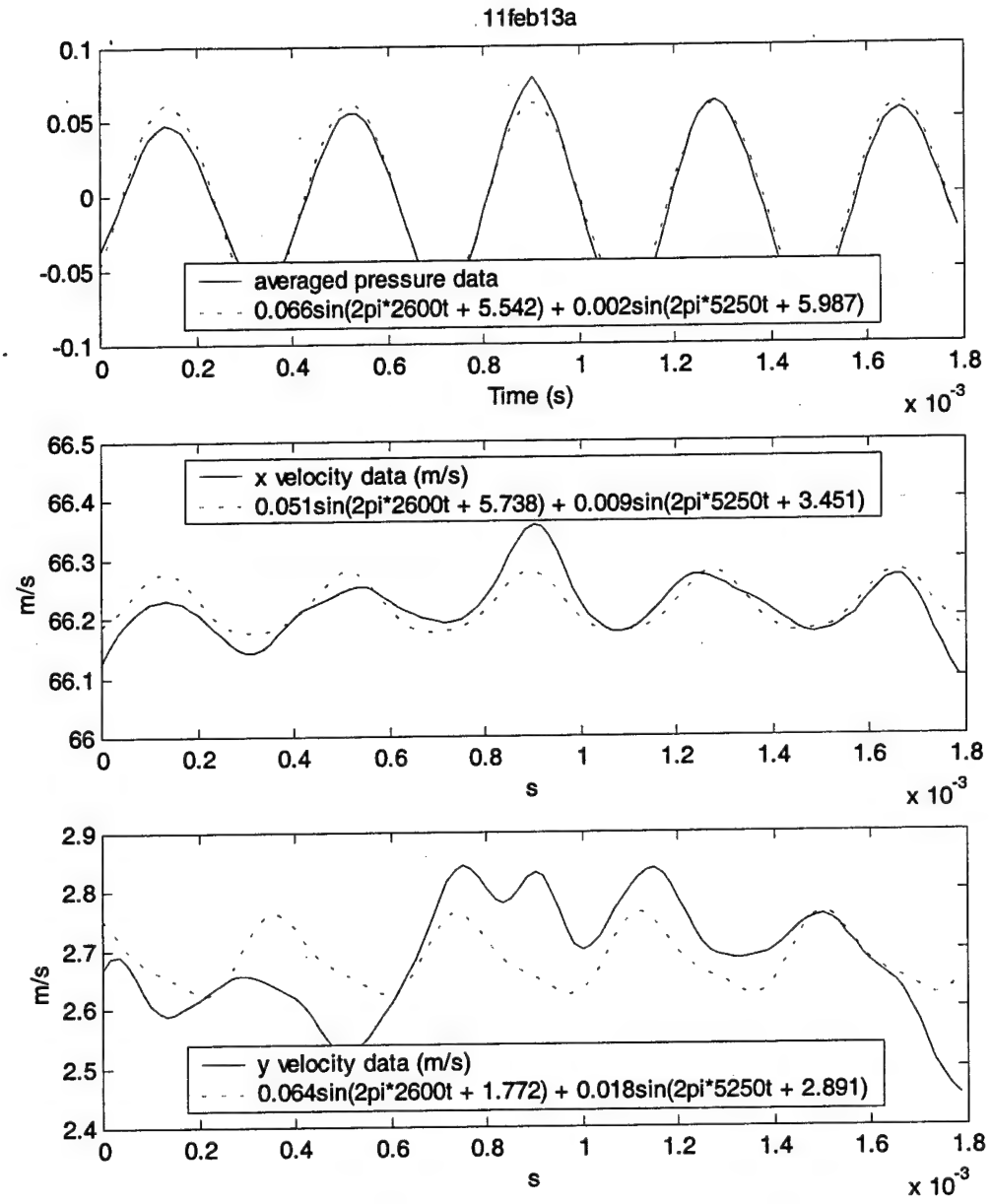

Figure 185. Data and two frequency approximation at x = -1 in, y = 1.375 in

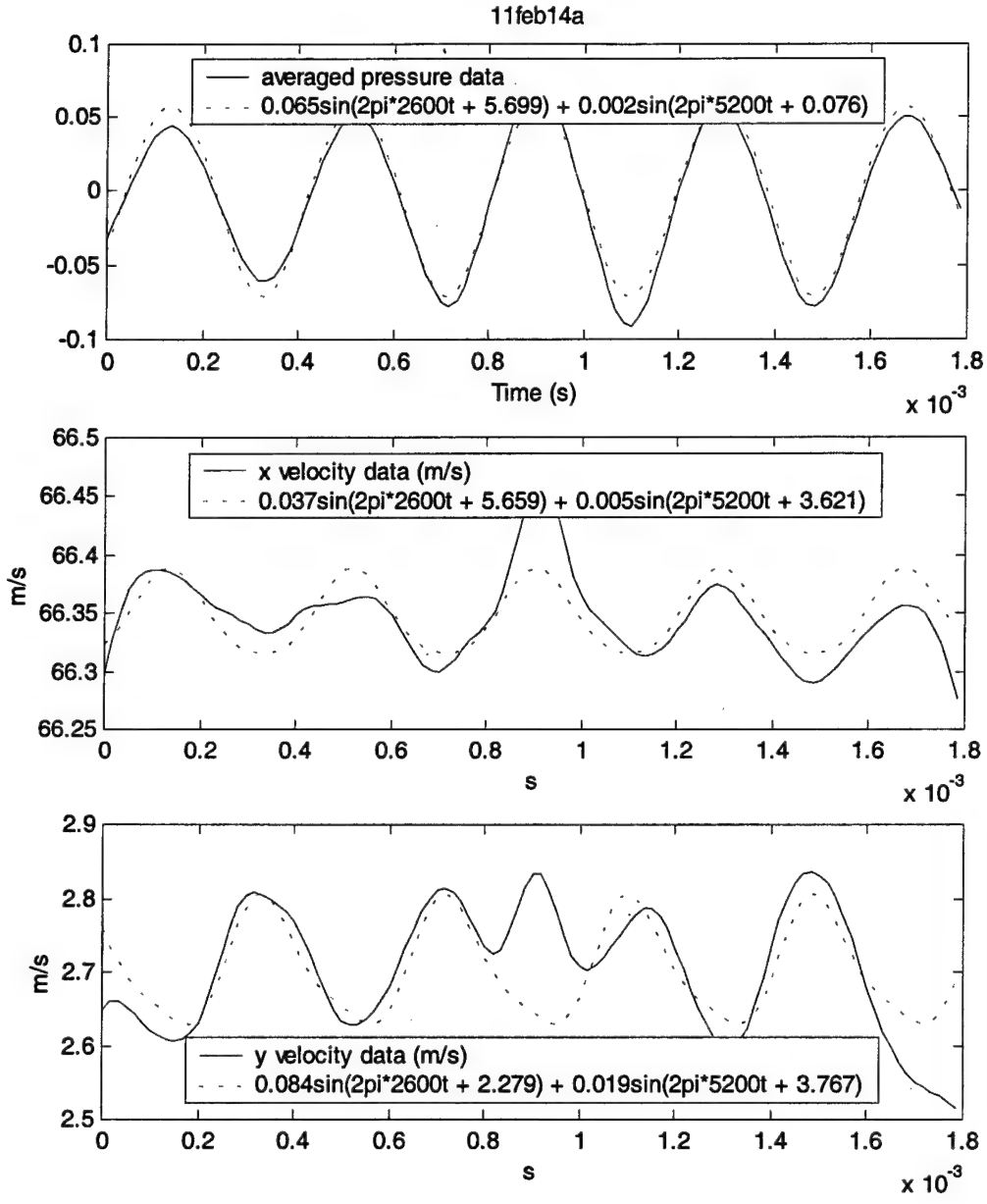

Figure 186. Data and two frequency approximation at x = -1 in, y = 1.625 in

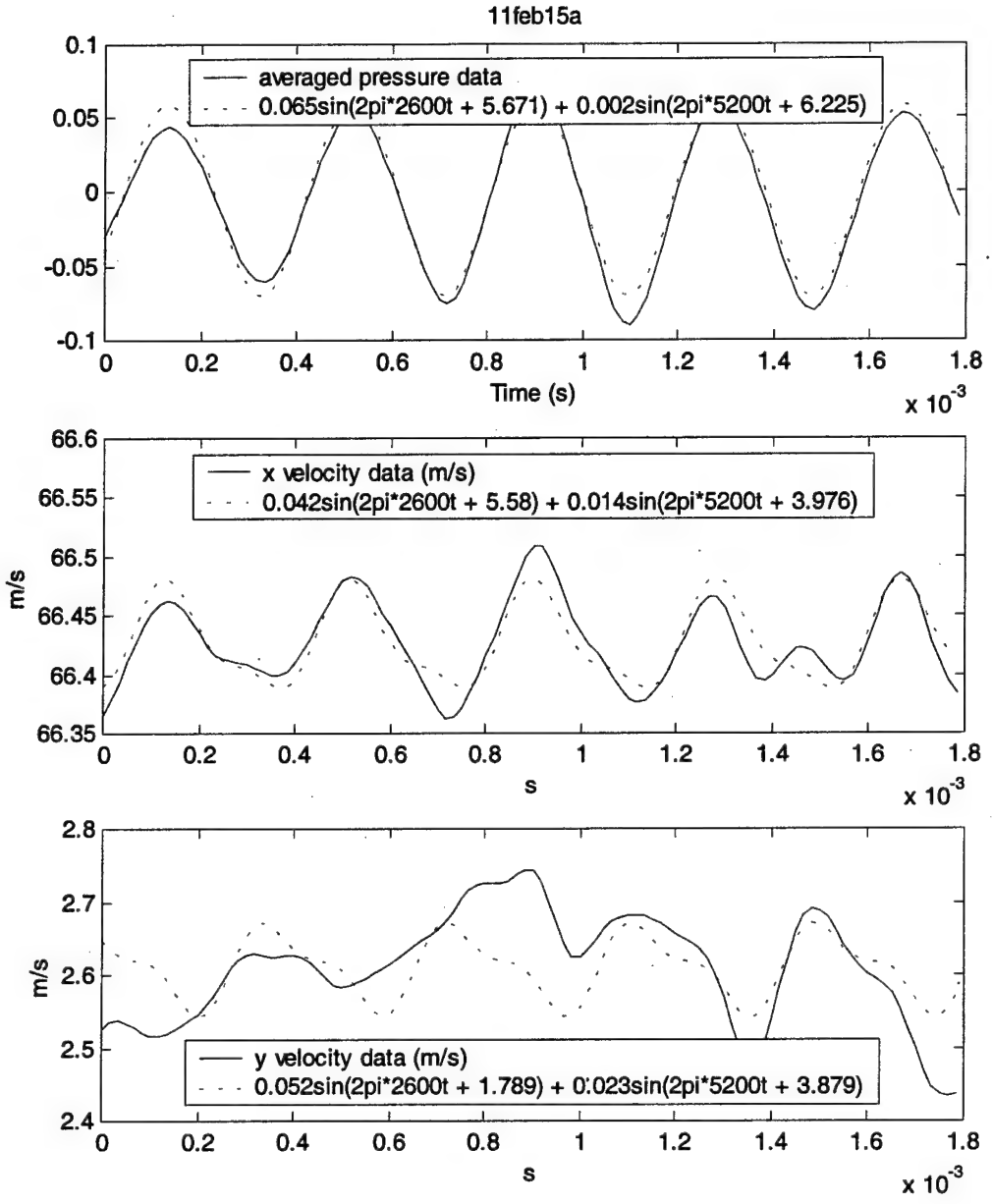

Figure 187. Data and two frequency approximation at x = -1 in, y = 1.875 in

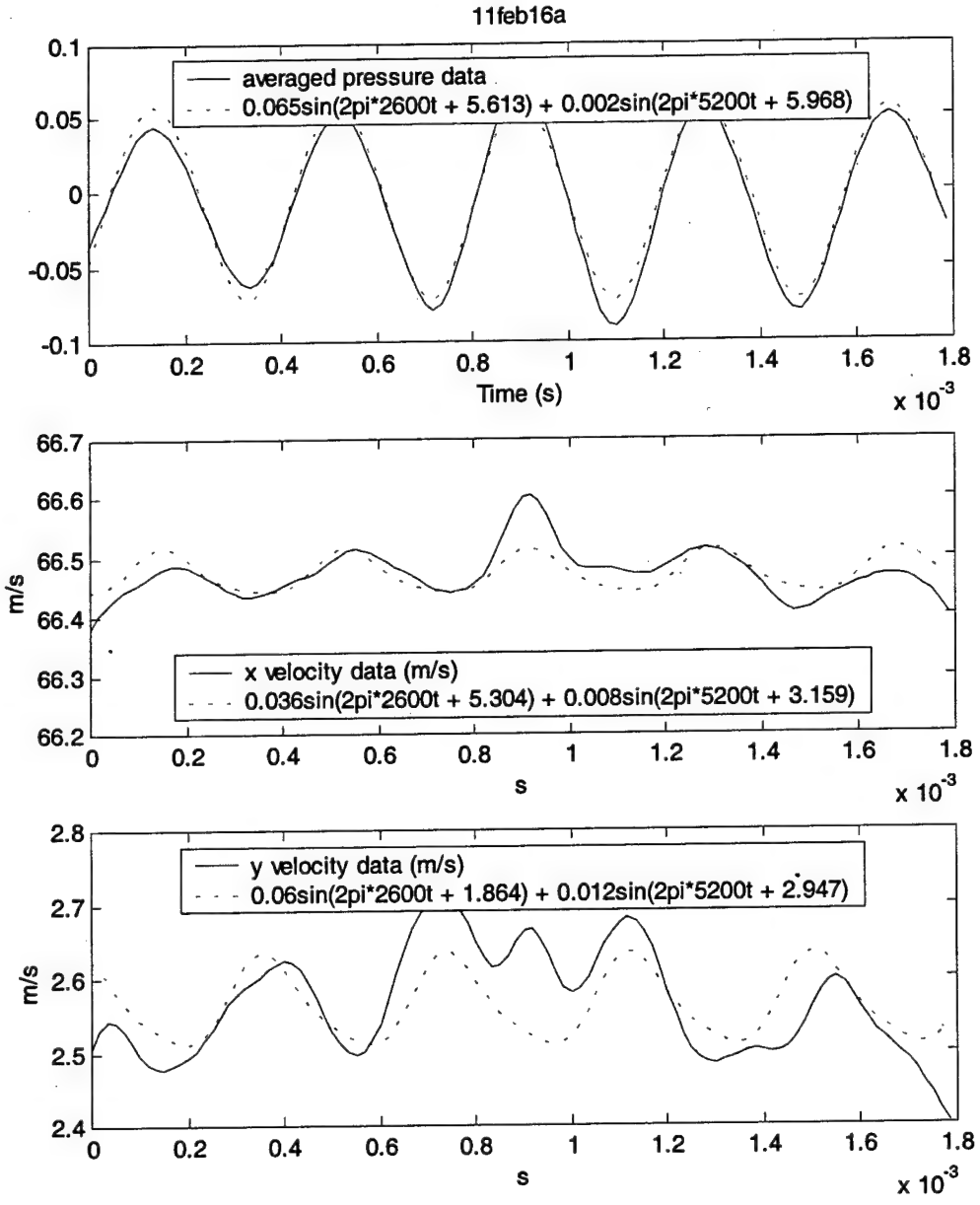

Figure 188. Data and two frequency approximation at x = -1 in, y = 2.125 in

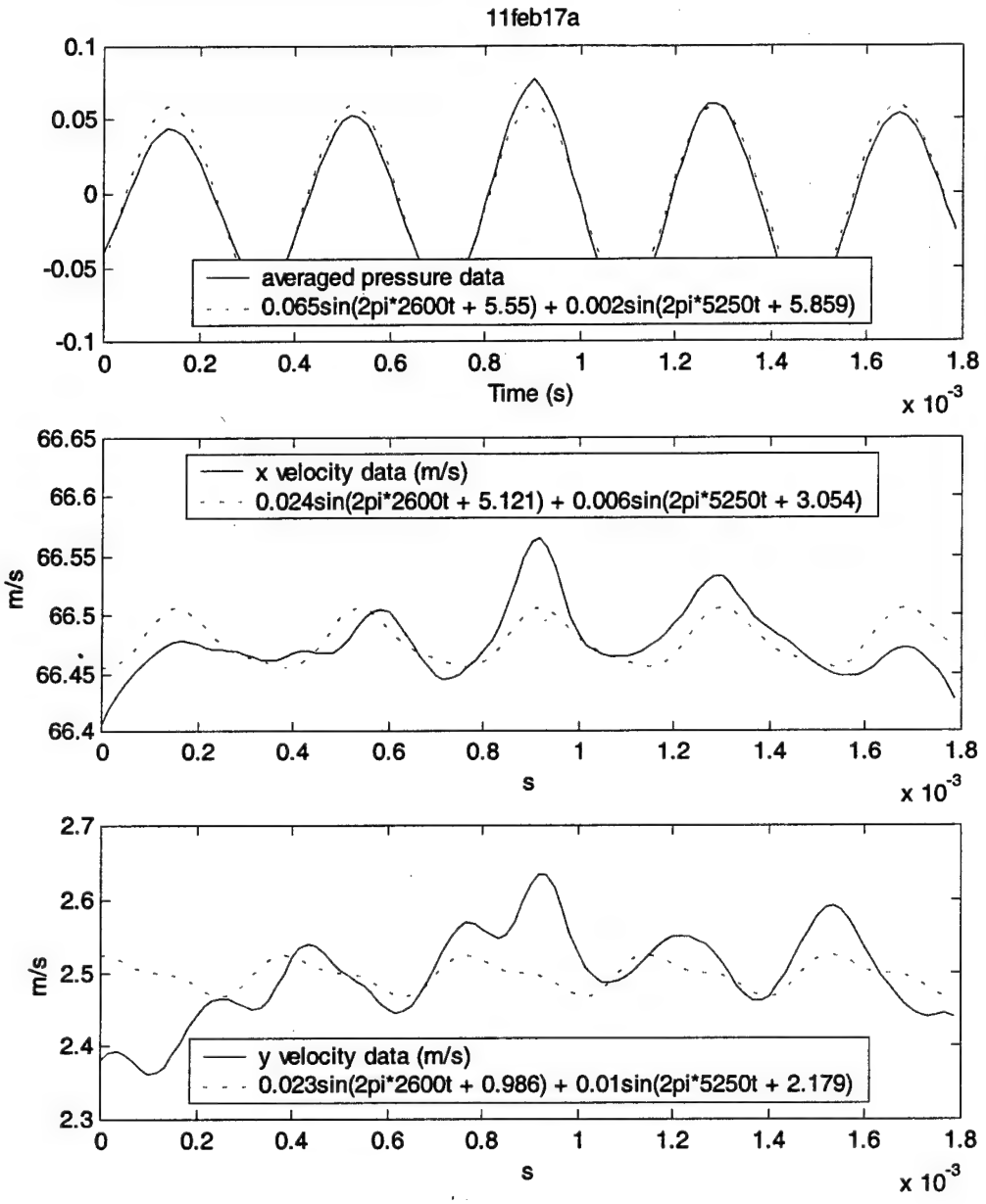

Figure 189. Data and two frequency approximation at x = -1 in, y = 2.375 in

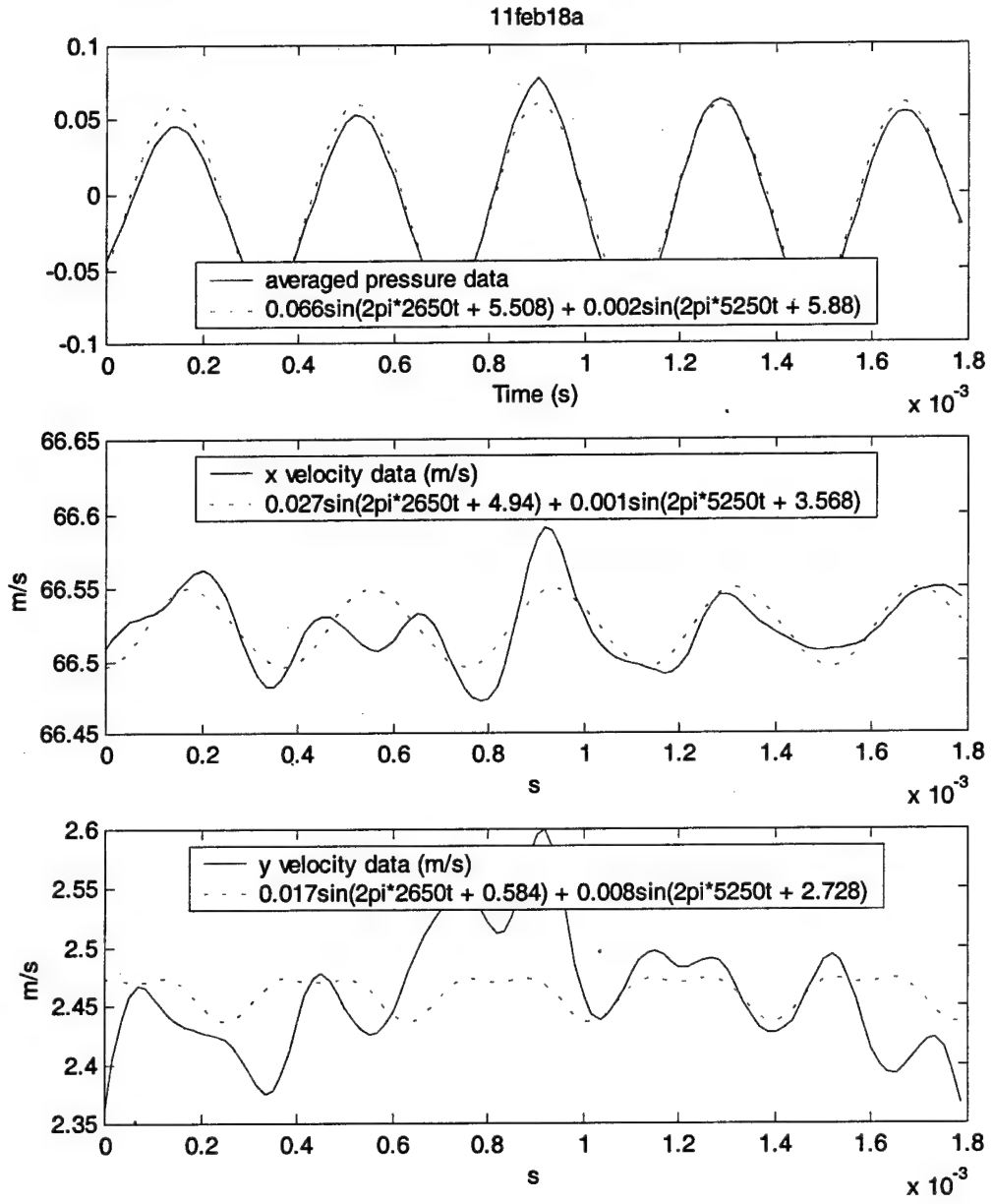

Figure 190. Data and two frequency approximation at x = -1 in, y = 2.625 in

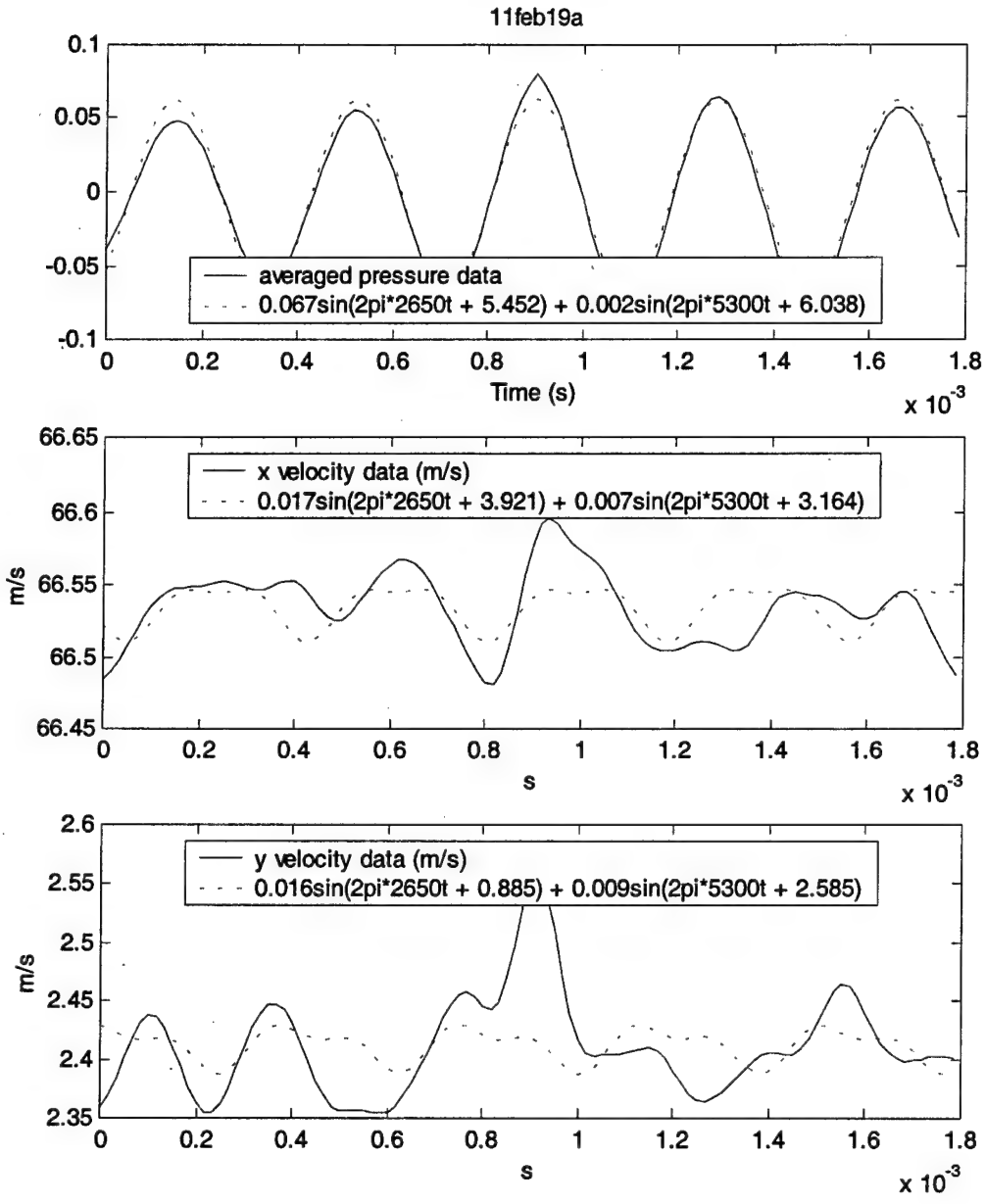

Figure 191. Data and two frequency approximation at x = -1 in, y = 2.875 in

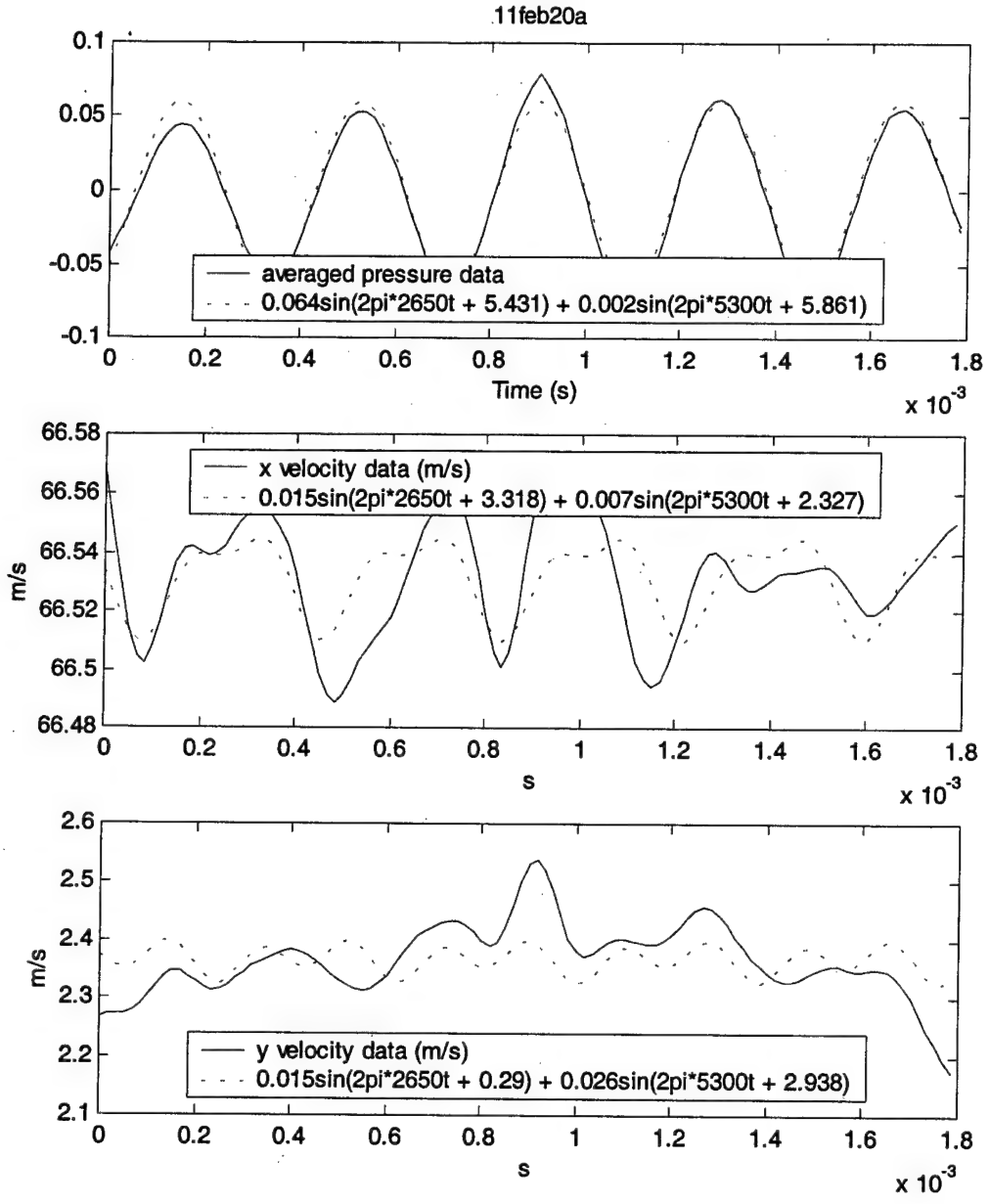

Figure 192. Data and two frequency approximation at x = -1 in, y = 3.125 in

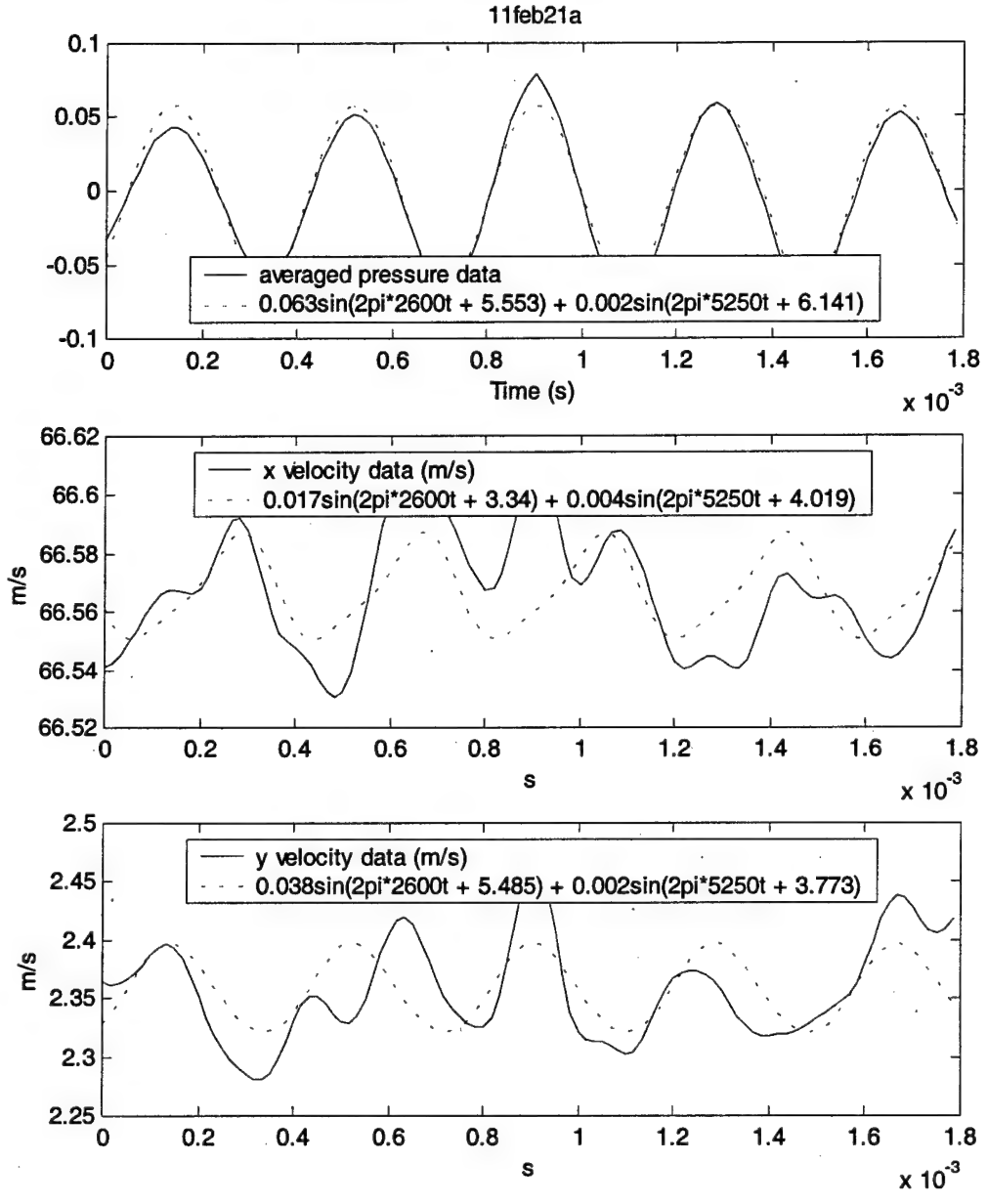

Figure 193. Data and two frequency approximation at x = -1 in, y = 3.375 in

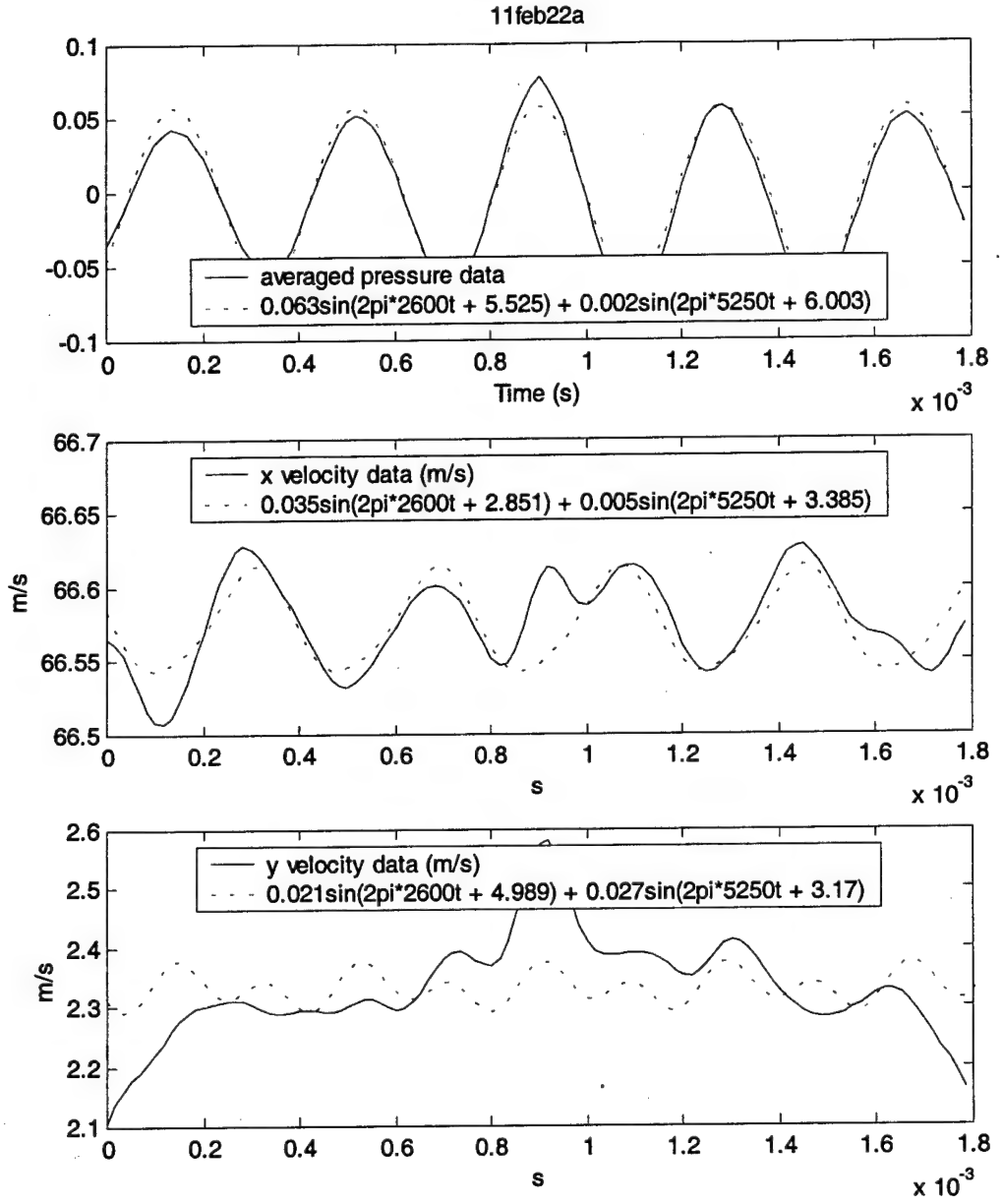

Figure 194. Data and two frequency approximation at x = -1 in, y = 3.625 in

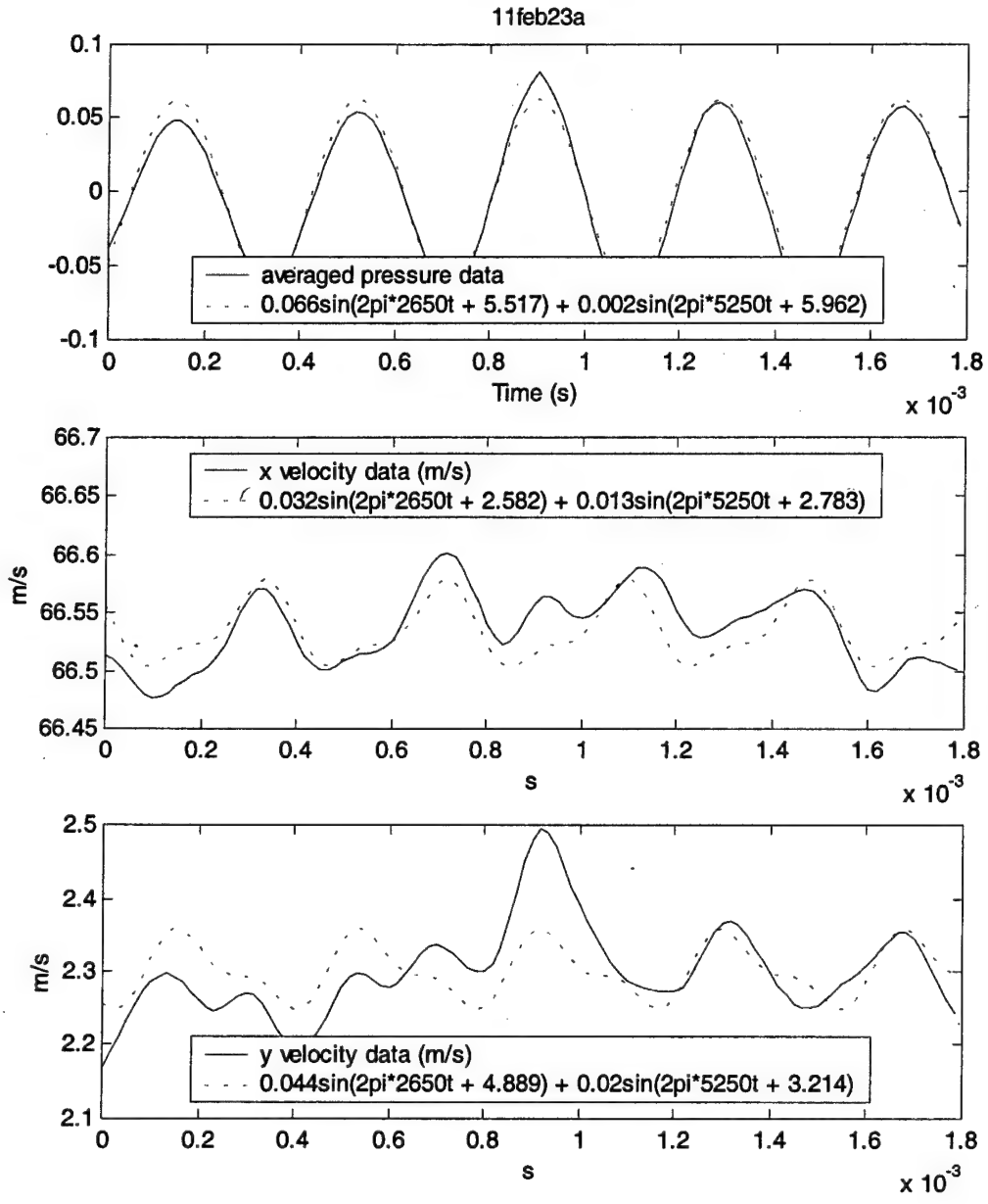

Figure 195. Data and two frequency approximation at x = -1 in, y = 3.875 in

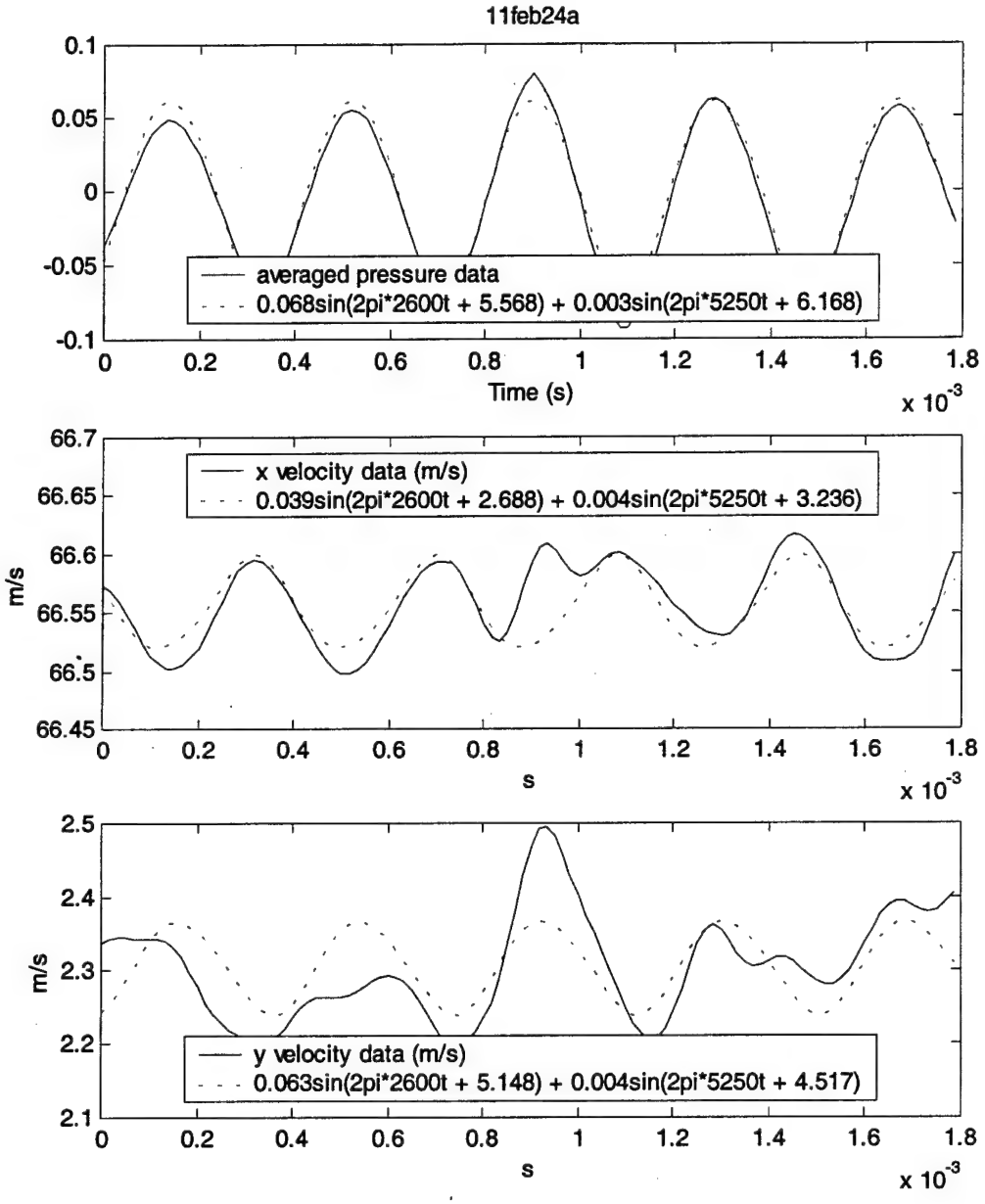

Figure 196. Data and two frequency approximation at x = -1 in, y = 4.125 in

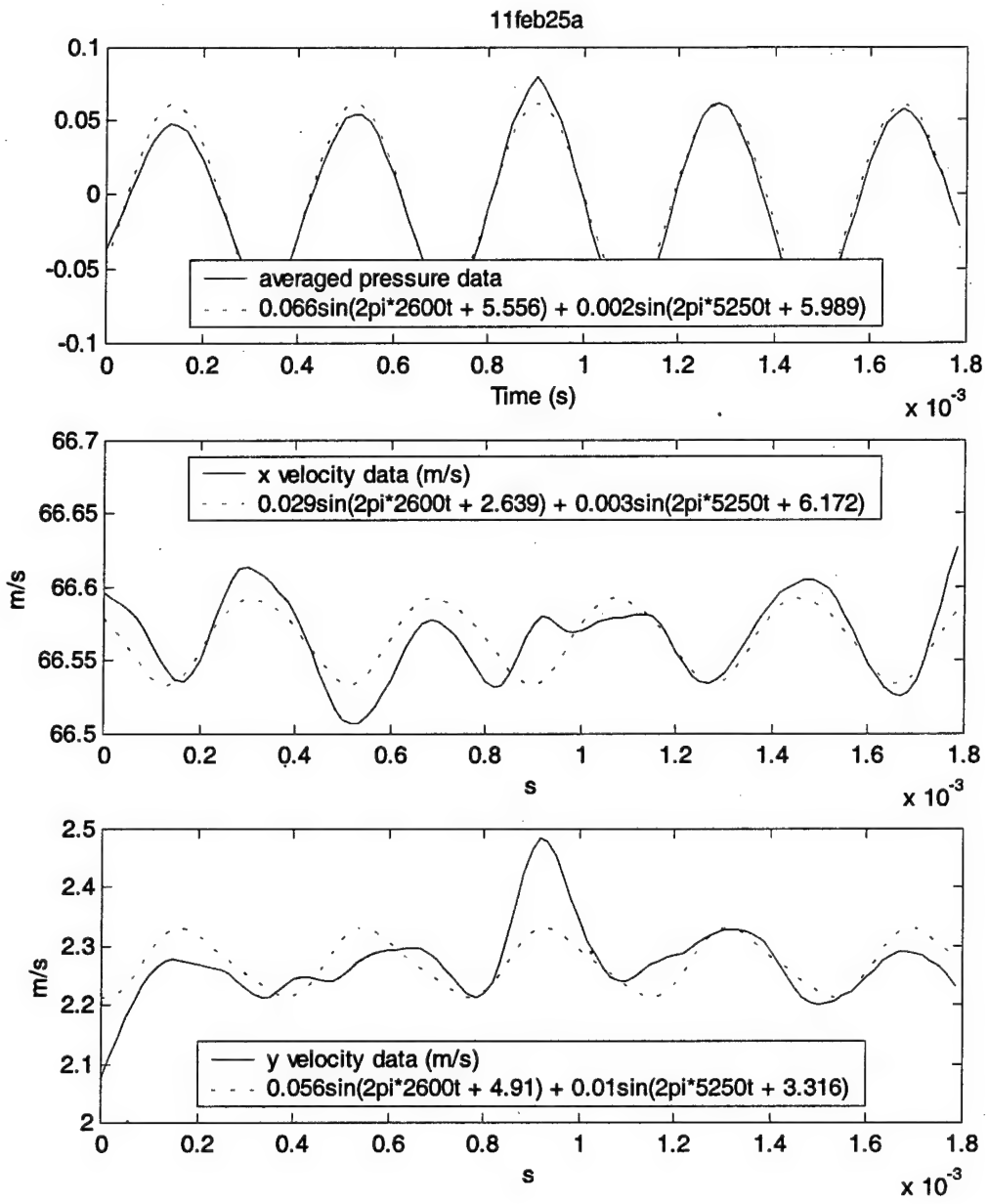

Figure 197. Data and two frequency approximation at x = -1 in, y = 4.375 in

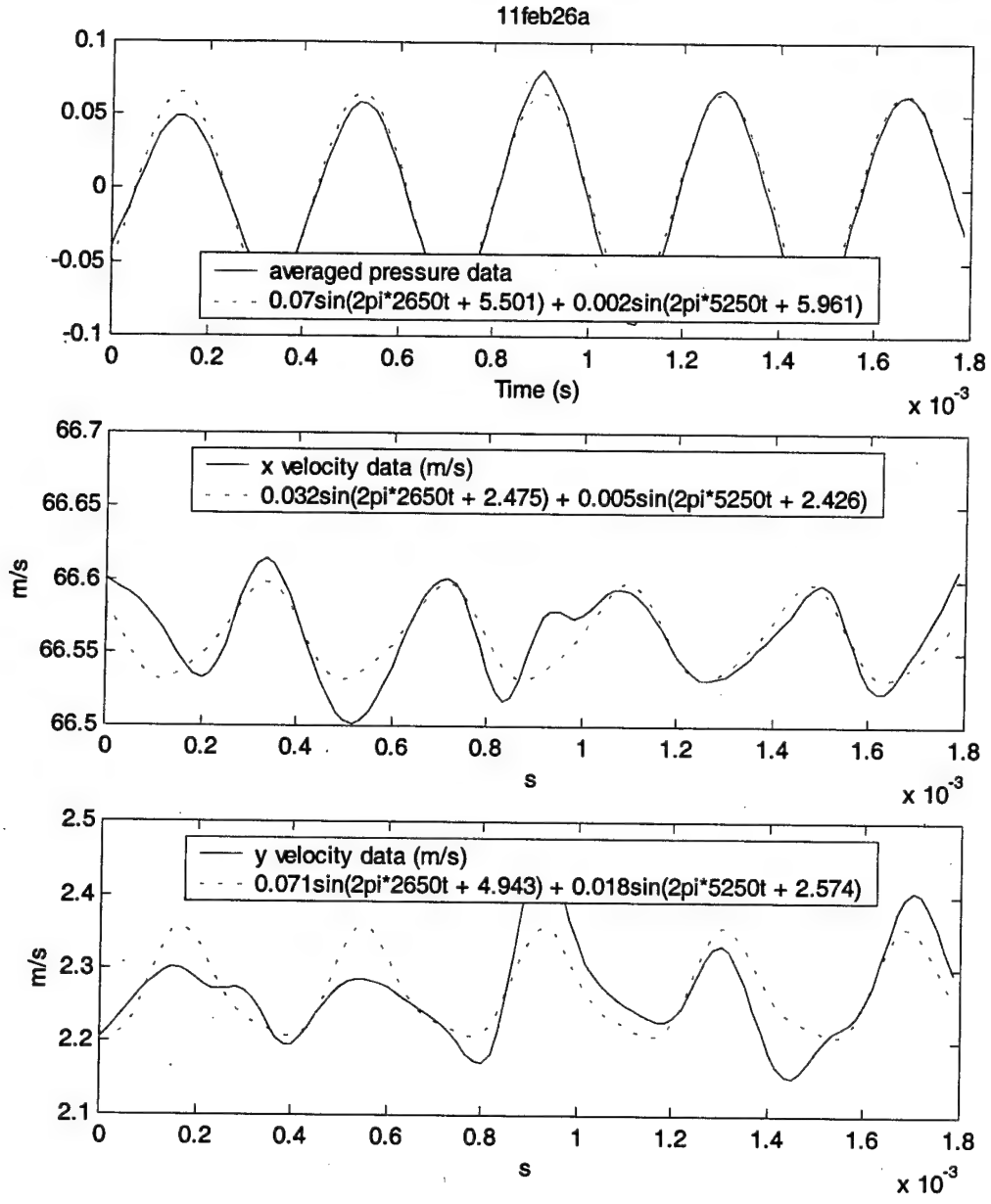

Figure 198. Data and two frequency approximation at x = -1 in, y = 4.625 in

Bibliography

[1] Hill, Philip and Carl Peterson. Mechanics and Thermodynamics of Propulsion, 384-393. Reading MA: Addison-Wesley Publishing Company, 1992.

[2] Korakianitis, Theodosius. "On the Propagation of Viscous Wakes and Potential Flow in Axial-Turbine Cascades," Journal of Turbomachinery, Vol. 115, January 1993, 118-127.

[3] Korakianitis, Theodosius. "Hierarchal Development of Three Direct-Design Methods for Two-Dimensional Axial-Turbomachinery Cascades," Journal of Turbomachinery, Vol. 115, April 1993, 314-324.

[4] Korakianitis, Theodosius. "Influence of Stator-Rotor Gap on Axial-Turbine Unsteady Forcing Functions," AIAA Journal, Vol. 31, July 1993, 1256-1264.

[5] Fabian, Michael K. Unsteady Pressure Distributions Around Compressor Vanes in an Unsteady, Transonic Cascade. Doctoral Dissertation, University of Notre Dame, 1995.

[6] Fabian, Michael K. and Eric J. Jumper. "Unsteady Pressure Distributions around Compressor Vanes in an Unsteady, Transonic Cascade," AIAA paper number 95-0302, 1995.

[7] Fabian, Michael K. and Eric J. Jumper. "Convected and Potential Unsteady Disturbances Interacting with an Unsteady Cascade," AIAA paper number 96-2672, 1996.

[8] Fabian, Michael K. and Eric J. Jumper. "Upstream-Propagating Acoustic Waves Interacting with a Compressible Cascade," AIAA paper number 97-0380, 1997.

[9] Fabian, Michael K. and Eric J. Jumper. "Rearward Forcing of an Unsteady Compressible Cascade," Journal of Propulsion and Power, Nov-Dec 1998.

[10] Wilson, David G. and Theodosius Korakianitis. The Design of High-Efficiency Turbomachinery and Gas Turbines: Upper Saddle River NJ: Prentice-Hall, 1998, 317-322.

[11] Falk, Eric A., Eric J. Jumper, and Michael K. Fabian. "An Experimental Study of Unsteady Forcing in the F-109 Turbofan Engine," AIAA paper number 97-3286, 1997.

[12] Falk, Eric A. and Eric J. Jumper. "Upstream Propagating Potential Waves in the F109 Turbofan Engine Inlet Flow," AIAA paper number 98-3294, 1998.

[13] Falk, Eric A. and Eric J. Jumper. "A Characterization of the Unsteady Velocity Field Aft of the F109 Turbofan Rotor," AIAA paper number 99-0237, 1999.

[14] Falk, Eric A., Eric J. Jumper, and Brenda A. Haven. "Upstream-Propagating Potential Waves Elicited from the Stator Row Downstream of a Fan," AIAA paper number 99-2805, 1999.

[15] Commerford, G. L. and F. O. Carta. "Unsteady Aerodynamic Response of a Two-Dimensional Airfoil at High Reduced Frequency," AIAA Journal, January 1974, 43-48.

[16] Roshko, Anatol. "Experiments on the Flow Past a Circular Cylinder at Very High Reynolds Number," Journal of Fluid Mechanics, Vol. 10, 1961, 345-356.

[17] Allison, Dennis M. Design and Evaluation of a Cascade Test Facility. MS Thesis, Air Force Institute of Technology, 1981.

[18] Costello, Michael J. Off-Design Performance of Crenulated Blades in a Linear Compressor Cascade. MS Thesis, Air Force Institute of Technology, 1993.

[19] TSI Incorporated. IFA 100 System Instruction Manual.

[20] St Germain, Barry W. Tip Vortex and Crenulation Effects in a Compressor with Moving Endwall. MS Thesis, Air Force Institute of Technology, 1999.

[21] Bruun, H. H. Hot-Wire Anemometry Principles and Signal Analysis. Oxford University Press, 1995.

[22] Decook, Steven J. Experimental Investigation of Trailing Edge Crenulation Effects on Losses in a Compressor Cascade. MS Thesis, Air Force Institute of Technology, 1991.

[23] Dantec Measurement Technology. Streamline® Installation and User's Guide.

[24] Schlichting, Hermann. Boundary-Layer Theory, 28-36. New York: McGraw-Hill Book Company, 1968.

[25] Brigham, E. Oran. The Fast Fourier Transform, 141-146. Englewood Cliffs NJ: Prentice-Hall, 1974.

[26] Karamcheti, Krishnamurty. Principles of Ideal-Fluid Aerodynamics, 376-389. New York: John Wiley and Sons, Inc., 1966.

Vita

Captain David Randall Hopper was born 2 May 1969 in Melbourne, Florida. He grew up in Kaysville, Utah, where he graduated from Davis High School in 1987. He then studied mechanical engineering at Brigham Young University in Provo, Utah. Between his freshman and sophomore years, he spent two years as a proselyting missionary for the Church of Jesus Christ of Latter Day Saints in Sendai, Japan. He received a bachelor of science degree in December of 1993 and was recognized as an AFROTC Distinguished graduate and nominated for a regular commission. His first assignment was to undergraduate pilot training at Reese Air Force Base, Texas. After eight months as a student pilot it was clear to both young Lieutenant Hopper and to the Air Force that he could best serve his country as an engineer. After a year as squadron section commander for the 8th Special Operations Squadron, Hurlburt Field, Florida, he became a flight test engineer for Detachment 1, 46th Operations Group, also at Hurlburt Field. As a flight test engineer, Captain Hopper planned and executed flight tests on MH-53J Pave Low and MH/HH-60G Pave Hawk aircraft and other special operations platforms. Captain Hopper was selected in 1998 to attend the Air Force Institute of Technology School of Engineering to earn a Masters of Science Degree in Aeronautical Engineering. After a tour at the National Air Intelligence Center at Wright-Patterson Air Force Base, Ohio, Captain Hopper will become an instructor in the Department of Aeronautics, United States Air Force Academy, Colorado Springs, Colorado. Captain Hopper is married to the former Jennifer Paige Frank of Argyle, New York, and they have two children, Lowell Mitchell and Jonas David.

Permanent Address:
196 East 1050 North
Kaysville, Utah 84037

REPORT DOCUMENTATION PAGE

Form Approved
OMB No. 0704-0188

1. REPORT DATE *(DD-MM-YYYY)*	2. REPORT TYPE	3. DATES COVERED *(From - To)*
18-04-2000	Master's Thesis	

4. TITLE AND SUBTITLE
MEASUREMENTS OF THE EFFECTS OF TUNNEL WALL PROXIMITY ON THE VELOCITY FIELD UPSTREAM OF A ROD WITH VORTEX SHEDDING IN LOW-SPEED FLOW

5a. CONTRACT NUMBER

5b. GRANT NUMBER

5c. PROGRAM ELEMENT NUMBER

6. AUTHOR(S)
Hopper, David R., Captain, USAF

5d. PROJECT NUMBER

5e. TASK NUMBER

5f. WORK UNIT NUMBER

7. PERFORMING ORGANIZATION NAME(S) AND ADDRESS(ES)
Air Force Institute of Technology
Graduate School of Engineering and Management (AFIT/EN)
2950 P Street, Building 640
WPAFB OH 45433-7765

8. PERFORMING ORGANIZATION REPORT NUMBER
AFIT/GAE/ENY/00M-07

9. SPONSORING/MONITORING AGENCY NAME(S) AND ADDRESS(ES)
AFOSR/NA
Attn: Dr. Tom Beutner
801 N Randolph Street
Arlington, VA 22203 (703) 696-6961

10. SPONSOR/MONITOR'S ACRONYM(S)

11. SPONSOR/MONITOR'S REPORT NUMBER(S)

12. DISTRIBUTION/AVAILABILITY STATEMENT
Approved for public release; distribution unlimited

13. SUPPLEMENTARY NOTES
Advisor: Dr. Paul I. King, (937) 255-3636 ext. 4628 paul.king@afit.af.mil

14. ABSTRACT
High cycle fatigue is an important consideration in blade design for turbomachinery. Blades in an engine undergo countless loading cycles in a lifetime, the result of pressure waves that propagate upstream and downstream from disturbances in the flow. Better understanding of these effects would allow blade designers to reduce many effects of high cycle fatigue. An experimental study was undertaken to determine the unsteady flowfield upstream a single cylinder in a subsonic flow. Von Karman vortex shedding from the cylinder produced a forcing function much like periodic blade passage in a turbine engine. A hot wire was used to measure the velocities upstream of the cylinder. Data were ensemble averaged and phase locked with the shedding from the cylinder. The phase and amplitude of unsteady velocity data taken at a series of upstream locations were compared to a model developed from potential theory. The potential model for a single cylinder did not accurately predict the phase and amplitude change upstream the cylinder except when the cylinder was near the center of the tunnel. When virtual cylinders were added to account for endwall reflection, the prediction more closely approximated the behavior of the data. The results of this study indicate that the flowfield upstream a disturbance may be reasonably predicted using elements of potential flow theory.

15. SUBJECT TERMS
Unsteady Flow, Vortices, Vortex Shedding, Wave Propagation, High-Cycle Fatigue, Potential Flow, Acoustic Reflection

16. SECURITY CLASSIFICATION OF:			17. LIMITATION OF ABSTRACT	18. NUMBER OF PAGES	19a. NAME OF RESPONSIBLE PERSON
a. REPORT	b. ABSTRACT	c. THIS PAGE			Paul I. King
Unclassified	Unclassified	Unclassified	UL	279	19b. TELEPHONE NUMBER *(Include area code)* (937) 255-3636 ext. 4628